Integro-differential equations for electromagnetic scattering : analysis and computation for objects with electric contrast

Integro-differential equations for electromagnetic scattering

Analysis and computation for objects with electric contrast

Integro-differential equations for electromagnetic scattering

Analysis and computation for objects with electric contrast

PROEFSCHRIFT

ter verkrijging van de graad van doctor aan de
Technische Universiteit Eindhoven, op gezag van de
Rector Magnificus, prof.dr. R.A. van Santen, voor een
commissie aangewezen door het College voor
Promoties in het openbaar te verdedigen
op dinsdag 16 september 2003 om 16.00 uur

door

Martijn Constant van Beurden

geboren te Mariaheide

Dit proefschrift is goedgekeurd door de promotoren:

prof.dr. A.G. Tijhuis
en
prof.dr.ir. A.P.M. Zwamborn

Copromotor:
dr.ir. S.J.L. van Eijndhoven

Contents

Chapter 1

Introduction

1.1 Analysis of interaction between objects and electromagnetic fields

Over the past century, electromagnetic research has developed from a branch of theoretical physics to a full engineering discipline with a set of tools that contains exact solutions for canonical problems, asymptotic analysis, experiments, and numerical simulations. Here, we will focus on the interaction between electromagnetic fields and objects. In many cases, the analysis of this interaction is part of a design process, in which we would like to find an optimal setting for the object under study, e.g., an optimal geometry of the object or an optimal excitation of the electromagnetic field. Before the advent of computers that are capable of handling large numerical problems, the design process was guided by experiments. Nowadays, the general opinion is that we need numerical methods, possibly combined with asymptotics or parameter extraction, such as reduced-order modeling [40], to simulate and analyze the behavior of the electromagnetic field in a real-life application. The results of these numerical studies can then be verified by a limited number of experiments.

Numerical methods can be very flexible with respect to the class of problems they solve. However, this flexibility comes at a price, in the sense that the computation time and computer resources to solve a problem with a brute-force technique may become prohibitively large, since these numerical methods frequently give rise to large linear systems to guar-

antee sufficient accuracy. This has caused increasing interest in iterative algorithms to solve such large linear systems, for which the matrix-vector product can be computed efficiently, e.g., by means of a Fast Fourier Transformation or by exploiting sparsity, see, e.g., [59, 84, 85, 86, 87]. Therefore, an important trend in computational electromagnetics has been, and still is, to devise numerical methods for which the linear system has an efficient matrix-vector product.

1.2   Parameter variations for design

According to "The concise Oxford dictionary" [69], engineering is the application of science to the design, building, and use of machines, constructions, etc. Therefore, the design process brings together science, art, and experience. A design is subject to a number of specifications, which should be met. Basically, a design is a blueprint together with a set of parameters, for which the proper values should be found. However, the odds of directly finding a parameter setting such that the design matches all specifications at once are negligible. Most design processes can be divided into three stages. In the first stage, there are many possibilities and many proposals are acceptable. At this stage, the blueprint is constructed and the parameters are identified. In the second stage, when several design decisions have already been made, parameter sweeps are used to establish acceptable ranges of the parameters. The parameter sweeps provide rough estimates for the parameter values and for the sensitivity of the design for changes in these parameter values. In the third stage, only small parameter changes are allowed and we have entered the fine-tuning stage of the design process.

From the above, it is clear that the last two stages of the design procedure mainly comprise parameter changes and the analysis of these changes with respect to the specifications. Irrespective of the strategy to change the parameters, the designer needs a tool to analyze the effect of the parameter changes. This tool has to be as time-efficient as possible to make sure that parameter studies can be performed thoroughly. An important advantage of numerical methods is that they allow for parameter studies in a straightforward manner by changing a number of parameter values in the input of these methods, whereas parameter studies in an experimental set-up are associated with the manufacturing of complete prototypes or at least parts of them. Although the fundamental problems of a parameter study have been overcome by resorting to numerical methods, in a real-life situation, the

computation time usually becomes excessively long. The iterative techniques, mentioned in Section 1.1, together with an efficient matrix-vector product can be employed to improve efficiency. However, for parameter studies with a large amount of parameter changes, the total computation time to analyse the design for all these parameter setting can still be longer than desirable for practical applications. In the early stages of parameter studies, the accuracy of the numerical method can be reduced in favor of reduced computation time. Along similar lines, several researchers in the field have come up with methods to further reduce the total computation time for parameter studies. As examples, we mention "space mapping" [5] and "reduced-order modeling", see e.g. [40]. Both techniques aim at the construction of a simplified model of the subject under study, to capture its main characteristics for a broad range of parameter values. The simplified model is constructed by analyzing a limited number of parameter settings and perform an interpolation for intermediate parameter values. As an alternative for these parameter-extraction methods, "marching on in anything" has been proposed [73, 74]. The key observation that led to "marching on in anything" is that, in general, we expect that small parameter changes cause small changes in the solution of the mathematical model, i.e., we have a robust model. This robustness is used to construct an initial estimate for an iterative solution method from solutions with preceding parameter values. Hence, "marching on in anything" still considers the full model, instead of a model based on parameter extraction.

The second aspect that characterizes the design process is the strategy to employ the information that results from parameter variation in such a way that proper values for the parameters can be established. If a designer is in control of this process, it is difficult to assess how these decisions are made. Alternatively, one could try to formulate the design problem in terms of a mathematical optimization problem. At present, several papers have appeared that deal with the formulation of realistic electromagnetic optimization problems for design, see e.g. [20] and references therein. However, there are still a lot of open questions in this field. For the solution of such optimization problems, many algorithms are available. Some authors have opted for statistically oriented optimizers, e.g., genetic algorithms or simulated annealing, while others base their strategy on optimization with the aid of gradient information. Since parameter values are changed gradually in the latter, this strategy is compatible with "marching on in anything". A disadvantage of the gradient-based optimizers is that they require the computation of the gradient with respect to all relevant parameters, which implies additional computational effort. Also, gradient-based optimizers readily end up in a local optimum, whereas statistical algorithms are less sensitive for local optima. On the other hand, gradient-based optimizers are frequently

much more efficient than statistically oriented optimizers.

1.3   Key ingredients for design

The construction of numerical methods to analyze objects in an electromagnetic environment requires a careful balance between factual details and realistic computer resources. This means that we should try to judge how important these details of the real-life situation are to capture the main trends in the behavior of the object in the presence of an electromagnetic field. If we think that a number of details are not crucial for this behavior, we should seriously consider neglecting these details in favor of simpler approximations. Well-known examples are the replacement of thin metallic sheets by infinitely thin perfectly conducting surfaces or the replacement of a complicated propagation path by free space. To study the efficiency of "marching on in anything" for parameter variations, we have chosen to start from simple representatives of a large class of scattering problems. Therefore, we consider three types of objects in free space to model real-life situations. The first one is a perfectly conducting cylinder with circular cross-section to model a wire antenna. The second one is a perfectly conducting infinitely thin flat plate, which represents a patch antenna. The third one is an inhomogeneous dielectric object as a model for the human body. We formulate the interaction between these objects and the electromagnetic field in terms of integro-differential equations and we demonstrate that "marching on in anything", applied to these integro-differential equations, leads to efficient parameter sweeps.

Although the integro-differential equations are meant to model a physical situation, it may happen that these equations do not admit reliable approximations. Therefore we analyze the mapping properties of the integro-differential equations, to find possible limitations in the model formulation. Equations that admit approximations of the solution that are stable for increasingly finer details are known as being "well-posed", whereas equations that do not admit a reliable approximation of the solution are referred to as being "ill-posed". For the thin wire, we show that the so-called reduced-kernel integral equation is ill-posed. As an alternative, we mention that the exact-kernel integral equation is well-posed, although its forcing function needs to be modified to obtain an exact description of the scattering problem. For the perfectly conducting flat plate, well-posedness has been established in the literature, and we briefly discuss these results. Finally, we analyze the integro-differential equation for the inhomogeneous dielectric body, and we show that it is

well-posed, under mild conditions for the dielectric properties of the object. The analysis also holds for the time-harmonic cases in which the object, or the background, or both are lossless. To the best of the author's knowledge, the latter result is not known in the literature.

The mapping properties of the integro-differential equations should be kept in mind when we construct a numerical method to solve these equations, since they indicate whether we can expect a reliable approximation of the solution. The first step in the process of constructing a numerical method is known as discretization. This results in a system of linear equations that can be solved by numerical linear-algebra techniques, such as the LU-decomposition, the singular-value decomposition, or the conjugate-gradient method. The first two techniques aim at an exact construction of the solution of the linear system, whereas the latter usually generates an approximate solution, since the algorithm is terminated after a prescribed error criterion has been satisfied. To arrive at a linear system with an efficient matrix-vector product, special attention is devoted to the discretization process. In particular, the choice of a uniform mesh is important, since it leads to a matrix-vector product in the form of discrete convolutions that can be computed by means of Fast Fourier Transformations. In this thesis, we construct numerical methods for the wire and the flat plate. With the aid of these numerical schemes, we illustrate the consequences of the ill-posedness of the thin-wire equation with reduced kernel and the conditional well-posedness of the perfectly conducting flat plate. Further, we improve the approximation of the solution of the thin-wire equation with reduced kernel by means of regularization and filtering. After the construction of these numerical schemes, we formulate an equation for the derivative with respect to one of the physical parameters. This second step is relevant for the application of gradient-based optimizers. In particular, we derive an equation and construct a numerical scheme for the derivative with respect to the physical parameter length of a perfectly conducting flat plate. We compare the results with two finite-difference schemes and we demonstrate that one of the finite-difference schemes provides accurate estimates for this derivative with respect to length. Subsequently, we show that the application of marching on in anything renders parameter sweeps much more efficient for our three problems. As a special case, we demonstrate the construction of a time-domain simulation by multiple-frequency computations on a fixed mesh, to overcome instabilities associated with a direct computation in the time domain by marching on in time.

Finally, in this thesis, we apply gradient-based non-linear optimization techniques to the

numerical methods for straight thin-wire antennas. We optimize the gain of a Yagi-Uda antenna and the radiation pattern of an array of straight wires. For the Yagi-Uda antenna, we compare two strategies. In the first one, we regard the set of linear equations for the current on the wire antenna as a set of non-linear constraints for the parameters. In the second strategy, we solve these equations for the current on the wire in an internal function. The results indicate that the latter strategy is less demanding for the non-linear optimizer than the first one. This points into the direction of applying marching on in anything to the internal process of solving the linear system, to obtain a more efficient design technique.

1.4   Outline of the thesis

In Chapter 2, we formulate integro-differential equations that describe the interaction between a perfectly conducting straight thin wire, a perfectly conducting flat plate, and a dielectric object on the one hand, and the electromagnetic field on the other hand. The mapping properties of these integro-differential equations are analyzed in Chapter 3, and in Chapter 4 we discuss the construction of efficient numerical methods for the wire and the flat plate. We formulate an integro-differential equation for the derivative with respect to the length of the perfectly conducting flat plate and demonstrate a numerical scheme for it in Chapter 5. In Chapter 6, we apply the marching-on-in-anything technique to the integro-differential equations of our three types of scattering problems and we show that this technique renders parameter sweeps much more efficient. In Chapter 7, we apply non-linear optimization techniques to the numerical methods for straight thin-wire antennas. Finally, our conclusions and recommendations are presented in Chapter 8.

Chapter 2

Formulations for the electromagnetic field

To model the behavior of the electromagnetic field in the presence of objects, we need a mathematical framework to formulate scattering problems for this field. We will consider three types of objects for which we will formulate integro-differential equations. These objects are a perfectly conducting straight thin wire, a perfectly conducting flat plate and an inhomogeneous dielectric object of arbitrary geometrical shape, all embedded in free space, together with the sources of the electromagnetic field. The thin wire is a model for a wire antenna, the flat plate is a model for a patch antenna, and the inhomogeneous dielectric object is a model for the human body. In all three cases, the integro-differential equations are obtained from integral representations for the scattered electromagnetic field.

2.1 Maxwell's equations

The behavior of electric and magnetic fields is governed by Maxwell's equations. These equations form a system of first-order partial differential equations, corresponding to a series of experiments. For continuously differentiable vector-fields, Maxwell's equations

are classically given by

$$\nabla_{\boldsymbol{r}} \times \boldsymbol{\mathcal{H}} = \boldsymbol{\mathcal{J}} + \partial_t \boldsymbol{\mathcal{D}}, \tag{2.1a}$$

$$\nabla_{\boldsymbol{r}} \times \boldsymbol{\mathcal{E}} = -\partial_t \boldsymbol{\mathcal{B}}, \tag{2.1b}$$

where $\boldsymbol{r}$ contains the space variables, $\boldsymbol{\mathcal{H}}$ is the magnetic-field strength, $\boldsymbol{\mathcal{J}}$ is the electric-current density, t is the time variable, $\boldsymbol{\mathcal{D}}$ is the electric-flux density, $\boldsymbol{\mathcal{E}}$ is the electric-field strength and $\boldsymbol{\mathcal{B}}$ is the magnetic-flux density. Maxwell's equations are supplemented with the law of conservation of charge, which is also known as the continuity equation for charge density and current density, viz.

$$\nabla_{\boldsymbol{r}} \cdot \boldsymbol{\mathcal{J}} + \partial_t \varrho = 0, \tag{2.2}$$

where ϱ is the electric-charge density. Both $\boldsymbol{\mathcal{J}}$ and ϱ concern the free charged particles. The above equation indicates that a time-rate of change in the electric-charge density amounts to an electric-current density. Further, we demand that the fields are causal in time, i.e., for every fixed point in space $\boldsymbol{r}$, there is a time $t_0(\boldsymbol{r})$, such that the electromagnetic field is identically zero for $t < t_0(\boldsymbol{r})$ in a neighborhood of $\boldsymbol{r}$. In particular, we assume that in a neighborhood of our objects under consideration, the electromagnetic field is identically zero for $t \leq 0$. The conservation of charge combined with Maxwell's equations and the causality principle gives rise to the following set of auxiliary equations

$$\nabla_{\boldsymbol{r}} \cdot \boldsymbol{\mathcal{B}} = 0, \tag{2.3a}$$

$$\nabla_{\boldsymbol{r}} \cdot \boldsymbol{\mathcal{D}} = \varrho. \tag{2.3b}$$

Although Maxwell's equations are coordinate-independent owing to the coordinate-free definition of the curl and divergence operators, actual computations require a coordinate system. We will use a right-handed Cartesian reference system with position vector $\boldsymbol{r}$

$$\boldsymbol{r} = x\boldsymbol{u}_x + y\boldsymbol{u}_y + z\boldsymbol{u}_z, \tag{2.4}$$

equipped with a scalar product denoted by $\cdot$ and a vector product denoted by $\times$. The length of a vector is expressed as

$$|\boldsymbol{r}| = \sqrt{\boldsymbol{r} \cdot \boldsymbol{r}} = \sqrt{x^2 + y^2 + z^2}. \tag{2.5}$$

To eliminate the temporal behavior of the electromagnetic fields, we apply a Laplace transformation with respect to the time variable to Eq. (2.1), according to

$$\boldsymbol{F}(s) = \int_0^\infty \boldsymbol{\mathcal{F}}(t) \exp(-st) dt, \quad \mathrm{Re}\{s\} \geq 0, \tag{2.6}$$

assuming that $\boldsymbol{\mathcal{F}}(t)$ is integrable with respect to t. Notice the change of notation between time-domain vectors and Laplace-domain vectors. The corresponding inverse of the Laplace transformation is given by

$$\boldsymbol{\mathcal{F}}(t) = \frac{1}{2\pi j} \int\limits_{\delta-j\infty}^{\delta+j\infty} F(s) \exp(st)ds = \frac{1}{2\pi} \int\limits_{-\infty}^{\infty} \boldsymbol{F}(\delta + j\omega) \exp[(\delta + j\omega)t]d\omega, \qquad (2.7)$$

and $\delta \geq 0$. Time-domain quantities are inherently real-valued. Hence, the integral along the Bromwich contour can be reduced to

$$\boldsymbol{\mathcal{F}}(t) = \frac{\exp(\delta t)}{\pi}\mathrm{Re}\left\{ \int\limits_{0}^{\infty} \boldsymbol{F}(\delta + j\omega) \exp(j\omega t)d\omega \right\}. \qquad (2.8)$$

In most cases we will let the real part of the Laplace parameter s become zero, which should be understood as

$$s = \lim_{\delta\downarrow 0} \delta + j\omega, \qquad (2.9)$$

where $\omega \geq 0$ is the radial frequency. Further, for $\delta = 0$, we define the frequency $f = \omega/2\pi$. After the Laplace transformation, Maxwell's equations read

$$\nabla \times \boldsymbol{H} = \boldsymbol{J} + s\boldsymbol{D}, \qquad (2.10a)$$

$$\nabla \times \boldsymbol{E} = -s\boldsymbol{B}, \qquad (2.10b)$$

supplemented with the law of conservation of charge

$$\nabla \cdot \boldsymbol{J} + s\rho = 0, \qquad (2.11)$$

and the auxiliary equations

$$\nabla \cdot \boldsymbol{B} = 0, \qquad (2.12a)$$

$$\nabla \cdot \boldsymbol{D} = \rho, \qquad (2.12b)$$

where we have replaced $\nabla_{\boldsymbol{r}}$ by ∇ for convenience, since there is no confusion with other coordinate systems. We will use this notation henceforth.

2.2   Boundary conditions and constitutive relations

To arrive at a system of partial differential equations with a unique solution, we must supplement Maxwell's equations by boundary conditions and constitutive relations, i.e.,

relations between the field quantities. With respect to the boundary conditions, we distinguish two kinds: one kind at the interface between two media with different material properties, also known as interface conditions, and one kind that describes the behavior of the fields at infinity, referred to as the radiation conditions. The radiation conditions will be discussed in Section 2.4. For the smooth interface $\partial \mathcal{D}$ between region 1 and region 2 with normal $\boldsymbol{n}$ pointing into region 2, we have

$$\boldsymbol{n} \times (\boldsymbol{E}_2 - \boldsymbol{E}_1) = \boldsymbol{0}, \tag{2.13a}$$

$$\boldsymbol{n} \times (\boldsymbol{H}_2 - \boldsymbol{H}_1) = \boldsymbol{J}_S, \tag{2.13b}$$

$$\boldsymbol{n} \cdot (\boldsymbol{B}_2 - \boldsymbol{B}_1) = 0, \tag{2.13c}$$

$$\boldsymbol{n} \cdot (\boldsymbol{D}_2 - \boldsymbol{D}_1) = \rho_S, \tag{2.13d}$$

where the subscripts 1 and 2 indicate the limits of the fields on opposite sides of the interface $\partial \mathcal{D}$ in region 1 and 2, respectively, $\boldsymbol{J}_S$ is an electric surface current density flowing along and tangential to the interface and ρ_S is the surface charge density at the interface. Additionally, we have the law of conservation of surface charge

$$\nabla_s \cdot \boldsymbol{J}_S + \boldsymbol{n} \cdot (\boldsymbol{J}_2 - \boldsymbol{J}_1) = -s\rho_S, \tag{2.14}$$

where $\nabla_s \cdot \boldsymbol{J}_S$ denotes the surface divergence of the surface current density. This relation is similar to the law of conservation of charge for volume densities. In Appendix A, the definition of the surface divergence is given and the law of conservation of surface charge is derived.

For the constitutive relations, the Laplace domain is particularly useful. These relations express the influence of matter on the electromagnetic field and vice versa. In free space we have

$$\boldsymbol{B} = \mu_0 \boldsymbol{H}, \tag{2.15a}$$

$$\boldsymbol{D} = \varepsilon_0 \boldsymbol{E}, \tag{2.15b}$$

$$\boldsymbol{J} = \boldsymbol{0}, \tag{2.15c}$$

where μ_0 is the permeability of free space and ε_0 is the permittivity of free space. In the presence of matter, contained in a volume $\mathcal{D}$, we have

$$\boldsymbol{B} = \mu_0 (\boldsymbol{H} + \boldsymbol{M}), \tag{2.16a}$$

$$\boldsymbol{D} = \varepsilon_0 \boldsymbol{E} + \boldsymbol{P}, \tag{2.16b}$$

where we have introduced the polarization field $\boldsymbol{P}$ and the magnetization field $\boldsymbol{M}$. The vector fields $\boldsymbol{J}$, $\boldsymbol{M}$, and $\boldsymbol{P}$ consist of a primary part and a secondary part. The primary part is not influenced by the electromagnetic field, i.e., it is independent of $\boldsymbol{E}$ and $\boldsymbol{H}$, whereas the secondary part expresses the interaction between matter and the electromagnetic field. For linearly reacting media with time-invariant reaction, we will use the generally accepted constitutive relations

$$\boldsymbol{J}^{sec} = \sigma(\boldsymbol{r}, s)\boldsymbol{E}, \tag{2.17a}$$

$$\boldsymbol{M}^{sec} = \chi_m(\boldsymbol{r}, s)\boldsymbol{H}, \tag{2.17b}$$

$$\boldsymbol{P}^{sec} = \varepsilon_0 \chi_e(\boldsymbol{r}, s)\boldsymbol{E}, \tag{2.17c}$$

where we have indicated the secondary part of the vector fields by a superscript ^{sec}. The functions σ, χ_m and χ_e are either scalars, in the isotropic case, or tensors from $\mathbb{C}^3 \times \mathbb{C}^3$ to $\mathbb{C}$, in case of anisotropy, and are known as the conductivity, the magnetic susceptibility, and the electric susceptibility of the medium, respectively. Upon combining Eqs (2.16) and (2.17), we arrive at

$$\boldsymbol{B} = \mu(\boldsymbol{r}, s)\boldsymbol{H} + \mu_0 \boldsymbol{M}^{prim}, \tag{2.18a}$$

$$\boldsymbol{D} = \varepsilon(\boldsymbol{r}, s)\boldsymbol{E} + \boldsymbol{P}^{prim}, \tag{2.18b}$$

$$\boldsymbol{J} = \sigma(\boldsymbol{r}, s)\boldsymbol{E} + \boldsymbol{J}^{prim}. \tag{2.18c}$$

Again, the functions μ and ε are either scalars, in the isotropic case, or tensors from $\mathbb{C}^3 \times \mathbb{C}^3$ to $\mathbb{C}$, in case of anisotropy. The function μ is known as the permeability of the medium and ε is the permittivity of the medium. The superscripts ^{prim} indicate primary matter fields, which appear as impressed sources in our problems.

At the interface between two penetrable media, i.e., on both sides of the interface, μ, ε, and σ remain finite, the surface current density in (2.13) appears only as a primary field. In case the relations (2.18) hold and the primary fields are absent, the set of boundary conditions can be written as

$$\boldsymbol{n} \times (\boldsymbol{E}_2 - \boldsymbol{E}_1) = \boldsymbol{0}, \tag{2.19a}$$

$$\boldsymbol{n} \times (\boldsymbol{H}_2 - \boldsymbol{H}_1) = \boldsymbol{0}, \tag{2.19b}$$

$$\boldsymbol{n} \cdot (\mu_2 \boldsymbol{H}_2 - \mu_1 \boldsymbol{H}_1) = 0, \tag{2.19c}$$

$$\boldsymbol{n} \cdot (\varepsilon_2 \boldsymbol{E}_2 - \varepsilon_1 \boldsymbol{E}_1) = \rho_S, \tag{2.19d}$$

$$\boldsymbol{n} \cdot (\sigma_2 \boldsymbol{E}_2 - \sigma_1 \boldsymbol{E}_1) = -s\rho_S. \tag{2.19e}$$

Upon combining Eqs (2.19d) and (2.19e), we arrive at

$$\boldsymbol{n} \cdot [(\sigma_2 + s\varepsilon_2)\boldsymbol{E}_2 - (\sigma_1 + s\varepsilon_1)\boldsymbol{E}_1] = 0. \tag{2.20}$$

In case region 1 represents a perfectly electric conducting medium, which is an example of an impenetrable medium, and region 2 is penetrable, the surface current density $\boldsymbol{J}_S$ will be present in general. If there are no primary fields present in region 1, the electromagnetic field in region 1 will vanish. In case the primary fields in both region 1 and 2 are absent, we obtain the boundary conditions

$$\boldsymbol{n} \times \boldsymbol{E}_2 = \boldsymbol{0}, \tag{2.21a}$$

$$\boldsymbol{n} \times \boldsymbol{H}_2 = \boldsymbol{J}_S, \tag{2.21b}$$

$$\boldsymbol{n} \cdot (\mu_2 \boldsymbol{H}_2) = 0, \tag{2.21c}$$

$$\boldsymbol{n} \cdot (\varepsilon_2 \boldsymbol{E}_2) = \rho_S. \tag{2.21d}$$

2.3   Energy and function spaces

Energy is one of the most fundamental concepts of physics. From a mathematical point of view, this concept leads to the identification of function spaces, in which we would like to find a description of the electromagnetic field. We discuss this in more detail in Chapter 3. In the time-harmonic case, i.e., in the Laplace domain with $\text{Re}\{s\} = 0$, energy is introduced through the complex Poynting vector $\boldsymbol{S}$

$$\boldsymbol{S} = \boldsymbol{E} \times \boldsymbol{H}^*, \tag{2.22}$$

where * indicates complex conjugation. The expression $\frac{1}{2}\text{Re}\{\boldsymbol{S}\}$ can be interpreted as the time-averaged power-flux density. Upon analyzing the divergence of the Poynting vector on a bounded domain $\mathcal{D}$ with sufficiently smooth boundary $\partial\mathcal{D}$ and using Maxwell's equations together with Eq. (2.18), we arrive at the complex power balance

$$
-\iiint\limits_{\mathcal{D}} (\boldsymbol{E} \cdot \boldsymbol{J}_0^* + \boldsymbol{K}_0 \cdot \boldsymbol{H}^*) \, dV = j\omega \iiint\limits_{\mathcal{D}} (\mu \boldsymbol{H} \cdot \boldsymbol{H}^* - \varepsilon^* \boldsymbol{E}^* \cdot \boldsymbol{E}) \, dV
$$
$$
+ \iiint\limits_{\mathcal{D}} \sigma \boldsymbol{E}^* \cdot \boldsymbol{E} \, dV + \oiint\limits_{\partial\mathcal{D}} (\boldsymbol{E} \times \boldsymbol{H}^*) \cdot \boldsymbol{n} \, dA, \tag{2.23}
$$

where

$$\boldsymbol{J}_0 = \boldsymbol{J}^{prim} + j\omega\boldsymbol{P}^{prim}, \tag{2.24a}$$

$$\boldsymbol{K}_0 = j\omega\mu_0\boldsymbol{M}^{prim}. \tag{2.24b}$$

From now on $\boldsymbol{n}$ will denote the outward-pointing unit normal vector on $\partial\mathcal{D}$, unless stated otherwise. Further, we have assumed that the conductivity σ is real-valued.

The integral on the left-hand side of the power balance represents the power generated by the primary sources $\boldsymbol{J}_0$ and $\boldsymbol{K}_0$. On the right-hand side we find the harmonic variation of the stored electromagnetic energy, which possibly involves losses, the dissipated power corresponding to Ohm's law, and the power radiated through the interface $\partial\mathcal{D}$. From the power balance we observe that, if the constitutive parameters remain finite and if the quantities $\boldsymbol{E} \cdot \boldsymbol{E}^*$ and $\boldsymbol{H} \cdot \boldsymbol{H}^*$ are integrable on the domain $\mathcal{D}$, the dissipated power and the stored energy in $\mathcal{D}$ remain finite, thereby introducing the function space

$$L^2(\mathcal{D})^3 = \left\{ \boldsymbol{f} \mid \boldsymbol{f} \cdot \boldsymbol{f}^* \in L^1(\mathcal{D}) \right\}, \tag{2.25}$$

where $L^1(\mathcal{D})$ is the space of Lebesgue-integrable functions, and the superscript [3] indicates three-dimensional vector fields. This leads to the conclusion that $L^2(\mathcal{D})^3$ is an appropriate function space for $\boldsymbol{E}$ and $\boldsymbol{H}$ under finite-energy conditions. The space $L^2(\mathcal{D})^3$ is a Hilbert space with inner product

$$(\boldsymbol{f}, \boldsymbol{g}) = \iiint\limits_{\mathcal{D}} \boldsymbol{f} \cdot \boldsymbol{g}^* dV, \tag{2.26}$$

and norm

$$\|\boldsymbol{f}\| = \sqrt{(\boldsymbol{f}, \boldsymbol{f})} = \left\{ \iiint\limits_{\mathcal{D}} \boldsymbol{f} \cdot \boldsymbol{f}^* dV \right\}^{\frac{1}{2}}, \tag{2.27}$$

for all $\boldsymbol{f}, \boldsymbol{g} \in L^2(\mathcal{D})^3$.

However, we can further identify the space of the electric and magnetic fields by taking into account Maxwell's equations, Eq. (2.10), for linearly reacting media. If we assume that the primary fields $\boldsymbol{J}^{prim}$, $\boldsymbol{M}^{prim}$, and $\boldsymbol{P}^{prim}$ also belong to $L^2(\mathcal{D})^3$, which excludes point sources and line sources, and that the material parameters remain bounded, then both $\nabla \times \boldsymbol{E}$ and $\nabla \times \boldsymbol{H}$ should belong to $L^2(\mathcal{D})^3$. So, naturally we arrive at the following function space for both $\boldsymbol{E}$ and $\boldsymbol{H}$, see e.g. [35]

$$H(\mathrm{curl}, \mathcal{D}) = \left\{ \boldsymbol{f} \mid \boldsymbol{f} \in L^2(\mathcal{D})^3, \nabla \times \boldsymbol{f} \in L^2(\mathcal{D})^3 \right\}, \tag{2.28}$$

with inner product and norm

$$(\boldsymbol{f}, \boldsymbol{g})_{\mathrm{curl}} = (\boldsymbol{f}, \boldsymbol{g}) + (\nabla \times \boldsymbol{f}, \nabla \times \boldsymbol{g}), \qquad (2.29\mathrm{a})$$

$$\|\boldsymbol{f}\|_{\mathrm{curl}} = \sqrt{(\boldsymbol{f}, \boldsymbol{f})_{\mathrm{curl}}}, \qquad (2.29\mathrm{b})$$

for all $\boldsymbol{f}, \boldsymbol{g} \in H(\mathrm{curl}, \mathcal{D})$.

Strictly speaking, these conclusions only apply to the time-harmonic case. However, since the time-harmonic case is included in the Laplace domain, we will assume that the conclusions from the derivation given above extend to the Laplace domain, i.e., we will assume that the primary matter fields belong to $L^2(\mathcal{D})^3$. In case the Laplace transforms $F(s)$ and $G(s)$, which correspond to real-valued time-domain quantities $f(t)$ and $g(t)$, are continuous for all s, with $\mathrm{Re}\{s\} \geq \delta$, and square integrable on the line $\mathrm{Re}\{s\} = \delta$, we have the identity

$$\int\limits_{-\infty}^{\infty} F(\delta + j\omega) G^*(\delta + j\omega) d\omega = \frac{1}{2\pi} \int\limits_{0}^{\infty} f(t) g(t) \exp(-2\delta t) dt. \qquad (2.30)$$

If we combine this equation with the power balance in the time domain for linearly reacting media in the domain $\mathcal{D}$, we arrive at the conclusion that the electromagnetic energy in $\mathcal{D}$ increases at most exponentially as $t \to \infty$, where the exponent is determined by 2δ. This means that the time-domain energy is a slowly increasing function in time, in the sense of the theory of tempered distributions.

At a first glance, we would expect that the continuously differentiable vector functions are the proper candidates for $\boldsymbol{E}$ and $\boldsymbol{H}$ and one may wonder how to get from the space of continuously differentiable vector functions to vector functions in $L^2(\mathcal{D})^3$ or $H(\mathrm{curl}, \mathcal{D})$. The basic idea is that the space of continuously differentiable vector functions is dense in $L^2(\mathcal{D})^3$ and $H(\mathrm{curl}, \mathcal{D})$ [11] and that continuously differentiable vector functions still allow an interpretation in terms of the power balance. Therefore, using the norms of these spaces to define the limiting process, we can interpret elements of $L^2(\mathcal{D})^3$ and $H(\mathrm{curl}, \mathcal{D})$ as the result of a limiting process of a sequence of continuously differentiable vector functions. In the same way we can apply the differential operator $\nabla \times$ to elements in $H(\mathrm{curl}, \mathcal{D})$. Distribution theory offers an alternative: we can define the operator $\nabla \times$ in a distributional sense, where we employ the duality between the space of testing functions $\mathscr{D}(\mathcal{D})$ and the space of distributions $\mathscr{D}'(\mathcal{D})$.

2.4   Radiation and potentials

One of the most striking properties of Maxwell's equations is their linearity, i.e., the superposition principle holds. This principle allows us to separate the electric and magnetic fields with respect to their origin. We will distinguish between incident fields, originating from a primary source in free space, and scattered fields, caused by the presence of objects from which the incident fields scatter. Hence we write

$$\boldsymbol{E} = \boldsymbol{E}^i + \boldsymbol{E}^s, \tag{2.31a}$$

$$\boldsymbol{H} = \boldsymbol{H}^i + \boldsymbol{H}^s. \tag{2.31b}$$

The superscript ^{i} indicates the incident field, whereas ^{s} indicates the scattered field. Although incident fields usually originate from primary sources, we will also consider source-free solutions of Maxwell's equations, e.g., plane waves in case of free space. These plane waves can also be interpreted as fields generated by sources at infinity.

Electromagnetic fields scattered by objects in free space exhibit radiation. To describe this mathematically, we construct a model by using Maxwell's equations, together with the constitutive relations and boundary conditions, as discussed in the preceding sections. In this model, certain assumptions are made, such as infinite free space, sharp corners and edges, perfectly conducting materials, etc. This may lead to mathematical difficulties that are not related to physical phenomena in the real world. Therefore, we aim to supplement these models with additional criteria to prevent this type of problems. An example of such criteria is given by the "radiation conditions".

Upon analyzing solutions of Maxwell's equations in the Laplace domain for a source in free space, we are left with the problem that there are two independent candidate solutions of the resulting equations. To describe these solutions, we have to distinguish between the cases $\mathrm{Re}\{s\} > 0$ and $\mathrm{Re}\{s\} = 0$. For $\mathrm{Re}\{s\} = 0$, the two solutions correspond to energy moving from the source towards infinity and energy coming from infinity and moving towards the source, for increasing time. It is clear that the second solution does not meet the requirement of causality, since the effect of a source on a wave field travels from the source towards the observation point. This relation between energy flow and causality is expressed by the "radiation conditions", which we will now introduce.

Consider a sphere of radius R. Let the boundary of the sphere be denoted by $\partial\mathcal{B}$. Then the following conditions for the scattered electromagnetic field should hold uniformly with

respect to the direction $\boldsymbol{n}$ as $R \to \infty$

$$|R\boldsymbol{E}^s|_{\partial\mathcal{B}}| \leq K, \tag{2.32a}$$

$$|R\boldsymbol{H}^s|_{\partial\mathcal{B}}| \leq K, \tag{2.32b}$$

$$R\left[(\omega\mu_0\boldsymbol{n} \times \boldsymbol{H}^s + k_0\boldsymbol{E}^s)|_{\partial\mathcal{B}}\right] \to \boldsymbol{0}, \tag{2.32c}$$

$$R\left[(k_0\boldsymbol{n} \times \boldsymbol{E}^s - \omega\mu_0\boldsymbol{H}^s)|_{\partial\mathcal{B}}\right] \to \boldsymbol{0}, \tag{2.32d}$$

$$\boldsymbol{E}^s, \boldsymbol{H}^s \in L^2_{loc}(\mathbb{R}^3)^3, \tag{2.32e}$$

where $k_0 = \omega\sqrt{\varepsilon_0\mu_0}$. Further, $\boldsymbol{f} \in L^2_{loc}(\mathbb{R}^3)^3$ means that, upon multiplying $\boldsymbol{f}$ by a C_0^∞ function with compact support, the resulting function must be an element of $L^2(\mathbb{R}^3)^3$. The conditions (2.32c) and (2.32d) are known as the Silver-Müller conditions [14]. Condition (2.32e) expresses the need for locally finite energy of the electromagnetic field.

The Silver-Müller conditions indicate that, for $\omega \neq 0$ and R sufficiently large, the electromagnetic field becomes locally transverse with respect to the direction $\boldsymbol{n}$, and that we can use the approximations (indicated by $\doteq$)

$$\boldsymbol{E}^s \doteq -Z_0(\boldsymbol{n} \times \boldsymbol{H}^s), \tag{2.33a}$$

$$\boldsymbol{H}^s \doteq Y_0(\boldsymbol{n} \times \boldsymbol{E}^s), \tag{2.33b}$$

where $Z_0 = Y_0^{-1} = \sqrt{\mu_0/\varepsilon_0}$. Taking the vector product of Eq. (2.33a) with $\boldsymbol{H}^{s*}$ and using Eq. (2.33b) yields

$$\boldsymbol{S} = \boldsymbol{E}^s \times \boldsymbol{H}^{s*} \doteq Z_0 |\boldsymbol{H}^s|^2 \boldsymbol{n}, \tag{2.34}$$

which indicates that, regarding the scattered fields, the Poynting vector $\boldsymbol{S}$ is pointing outwards for $\omega \neq 0$ and R sufficiently large. Hence, energy of the scattered electromagnetic field is flowing away from the object towards infinity.

For $\text{Re}\{s\} > 0$, the two solutions are characterized by exponentially increasing and exponentially decaying electromagnetic fields when the point of observation moves from the object towards infinity. If we consider the integrals

$$I_e = \iiint_\mathcal{D} \boldsymbol{E}^s \cdot \boldsymbol{E}^{s*} dV, \tag{2.35a}$$

$$I_m = \iiint_\mathcal{D} \boldsymbol{H}^s \cdot \boldsymbol{H}^{s*} dV, \tag{2.35b}$$

for increasing volumes $\mathcal{D}$, I_e and I_m increase without bound for the exponentially increasing solution. Therefore, this solution does not satisfy $\boldsymbol{E}^s, \boldsymbol{H}^s \in L^2(\mathbb{R}^3)^3$. Hence, for $\text{Re}\{s\} > 0$,

the first four conditions of the radiation conditions are replaced by demanding exponential decay of the electric and magnetic field components. Alternatively, the complete set of conditions can be replaced by

$$\boldsymbol{E}^s, \ \boldsymbol{H}^s \in L^2(\mathbb{R}^3)^3. \tag{2.36}$$

Under this condition, the solution for $\delta \downarrow 0$ coincides with the solution for which the Silver-Müller conditions hold.

For a bounded object in free space with finite constitutive parameters and a finite number of sharp corners in these parameters, the radiation conditions ensure that Maxwell's equations have a unique solution. For an object consisting of a lossless medium surrounded by a perfectly conducting shell, uniqueness cannot be proven for $\mathrm{Re}\{s\} = 0$, unless the object has no interior, e.g., in case of a perfectly conducting infinitely thin plate. This non-uniqueness corresponds to an interior resonance. However, the exterior electromagnetic field problem, i.e., the solution to Maxwell's equations outside the perfectly conducting object, is unique provided that the shell of the object contains a finite number of sharp corners and edges. These uniqueness results were proven by Jones [36, Chapter 9], using an argument introduced by Vekua [79, p. 318] and Rellich [53].

We now turn our attention to solving Maxwell's equations in free space with an electric-current density $\boldsymbol{J}$ as source,

$$\nabla \times \boldsymbol{H} = \boldsymbol{J} + s\varepsilon_0 \boldsymbol{E}, \tag{2.37a}$$

$$\nabla \times \boldsymbol{E} = -s\mu_0 \boldsymbol{H}, \tag{2.37b}$$

subject to the radiation conditions (2.32) or (2.36). Owing to the fact that $\boldsymbol{B}$ and therefore in this case also $\boldsymbol{H}$ is source-free (solenoidal), which is indicated by Eq. (2.12a), the Helmholtz decomposition [78] allows us to introduce a vector potential $\boldsymbol{A}$ as

$$\boldsymbol{H} = \nabla \times \boldsymbol{A}, \tag{2.38}$$

which we substitute in Eq. (2.37b). A further application of the Helmholtz decomposition yields

$$\boldsymbol{E} = -s\mu_0 \boldsymbol{A} - \frac{\nabla \Phi}{s\varepsilon_0}, \tag{2.39}$$

where we have introduced the scalar potential Φ. To arrive at a system of partial differential equations for the scalar and vector potentials, we combine Eqs (2.37a), (2.38) and (2.39), and apply the Lorenz gauge

$$\nabla \cdot \boldsymbol{A} = -\Phi. \tag{2.40}$$

We then find that the vector and scalar potential satisfy the Helmholtz equations

$$\nabla^2 \boldsymbol{A} - s^2 \varepsilon_0 \mu_0 \boldsymbol{A} = -\boldsymbol{J}, \qquad (2.41a)$$

$$\nabla^2 \Phi - s^2 \varepsilon_0 \mu_0 \Phi = \nabla \cdot \boldsymbol{J}, \qquad (2.41b)$$

where we have assumed the existence of the divergence of the electric-current density. The Lorenz gauge also allows us to represent the electric field in terms of the vector potential $\boldsymbol{A}$ only, i.e.,

$$\boldsymbol{E} = \frac{1}{s\varepsilon_0} \left(\nabla \nabla \cdot \boldsymbol{A} - s^2 \varepsilon_0 \mu_0 \boldsymbol{A} \right). \qquad (2.42)$$

To solve the Helmholtz equations, we require a condition for the vector and scalar potential to describe their behavior at infinity. Taking into consideration the requirement of exponential decay for $\mathrm{Re}\{s\} > 0$ or into consideration the outward-travelling energy of the electromagnetic field for $\mathrm{Re}\{s\} = 0$, we apply the same principles to the potentials, i.e., the potentials should exhibit the exponentially decaying behavior or they should correspond to outward-travelling waves. For continuously differentiable $\boldsymbol{J}$ and $\nabla \cdot \boldsymbol{J}$ and describing the vector fields by a Cartesian vector field, the solutions to the Helmholtz equations (2.41a) and (2.41b) are

$$\boldsymbol{A}(\boldsymbol{r}) = \iiint_{\mathcal{V}} G(\boldsymbol{r} - \boldsymbol{r}') \boldsymbol{J}(\boldsymbol{r}') dV', \qquad (2.43a)$$

$$\Phi(\boldsymbol{r}) = - \iiint_{\mathcal{V}} G(\boldsymbol{r} - \boldsymbol{r}') \nabla \cdot \boldsymbol{J}(\boldsymbol{r}') dV', \qquad (2.43b)$$

where

$$G(\boldsymbol{r} - \boldsymbol{r}') = \frac{\exp(-s|\boldsymbol{r} - \boldsymbol{r}'|/c_0)}{4\pi|\boldsymbol{r} - \boldsymbol{r}'|}, \qquad (2.44)$$

which is known as the Green's function in free space. Further, $c_0 = 1/\sqrt{\varepsilon_0 \mu_0}$, the velocity of light in free space. The volume integration is over the primed variable in the volume $\mathcal{V}$, i.e., $\boldsymbol{r}'$ denotes the source coordinates. Further, $\nabla \cdot \boldsymbol{J}(\boldsymbol{r}') = \nabla_{\boldsymbol{r}'} \cdot \boldsymbol{J}(\boldsymbol{r}')$ is the divergence of the current density operating in the primed coordinates. The unprimed coordinate $\boldsymbol{r}$ refers to the point of observation. In case the Laplace parameter s is purely imaginary, the introduction of the velocity of light allows us to introduce the wavelength λ as

$$\lambda = \frac{2\pi c_0}{\omega} = \frac{c_0}{f}. \qquad (2.45)$$

2.5 Perfectly conducting objects

We now consider a perfectly conducting object occupying the domain $\mathcal{D}$, with a piecewise-smooth boundary $\partial\mathcal{D}$ with an orientable normal, surrounded by free space. We assume that an electromagnetic field is incident on the object and that its source lies in the domain $\mathbb{R}^3 \setminus \overline{\mathcal{D}}$, where $\overline{\mathcal{D}} = \mathcal{D} \cup \partial\mathcal{D}$. From Eq. (2.21b), we know that the jump occurring in the magnetic field at the interface $\partial\mathcal{D}$ corresponds to an electric surface current density $\boldsymbol{J}_S$. It is shown in Appendix A that the vector and scalar potentials, introduced in Eqs (2.38) and (2.39), are given by

$$\boldsymbol{A}(\boldsymbol{r}) = \iint\limits_{\partial\mathcal{D}} G(\boldsymbol{r} - \boldsymbol{r}')\boldsymbol{J}_S(\boldsymbol{r}')dA', \tag{2.46a}$$

$$\Phi(\boldsymbol{r}) = -\iint\limits_{\partial\mathcal{D}} G(\boldsymbol{r} - \boldsymbol{r}')\nabla_s \cdot \boldsymbol{J}_S(\boldsymbol{r}')dA', \tag{2.46b}$$

where $\nabla_s \cdot \boldsymbol{J}_S(\boldsymbol{r}')$ denotes the surface divergence of the surface current density with respect to the primed coordinates. Hence, the electric and magnetic fields in $\mathbb{R}^3 \setminus \overline{\mathcal{D}}$ can be written as

$$\boldsymbol{H}(\boldsymbol{r}) = \boldsymbol{H}^i(\boldsymbol{r}) + \nabla \times \boldsymbol{A}(\boldsymbol{r}), \tag{2.47a}$$

$$\boldsymbol{E}(\boldsymbol{r}) = \boldsymbol{E}^i(\boldsymbol{r}) - \frac{1}{s\varepsilon_0}\left[\nabla\Phi(\boldsymbol{r}) + \frac{s^2}{c_0^2}\boldsymbol{A}(\boldsymbol{r})\right] \tag{2.47b}$$

$$= \boldsymbol{E}^i(\boldsymbol{r}) + \frac{1}{s\varepsilon_0}\left[\nabla\nabla \cdot \boldsymbol{A}(\boldsymbol{r}) - \frac{s^2}{c_0^2}\boldsymbol{A}(\boldsymbol{r})\right]. \tag{2.47c}$$

To arrive at an integro-differential equation for the surface current density, we should perform the limiting process in which the observation point $\boldsymbol{r}$ approaches the boundary $\partial\mathcal{D}$ from the exterior region $\mathbb{R}^3 \setminus \overline{\mathcal{D}}$. The limiting process is by no means a simple matter of replacing $\boldsymbol{r}$ by $\boldsymbol{r}|_{\partial\mathcal{D}}$. For a smooth boundary $\partial\mathcal{D}$ with continuously varying outward-pointing unit normal $\boldsymbol{n}(\boldsymbol{r})$ and for continuously differentiable $\boldsymbol{J}_S(\boldsymbol{r})$ and $\nabla_s \cdot \boldsymbol{J}_S(\boldsymbol{r})$ for $\boldsymbol{r} \in \partial\mathcal{D}$, a careful examination shows that [14, Sections 2.5 &2.6]

$$\lim_{h\downarrow 0}\boldsymbol{H}(\boldsymbol{r} + h\boldsymbol{n}(\boldsymbol{r})) = \boldsymbol{H}^i(\boldsymbol{r}) - \frac{\boldsymbol{n}(\boldsymbol{r}) \times \boldsymbol{J}_S(\boldsymbol{r})}{2} + (\nabla \times \boldsymbol{A})(\boldsymbol{r}), \tag{2.48a}$$

$$\lim_{h\downarrow 0}\boldsymbol{E}(\boldsymbol{r} + h\boldsymbol{n}(\boldsymbol{r})) = \boldsymbol{E}^i(\boldsymbol{r}) - \frac{\boldsymbol{n}(\boldsymbol{r})\nabla_s \cdot \boldsymbol{J}_S(\boldsymbol{r})}{2s\varepsilon_0} - \frac{1}{s\varepsilon_0}\left[(\nabla\Phi)(\boldsymbol{r}) + \frac{s^2}{c_0^2}\boldsymbol{A}(\boldsymbol{r})\right] \tag{2.48b}$$

$$= \boldsymbol{E}^i(\boldsymbol{r}) - \frac{\boldsymbol{n}(\boldsymbol{r})\nabla_s \cdot \boldsymbol{J}_S(\boldsymbol{r})}{2s\varepsilon_0} + \frac{1}{s\varepsilon_0}\left[(\nabla\nabla \cdot \boldsymbol{A})(\boldsymbol{r}) - \frac{s^2}{c_0^2}\boldsymbol{A}(\boldsymbol{r})\right], \tag{2.48c}$$

for $\boldsymbol{r} \in \partial\mathcal{D}$. Further, the integrals in Eq. (2.46) should be understood in the sense of Cauchy principal values. Also, we have implicitly assumed that the incident fields are continuous across the boundary $\partial\mathcal{D}$. Finally, we apply the boundary conditions (2.21a) and (2.21b) to arrive at

$$\boldsymbol{n}(\boldsymbol{r}) \times \boldsymbol{H}^i(\boldsymbol{r}) = \frac{\boldsymbol{J}_S(\boldsymbol{r})}{2} - \boldsymbol{n}(\boldsymbol{r}) \times [\nabla \times \boldsymbol{A}](\boldsymbol{r}), \tag{2.49a}$$

$$-s\varepsilon_0 \left[\boldsymbol{n}(\boldsymbol{r}) \times \boldsymbol{E}^i(\boldsymbol{r})\right] = -\boldsymbol{n}(\boldsymbol{r}) \times \left[(\nabla\Phi)(\boldsymbol{r}) + \frac{s^2}{c_0^2}\boldsymbol{A}(\boldsymbol{r})\right] \tag{2.49b}$$

$$= \boldsymbol{n}(\boldsymbol{r}) \times \left[(\nabla\nabla \cdot \boldsymbol{A})(\boldsymbol{r}) - \frac{s^2}{c_0^2}\boldsymbol{A}(\boldsymbol{r})\right], \tag{2.49c}$$

for $\boldsymbol{r} \in \partial\mathcal{D}$. The integro-differential equations are known as the magnetic-field integral equation (MFIE) and the electric-field integral equation (EFIE) [51], respectively. Both EFIE and MFIE suffer from a non-uniqueness problem at certain real-valued frequencies. This non-uniqueness corresponds to an interior resonance of the object. A possible remedy is to consider a normalized combination of the EFIE and MFIE, which is known as the combined-field integral equation (CFIE) [51]. If $\mathcal{D}$ no longer represents a volume surrounded by a perfectly conducting shell, the magnetic-field integral equation breaks down. This is due to the fact that the boundary condition in (2.21b) ceases to be valid and should be replaced by condition (2.13b). The problem is that we no longer know what the magnetic field on the other side of the boundary should be, which is essential for the formulation. The electric-field integral equation remains valid for this case, i.e., the open-screen problem.

2.5.1 Thin-wire equations

In electromagnetics, scattering by structures composed of thin wires has been studied by many authors. Most authors use one of two so-called thin-wire equations. Both equations can be derived through the application of the scattered-electric-field integral representation (2.39) or (2.42) and by the introduction of some approximations for the electric surface current density. However, for a straight thin-wire segment with circular cross-section, we can show that both thin-wire equations are exact, except for end effects. We model the thin-wire segment as a perfectly conducting circular cylinder, as shown in Figure 2.1, with radius a and length L. The axis of the cylinder coincides with the z-axis. To describe the surface current density on the mantle of the cylinder, we use the cylindrical coordinate
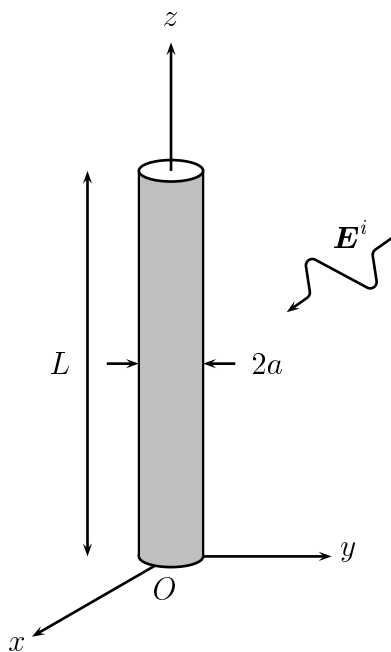
Figure 2.1: straight thin-wire segment with incident field.

system $\{r, \phi, z\}$. The mantle of the wire is parameterized by $r = a$, $\phi \in (-\pi, \pi]$ and $z \in (0, L)$. In the following, we will assume that we can neglect the effect of the surface current density at the end faces.

For a thin wire, i.e., $a \ll \lambda = (2\pi c_0)/\omega$, for which the central axis is parallel to the z-axis, the scattered field components E_θ^s and H_ϕ^s in the far-field region are dominated by the ϕ-independent part of the z-directed component of the electric surface current density $\boldsymbol{J}_S$, as shown in Appendix B. The ϕ-independent part of the z-directed surface current density corresponds to the total current in the z-direction, as defined by

$$I_z(z) = \int\limits_{-\pi}^{\pi} \boldsymbol{J}_S(\phi, z) \cdot \boldsymbol{u}_z a d\phi. \tag{2.50}$$

The results of Section 2.5 and the fact that the unit vector in the z-direction $\boldsymbol{u}_z$ of the cylindrical coordinate system coincides with the unit vector in the z-direction of the Cartesian coordinate system show that the z-component of the scattered electric field can be

represented as

$$E_z^s(r, \phi, z) = \frac{1}{s\varepsilon_0} \left[\partial_z \int_0^L \int_{-\pi}^{\pi} g(r, \phi - \phi', z - z', a) \nabla_s \cdot \boldsymbol{J}_S(\phi', z') a d\phi' dz' \right.$$

$$\left. - \frac{s^2}{c_0^2} \int_0^L \int_{-\pi}^{\pi} g(r, \phi - \phi', z - z', a) \boldsymbol{J}_S(\phi', z') \cdot \boldsymbol{u}_z a d\phi' dz' \right], \quad (2.51)$$

where

$$g(r, \phi, z, a) = \frac{\exp\left[-(s/c_0)\sqrt{r^2 + a^2 - 2ra\cos(\phi) + z^2}\right]}{4\pi\sqrt{r^2 + a^2 - 2ra\cos(\phi) + z^2}}, \quad (2.52)$$

which is the Green's function of Eq. (2.44) in cylindrical coordinates, and

$$\nabla_s \cdot \boldsymbol{J}_S(\boldsymbol{r}') = \frac{1}{a}\partial_{\phi'} J_{S,\phi'}(\phi', z') + \partial_{z'} J_{S,z'}(\phi', z'). \quad (2.53)$$

At this point, the formulations of the two thin-wire equations depart.

For the so-called integral equation with reduced kernel, the observation point of the scattered field is taken at the z-axis [72]. For this choice, the Green's function g no longer depends on ϕ' and we can evaluate the integrals over ϕ' in closed form, which yields

$$E_z^s(r = 0, z) = \frac{1}{s\varepsilon_0} \left[\partial_z \int_0^L g_a(z - z') \partial_{z'} I_z(z') dz' - \frac{s^2}{c_0^2} \int_0^L g_a(z - z') I_z(z') dz' \right], \quad (2.54)$$

where

$$g_a(z - z') = \frac{\exp\left[-(s/c_0)\sqrt{a^2 + (z - z')^2}\right]}{4\pi\sqrt{a^2 + (z - z')^2}}, \quad (2.55)$$

is the so-called approximate or reduced kernel.

To obtain the so-called integral equation with exact kernel, we observe that the Green's function g is a periodic function of $\phi - \phi'$. Hence, integration over a full period of ϕ also amounts to removing the ϕ' dependence of the integrated Green's function. Therefore, the integration over ϕ' can also be evaluated. We integrate over a circle with constant radius $r \leq a$. This yields

$$\int_{-\pi}^{\pi} E_z^s(r, \phi, z) d\phi = \frac{1}{s\varepsilon_0} \left[\partial_z \int_0^L g_e(r, z - z', a) \partial_{z'} I_z(z') dz' \right.$$

$$\left. - \frac{s^2}{c_0^2} \int_0^L g_e(r, z - z', a) I_z(z') dz' \right], \quad (2.56)$$

where

$$g_e(r, z, a) = \int\limits_{-\pi}^{\pi} g(r, \phi, z, a) d\phi, \tag{2.57}$$

which, for $r = a$, is known as the exact kernel. Note that we have employed $d\phi$ instead of $rd\phi$ to integrate over ϕ, owing to the circular integration contour.

We complete the formulation of the thin-wire equations by noting that the total field inside a perfectly conducting object is zero. This also applies to a linear combination (integration) of the electric field inside the object. Therefore, Eqs (2.54) and (2.56) lead to the following integro-differential equations for $z \in (0, L)$:

$$-s\varepsilon_0 E_z^i(r = 0, z) = \left[\partial_z^2 - \frac{s^2}{c_0^2}\right] \int\limits_0^L g_a(z - z') I_z(z') dz', \tag{2.58a}$$

$$-s\varepsilon_0 \int\limits_{-\pi}^{\pi} E_z^i(a, \phi, z) d\phi = \left[\partial_z^2 - \frac{s^2}{c_0^2}\right] \int\limits_0^L g_e(a, z - z', a) I_z(z') dz'. \tag{2.58b}$$

We have replaced the partial derivative with respect to z' by a derivative with respect to z outside the integral, using the translation invariance of the Green's functions with respect to $z - z'$, and the fact that $I_z(0) = I_z(L) = 0$, which implies that the current is confined to the wire. Further, in the second equation we have taken $r = a$, i.e., the observation coordinate lies on the mantle of the wire. Eq. (2.58a) is known as the approximate or reduced-kernel integral equation. We will refer to Eq. (2.58b) as the exact-kernel integral equation. From a historical perspective, we note that most authors apply the incident electric field on the axis of the wire as the excitation for the right-hand side of Eq. (2.58b). Here, we should remark that we have not taken into account the surface current density at the end faces. For the exact kernel this amounts to modeling a hollow tube and the integral equation is exact for that configuration. For the reduced-kernel integral equation, neglecting the effect of the end faces remains an approximation. It is possible to take into account the end faces, at the expense of extra terms in both thin-wire equations and extra equations for the end faces. The formulation becomes more involved due to these corrections, which explains why most authors neglect the effect of the end faces. An argument in favor of this approximation can be found in [72].

2.5.2 Perfectly conducting flat plate

Regarding the formulation, the simplest example of a perfectly conducting open screen is a perfectly conducting flat plate, as shown in Figure 2.2. For an electric field $\boldsymbol{E}^i$ incident on a flat plate $\mathcal{P}$, located in the plane $z = 0$, the electric-field integral equation reduces to

$$-s\varepsilon_0 E_x^i(\boldsymbol{r}) = \left[\partial_x^2 - \frac{s^2}{c_0^2}\right] A_x(\boldsymbol{r}) + \partial_x\partial_y A_y(\boldsymbol{r}), \qquad\qquad \boldsymbol{r} \in \mathcal{P}, \qquad\qquad (2.59\text{a})$$

$$-s\varepsilon_0 E_y^i(\boldsymbol{r}) = \left[\partial_y^2 - \frac{s^2}{c_0^2}\right] A_y(\boldsymbol{r}) + \partial_y\partial_x A_x(\boldsymbol{r}), \qquad\qquad \boldsymbol{r} \in \mathcal{P}, \qquad\qquad (2.59\text{b})$$

where the subscript of the potential and the electric field indicates the component of the vector in Cartesian coordinates. Notice that we choose to use the vector potential only, i.e., Eq. (2.42).
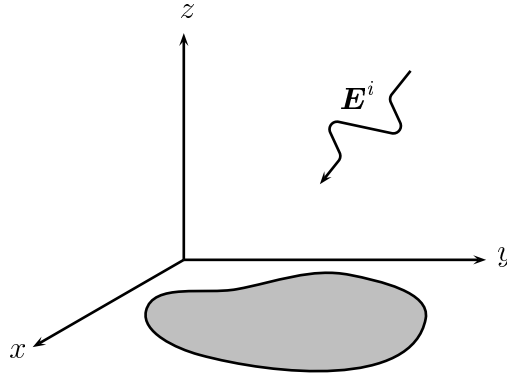
Figure 2.2: perfectly conducting flat plate with incident field.

2.6 Dielectric objects

A dielectric object, occupying the bounded domain $\mathcal{D}$, is described by a permittivity function $\varepsilon(\boldsymbol{r})$, which is a scalar (in the isotropic case) or a 3×3 matrix function (in the anisotropic case). Note that the permittivity tensor is now represented by a 3×3 matrix, since we use an explicit reference system. The configuration is depicted in Figure 2.3. Outside $\overline{\mathcal{D}} = \mathcal{D} \cup \partial\mathcal{D}$, the permittivity function equals the permittivity of free space. We will assume that the permeability equals μ_0 everywhere. For the moment, we will also assume that σ is identically zero everywhere, and we will come back to this at the end
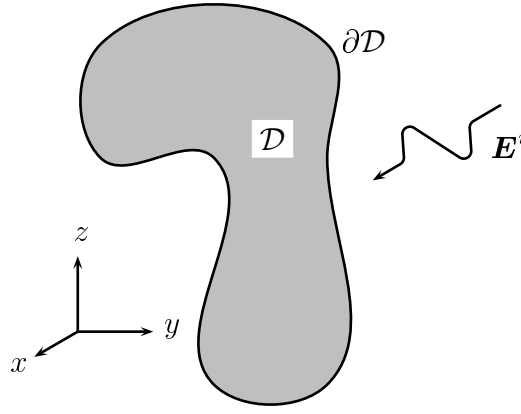
Figure 2.3: dielectric object with incident field.

of this section. We decompose the electric and magnetic field according to Eq. (2.31). Consequently, the scattered fields satisfy

$$\nabla \times \boldsymbol{H}^s = s\varepsilon_0 \boldsymbol{E}^s + s\varepsilon_0 \chi \boldsymbol{E} = s\varepsilon_0 \boldsymbol{E}^s + \boldsymbol{J}^c, \tag{2.60a}$$

$$\nabla \times \boldsymbol{E}^s = -s\mu_0 \boldsymbol{H}^s, \tag{2.60b}$$

subject to the radiation conditions. We have introduced $\chi(\boldsymbol{r})$, which is a scalar or a 3×3 matrix function with $\chi(\boldsymbol{r}) = (\varepsilon(\boldsymbol{r})/\varepsilon_0 - 1)$ or $\chi_{k,\ell}(\boldsymbol{r}) = (\varepsilon_{k,\ell}(\boldsymbol{r}) - \varepsilon_0 \delta_{k,\ell})/\varepsilon_0$, respectively. Also, we assume that the permittivity is bounded, i.e., $\max_{\boldsymbol{r} \in \overline{\mathcal{D}}} |\chi(\boldsymbol{r})| = \chi_{max}$ or $\max_{k,\ell,\boldsymbol{r} \in \overline{\mathcal{D}}} |\chi_{k,\ell}(\boldsymbol{r})| = \chi_{max}$. Further, we have defined the contrast-current density $\boldsymbol{J}^c$, which has support $\overline{\mathcal{D}}$. In absence of a primary polarization field, another useful definition of the contrast-current density is

$$\boldsymbol{J}^c = s\varepsilon_0 \chi \varepsilon^{-1} \boldsymbol{D}. \tag{2.61}$$

In general, the divergence of the contrast-current density is undefined, since it does not correspond to a physical electric-current density. Hence, the vector-potential description of the scattered electric field in Eq. (2.42) is appropriate. To arrive at a domain integro-differential equation for the contrast-current density, we write the total electric field as the sum of the incident field and the scattered field. The resulting expression is

$$s\varepsilon_0 \boldsymbol{E}^i = s\varepsilon_0 \left(\boldsymbol{E} - \boldsymbol{E}^s \right) = s\varepsilon_0 \boldsymbol{E} + \frac{s^2}{c_0^2} \boldsymbol{A} - \nabla\nabla \cdot \boldsymbol{A}, \tag{2.62}$$

which together with Eq. (2.43a), i.e.,

$$\boldsymbol{A}(\boldsymbol{r}) = \iiint_{\mathcal{V}} G(\boldsymbol{r} - \boldsymbol{r}') \boldsymbol{J}^c(\boldsymbol{r}') dV', \tag{2.63}$$

is a domain integro-differential equation for $\boldsymbol{E}$ if we use the definition in Eq. (2.60a) for $\boldsymbol{J}^c$. Alternatively, we can obtain a domain integro-differential equation for $\boldsymbol{D}$, by using the constitutive relation between $\boldsymbol{E}$ and $\boldsymbol{D}$, which leads to

$$s\varepsilon_0\boldsymbol{E}^i = s\varepsilon_0\varepsilon^{-1}\boldsymbol{D} + \frac{s^2}{c_0^2}\boldsymbol{A} - \nabla\nabla\cdot\boldsymbol{A}. \tag{2.64}$$

In the derivation of Eq. (2.64), we have used definition (2.61) for the contrast-current density. Finally, we obtain a domain integro-differential equation for $\boldsymbol{J}^c$ by multiplying Eq. (2.62) by the contrast function χ and using the definition of $\boldsymbol{J}^c$, which results in

$$s\varepsilon_0\chi\boldsymbol{E}^i = \boldsymbol{J}^c + \chi\left[\frac{s^2}{c_0^2}\boldsymbol{A} - \nabla\nabla\cdot\boldsymbol{A}\right]. \tag{2.65}$$

As mentioned above, we have assumed that σ is identically zero everywhere. However, it is also possible to take objects with a finite conductivity into account. In that case, we have to replace $\varepsilon(\boldsymbol{r})$ by $\sigma(\boldsymbol{r})/s + \varepsilon(\boldsymbol{r})$. Further, $s\boldsymbol{D}$ should be replaced by $\boldsymbol{J} + s\boldsymbol{D}$ and we have to assume that both the primary polarization and the primary electric-current density are absent. Hence, $\chi(\boldsymbol{r}) = (\sigma(\boldsymbol{r})/s\varepsilon_0 + \varepsilon(\boldsymbol{r})/\varepsilon_0 - 1)$ in the isotropic case or $\chi_{k,\ell}(\boldsymbol{r}) = (\sigma_{k,\ell}(\boldsymbol{r})/s + \varepsilon_{k,\ell}(\boldsymbol{r}) - \varepsilon_0\delta_{k,\ell})/\varepsilon_0$ in the anisotropic case. The counterpart of Eq. (2.64) becomes

$$s\varepsilon_0\boldsymbol{E}^i = \varepsilon_0(\sigma/s + \varepsilon)^{-1}(\boldsymbol{J} + s\boldsymbol{D}) + \frac{s^2}{c_0^2}\boldsymbol{A} - \nabla\nabla\cdot\boldsymbol{A}, \tag{2.66}$$

where the contrast-current density is given by

$$\boldsymbol{J}^c = \varepsilon_0\chi(\sigma/s + \varepsilon)^{-1}(\boldsymbol{J} + s\boldsymbol{D}). \tag{2.67}$$

Note that Eqs (2.62), (2.64), and (2.66) are also integral representations for the electric field, the electric-flux density, and the electric-current and the electric-flux density in $\mathbb{R}^3$, whereas Eq. (2.65) is an identity outside $\overline{\mathcal{D}}$.

Chapter 3

Mapping properties of the integro-differential equations

From the formulation of the various integro-differential equations formulated in the preceding chapter, we would like to find the analytic solutions. However, an explicit expression can only be found for a very limited number of configurations, such as stratified spheres, circular cylinders and planes [9]. In most cases, we have to resort to some kind of numerical approximation. To analyze the approximation properties of the resulting numerical method or to understand the origin of breakdown of a method, we need to examine whether or not the equations give rise to a well-posed problem.

3.1   Principles for analyzing mapping properties

A problem is well-posed (in the sense of Hadamard) if each of the following conditions is satisfied.

1. A solution to the problem exists.

2. If a solution to the problem exists, it is unique.

3. The solution to the problem depends continuously on the given data.

If, for a given problem, one of these conditions is not satisfied, it will be extremely difficult (or impossible if the first condition is violated) to find an approximation of the solution. Such a problem is referred to as ill-posed. To establish whether or not a problem (or an equation) is well-posed, we have to recall some definitions and theorems from functional analysis, assuming basic knowledge of Banach and Hilbert spaces. We will denote the norm by $\| \cdot \|$ and the inner product by $(\cdot, \cdot)$, with its corresponding norm. In case we employ more than one norm or inner product, we will use a subscript to indicate which norm or inner product we use. For the proofs of the theorems we will refer to standard literature at the end of each theorem. Further, we will comment on the consequences of the definitions and theorems.

Definition 1
A mapping L from a linear space X into a linear space Y, denoted by $L : X \to Y$, is called linear if

$$L(\alpha x + \beta y) = \alpha L x + \beta L y, \tag{3.1}$$

for any $x, y \in X$ and any scalars α and β.

The concept of linearity gives rise to the superposition principle. The integro-differential equations in Chapter 2 are of the form

$$Lu = f, \tag{3.2}$$

where L is the linear integro-differential operator, u is the unknown current density, and f is the excitation or forcing function in the form of the incident field.

Definition 2
Let L be a linear operator from X to Y. The null space of L, denoted by $\mathcal{N}(L)$, is the subspace

$$\mathcal{N}(L) = \{x \mid x \in X,\ Lx = 0\}. \tag{3.3}$$

The range of L, denoted by $\mathcal{R}(L)$, is the subspace

$$\mathcal{R}(L) = \{y \mid y \in Y,\ y = Lx \text{ for some } x \in X\}. \tag{3.4}$$

If the linear operator $L : X \to \mathcal{R}(L)$ has $\mathcal{N}(L) = \{0\}$, then L is called one-to-one or injective. This means that if a solution exists, it is unique. For a linear mapping L that is one-to-one, we can construct the inverse operator of L, denoted by L^{-1}, and L^{-1} is a mapping from $\mathcal{R}(L)$ to X. Hence, if $f \in \mathcal{R}(L)$, then the solution u of the equation

$Lu = f$ exists and is given by $u = L^{-1}f$. To analyze the third condition of well-posedness, we introduce the concept of bounded linear operator.

Definition 3
Let X and Y be normed linear spaces and let $L : X \rightarrow Y$ be a linear operator. If the number

$$\|L\| = \sup_{\|x\|_X = 1} \|Lx\|_Y \tag{3.5}$$

is finite for any $x \in X$ with $\|x\|_X = 1$, then L is called a bounded linear operator on Y, and $\|L\|$ is called the norm of L.

For the boundedness of the inverse operator L^{-1} we define

Definition 4
For a linear mapping $L : X \rightarrow Y$, the inverse operator L^{-1} is called bounded if L is one-to-one and L^{-1} is bounded from $\mathcal{R}(L)$ to X.

Consider two problems

$$Lu_1 = f_1, \tag{3.6a}$$

$$Lu_2 = f_2, \tag{3.6b}$$

where $L : X \rightarrow Y$ and let X and Y be normed spaces. Under the conditions that L is one-to-one, L^{-1} is bounded, and f_1 and f_2 belong to $\mathcal{R}(L)$, we have

$$\|u_1 - u_2\|_X = \|L^{-1}f_1 - L^{-1}f_2\|_X \leq \|L^{-1}\| \cdot \|f_1 - f_2\|_Y. \tag{3.7}$$

Hence, to prove that the linear problem $Lu = f$, for a given f, is well-posed amounts to proving that $\mathcal{N}(L) = \{0\}$, that $f \in \mathcal{R}(L)$, and that L^{-1} is a bounded linear operator from $\mathcal{R}(L)$ to X. One of the merits of this observation is that when we consider an approximation u_n of u, we have the approximation property

$$\|u_n - u\|_X = \|u_n - L^{-1}f\|_X \leq \|L^{-1}\| \cdot \|Lu_n - f\|_Y. \tag{3.8}$$

Hence the norm of the residual error, i.e., $\|Lu_n - f\|_Y$, gives a bound for the approximation error of u.

If the domain and range of the operator L are Banach spaces, the Open Mapping Theorem gives sufficient conditions for which the inverse of an operator is bounded:

Theorem 1 (Open Mapping Theorem)

Let L be a bounded linear operator from X to Y and let X and Y be Banach spaces. If L is one-to-one and $\mathcal{R}(L)$ is closed, then $L^{-1} : \mathcal{R}(L) \to X$ is bounded [32].

The consequence of this theorem is that if the first two conditions of well-posedness are satisfied for $Lu = f$ and L is a bounded linear operator, then the third condition (continuity) is also satisfied, provided that the domain and range of L are Banach spaces. From the Open Mapping Theorem and the identity $L^{-1}Lx = x$, we obtain the following theorem.

Theorem 2

Let $L : X \to Y$, then L is one-to-one and $\mathcal{R}(L)$ is closed if and only if $\|Lx\|_Y > \alpha\|x\|_X$ for all $x \in X$, for some $\alpha > 0$.

Another important property of linear operators is compactness.

Definition 5

Let X and Y be normed spaces. A linear operator $L : X \to Y$ is called compact (or completely continuous) if for every bounded sequence $\{x_n\}$ in X, the sequence $\{Lx_n\}$ has a density point, i.e., it contains a convergent subsequence.

Hence, compactness gives rise to an existence result in the sense that, in many cases, the sequence $\{x_n\}$ is an approximation sequence, i.e., there is density point.

Finite-rank operators, i.e., operators for which the dimension of their range is finite, are examples of compact operators. Compactness is closely tied to the choice of the norm of the vector space on which we consider the operator. Therefore, compactness can be lost or gained by changing the norm on X or Y.

Theorem 3

The identity operator on a normed space X, denoted by $I : X \to X$ is compact if and only if X has finite dimension [14, 42].

The above theorem assumes that a fixed norm is used on X. Given a vector space X with norms $\|\cdot\|_1$ and $\|\cdot\|_2$, it may happen that the identity operator is compact. In that case we say that there is a compact embedding. As an example of a compact embedding, we mention the Sobolev space $H^1(\mathbb{R})$ with norm $\|\cdot\|_{H^1}$ and norm $\|\cdot\|_{L^2}$, where $H^1(\mathbb{R})$ is a Hilbert space in which each element and its generalized first derivative belong to $L^2(\mathbb{R})$.

Theorem 4
Let A be a compact operator and B a bounded linear operator, then AB and BA are compact operators [14, 42].

The preceding two theorems can be combined to characterize the inverse of a compact operator:

Theorem 5
Let L be a compact operator, $L : X \to Y$. If $L^{-1} : \mathcal{R}(L) \to X$ exists, i.e., L is one-to-one, then L^{-1} is unbounded if X is infinite-dimensional.

If X is an infinitely dimensional normed space and L is a compact linear operator from X to Y, then the equation $Lu = f$ is ill-posed on $\mathcal{R}(L)$, since it does not satisfy the third condition of a well-posed problem. Combined with the Open Mapping Theorem, the above theorem shows that either X or $\mathcal{R}(L)$ is not a Banach space. So, if X is a Banach space, $\mathcal{R}(L)$ is not closed with respect to the norm of Y. In Section 3.3.3, we will show that the thin-wire integral operator with reduced kernel in Eq. (2.58a) is compact for a large class of Banach spaces. Hence, the range of the operator is not closed with respect to the norms on these Banach spaces.

We will now consider operators of the form $L = I + A$ from X to X, where A is a compact operator and X is a normed space. Sometimes, $I + A$ is referred to as a compact perturbation of I. The MFIE of Eq. (2.49a) for a smooth boundary $\partial\mathcal{D}$ is an example of such an operator. The study of operators of this form was initiated by Fredholm, who considered integral equations of the form

$$(I + A)u = u(z) + \int_a^b g(z, z')u(z')dz' = f(z), \tag{3.9}$$

and X is the space of continuous functions, where the kernel $g(z, z')$ is bounded and continuous. Integral equations of this form are known as Fredholm integral equations of the second kind, whereas integral equations of the form

$$Au = \int_a^b g(z, z')u(z')dz' = f(z), \tag{3.10}$$

are referred to as Fredholm integral equations of the first kind. Since A is compact, Fredholm integral equations of the first kind are ill-posed. Operators of the form $I + A$ are

completely characterized by the three Riesz theorems. In the following theorem, we will give the most important results of the three Riesz theorems.

Theorem 6

Let X be a Banach space and let A be a compact operator from X to X, then [14, 42, 54]

1. $\mathcal{N}(I + A)$ is finite dimensional,

2. $\mathcal{R}(I + A)$ is closed, i.e., $\mathcal{R}(I + A) = \overline{\mathcal{R}(I + A)}$,

3. $\mathcal{N}(I + A) = \{0\}$ if and only if $\mathcal{R}(I + A) = X$.

The consequence of the three Riesz theorems is that we can establish existence and boundedness of the inverse $(I + A)^{-1} : X \to X$ by proving uniqueness.

The above theorem also holds for operators of the form $L = T + A$, where T is a bounded linear operator on X with $X = \mathcal{R}(T)$ and T^{-1} bounded, and A is compact from X to X. This is a consequence of the fact that $T^{-1}A$ is also compact from X to X, by Theorem 4. Hence, we have

Theorem 7

Let X be a Banach space, let A be a compact operator from X to X and let T be a bounded linear operator on X with $X = \mathcal{R}(T)$ and T^{-1} bounded. If $T + A$ is one-to-one, then the inverse operator $(T + A)^{-1} : X \to X$ exists and is bounded. [14, 42]

This observation is used in so-called analytical regularization techniques, which have been developed in the former Soviet Union, see e.g. [49, 80] and references therein.

One way to prove that a bounded linear operator T on a Hilbert space has a bounded inverse, is to show that T is coercive.

Definition 6

Let H be a Hilbert space. A linear operator $T : H \to H$ is called coercive if

$$|(Tx, x)| \geq \alpha \|x\|^2, \tag{3.11}$$

for all $x \in H$.

Theorem 8

Let T be a bounded coercive linear operator on a Hilbert space H, then $\mathcal{R}(T) = H$ and T^{-1} is bounded [42].

Theorem 9

Let H be a Hilbert space. A bounded linear operator of the form $L = T + A$ with $T : H \to H$ a bounded coercive linear operator and $A : H \to H$ a compact operator, has a bounded inverse if and only if $\mathcal{N}(T + A) = \{0\}$.

The above theorem expresses that if we can decompose a bounded linear operator into a coercive part and a compact part, we can prove well-posedness by proving uniqueness. This result outlines the standard strategy to analyze integral equations of the first kind with singular kernel in a Hilbert space.

Finally, we introduce the concept of duality. Duality is defined in terms of functionals, which are bounded linear operators mapping a real or complex normed linear space into $\mathbb{R}$ or $\mathbb{C}$, respectively. Eigenvalue analyses should always be considered in complex linear spaces, since eigenvalues are complex in general.

Definition 7

The linear space of all bounded linear functionals on a normed linear space X is called the dual space of X, denoted by X'. X' is endowed with the norm

$$\|F\| = \sup_{\|x\|=1} |Fx|. \tag{3.12}$$

X' is a Banach space with respect to this norm.

Definition 8

Two normed spaces X and Y form a dual system $\langle X, Y \rangle$ if there is a complex function $\langle \cdot, \cdot \rangle$ defined on $X \times Y$, such that $\langle \cdot, \cdot \rangle$ is a bounded, non-degenerate, bilinear (or, alternatively, a sesquilinear) form on $X \times Y$, i.e.,

$|\langle x, y \rangle| \leq K \|x\|_X \|y\|_Y$ for $x \in X$, $y \in Y$ and $K \in \mathbb{R}$,

$\langle x_0, y \rangle = 0$ for some $x_0 \in X$ and all $y \in Y$ implies $x_0 = 0$,

$\langle x, y_0 \rangle = 0$ for some $y_0 \in Y$ and all $x \in X$ implies $y_0 = 0$.

The above definition of a dual system implies that Y is continuously embedded in X', denoted by $Y \hookrightarrow X'$, i.e., for each $y \in Y$ there is a bounded linear functional F_y on X such that $\langle x, y \rangle = F_y(x)$ and the mapping $y \to F_y$ is continuous. The converse, i.e., each

$F \in X'$ can be represented by a $y \in Y$, does not necessarily hold. A counter example is given below.

Example

We denote the space of continuous functions on the interval $[-1, 1]$ by $C(-1, 1)$ and the norm is the supremum norm. We chose $X = Y = C(-1, 1)$, and

$$\langle f, g \rangle = \int\limits_{-1}^{1} f(x)g(x)dx, \tag{3.13}$$

for $f, g \in C(-1, 1)$. The system $\langle C(-1, 1), C(-1, 1) \rangle$ is a dual system [42]. However, the bounded linear functional $F(f) = f(0)$ cannot be represented by a $g(x) \in C(-1, 1)$. This can be shown by choosing $f(x) = x^n$, $n = 1, 2, \ldots$, which means that $F(x^n) = 0$. From the orthogonality relation of the Legendre polynomials, we infer that $g(x)$ is constant on $[-1, 1]$, which is impossible.

Given a Hilbert space, another example of a dual system is this Hilbert space together with its inner product. The following theorem indicates the isomorphism between a Hilbert space and its dual space.

Theorem 10 (Riesz Representation Theorem)

Let F be a functional on a Hilbert space H. There exists exactly one $x_0 \in H$ such that $Fx = (x, x_0)$ for all $x \in H$. Moreover, we have $\|F\| = \|x_0\|$ [32].

3.2   Projection Methods

Projection methods cover a large class of numerical methods. We follow the description of Krasnosel'skii [41] to define projection methods:

Let X and Y be Banach spaces. Consider the equation

$$Lu = f, \tag{3.14}$$

where L is a surjective linear operator from X to Y, i.e., $\mathcal{R}(L) = Y$. The projection method to solve this equation consists of the following steps. We choose an n-dimensional space $X_n \subset X$, spanned by the set of basis or expansion functions $\mathscr{B}_n$, and an n-dimensional

space $Y_n \subset Y$. We define a projection operator P_n from Y to Y_n, i.e., $\mathcal{R}(P_n) = Y_n$ and $P_n^2 = P_n$. The projection operator P_n can be constructed by using a dual system $\langle W, Y \rangle_1$ in the following way.

Let $Y_n = \mathrm{span}\{y_1, \ldots, y_n\}$ and $W_n = \mathrm{span}\{w_1, \ldots, w_n\}$, where $\{w_1, \ldots, w_n\}$ is a basis in W_n dual to $\{y_1, \ldots, y_n\}$, i.e.,

$$\langle w_k, y_\ell \rangle_1 = \delta_{k,\ell}, \tag{3.15}$$

where $\delta_{k,\ell}$ is the Kronecker delta. The subscript $_1$ indicates a dual system that is related to $\mathcal{R}(L)$. The definition of a dual system guarantees the existence of the dual basis for W_n. Further, $\{w_1, \ldots, w_n\}$ is known as the set of weighting or testing functions $\mathscr{T}_n$. The projection operator P_n is now given by

$$P_n y = \sum_{k=1}^{n} \langle w_k, y \rangle_1 \, y_k. \tag{3.16}$$

In the same way, we can define a projection operator $Q_n : X \to X_n$, by means of a dual system $\langle X, V \rangle_2$, i.e., let $X_n = \mathrm{span}\{x_1, \ldots, x_n\}$ and let $\{v_1, \ldots, v_n\}$ be a dual basis in V spanning the space V_n, then

$$Q_n x = \sum_{\ell=1}^{n} \langle x, v_\ell \rangle_2 \, x_\ell, \tag{3.17}$$

where the subscript $_2$ indicates a dual system that is related to the domain of L. Now we replace the equation $Lu = f$ by the system

$$P_n L Q_n u = P_n f. \tag{3.18}$$

From the definition of Q_n we see that we can write

$$Q_n u = \sum_{\ell=1}^{n} \alpha_\ell x_\ell, \tag{3.19}$$

where the set of coefficients $\{\alpha_\ell\}$ is still unknown, since u is unknown. However, substituting this representation of $Q_n u$ in Eq. (3.18), we arrive at

$$\sum_{k=1}^{n} \left(\sum_{\ell=1}^{n} \langle w_k, Lx_\ell \rangle_1 \, \alpha_\ell \right) y_k = \sum_{k=1}^{n} \langle w_k, f \rangle_1 \, y_k, \tag{3.20}$$

if $\langle \cdot, \cdot \rangle_1$ is linear in the second argument, i.e., it contains no complex conjugation. Hence, we can determine α_ℓ from the system

$$\sum_{\ell=1}^{n} \langle w_k, Lx_\ell \rangle_1 \, \alpha_\ell = \langle w_k, f \rangle_1, \quad k = 1, \ldots, n, \tag{3.21}$$

provided that the square matrix on the left-hand side has full rank, which essentially restricts the choices for $\mathscr{B}_n$ and $\mathscr{T}_n$. If the above system does not have full rank, the matrix, formed by the elements $\langle w_k, L x_\ell \rangle_1$, is neither injective, nor surjective, since for finite-dimensional matrices the column rank and row rank are equal. Hence, the numerical system has become ill-posed, in spite of the fact that the original system $Lu = f$ may be well-posed. In that case, the linear system with forcing function equal to zero admits a non-trivial solution, which is called a "spurious mode", see e.g. [67] and references therein. This is the result of an improper choice for either $\mathscr{B}_n$ or $\mathscr{T}_n$.

The process to obtain a finite set of equations is also known as discretization. The aim of a projection method is to construct a sequence of subspaces $\{X_n\}$ and $\{W_n\}$ which are ultimately dense in X and W, respectively, for $n \to \infty$. A sequence of subspaces $\{X_n\}$ is ultimately dense in a normed space X if for every $x \in X$ we have

$$\inf_{x_n \in X_n} \|x - x_n\| \to 0 \quad \text{for} \quad n \to \infty. \tag{3.22}$$

In general, we cannot expect convergence to the exact solution for $n \to \infty$, unless X_n and W_n are ultimately dense in X and W, respectively, and W is isomorphic to Y', i.e., the dual space of Y. A detailed analysis of projection methods, together with conditions for convergence for $n \to \infty$ can be found in [41, 42].

3.3   Thin wire

For the infinitely long thin wire in free space, we will find a closed-form solution for the current on the wire, generated by an incident field that is caused by a source outside the wire. Further, we will show that the thin-wire equations with exact and reduced kernel are equivalent in this case. For the finite wire in the same setting, we will examine the mapping properties of the integral equation with reduced kernel.

3.3.1   Infinitely long wire

Consider an infinitely long circular cylinder in free space with radius a and central axis along the z-direction. Maxwell's equations, after we have applied the Laplace transformation (cf.

Eq. (2.10)), read:

$$\nabla \times \boldsymbol{E} = -s\mu_0 \boldsymbol{H}, \tag{3.23a}$$

$$\nabla \times \boldsymbol{H} = s\varepsilon_0 \boldsymbol{E}, \tag{3.23b}$$

where $\text{Re}\{s\} \geq 0$. We perform a spatial Fourier transformation in the z-direction

$$\hat{F}(r, \phi, k_z) = \int_{-\infty}^{\infty} F(r, \phi, z) \exp(jk_z z) dz, \tag{3.24a}$$

$$F(r, \phi, z) = \frac{1}{2\pi} \int_{-\infty}^{\infty} \hat{F}(r, \phi, k_z) \exp(-jk_z z) dk_z, \tag{3.24b}$$

after which we decompose the fields into their z-components and transverse parts (with subscript $_T$). We obtain

$$\left(k_z^2 + \frac{s^2}{c_0^2} \right) \hat{\boldsymbol{E}}_T = jk_z \nabla_T \hat{E}_z - s\mu_0 \left(\boldsymbol{u}_z \times \nabla_T \hat{H}_z \right), \tag{3.25a}$$

$$\left(k_z^2 + \frac{s^2}{c_0^2} \right) \hat{\boldsymbol{H}}_T = jk_z \nabla_T \hat{H}_z + s\varepsilon_0 \left(\boldsymbol{u}_z \times \nabla_T \hat{E}_z \right), \tag{3.25b}$$

$$\nabla_T^2 \hat{E}_z - \left(\frac{s^2}{c_0^2} + k_z^2 \right) \hat{E}_z = 0, \tag{3.25c}$$

$$\nabla_T^2 \hat{H}_z - \left(\frac{s^2}{c_0^2} + k_z^2 \right) \hat{H}_z = 0, \tag{3.25d}$$

where $c_0 = 1/\sqrt{\varepsilon_0 \mu_0}$ and where

$$\nabla_T = \boldsymbol{u}_r \partial_r + \boldsymbol{u}_\phi \frac{1}{r} \partial_\phi, \tag{3.26a}$$

$$\nabla_T^2 = \frac{1}{r} \partial_r r \partial_r + \frac{1}{r^2} \partial_\phi^2. \tag{3.26b}$$

In view of the circular symmetry, we employ a Fourier series expansion in the ϕ-direction

$$\breve{F}(r, m, k_z) = \frac{1}{2\pi} \int_0^{2\pi} \hat{F}(r, \phi, k_z) \exp(jm\phi) d\phi, \tag{3.27a}$$

$$\hat{F}(r, \phi, k_z) = \sum_{m=-\infty}^{\infty} \breve{F}(r, m, k_z) \exp(-jm\phi), \tag{3.27b}$$

which, for the individual components of the fields, yields

$$\left(k_z^2 + \frac{s^2}{c_0^2}\right)\breve{E}_r = jk_z\partial_r\breve{E}_z - \frac{jms\mu_0}{r}\breve{H}_z, \tag{3.28a}$$

$$\left(k_z^2 + \frac{s^2}{c_0^2}\right)\breve{H}_r = jk_z\partial_r\breve{H}_z + \frac{jms\varepsilon_0}{r}\breve{E}_z, \tag{3.28b}$$

$$\left(k_z^2 + \frac{s^2}{c_0^2}\right)\breve{E}_\phi = \frac{k_z m}{r}\breve{E}_z - s\mu_0\partial_r\breve{H}_z, \tag{3.28c}$$

$$\left(k_z^2 + \frac{s^2}{c_0^2}\right)\breve{H}_\phi = \frac{k_z m}{r}\breve{H}_z + s\varepsilon_0\partial_r\breve{E}_z, \tag{3.28d}$$

$$\left[\partial_r^2 + \frac{1}{r}\partial_r - \left(\frac{m^2}{r^2} + \frac{s^2}{c_0^2} + k_z^2\right)\right]\breve{E}_z = 0, \tag{3.28e}$$

$$\left[\partial_r^2 + \frac{1}{r}\partial_r - \left(\frac{m^2}{r^2} + \frac{s^2}{c_0^2} + k_z^2\right)\right]\breve{H}_z = 0. \tag{3.28f}$$

As mentioned in Section 2.5.1, we are interested in the total current $I_z(z)$ in the z-direction:

$$\hat{I}_z(k_z) = \int_0^{2\pi}\hat{H}_\phi(a,\phi,k_z)a\,d\phi = 2\pi a\breve{H}_\phi(a,0,k_z) = \frac{2\pi a s\varepsilon_0}{k_z^2 + (s^2/c_0^2)}\,\partial_r\breve{E}_z(r,0,k_z)\Big|_{r=a}. \tag{3.29}$$

For $m = 0$, the above system of equations decouples into two independent systems, such that the total current in the z-direction is independent of $\breve{H}_z$.

For an incident field originating from outside the wire, i.e., the source of the incident field has radial coordinate $r = b > a$, we can write the total field in the z-direction for $m = 0$ in the interval $a < r < b$, as

$$\breve{E}_z(r,0,k_z) = A_0 I_0\left(\kappa r\right) + B_0 K_0\left(\kappa r\right). \tag{3.30}$$

where I_0 and K_0 are modified Bessel functions of the first and second kind of order zero, respectively, and $\kappa = \sqrt{k_z^2 + (s^2/c_0^2)}$. The term with I_0 represents a constituent of the incident field and the term with K_0 represents a constituent of the field scattered by the cylinder. The incident field, after Fourier transformation in the z-direction, in the area $r < b$ can be written as

$$\hat{E}_z^i(r,\phi,k_z) = \sum_{m=-\infty}^{\infty} A_m(k_z)I_m\left(\kappa r\right)\exp(-jm\phi). \tag{3.31}$$

We now enforce the boundary condition at the mantle of the cylinder, i.e.,

$$\breve{E}_z(a,0,k_z) = 0$$

$$\Rightarrow \breve{E}_z(r,0,k_z) = A_0(k_z)\left[I_0\left(\kappa r\right) - \frac{I_0\left(\kappa a\right)}{K_0\left(\kappa a\right)}K_0\left(\kappa r\right)\right], \tag{3.32}$$

for $a \leq r < b$. For the total current in the z-direction we obtain through Eq. (3.29)

$$\hat{I}_z(k_z) = -\frac{2\pi s \varepsilon_0}{k_z^2 + (s^2/c_0^2)} \frac{A_0(k_z)\kappa a}{K_0(\kappa a)} \left[I_0(\kappa a) K_0'(\kappa a) - I_0'(\kappa a) K_0(\kappa a)\right],\tag{3.33}$$

where the primes refer to the derivative with respect to the argument. The term between brackets is recognized as the Wronskian and equals $-(\kappa a)^{-1}$. Thus we obtain the result

$$\hat{I}_z(k_z) = \frac{2\pi s \varepsilon_0}{k_z^2 + (s^2/c_0^2)} \frac{A_0(k_z)}{K_0(\kappa a)},\tag{3.34}$$

or

$$\left(k_z^2 + \frac{s^2}{c_0^2}\right) K_0(\kappa a) \hat{I}_z(k_z) = 2\pi s \varepsilon_0 A_0(k_z).\tag{3.35}$$

Finally, we would like to express $A_0(k_z)$ in terms of the incident field. With reference to Eq. (3.31), and by noting that $I_m(0) = 0$ for $m \neq 0$ and $I_0(0) = 1$, we see that

$$\hat{E}_z^i(0, \phi, k_z) = A_0(k_z),\tag{3.36a}$$

$$\int\limits_0^{2\pi} \hat{E}_z^i(a, \phi, k_z)d\phi = 2\pi A_0(k_z)I_0(\kappa a).\tag{3.36b}$$

Therefore, we can relate the total current on the wire in the z-direction to either E_z^i on the axis of the wire or to the average of E_z^i on the wire boundary, according to

$$\left(-k_z^2 - \frac{s^2}{c_0^2}\right) \frac{1}{2\pi} K_0(\kappa a) \hat{I}_z(k_z) = -s\varepsilon_0 \hat{E}_z^i(0, \phi, k_z),\tag{3.37a}$$

$$\left(-k_z^2 - \frac{s^2}{c_0^2}\right) I_0(\kappa a) K_0(\kappa a) \hat{I}_z(k_z) = -s\varepsilon_0 \int\limits_0^{2\pi} \hat{E}_z^i(a, \phi, k_z)d\phi.\tag{3.37b}$$

Employing the identity (see Appendix B)

$$\frac{\exp(-sR/c_0)}{4\pi R} =$$
$$\frac{1}{4\pi^2} \int\limits_{-\infty}^{\infty} \sum_{m=-\infty}^{\infty} I_m(\kappa r_<) K_m(\kappa r_>) \exp[-jm(\phi - \phi')] \exp[-jk_z(z - z')]dk_z,\tag{3.38}$$

where $R = |\boldsymbol{r} - \boldsymbol{r'}| = \sqrt{r^2 + r'^2 - 2rr'\cos(\phi - \phi') + (z - z')^2}$, $r_> = \max\{r, r'\}$ and $r_< = \min\{r, r'\}$, we deduce that

$$\int\limits_{-\infty}^{\infty} \frac{\exp(-sR_a/c_0)}{4\pi R_a} \exp[jk_z(z - z')]dz = \frac{1}{2\pi} K_0(a\kappa),\tag{3.39a}$$

$$\int\limits_{-\infty}^{\infty} \int\limits_0^{2\pi} \frac{\exp(-sR_e/c_0)}{4\pi R_e} \exp[jk_z(z - z')]d\phi dz = I_0(\kappa a) K_0(\kappa a),\tag{3.39b}$$

where $R_a = \sqrt{a^2 + (z - z')^2}$ and $R_e = \sqrt{2a^2 - 2a^2 \cos(\phi - \phi') + (z - z')^2}$. The subscript a stands for "approximate" and the subscript e stands for "exact". Upon combining Eqs (2.55), (2.57), (3.37) and (3.39), and transforming back to the spatial domain, we obtain the integro-differential equations

$$\left(\partial_z^2 - \frac{s^2}{c_0^2}\right) \int_{-\infty}^{\infty} g_a(z - z') I_z(z') dz' = -s\varepsilon_0 E_z^i(0, \phi, z), \tag{3.40a}$$

$$\left(\partial_z^2 - \frac{s^2}{c_0^2}\right) \int_{-\infty}^{\infty} g_e(a, z - z', a) I_z(z') dz' = -s\varepsilon_0 \int_0^{2\pi} E_z^i(a, \phi, z) d\phi, \tag{3.40b}$$

for $z \in \mathbb{R}$, and where the ϕ'-dependence of the second equation drops out of the left-hand side owing to the integration over the full period of ϕ.

Consequently, both thin-wire integral equations for the infinitely long wire with circular cross-section are exact for the total current in the z-direction, provided that the proper right-hand side is used. We also mention here that the equations are valid for any radius a of the circular cross-section of the wire. Hence, the word "thin" does not apply here.

3.3.2   Finite wire

For the integral equation with exact kernel (2.58b), existence and uniqueness was proven by Jones [37] for excitations that are continuous and have finite derivative with respect to the axial variable. Later, the existence results were extended by Rynne [55, 56, 57, 58] to a large class of vector spaces. This means that we can assume that the solution to the integral equation with exact kernel exists. We will use this fact to analyze the properties of the integral equation with reduced kernel. In [72] it was shown that the integral representation with reduced kernel represents exactly the z-component of a scattered electric field on the axis of the wire due to the current on the mantle. Therefore, in the present context, the only question is which incident field should be chosen for the forcing function.

To answer this question, we turn our attention to the following functions.

$$F_z^s(r, z) = \left[\partial_z^2 - \frac{s^2}{c_0^2}\right] \int\limits_{z'=0}^{L} g_e(r, z - z', a) I_z(z') dz',$$

(3.41a)

$$F_z^i(r, z) = s\varepsilon_0 \int\limits_{\phi=0}^{2\pi} E_z^i(r, \phi, z) d\phi,$$

(3.41b)

where I_z is the total current in the z-direction on the wire obtained through the integral equation with exact kernel in Eq. (2.58b), and E_z^i is the incident field. If we set $r = a$, we obtain the integral equation with exact kernel for $F_z^s + F_z^i = 0$. For $r = 0$ we obtain the traditional integral equation with reduced kernel (Eq. (2.58a)) for $F_z^s + F_z^i = 0$ (except for a factor 2π). The latter can be verified from the fact that the Green's function no longer depends on ϕ.

We assume that the incident field has a source that lies outside the domain $0 \leq r \leq a$, $0 \leq z \leq L$. Under this assumption, both the incident field $\boldsymbol{E}^i$ and the scattered field $\boldsymbol{E}^s$, due to the current on the mantle of the wire, are regular inside this domain. Further, both functions under the integral over ϕ satisfy the source-free scalar Helmholtz equation inside the domain $0 \leq r < a$, $0 < z < L$. Hence the functions F_z^s and F_z^i satisfy

$$\left(\partial_r^2 + \frac{1}{r}\partial_r + \partial_z^2 - \frac{s^2}{c_0^2}\right) F_z^\alpha(r, z) = 0,$$

(3.42)

where $\alpha \in \{i, s\}$.

We would like to find a forcing function on the axis of the wire. The thin-wire equation with exact kernel yields a current I_z, owing to the above mentioned existence results, and therefore we have

$$\left(\partial_r^2 + \frac{1}{r}\partial_r + \partial_z^2 - \frac{s^2}{c_0^2}\right) (F_z^i + F_z^s)(r, z) = 0,$$

(3.43a)

$$\begin{cases} F_z^i(a, z) + F_z^s(a, z) = 0 & \text{for } 0 < z < L, \\ F_z^i(r, z) + F_z^s(r, z) & \text{regular for } 0 \leq r \leq a, \ 0 < z < L. \end{cases}$$

(3.43b)

However, the solution to the system above is *not unique*. The solution can be described in terms of modes of a hollow cylinder:

$$F_z^i(r, z) + F_z^s(r, z) = \sum_{m=1}^{\infty} J_0\left(p_m \frac{r}{a}\right) \left(A_m \exp[-\gamma_m(L - z)] + B_m \exp[-\gamma_m z]\right),$$

(3.44)

where p_m is the m-th zero of J_0, $\gamma_m = \sqrt{(p_m/a)^2 + (s/c_0)^2}$ and A_m and B_m are unknown mode coefficients. Further, the branch cuts of γ_m are chosen such that $\mathrm{Re}\{\gamma_m\} \geq 0$ and $\mathrm{Im}\{\gamma_m\} \geq 0$ for $\omega > 0$. In general, the mode coefficients will not be zero. They are determined by the fields at the end faces, which result after applying appropriate boundary conditions at the end faces at $z = 0$ and $z = L$. Therefore, from the results for the integral equation with exact kernel, we immediately obtain existence for the integral equation with reduced kernel (under finite-energy conditions) for specific values of the coefficients A_m and B_m:

$$F_z^s(0, z) = -F_z^i(0, z) + \sum_{m=1}^{\infty} \left(A_m \exp[-\gamma_m(L - z)] + B_m \exp(-\gamma_m z) \right), \qquad (3.45)$$

at the expense of taking into account the boundary conditions at the end faces. Another way to formulate the problem of finding the coefficients A_m and B_m is to use the Stratton-Chu formulas, e.g., [65, Section 8.14].

To obtain a uniqueness result for the integral equation with reduced kernel, we use the uniqueness result for the integral equation with exact kernel. The idea is as follows. Suppose that there is a current $I_z \neq 0$ that satisfies

$$F_z^s(0, z) = 0 \quad \text{for } 0 < z < L. \qquad (3.46)$$

If we can show that

$$F_z^s(a, z) = 0 \quad \text{for } 0 < z < L, \qquad (3.47)$$

then the uniqueness result for the exact kernel integral equation guarantees that $I_z = 0$ and uniqueness for the reduced kernel integral equation follows immediately. Therefore, the uniqueness problem reduces to the problem of proving that if a function $F_z^s(r, z)$ satisfies

$$\left(\partial_r^2 + \frac{1}{r}\partial_r + \partial_z^2 - \frac{s^2}{c_0^2} \right) F_z^s(r, z) = 0, \qquad (3.48a)$$

$$\begin{cases} F_z^s(0, z) = 0 & \text{for } 0 < z < L, \\ F_z^s(r, z) \text{ regular} & \text{for } 0 \leq r \leq a, \ 0 < z < L, \end{cases} \qquad (3.48b)$$

then $F_z^s(a, z) = 0$.

To find a solution to the above problem, we use a Fourier series expansion for $F_z^s(r, z)$ in the z-direction on the interval $[0, L]$. We obtain

$$F_z^s(r, z) = \sum_{m=-\infty}^{\infty} f_m(r) \exp(-2\pi jmz/L), \qquad (3.49)$$

where $f_m(r)$ satisfies

$$\left[\partial_r^2 + \frac{1}{r}\partial_r - \left(\frac{2\pi m}{L}\right)^2 - \frac{s^2}{c_0^2} \right] f_m(r) = 0, \tag{3.50a}$$

$$\begin{cases} f_m(0) = 0 \\ f_m(r) \text{ regular} \quad \text{for } 0 \leq r \leq a. \end{cases} \tag{3.50b}$$

The regular solution to the above ordinary differential equation is

$$f_m(r) = A_m I_0\left(\gamma_m r\right), \tag{3.51}$$

where I_0 is the modified Bessel function of the first kind of order zero, and

$$\gamma_m^2 = \left(\frac{2\pi m}{L}\right)^2 + \frac{s^2}{c_0^2}. \tag{3.52}$$

Since $I_0(0) = 1$, we observe that $A_m = 0$ for all $m \in \mathbb{Z}$. Hence, we have proven that $F_z^s(a, z) = 0$ and at the same time we have established that, if a solution to the integral equation with reduced kernel exists, it is unique. For completeness, we mention that the statement made in the title of [22] is too restrictive in the sense that a solution of the integral equation with reduced kernel *can* exist for a properly chosen incident field. Otherwise, the integral equation with exact kernel would not admit a solution either.

Upon closer inspection, we observe that, in case the wire is sufficiently thin with respect to the wavelength, all modes are evanescent and therefore take effect only in proximity of the end faces of the wire. It is in this respect that we should understand the approximation in [72] that the end effects are negligible. Also, the frequently occurring numerical breakdown near the end faces of implementations of the integral equation with reduced kernel can be understood in this way, since the coefficients A_m and B_m are taken identically zero.

3.3.3 The ill-posed nature of the integral equation with reduced kernel

Since we can now conclude that we can solve the same thin-wire problem in two different ways, the question arises which equation is the preferred one. From a numerical point of view, the integral equation with exact kernel is well-posed as has been shown by Rynne in a series of papers [55, 56, 57, 58], whereas the integral equation with reduced kernel,

regarded as an integral operator equation, is ill-posed for Lebesgue spaces and for all standard Sobolev spaces $W^{r,p}(0,L)$ with positive and finite r and $1 \leq p < \infty$. For the Sobolev spaces, ill-posedness is a consequence of the compact-imbedding theorem [3].

The argument is as follows: the reduced kernel is a C^∞ function. Therefore, the application of the integral to an integrable current and the kernel yields a C^∞ function. However, the set of C^∞ functions is only a subset of the Lebesgue spaces and the Sobolev spaces. Therefore, we can take a forcing function in a Lebesgue or Sobolev space that does not belong to the set of C^∞ function and existence of the solution cannot be guaranteed for these spaces.

However, even if we have a forcing function that is smooth enough to guarantee existence of the solution, we have the problem that the inverse operator is unbounded. The crucial observation is that the operator is *compact*. The range of the operator is a subset of $C^\infty([0,L])$, and $C^\infty([0,L])$ is dense in all standard Lebesgue and Sobolev spaces. Suppose we choose $W^{r_1,p_1}(0,L)$ as the space for the forcing function. Due to the compact-imbedding theorem we can *always* find a space $W^{r_2,p_2}(0,L)$, which has compact imbedding in the space $W^{r_1,p_1}(0,L)$. Since the set of $C^\infty([0,L])$ functions is also a subset of $W^{r_2,p_2}(0,L)$, the integral operator is compact in $W^{r_1,p_1}(0,L)$. We now invoke Theorem 5, which states that the inverse of the integral equation is unbounded, and we conclude that the thin-wire integral equation with reduced kernel is ill-posed. Hence, finding a numerical approximation to an existing solution will require special care.

From the above, it may seem that two independent conditions for well-posedness are violated. However, the fact that the range of the operator is not closed causes the unboundedness of the inverse operator. Therefore, if we can find a norm for which the range of the operator is closed and restrict ourselves to forcing functions for which this norm is finite, then we have automatically solved the problem of the unbounded inverse. This is a consequence of the Open Mapping Theorem. As a direct consequence, we observe that the operator must have lost its compactness property for this norm. Unfortunately, within the framework of standard Lebesgue and Sobolev spaces it is impossible to find a norm, for which the range of the operator is closed.

The ill-posed nature of the problem can be quantified by invoking a theorem on the singular values of an integral equation with an analytic kernel [42, 46], which states that if we consider the thin-wire integral operator as a mapping from $L^2(0,L)$ to $L^2(0,L)$, i.e., we

use basis and testing functions belonging to $L^2(0, L)$ and use the $L^2(0, L)$ inner product, the singular values decay exponentially. This renders the integral equation with reduced kernel severely ill-posed.

In other words, regarding the discretized system we can expect (exponentially) increasing condition numbers for an increasingly finer discretization if we use the reduced-kernel integral equation. In case we take a fixed discretization, which corresponds to a fixed level of accuracy, we can still compute an approximation to the current by means of the reduced-kernel integral equation. For the reduced kernel, there is a transition from a region with coarse discretization and a limited condition number to a region with rapidly increasing condition number and fine discretization. The accuracy in the first region is limited by the discretization and in the second region by the increasing condition number. The optimal discretization, corresponding to the highest obtainable accuracy, is determined by the smoothness of the kernel, which in this case depends on the radius of the circular cross-section of the wire, a, and the ratio s/c_0.

On the other hand, the integral equation with exact kernel is more difficult to discretize than the integral equation with reduced kernel, due to the angular integral. In practical applications, for which the end effects can be neglected, we are interested in a reasonable approximation obtainable by the discretization. Hence, the reduced kernel equation may be a convenient alternative with a better performance under certain conditions. In this respect the thin-wire equation with reduced kernel is truly limited to *thin* wires.

3.3.4   Regularization methods for ill-posed problems

In the preceding section, we have shown that the thin-wire integral equation with reduced kernel is ill-posed. A way to obtain stable approximate solutions of such ill-posed problems, denoted as $Lu = f$, is to apply a regularization method. The idea of a regularization method is to modify the linear operator L in such a way that the modified operator is bounded and has a bounded inverse. The classical interpretation is based on the minimization of a functional. First of all, if the solution of the equation $Lu = f$ exists, then u is also the solution of the problem

$$\min_{u \in X} \|Lu - f\|_Y^2, \tag{3.53}$$

where we have considered the operator L as a mapping from a Hilbert space X to a Hilbert space Y. If the solution to $Lu = f$ does not exist, then we define the solution u as the solution of the above minimization problem, provided that $L^a L$ is invertible, where L^a is the adjoint of L, i.e.,

$$(Lx, y)_Y = (x, L^a y)_X, \tag{3.54}$$

for all $x \in X$ and $y \in Y$. However, due to the conditional existence of u and the unboundedness of $(L^a L)^{-1}$, the norm of u can become unbounded. The norm applied to u does not have to be the same norm as in problem (3.53). If there is a bounded linear operator $B : X \to Y$ with a bounded inverse $B^{-1} : Y \to X$, then $\|u\|_X$ and $\|Bu\|_Y$ are equivalent norms. To suppress unbounded solutions in the minimization problem of Eq.(3.53), we add a penalty function, viz.

$$\min_{u \in X} \|Lu - f\|_Y^2 + \alpha \|Bu\|_Y^2, \tag{3.55}$$

where $\alpha > 0$ is the so-called regularization parameter. In general, α should be small, to make sure that the penalty function $\|Bu\|_Y^2$ does not alter the solution too much. Now suppose u_α solves the above minimization problem, i.e.,

$$\min_{u \in X} \|Lu - f\|_Y^2 + \alpha \|Bu\|_Y^2 = \|Lu_\alpha - f\|_Y^2 + \alpha \|Bu_\alpha\|_Y^2, \tag{3.56}$$

then we have

$$\|L(u_\alpha + \beta \delta u) - f\|_Y^2 + \alpha \|B(u_\alpha + \beta \delta u)\|_Y^2 - \|Lu_\alpha - f\|_Y^2 - \alpha \|Bu_\alpha\|_Y^2 \geq 0, \tag{3.57}$$

for any $\beta \in \mathbb{C}$ and $\delta u \in X$. Owing to the fact that X and Y are Hilbert spaces, we can write

$$\begin{aligned} &\|L(u_\alpha + \beta \delta u) - f\|_Y^2 + \alpha \|B(u_\alpha + \beta \delta u)\|_Y^2 - \|Lu_\alpha - f\|_Y^2 - \alpha \|Bu_\alpha\|_Y^2 \\ &= |\beta|^2 \left(\|L\delta u\|_Y^2 + \alpha \|B\delta u\|_Y^2 \right) + 2 \operatorname{Re} \{ \beta (\delta u, L^a L u_\alpha + \alpha B^a B u_\alpha - L^a f)_X \} \geq 0, \end{aligned} \tag{3.58}$$

where the adjoint operator B^a is defined as

$$(Bx, y)_Y = (x, B^a y)_X, \tag{3.59}$$

for all $x \in X$ and $y \in Y$. For the specific choice

$$\beta = -\frac{(L^a L u_\alpha + \alpha B^a B u_\alpha - L^a f, \delta u)_X}{\|L\delta u\|_Y^2 + \alpha \|B\delta u\|_Y^2}, \tag{3.60}$$

we obtain

$$-\frac{\left| (L^a L u_\alpha + \alpha B^a B u_\alpha - L^a f, \delta u)_X \right|^2}{\|L\delta u\|_Y^2 + \alpha \|B\delta u\|_Y^2} \geq 0, \tag{3.61}$$

for all $\delta u \in X$, $\|\delta u\| \neq 0$. Hence, the solution of the minimization problem satisfies the linear equation

$$(\alpha B^a B + L^a L) \, u_\alpha = L^a f. \tag{3.62}$$

The operator $\alpha B^a B + L^a L$ is coercive and bounded from X to X, and therefore, by Theorem 8, it has a bounded inverse from X to X. Apparently, we have replaced the ill-posed problem $Lu = f$ by the well-posed problem of Eq. (3.62). The remaining choices are the value of α and the operator B. In case $X \subset Y$ and $B = I$, the above regularization method is known as Tikhonov regularization [42].

3.4   Perfectly conducting plate

The aim of this section is to summarize results from the literature, with respect to the solvability of the electric-field integral equation (EFIE) for an open screen, without developing any new theory. To this end, we will introduce a class of Hilbert spaces, that are known as Sobolev spaces. These spaces are used to analyze a weak form of the electric-field integral equation, instead of the classical strong form. The weak form results from the observation that the EFIE cannot be evaluated pointwise at the edges of the screen, due to the singular behavior of the fields. These results will be used to explain the difference in performance of two numerical schemes for the flat plate in Chapter 4.

For the perfectly conducting plate, results regarding the well-posedness have been established independently by Abboud & Starling [1] and Smirnov [61]. The results in [61] are slightly more general than those in [1], in the sense that the analysis in the latter requires a smoother incident field. In both papers, the mapping properties of the EFIE are analyzed, with the aid of a generalization of Theorem 9. The coercive part of the operator is formed by the surface integral over the surface current density and the static Green's function

$$G_s(\boldsymbol{r}) = \frac{1}{4\pi|\boldsymbol{r}|}, \tag{3.63}$$

or, alternatively, the function

$$G_c(\boldsymbol{r}) = \frac{\exp(-|\boldsymbol{r}|)}{4\pi|\boldsymbol{r}|}, \tag{3.64}$$

for which the Fourier transformation over $\mathbb{R}^2$ is

$$\frac{1}{2}(1 + |\boldsymbol{k}|^2)^{-1/2}, \tag{3.65}$$

where $\boldsymbol{k}$ spans the two-dimensional wave-vector space space and where $\boldsymbol{r}$ denotes normal-ized coordinates. The analysis with G_s is more difficult in the Fourier domain, due to a singular at $\boldsymbol{k} = \boldsymbol{0}$.

To state the main result of these papers and to explain its consequences, we need to introduce Sobolev spaces. The Fourier transformation on $\mathbb{R}^n$, for $n \in \{2, 3\}$, can be extended to the function space $\mathscr{S}'(\mathbb{R}^n)$ of Schwartz's tempered distributions [45, p. 4]. We define the Sobolev space $H^{\mathrm{s}}(\mathbb{R}^n)$, $\mathrm{s} \in \mathbb{R}$, as [45, p. 30]

$$H^{\mathrm{s}}(\mathbb{R}^n) = \{u \mid u \in \mathscr{S}'(\mathbb{R}^n),\, (1 + |\boldsymbol{k}|^2)^{\mathrm{s}/2} \hat{u} \in L^2(\mathbb{R}^n)\}, \tag{3.66}$$

and the norm by

$$\|u\|^2 = \int\limits_{\mathbb{R}^n} (1 + |\boldsymbol{k}|^2)^{\mathrm{s}} \, |\hat{u}|^2 \, d\boldsymbol{k}, \tag{3.67}$$

where $\boldsymbol{k}$ is now the n-dimensional vector spanning the n-dimensional Fourier space and $\hat{u}$ denotes the Fourier transformation of u. Further, $\hat{u}$ is a locally integrable function, such that the norm in Eq. (3.67) is finite. The advantage of this definition is that we can work with functions $\hat{u}$ in the Fourier domain, whereas their counterparts u are distributions, in general. As an example, we consider the δ-distribution in $\mathbb{R}^n$. Since the modulus of the Fourier transform of the δ-distribution equals one everywhere, we conclude that this distribution belongs to $H^{\mathrm{s}}(\mathbb{R}^n)$ for $\mathrm{s} < -n/2$. Since the δ-distribution acts on continuous functions, we find, by duality, that functions that belong to $H^{\mathrm{s}}(\mathbb{R}^n)$, with $\mathrm{s} > n/2$, are continuous.

The above definition can be used to define Sobolev spaces on a bounded volume Ω with boundary $\partial\Omega$. However, without restrictions on the boundary $\partial\Omega$, this is difficult. If the boundary $\partial\Omega$ is sufficiently smooth, then we can employ a partition of unity. This gives rise to $H^{\mathrm{s}}(\partial\Omega)$, $\mathrm{s} \in \mathbb{R}$. At the same time, this gives rise to the definition of Sobolev spaces $H^{\mathrm{s}}(\Omega) \subset H^{\mathrm{s}}(\mathbb{R}^n)$, $\mathrm{s} \geq 0$, on the domain Ω [45, p. 34&40]. Then, one can study the closure of $C_0^\infty(\Omega)$, the set of infinitely differentiable continuous functions with compact support in Ω, under the norms of these Sobolev spaces, thus introducing the spaces $H_0^{\mathrm{s}}(\Omega) \subset H^{\mathrm{s}}(\Omega)$, $\mathrm{s} \geq 0$, [45, p. 55]. Finally, the spaces $H^{-\mathrm{s}}(\Omega)$, $\mathrm{s} \geq 0$, are introduced as the dual spaces of $H_0^{\mathrm{s}}(\Omega)$ with respect to the $L^2(\Omega)$ inner product [45, p. 70].

Although these definitions apply to scalar functions, they can be extended to vector fields by demanding that each of the Cartesian components of a vector field belongs to the same scalar Sobolev space. This has inspired the definitions of normal and transverse spaces

as [1]

$$NH^{\text{s}}(\partial\Omega) = \{\boldsymbol{u} \mid \boldsymbol{u} = v\boldsymbol{n},\, v \in H^{\text{s}}(\partial\Omega)\}, \tag{3.68a}$$

$$TH^{\text{s}}(\partial\Omega) = \{\boldsymbol{u} \mid \boldsymbol{u} \in H^{\text{s}}(\partial\Omega)^3,\, \boldsymbol{u} \cdot \boldsymbol{n} = 0\}, \tag{3.68b}$$

where $\boldsymbol{n}$ is the outward unit normal vector on $\partial\Omega$ and $H^{\text{s}}(\partial\Omega)^3$ is the three-dimensional vectorial counterpart of $H^{\text{s}}(\partial\Omega)$.

For a continuous function u on $\overline{\Omega} = \Omega \cup \partial\Omega$, we can examine the limit

$$\lim_{\boldsymbol{r}\to\tilde{\boldsymbol{r}}} u(\boldsymbol{r}) = u|_{\partial\Omega} \quad \tilde{\boldsymbol{r}} \in \partial\Omega, \tag{3.69}$$

which is called the trace of u on $\partial\Omega$. The concept of trace can be generalized for $u \in H^{\text{s}}(\Omega)$. The problem is that the trace may no longer be a function on the boundary, i.e., it will be a distribution. The generalization is contained in the trace theorem, which states that, for a regular boundary $\partial\Omega$ and $u \in H^{\text{s}}(\Omega)$, the trace of u on $\partial\Omega$ belongs to $H^{\text{s}-1/2}(\partial\Omega)$ [45, p. 41&42]. Note that if Ω is a volume in $\mathbb{R}^3$ with a sufficiently smooth boundary $\partial\Omega$, the trace of $u \in H^{\text{s}}(\Omega)$ is *not* a continuous function on $\partial\Omega$, for s $\leq 3/2$.

For a sufficiently regular $\Omega \subset \mathbb{R}^3$, we define the space

$$TH^{-1/2}(\text{div}, \partial\Omega) = \{\boldsymbol{u} \mid \boldsymbol{u} \in TH^{-1/2}(\partial\Omega),\, \nabla_s \cdot \boldsymbol{u} \in H^{-1/2}(\partial\Omega)\}, \tag{3.70}$$

where $\nabla_s \cdot \boldsymbol{u}$ is the surface divergence of $\boldsymbol{u}$, as defined in Appendix A. With the aid of this definition, we can state a trace theorem for vector functions belonging to $H(\text{curl}, \Omega)$, as defined in Section 2.3, [1, 11]:

Theorem 11
The mapping $\boldsymbol{u} \in C^1(\overline{\Omega}) \to \boldsymbol{n} \times \boldsymbol{u}|_{\partial\Omega}$ can be uniquely extended to a surjective continuous operator γ_τ from $H(\text{curl}, \Omega)$ to $TH^{-1/2}(\text{div}, \partial\Omega)$, where $\partial\Omega$ is at least twice normal differentiable.

This theorem is based on the following identity for continuously differentiable vector functions $\boldsymbol{u}$ and $\boldsymbol{v}$:

$$\iiint\limits_{\Omega} \boldsymbol{v} \cdot (\nabla \times \boldsymbol{u}) - \boldsymbol{u} \cdot (\nabla \times \boldsymbol{v})\, dV = \oiint\limits_{\partial\Omega} (\boldsymbol{u} \times \boldsymbol{v}) \cdot \boldsymbol{n}\, dA = \oiint\limits_{\partial\Omega} (\boldsymbol{n} \times \boldsymbol{u}) \cdot \boldsymbol{v}\, dA. \tag{3.71}$$

From the above theorem, we infer that the surface current density $\boldsymbol{J}_S$ on a perfectly conducting, sufficiently regular closed surface $\partial\Omega$, e.g., a perfectly conducting sphere, belongs

to $TH^{-1/2}(\text{div}, \partial\Omega)$ under finite energy conditions, i.e., for incident fields which belong to $H_{loc}(\text{curl}, \mathbb{R}^3)$ (cf. the remarks below Eq. (2.32)). Actually, for surfaces with continuously differentiable normal, it can be shown that the surface current density belongs to $TH^{1/2}(\text{div}, \partial\Omega)$, provided that the incident field is sufficiently regular, i.e., $\boldsymbol{n} \times \boldsymbol{E}^i \in TH^{1/2}(\text{div}, \partial\Omega)$ [35]. For the open-screen problem, the results depend rather delicately on the exact definition of the function spaces and the value of s in the definition of $H^s(\partial\Omega)$. It is at this point that various notations exist. We will use the notation of E. Stephan, which is also used in [1]. The link between this notation and the notation in [45] is given in the footnotes of [1].

Let $\mathcal{P}$ be the surface of the perfectly conducting open screen under consideration. If $\mathcal{P}$ is twice normal differentiable, we can construct a volume Ω with boundary $\partial\Omega$, such that $\mathcal{P}$ is a smooth part of $\partial\Omega$. Then we define [1]

$$TH^{-1/2}(\text{curl}, \partial\Omega) = \{\boldsymbol{u} \mid \boldsymbol{u} \in TH^{-1/2}(\partial\Omega), \nabla_s \times \boldsymbol{u} \in H^{-1/2}(\partial\Omega)\}, \tag{3.72a}$$

$$TH^{-1/2}(\text{curl}, \mathcal{P}) = TH^{-1/2}(\text{curl}, \partial\Omega)/TH^{-1/2}_{\partial\Omega\setminus\overline{\mathcal{P}}}(\text{curl}, \partial\Omega), \tag{3.72b}$$

$$\widetilde{TH}^{-1/2}(\text{div}, \mathcal{P}) = r_{\mathcal{P}}(TH^{-1/2}_{\overline{\mathcal{P}}}(\text{div}, \partial\Omega)), \tag{3.72c}$$

where $\nabla_s \times \boldsymbol{u} = \nabla_s \cdot (\boldsymbol{u} \times \boldsymbol{n})$ denotes the surface curl of $\boldsymbol{u}$, and

$$TH^{-1/2}_{\partial\Omega\setminus\overline{\mathcal{P}}}(\text{curl}, \partial\Omega) = \left\{\boldsymbol{u} \mid \boldsymbol{u} \in TH^{-1/2}(\text{curl}, \partial\Omega), \text{supp}(\boldsymbol{u}) \subset \partial\Omega \setminus \overline{\mathcal{P}}\right\}, \tag{3.73}$$

where $\text{supp}(\boldsymbol{u})$ denotes the support of $\boldsymbol{u}$, i.e., the largest compact set such that $(\boldsymbol{\varphi}, \boldsymbol{u}) = 0$ for all sufficiently smooth testing functions $\boldsymbol{\varphi}$ with support in $\partial\Omega \setminus \text{supp}(\boldsymbol{u})$. Further, $r_{\mathcal{P}}$ is the restriction operator on $\mathcal{P}$, which restricts the domain of definition of its argument to the domain $\mathcal{P}$. The space $TH^{-1/2}(\text{curl}, \mathcal{P})$ is defined as a quotient space to which the standard quotient topology is assigned, see e.g. [32]. The definition of the quotient space implies an equivalence relation between vector functions defined on $\partial\Omega$, i.e., all vector fields which are equal on $\overline{\mathcal{P}}$ are considered equivalent, provided that they all belong to $TH^{-1/2}(\text{curl}, \partial\Omega)$, irrespective of their behavior on the rest of $\partial\Omega$. The following lemma is based on this equivalence relation [1] (see also [45, p. 78 & 79]).

Lemma 1
$TH^{-1/2}(\text{curl}, \mathcal{P})$ and $\widetilde{TH}^{-1/2}(\text{div}, \mathcal{P})$ are dual spaces of one another with respect to the $L^2(\mathcal{P})^2$ inner product.

Since the surface current density $\boldsymbol{J}_S$ on a perfectly conducting screen is zero outside the screen (owing to the continuity of the tangential magnetic field), the appropriate function

space for $\boldsymbol{J}_S$ is $\widetilde{TH}^{-1/2}(\text{div}, \mathcal{P})$. Elements of this function space are characterized by the following lemma [1].

Lemma 2

1. Let $\boldsymbol{u}$ be such that $\boldsymbol{u} \in \widetilde{TH}^{-1/2}(\mathcal{P})$, and $\nabla_s \cdot \boldsymbol{u} \in \widetilde{H}^{-1/2}(\mathcal{P})$. Thus, we can define the normal trace $\gamma_\nu \boldsymbol{u}$ on $\partial \mathcal{P}$, i.e., the boundary contour of $\mathcal{P}$, in each point $\boldsymbol{r} \in \partial \mathcal{P}$ in the tangent plane at $\boldsymbol{r} \in \overline{\mathcal{P}}$, in the space $H^{-1}(\partial \mathcal{P})$. This trace is given by the following formula:

$$\langle \gamma_\nu \boldsymbol{u}, \phi \rangle = \langle \boldsymbol{u}, \nabla_s R\phi \rangle + \langle \nabla_s \cdot \boldsymbol{u}, R\phi \rangle, \qquad (3.74)$$

where $R\phi$ is an arbitrary function of $H^{3/2}(\mathcal{P})$ whose trace ϕ on $\partial \mathcal{P}$ belongs to $H^1(\partial \mathcal{P})$, and $\nabla_s R\phi$ is the surface gradient of $R\phi$ on $\mathcal{P}$.

2. We have $\boldsymbol{u} \in \widetilde{TH}^{-1/2}(\text{div}, \mathcal{P})$ if and only if $\gamma_\nu \boldsymbol{u} = 0$.

The theorem in [61] on the solvability of the EFIE can be stated as follows.

Theorem 12

If $\text{Re}\{s\} \geq 0$, $s \neq 0$, where s denotes the Laplace parameter, the electric field integro-differential operator for a sufficiently regular open screen $\mathcal{P}$ is a mapping from $\widetilde{TH}^{-1/2}(\text{div}, \mathcal{P})$ to $TH^{-1/2}(\text{curl}, \mathcal{P})$ and is continuously invertible on these spaces.

This theorem, together with Lemma 1, implies that we can use the Galerkin method together with the $L^2(\mathcal{P})^2$ inner product on the surface of the scatterer to discretize the EFIE. In that case, the basis and testing functions should belong to $\widetilde{TH}^{-1/2}(\text{div}, \mathcal{P})$. A minimal requirement for such functions is given in the second part of Lemma 2. The rooftop functions defined in [28] and the Rao-Wilton-Glisson functions of [52] are examples of such functions.

3.5 Dielectric object

In Section 2.6, we have distinguished between three types of domain integro-differential equations for a dielectric object. The domain integro-differential equation (2.62) was an-alyzed in [47], under the assumption that the permittivity functions are continuously dif-ferentiable with respect to the spatial variables. However, for a permittivity function with

discontinuities, sharp edges, or corners, the analysis in [47] breaks down. Recently, the
same domain integro-differential equation was analyzed by means of the Banach contrac-
tion theorem in [82] under finite energy conditions. In this analysis, no assumptions are
made on the smoothness of the permittivity functions, although both the object and the
background need to be lossy. Here, we present an analysis of the domain integro-differential
equation (2.65) in the presence of discontinuities, sharp edges, and corners in the permit-
tivity function, including the cases in which the background or the object (or both) are
lossless and $\mathrm{Re}\{s\} = 0$.

First, we need to establish some properties of the permittivity function, assuming that σ
is identically zero. In general, $\varepsilon(\boldsymbol{r}, s)$ is a 3×3 matrix function, that is invertible at every
(fixed) space coordinate for a fixed value of s. Further, the modulus of every element of
the matrix is bounded from above. After splitting ε in a real and imaginary part, i.e.,

$$\varepsilon = \varepsilon' - j\varepsilon'', \tag{3.75}$$

we can pose even stronger hypotheses on ε, based on causality and energy:

$$0 \leq \boldsymbol{\xi}^* \cdot (\varepsilon' \boldsymbol{\xi}) \leq a' \boldsymbol{\xi}^* \cdot \boldsymbol{\xi}, \tag{3.76a}$$

$$0 \leq \boldsymbol{\xi}^* \cdot (\varepsilon'' \boldsymbol{\xi}) \leq a'' \boldsymbol{\xi}^* \cdot \boldsymbol{\xi}, \tag{3.76b}$$

for $\boldsymbol{\xi} \in \mathbb{C}^3$ and where * denotes complex conjugation. Further, the coefficients a' and a''
are independent of $\boldsymbol{r}$ and s. These relations should hold for any fixed point in space and
indicate that both ε' and ε'' are positive semi-definite. Furthermore, we will assume that
if the real part is indefinite at some point in space, the imaginary part will be definite and
vice versa, for a fixed s. This guarantees the existence of the inverse of $\varepsilon(\boldsymbol{r}, s)$ at any point
in space. Hence, for a domain $\mathcal{G}$ that contains the dielectric object, we have

$$\left| \iiint_{\mathcal{G}} \boldsymbol{f}^* \cdot (\varepsilon \boldsymbol{f}) \, dV \right| \geq \alpha \iiint_{\mathcal{G}} \boldsymbol{f} \cdot \boldsymbol{f}^* dV, \tag{3.77}$$

for some $\alpha > 0$. A discussion of these hypotheses can be found in [11, Chapter 1]. In case
the object contains Ohmic losses, similar inequalities can be derived for $\sigma(\boldsymbol{r}, s)/s + \varepsilon(\boldsymbol{r}, s)$.

3.5.1 Helmholtz decomposition

To analyze the domain integro-differential equation, we extend the domain $\mathcal{D}$ to the cube
$\mathcal{K}$, with boundary $\partial\mathcal{K}$, such that $\mathcal{D}$ is contained in $\mathcal{K}$ and the distance d between $\mathcal{D}$ and
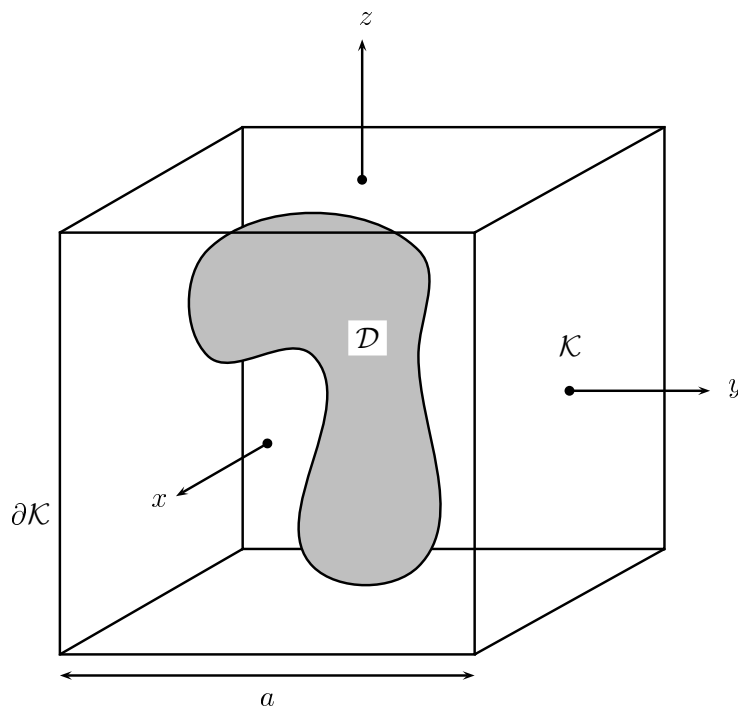
Figure 3.1: extension of the domain $\mathcal{D}$ to $\mathcal{K}$.

$\partial \mathcal{K}$ is positive. This is shown in Figure 3.1. We choose a Cartesian coordinate system such that its origin coincides with the center of the cube, the axes are oriented parallel to the edges of the cube and these edges have length $2a$. Further, we extend the definition of the contrast-current density $\boldsymbol{J}^c$ to $\mathcal{K}$ by extending $\boldsymbol{J}^c$ by zero outside $\overline{\mathcal{D}}$.

Let $\boldsymbol{f}$ be a continuously differentiable vector field on $\mathcal{K}$, i.e., $\boldsymbol{f} \in C^1(\mathcal{K})^3 \cap C(\overline{\mathcal{K}})^3$. Then the Helmholtz decomposition allows a decomposition of $\boldsymbol{f}$ as [18]

$$\boldsymbol{f}(\boldsymbol{r}) = \nabla p(\boldsymbol{r}) + \nabla \times \boldsymbol{w}(\boldsymbol{r}), \tag{3.78}$$

where $p \in C^2(\mathcal{K})$ and $\boldsymbol{w} \in C^1(\mathcal{K})^3 \cap C(\overline{\mathcal{K}})^3$, for $\boldsymbol{r} \in \mathcal{K}$. We can supplement the Helmholtz decomposition by a boundary condition for $\boldsymbol{w}$

$$\boldsymbol{n} \times \boldsymbol{w}\big|_{\partial \mathcal{K}} = \boldsymbol{0}, \tag{3.79}$$

where $\boldsymbol{n}$ is the outward-pointing unit normal vector of $\partial \mathcal{K}$. Using the identity

$$\nabla \cdot (\boldsymbol{g} \times \boldsymbol{h}) = \boldsymbol{h} \cdot \nabla \times \boldsymbol{g} - \boldsymbol{g} \cdot \nabla \times \boldsymbol{h}, \tag{3.80}$$

where $\cdot$ indicates the (non-complex) scalar product between two vectors, we have

$$\iiint_{\mathcal{K}} \nabla \cdot (\boldsymbol{w}^* \times \nabla p) dV = \iiint_{\mathcal{K}} \nabla p \cdot \nabla \times \boldsymbol{w}^* dV, \tag{3.81}$$

where $*$ indicates complex conjugation. From Gauss's theorem and Eq. (3.79), we obtain the orthogonality relation

$$\iiint_{\mathcal{K}} \nabla p \cdot \nabla \times \boldsymbol{w}^* dV = \oiint_{\partial\mathcal{K}} \nabla p \cdot (\boldsymbol{n} \times \boldsymbol{w}^*) dA = 0. \tag{3.82}$$

Further, it can be proven [17, p. 245-248&314] that

$$s(\boldsymbol{r}) = \iiint_{\mathcal{K}} G(\boldsymbol{r} - \boldsymbol{r}') p(\boldsymbol{r}') dV', \tag{3.83}$$

where

$$G(\boldsymbol{r}) = \frac{\exp(-s|\boldsymbol{r}|/c_0)}{4\pi|\boldsymbol{r}|}, \tag{3.84}$$

satisfies the inhomogeneous Helmholtz equation

$$\nabla^2 s(\boldsymbol{r}) - \frac{s^2}{c_0^2} s(\boldsymbol{r}) = -p(\boldsymbol{r}), \tag{3.85}$$

for $\boldsymbol{r} \in \mathcal{K}$. For a continuously differentiable scalar function $q(\boldsymbol{r})$, we can show by straight-forward integration by parts and by using the translation invariance of $G(\boldsymbol{r} - \boldsymbol{r}')$ that

$$\iiint_{\mathcal{K}} G(\boldsymbol{r} - \boldsymbol{r}') \partial_{i'} q(\boldsymbol{r}') dV' =$$
$$\partial_i \iiint_{\mathcal{K}} G(\boldsymbol{r} - \boldsymbol{r}') q(\boldsymbol{r}') dV' + \iint_{\partial\mathcal{K}|_{i=a}} G(\boldsymbol{r} - \boldsymbol{r}') q(\boldsymbol{r}') dA' - \iint_{\partial\mathcal{K}|_{i=-a}} G(\boldsymbol{r} - \boldsymbol{r}') q(\boldsymbol{r}') dA', \tag{3.86}$$

where $i \in \{x, y, z\}$, $i' \in \{x', y', z'\}$, $\partial\mathcal{K}|_{i=a}$ is the surface of the cube described by $i = a$ and $\partial\mathcal{K}|_{i=-a}$ is the surface of the cube described by $i = -a$, e.g., $\partial\mathcal{K}|_{x=a}$ is given by $x = a$, $-a < y < a$, $-a < z < a$. This identity, applied to the separate components in the Helmholtz decomposition, together with Eq. (3.79), yields

$$\iiint_{\mathcal{K}} G(\boldsymbol{r} - \boldsymbol{r}') \nabla' \times \boldsymbol{w}(\boldsymbol{r}') dV' = \nabla \times \iiint_{\mathcal{K}} G(\boldsymbol{r} - \boldsymbol{r}') \boldsymbol{w}(\boldsymbol{r}') dV', \tag{3.87a}$$

$$\iiint_{\mathcal{K}} G(\boldsymbol{r} - \boldsymbol{r}') \nabla' p(\boldsymbol{r}') dV' = \nabla \iiint_{\mathcal{K}} G(\boldsymbol{r} - \boldsymbol{r}') p(\boldsymbol{r}') dV' +$$
$$\oiint_{\partial\mathcal{K}} G(\boldsymbol{r} - \boldsymbol{r}') p(\boldsymbol{r}') \boldsymbol{n}(\boldsymbol{r}') dA'. \tag{3.87b}$$

We note that the term containing the volume integral over p is identical to $\nabla s(\boldsymbol{r})$ in Eq. (3.83). From Eqs (2.42) and (2.43a), we observe that the scattered electric field is of the form

$$s\varepsilon_0 \boldsymbol{E}^s(\boldsymbol{r}) = \left(\nabla\nabla\cdot -\frac{s^2}{c_0^2}\right)\iiint\limits_{\mathcal{K}} G(\boldsymbol{r}-\boldsymbol{r}')\boldsymbol{f}(\boldsymbol{r}')dV', \tag{3.88}$$

where $\boldsymbol{f}(\boldsymbol{r})$ represents the contrast-current density $\boldsymbol{J}^c(\boldsymbol{r})$, after extension to $\mathcal{K}$. If we apply the results of Eqs (3.78), (3.83), (3.85), and (3.87) to the representation of the scattered electric field, we obtain

$$\begin{aligned}\left(\nabla\nabla\cdot -\frac{s^2}{c_0^2}\right)\iiint\limits_{\mathcal{K}} G(\boldsymbol{r}-\boldsymbol{r}')\boldsymbol{f}(\boldsymbol{r}')dV' = {} & \left(\nabla\nabla\cdot -\frac{s^2}{c_0^2}\right)\oiint\limits_{\partial\mathcal{K}} G(\boldsymbol{r}-\boldsymbol{r}')p(\boldsymbol{r}')\boldsymbol{n}(\boldsymbol{r}')dA' \\ & -\nabla p -\frac{s^2}{c_0^2}\iiint\limits_{\mathcal{K}} G(\boldsymbol{r}-\boldsymbol{r}')\nabla\times\boldsymbol{w}(\boldsymbol{r}')dV',\end{aligned} \tag{3.89}$$

for $\boldsymbol{r}\in\mathcal{K}$.

3.5.2 Mapping properties under finite energy conditions

In view of the radiation conditions discussed in Section 2.4, we expect $\boldsymbol{J}^c$ to belong to the space $L^2(\mathcal{K})^3$, provided that $\chi\boldsymbol{E}^i$ also belongs to $L^2(\mathcal{K})^3$. Therefore, it is useful to investigate the mapping properties of the domain integro-differential equation (2.65) as a mapping from $L^2(\mathcal{K})^3$ to $L^2(\mathcal{K})^3$. Based on the fact that the continuously differentiable functions are dense in $L^2(\mathcal{K})$, the Helmholtz decomposition can be extended to vector fields in $L^2(\mathcal{K})^3$ in the sense of Eq. (3.78) and the boundary condition (3.79) [18, Corollary 6, p. 226]. Accordingly, we have $p\in H^1(\mathcal{K})$ and $\boldsymbol{w}\in H^1_{t0}(\mathcal{K})^3$, where

$$H^1(\mathcal{K}) = \left\{g \mid g\in L^2(\mathcal{K}),\ \nabla g\in L^2(\mathcal{K})^3\right\}, \tag{3.90a}$$

$$H^1_{t0}(\mathcal{K})^3 = \left\{\boldsymbol{g} \mid \boldsymbol{g}\in H^1(\mathcal{K})^3,\ \boldsymbol{n}\times\boldsymbol{g}|_{\partial\mathcal{K}} = \boldsymbol{0}\right\}. \tag{3.90b}$$

The element p is uniquely determined up to a constant and $\boldsymbol{w}$ is unique under the supplementary condition

$$\oiint\limits_{S}\boldsymbol{w}\cdot\boldsymbol{n}\,dA = 0, \tag{3.91}$$

for each regular closed surface $S\in\overline{\mathcal{K}}$. We will assume that the remaining constant of p has been fixed by demanding

$$\iiint\limits_{\mathcal{K}} p\,dV = 0. \tag{3.92}$$

Owing to the same density properties, the results of Eq. (3.89) can be generalized to $\boldsymbol{f} \in L^2(\mathcal{K})^3$. To this end, we introduce the operators

$$I\boldsymbol{f} = \boldsymbol{f}, \qquad\qquad\qquad\qquad I : L^2(\mathcal{K})^3 \to L^2(\mathcal{K})^3, \qquad (3.93\text{a})$$

$$P\boldsymbol{f} = \nabla p, \qquad\qquad\qquad\qquad P : L^2(\mathcal{K})^3 \to L^2(\mathcal{K})^3, \qquad (3.93\text{b})$$

$$Q\boldsymbol{f} = (I - P)\boldsymbol{f} = \nabla \times \boldsymbol{w}, \qquad\qquad Q : L^2(\mathcal{K})^3 \to L^2(\mathcal{K})^3, \qquad (3.93\text{c})$$

$$K\boldsymbol{f} = \frac{s^2}{c_0^2} \iiint\limits_{\mathcal{K}} G(\boldsymbol{r} - \boldsymbol{r}')\boldsymbol{f}(\boldsymbol{r}')dV', \qquad\qquad K : L^2(\mathcal{K})^3 \to H^2(\mathcal{K})^3, \qquad (3.93\text{d})$$

$$L\boldsymbol{f} = \left(\frac{s^2}{c_0^2} - \nabla\nabla\cdot\right) \oiint\limits_{\partial\mathcal{K}} p(\boldsymbol{r}')G(\boldsymbol{r} - \boldsymbol{r}')\boldsymbol{n}(\boldsymbol{r}')dA', \qquad L : L^2(\mathcal{K})^3 \to C^\infty(\mathcal{K})^3, \qquad (3.93\text{e})$$

$$M_\chi \boldsymbol{f} = \chi\boldsymbol{f}, \qquad\qquad\qquad\qquad M_\chi : L^2(\mathcal{K})^3 \to L^2(\mathcal{K})^3. \qquad (3.93\text{f})$$

The operator L exists if p has been fixed according to Eq. (3.92), since in that case p is uniquely determined by $\boldsymbol{f}$. Further, the operators P and Q are mutually orthogonal projection operators, by Eq. (3.82), in line with the Helmholtz decomposition. Using these definitions and the preceding results for the Helmholtz decomposition of Eq. (3.89), we can write, for $\boldsymbol{J}^c \in L^2(\mathcal{K})^3$,

$$s\varepsilon_0\chi\boldsymbol{E}^i = \boldsymbol{J}^c + \chi\left[\frac{s^2}{c_0^2}\boldsymbol{A}(\boldsymbol{J}^c) - \nabla\nabla \cdot \boldsymbol{A}(\boldsymbol{J}^c)\right] = [I + M_\chi P + M_\chi KQ + M_\chi L]\,\boldsymbol{J}^c. \quad (3.94)$$

For this combination of operators, the following properties hold.

- $I + M_\chi P$ has a bounded inverse. This will be proven in Section 3.5.4.

- The Green's function G in the operator K is square integrable on $\mathcal{K}$ and therefore K is a Hilbert-Schmidt operator. In particular, K is compact from $L^2(\mathcal{K})^3$ to $L^2(\mathcal{K})^3$ [32]. This implies that the product $M_\chi KQ$ is compact from $L^2(\mathcal{K})^3$ to $L^2(\mathcal{K})^3$, since both M_χ and Q are bounded.

We intend to cast the operator on the right-hand side of Eq. (3.94) in the form

$$T + C, \qquad\qquad\qquad\qquad\qquad\qquad (3.95)$$

such that the inverse of T exists and is bounded from $L^2(\mathcal{K})^3$ to $L^2(\mathcal{K})^3$, while C is compact from $L^2(\mathcal{K})^3$ to $L^2(\mathcal{K})^3$. In that case, we can apply Theorem 7 to establish well-posedness of the scattering problem. This leaves us with the operator product $M_\chi L$. We observe that

the function $\chi(\boldsymbol{r})$ is identically zero for $\boldsymbol{r}$ outside $\overline{\mathcal{D}}$. Therefore, we introduce an auxiliary operator M_ϕ in the following way

$$M_\phi \boldsymbol{f}(\boldsymbol{r}) = \phi(\boldsymbol{r}) \boldsymbol{f}(\boldsymbol{r}), \tag{3.96}$$

where $\phi(\boldsymbol{r})$ is a $C_0^\infty(\mathcal{K})$ function such that

$$\begin{cases} \phi(\boldsymbol{r}) = 1 & \text{for} \quad \inf_{\boldsymbol{x} \in \partial\mathcal{K}} |\boldsymbol{x} - \boldsymbol{r}| \geq 2d/3, \\ 0 \leq \phi(\boldsymbol{r}) \leq 1 & \text{for} \quad d/3 < \inf_{\boldsymbol{x} \in \partial\mathcal{K}} |\boldsymbol{x} - \boldsymbol{r}| < 2d/3, \\ \phi(\boldsymbol{r}) = 0 & \text{for} \quad \inf_{\boldsymbol{x} \in \partial\mathcal{K}} |\boldsymbol{x} - \boldsymbol{r}| \leq d/3, \end{cases} \tag{3.97}$$

for $\boldsymbol{r} \in \mathcal{K}$, and d is the minimum distance between the boundary $\partial\mathcal{K}$ and the domain $\mathcal{D}$. We can now write

$$\chi(\boldsymbol{r}) = \chi(\boldsymbol{r})\phi(\boldsymbol{r}) + \chi(\boldsymbol{r})(1 - \phi(\boldsymbol{r})) = \chi(\boldsymbol{r})\phi(\boldsymbol{r}), \tag{3.98}$$

owing to the fact that $\chi(\boldsymbol{r}) = 0$ outside the domain of the dielectric object. Hence,

$$M_\chi = M_{\chi\phi} + M_{\chi(1-\phi)} = M_{\chi\phi} = M_\chi M_\phi \,, \tag{3.99a}$$

$$\Rightarrow M_\chi L = M_\chi M_\phi L. \tag{3.99b}$$

We shall prove that $M_\phi L$ is compact. The operator $M_\phi L$ is a mapping from $L^2(\mathcal{K})^3$ to $C_0^\infty(\mathcal{K})^3$. This is a consequence of the fact that the function G is a C^∞ function outside its singularity. The singularity is confined to $\partial\mathcal{K}$, since the integration is restricted to $\partial\mathcal{K}$. Further, $C_0^\infty(\mathcal{K})^3$ is a subset of $H^1(\mathcal{K})^3$. Owing to the compact-imbedding theorem for Sobolev spaces [3, p. 144], $M_\phi L$ is a compact operator from $L^2(\mathcal{K})^3$ to $L^2(\mathcal{K})^3$. Finally, the operator M_χ is bounded, since $\chi(\boldsymbol{r})$ is bounded. Hence, by Theorem 4, the operator $M_\chi M_\phi L$ is compact from $L^2(\mathcal{K})^3$ to $L^2(\mathcal{K})^3$. We conclude that $M_\chi L$ is a compact operator. It is for this reason that we have extended the domain $\mathcal{D}$ to the cube $\mathcal{K}$. Moreover, the cube allows for an elementary Helmholtz decomposition since it is connected and simply connected. From the point of view of numerical methods, the cube is also a logical choice, since it allows straightforward meshing and the application of algorithms such as the Fast Fourier Transformation.

We end up with an operator in the form of (3.95), with

$$T = I + M_\chi P, \tag{3.100a}$$

$$C = M_\chi KQ + M_\chi LS. \tag{3.100b}$$

To prove existence and boundedness of the inverse we still have to prove that the solution of the operator is unique. Therefore, the next step is to prove uniqueness.

3.5.3   Uniqueness

Uniqueness of the solution to Maxwell's equations, subject to the radiation conditions, for a dielectric object of finite size, i.e., the domain of the object is bounded in $\mathbb{R}^3$, with a finite number of sharp corners and edges in a homogeneous background was proven by Jones [36, Chapter 9]. In the proof, the continuity of the tangential electric and magnetic fields at the interface between the homogeneous background and the dielectric object is used. Therefore, we can assume that the following system has only the trivial solution:

$$\begin{cases} \nabla \times \boldsymbol{H}^s = s\varepsilon \boldsymbol{E}^s, \\ \nabla \times \boldsymbol{E}^s = -s\mu_0 \boldsymbol{H}^s, \\ \text{radiation conditions}, \end{cases} \tag{3.101}$$

where ε equals ε_0 outside a bounded domain. Let us now assume that both $\boldsymbol{J}_1^c$ and $\boldsymbol{J}_2^c$ are solutions of Eq. (2.65) with the same excitation. Then $\boldsymbol{J}_3^c = \boldsymbol{J}_1^c - \boldsymbol{J}_2^c$ is a solution of the homogeneous counterpart of Eq. (2.65). The corresponding scattered fields $\boldsymbol{E}_3^s$ and $\boldsymbol{H}_3^s$ generated by this current density, and subject to the radiation conditions follow from Eqs (2.38), (2.42), and (2.43a). By definition of the current densities $\boldsymbol{J}_1^c = s\varepsilon_0\chi(\boldsymbol{E}^i + \boldsymbol{E}_1^s)$ and $\boldsymbol{J}_2^c = s\varepsilon_0\chi(\boldsymbol{E}^i + \boldsymbol{E}_2^s)$ we have $\boldsymbol{J}_3^c = s\varepsilon_0\chi(\boldsymbol{E}_1^s - \boldsymbol{E}_2^s) = s\varepsilon_0\chi\boldsymbol{E}_3^s$. Consequently, the fields $\boldsymbol{E}_3^s$ and $\boldsymbol{H}_3^s$ satisfy Eq. (3.101). Therefore, we can conclude that $\boldsymbol{E}_3^s = \boldsymbol{0}$. Hence, $\boldsymbol{J}_3^c = \boldsymbol{0}$ and the integro-differential equation (2.65) has a unique solution, provided that the solution is restricted to $L_{loc}^2(\mathbb{R}^3)^3$.

3.5.4   The operator $I + M_\chi P$

From Section 3.5.3, it follows that the equation

$$(T + C)\boldsymbol{J}^c = s\varepsilon_0 M_\chi \boldsymbol{E}^i, \tag{3.102}$$

has a unique solution, so it remains to prove that the solution exists. In Section 3.5.2, we have shown that the solution exists if the operator $T = I + M_\chi P$ is bounded and has a bounded inverse. The boundedness of T is a simple consequence of the boundedness of $\varepsilon(\boldsymbol{r}, s)$. To prove the existence and boundedness of the inverse, we decompose the operator T in the form of a 2×2 operator matrix. This is possible, since P and Q are mutually orthogonal projection operators and $\mathcal{R}(P) \cup \mathcal{R}(Q) = L^2(\mathcal{K})^3$.

$$T = \begin{bmatrix} P + PM_\chi P & 0 \\ QM_\chi P & Q \end{bmatrix} = \begin{bmatrix} PM_{I+\chi}P & 0 \\ QM_\chi P & Q \end{bmatrix}, \tag{3.103}$$

where we have used the fact that $I + M_\chi = M_{I+\chi}$ and that P is idempotent, since it is a projection operator. Hence, we can denote the mapping properties of T as

$$T : \begin{pmatrix} \mathcal{R}(P) \\ \mathcal{R}(Q) \end{pmatrix} \to \begin{pmatrix} \mathcal{R}(P) \\ \mathcal{R}(Q) \end{pmatrix}. \tag{3.104}$$

Further, P is equal to the identity operator on $\mathcal{R}(P)$ and Q is equal to the identity operator on $\mathcal{R}(Q)$. Therefore, straightforward linear algebra shows that we can construct an inverse of the form

$$T = \begin{bmatrix} PAP & 0 \\ -QM_\chi PAP & Q \end{bmatrix}, \tag{3.105}$$

where PAP should be the inverse of $PM_{I+\chi}P$ on $\mathcal{R}(P)$. At the same time, if PAP does not exist, then the inverse of T does not exist. Therefore, a necessary and sufficient condition for the existence of the inverse of $I + M_\chi P$ is that PAP exists. However, the operator $M_{I+\chi}$ is coercive, as can be seen from the hypotheses on ε in Eq. (3.77), since $I + \chi = \varepsilon/\varepsilon_0$, or $I + \chi = (\sigma/s + \varepsilon)/\varepsilon_0$ in case Ohmic losses are present. Further, the range of P is a Hilbert space with respect to the $L^2(\mathcal{K})^3$ inner product, and the coercivity of $PM_{I+\chi}P$ on $\mathcal{R}(P)$ is a direct consequence of the coerciveness of $M_{I+\chi}$, i.e., $PM_{I+\chi}P$ is a bounded coercive linear operator on $\mathcal{R}(P)$. Theorem 8 guarantees the existence and boundedness of the inverse of $PM_{I+\chi}P$ on $\mathcal{R}(P)$, which is denoted as PAP.

Along the same lines and under the same conditions for $\varepsilon(\boldsymbol{r}, s)$ or $\sigma(\boldsymbol{r}, s)/s + \varepsilon(\boldsymbol{r}, s)$, it can be proven that the operator in Eq. (2.62) is an invertible mapping from $H(\mathrm{curl}, \mathcal{G})$ to $H(\mathrm{curl}, \mathcal{G})$, where $\mathcal{G}$ is a regular domain in $\mathcal{K}$ that contains $\overline{\mathcal{D}}$ in its interior. Finally, Eq. (2.64) and Eq. (2.66) are invertible mappings from $H(\mathrm{div}, \mathcal{G})$ to $H(\mathrm{curl}, \mathcal{G})$, owing to the mapping properties of $\varepsilon(\boldsymbol{r}, s)$ and $\sigma(\boldsymbol{r}, s)/s + \varepsilon(\boldsymbol{r}, s)$, respectively.

3.5.5   Summary for the dielectric object

We have shown that, under very general assumptions with respect to the properties of a dielectric object, the domain integro-differential equation for the contrast-current density has a bounded inverse from $L^2(\mathcal{K})^3$ to $L^2(\mathcal{K})^3$ by showing that it can be reduced to a Fredholm integral equation of the second kind with a unique solution. In other words, the problem is well-posed from $L^2(\mathcal{K})^3$ to $L^2(\mathcal{K})^3$. For a projection method, this means that we can adopt the Galerkin method with respect to the $L^2(\mathcal{K})^3$ inner product and with basis and testing functions belonging to $L^2(\mathcal{K})^3$. Alternatively, one could construct basis

and testing functions for the Helmholtz decomposition. However, the presented analysis is not directly applicable in a practical numerical tool that employs local basis and testing functions.

At present, numerical schemes based on Eq. (2.62) [2] and Eq. (2.64) or Eq. (2.66) [60, 84, 86, 87] are available. In these schemes, which employ the $L^2(\mathcal{D})^3$ inner product, the term $\nabla\nabla \cdot \boldsymbol{A}$ is tackled by bringing the gradient operator over to the testing function, which is piecewise linear in the longitudinal direction. As a result, a finite-difference formula is obtained for the differential operator. For the formulation where the Green's function has been replaced by a spatially averaged version of the Green's function [2, 84, 86, 87], this approximation is valid, since the weak Green's function is continuous everywhere. It has been demonstrated that the weak Green's function converges to the original Green's function when the radius of the sphere, on which the Green's function is averaged, goes to zero. However, further research is required to examine whether this also holds for the combination of the integro-differential equation and the weak Green's function. For all of the methods mentioned above, it is not clear that the dual space of the range space of the domain-integro-differential operator can be spanned by the proposed testing functions, since the differentiability of these testing functions is used explicitly. This results in a solution space for the contrast-current density that is larger than $L^2(\mathcal{K})^3$. In turn, this larger space may no longer give rise to a unique solution of the domain integro-differential equations. Therefore, we cannot guarantee *convergence in norm* for these methods. Recently, a "potential integral equation method" was proposed [19]. The advantage of its formulation is that the second-order spatial derivatives operating on the vector potential ($\nabla\nabla\cdot\boldsymbol{A}$) have been removed, at the expense of spatial derivatives operating on the permittivity function. Therefore, this formulation is restricted to sufficiently smooth profiles. The numerical scheme proposed for this formulation is based on point-matching, which implies that convergence in an optimal norm cannot be expected.

Chapter 4

Discretization and solution strategy

For the thin wire and the perfectly conducting flat plate, we will demonstrate the steps to arrive at a discretized system of equations. Further, we will discuss the conjugate-gradient method to solve these systems in an efficient manner. The dielectric object will not be discussed here, since we have not developed a discretization for the corresponding integro-differential equation. We will consider the dielectric object again in Chapter 6, where we will use a standard discretization.

4.1 Straight thin-wire segment

For the thin-wire problem, we will consider the reduced-kernel integral equation only. We repeat the pertaining equation:

$$-s\varepsilon_0 E_z^i(r = 0, z) = \left[\partial_z^2 - \frac{s^2}{c_0^2}\right] \int\limits_0^L g_a(z - z') I_z(z') dz', \tag{4.1}$$

for $z \in (0, L)$. The discretization of this equation leads to simpler expressions than the discretization of the integral equation with exact kernel. Also, this equation allows us to demonstrate the consequences of using an ill-posed formulation.

4.1.1   Hallén's equation for the thin wire

From the above equation, we will derive Hallén's equation by noticing that the operator in front of the integral is the Laplace-transformed one-dimensional wave operator. The fundamental solution of this wave operator can be found by solving the equation

$$\left[\partial_z^2 - \left(\frac{s}{c_0}\right)^2\right] G_1(z, z_0) = -\delta(z - z_0). \tag{4.2}$$

The solution for $z \in \mathbb{R}$ that satisfies the one-dimensional radiation condition is given by

$$G_1(z, z_0) = \frac{c_0}{2s} \exp\left(-\frac{s}{c_0} |z - z_0|\right), \tag{4.3}$$

which is the so-called one-dimensional Green's function. We now use a one-dimensional version of Green's theorem, viz.

$$\int_0^L f(z)g''(z) - f''(z)g(z)dz = [f(z)g'(z) - f'(z)g(z)]_0^L. \tag{4.4}$$

We set

$$f(z) = \int_0^L g_a(z - z')I_z(z')dz', \tag{4.5a}$$

$$g(z) = \frac{c_0}{2s} \exp\left(-\frac{s}{c_0} |z - z_0|\right), \tag{4.5b}$$

and use Eqs (4.1) and (4.2) for the second derivatives of $f(z)$ and $g(z)$. This results in

$$\int_0^L g_a(z_0 - z')I_z(z')dz' = \frac{Y_0}{2} \int_0^L E_z^i(r = 0, z) \exp\left(-\frac{s}{c_0} |z_0 - z|\right) dz$$
$$+ F_0 \exp\left(-\frac{s}{c_0} z_0\right) + F_L \exp\left[-\frac{s}{c_0}(L - z_0)\right], \tag{4.6}$$

for $z_0 \in (0, L)$ and where $Y_0 = \sqrt{\varepsilon_0/\mu_0}$. Eq. (4.6) is known as Hallén's equation. The major attraction of Hallén's equation is that the spatial derivatives have been removed. The terms with F_0 and F_L correspond to the boundary terms in Eq. (4.4). Strictly speaking, F_0 and F_L depend on $I_z(z)$, but we will treat them as independent variables. For the formulation of Hallén's equation, the choice of the integral equation with exact kernel would have

produced the same expression as in Eq. (4.6), with $g_a(z)$ replaced by $g_e(z)$. For Hallén's equation with exact kernel, Jones [37] has proven existence and uniqueness if the additional boundary conditions $I_z(0) = I_z(L) = 0$ are used. In that case, the additional constants F_0 and F_L are in fact independent variables and Hallén's equation is equivalent to Eq. (2.58b). For Hallén's equation with reduced kernel, such results are not known. A way to eliminate the additional constants F_0 and F_L in case of Hallén's equation with reduced kernel would be to enforce the equality sign at the additional points $z = 0$ and $z = L$. This is discussed in [72] for Hallén's equation in the time domain. However, it is not clear whether the additional boundary conditions $I_z(0) = I_z(L) = 0$ guarantee the independence of F_0 and F_L in this case.

4.1.2 Discretization of Hallén's equation

To obtain an approximation of the current, we divide the wire into N equal segments of length $\Delta = L/N$. Then we enforce Hallén's equation at the points $z_0 = n\Delta$, $n \in \{0, \ldots, N\}$, which results in a linear system of $N + 1$ equations for the current $I_z(z')$, and F_0 and F_L. Traditional numerical schemes introduce a set of basis functions for the current and try to evaluate the resulting integrals over the kernel g_a and the basis functions. However, in almost all cases the analytical evaluation of the resulting integral is hampered by the exponential function in the reduced kernel. This problem can be resolved by approximating the exponential and the current at the same time. Therefore, we employ the approximation [72]

$$
I_z(z') \exp\left[-\frac{s}{c_0}\sqrt{a^2 + (n\Delta - z')^2}\right] \doteq \sum_{n'=1}^{N-1} \Lambda_\Delta(z' - n'\Delta) \cdot I_z(n'\Delta)
$$
$$
\times \exp\left[-\frac{s}{c_0}\sqrt{a^2 + (n\Delta - n'\Delta)^2}\right],
\tag{4.7}
$$

where

$$
\Lambda_\Delta(z) = \begin{cases} 1 - \frac{|z|}{\Delta} & \text{for} \quad |z| < \Delta, \\ 0 & \text{elsewhere.} \end{cases}
\tag{4.8}
$$

This is a linear-spline interpolation. The approximation of the exponential is justified by the fact that the current and the exponential function exhibit oscillations of approximately the same period if the real part of the Laplace parameter is small. In that case, the mesh width should be much smaller than the wavelength to capture the oscillating behavior of

the current by piecewise-linear functions. Also, there is no reason to take into account the behavior of the exponential function more accurately than the behavior of the current, since the approximation of their product determines the accuracy of the computed integral.

The resulting set of equations is

$$\sum_{n'=1}^{N-1} W_{n-n'} \exp\left(-\frac{s}{c_0} R_{n-n'}\right) I_z(n'\Delta) = \frac{Y_0}{2} \sum_{n'=0}^{N} w_{n'} \exp\left(-\frac{s}{c_0}|n-n'|\Delta\right) E_z^i(n'\Delta)$$
$$+ F_0 \exp\left(-\frac{s}{c_0} n\Delta\right) + F_L \exp\left(-\frac{s}{c_0}(L-n\Delta)\right), \tag{4.9}$$

for $n \in \{0, \ldots, N\}$. Further, $R_n = \sqrt{n^2 \Delta^2 + a^2}$, and closed-form expressions are available for the weighting coefficients W_n, which are defined as

$$W_n = \int_{-\Delta}^{\Delta} \frac{\Lambda_\Delta(z')dz'}{4\pi\sqrt{a^2 + (n\Delta - z')^2}}. \tag{4.10}$$

The summation involving the incident field E_z^i is obtained by approximating the pertaining integral by a repeated trapezoidal rule, which gives rise to the coefficients

$$w_n = \int_{z=0}^{L} \Lambda(z - n\Delta)dz = \begin{cases} \Delta & n = 1, \ldots, N-1, \\ \Delta/2 & n = 0, N. \end{cases} \tag{4.11}$$

This is allowed for sufficiently smooth incident fields only. In case of plane waves and delta-gap sources, a closed-form expression of the integral over the incident field is available. The left-hand side of Eq. (4.9) can be recognized as a discrete convolution, which can be efficiently computed by the Fast Fourier Transformation (FFT). The discrete convolution has been obtained owing to the continuous convolution of the original thin-wire equation and to the discrete translation invariance in the basis and testing functions, i.e., the sets of basis and testing functions consist of a single function with equidistant shifts. Eq. (4.9) could have been obtained directly from Eqs (4.1) and (4.7) by choosing testing functions

$$T^H(z - n\Delta) = \frac{c_0}{2s} \exp\left(-\frac{s}{c_0}|z - n\Delta|\right), \tag{4.12}$$

for $z \in (0, L)$. Anticipating the discussion in Section 4.2.3, we remark that we can remove the boundary terms with F_0 and F_L by using the testing functions

$$T(z - n\Delta) = \begin{cases} A \sinh\left[(s/c_0)(\Delta - |z - n\Delta|)\right] & \text{for } |z - n\Delta| < \Delta, \\ 0 & \text{elsewhere,} \end{cases} \tag{4.13}$$

for $n \in \{1, \ldots, N-1\}$. The coefficient A is introduced to scale the equations. We will refer to these functions as piecewise-sinusoidal testing functions, although they are a generalization of these functions. The merit of this formulation is that we save two equations and two unknowns, viz. F_0 and F_L, which becomes more important when we consider an array of wires. A sensible choice for the coefficient A would be

$$A(s) = \frac{1}{\sinh(s\Delta/c_0)}. \tag{4.14}$$

Applying the testing procedure to the right-hand side of Eq. (4.1) yields

$$
\begin{aligned}
\int_0^L T(z - n\Delta) & \left[\partial_z^2 - \frac{s^2}{c_0^2} \right] f(z) dz = \\
& \frac{As}{c_0} \left\{ f((n-1)\Delta) - 2\cosh\left(\frac{s}{c_0}\Delta\right) f(n\Delta) + f((n+1)\Delta) \right\},
\end{aligned} \tag{4.15}
$$

where we have used the notation of Eq. (4.5a). Hence, the one-dimensional Laplace-transformed wave operator has been replaced by a natural generalization of the central differences for $\partial_z^2 - s^2/c_0^2$, which becomes exact for $\Delta \to 0$ and the above choice for A. Usually, difference formulas are obtained from an interpolation polynomial for the expansion functions. However, in this case we obtain the difference formulas from the choice of testing functions. As a result of the testing procedure, we usually end up with approximations in the forcing function.

4.1.3   Finite array of straight thin wires

We continue the discretization process for an array of straight thin wires, consisting of M wires with circular cross-section, all with radius a. Further, the axes of all wires are aligned parallel to the z-axis in the plane $y = 0$. The axis of wire k has coordinates $(x, y, z) = (x_k, 0, z)$ for $z \in (-L_k/2, L_k/2)$, where L_k indicates the length of the k-th wire. This means that the center of every wire is located at $z = 0$. This problem can be modeled with the aid of the thin-wire equation with reduced kernel. On the axis of wire k, i.e., $x = x_k$, $y = 0$, $z \in (-L_k/2, L_k/2)$, we can write

$$(\partial_z^2 - \frac{s^2}{c_0^2})A_z(x_k, z) = -s\varepsilon_0 E_z^i(x_k, z), \tag{4.16}$$

for $k = 1, \ldots, M$, where

$$
\begin{aligned}
A_z(x_k, z) &= \int_{-L_k/2}^{L_k/2} I_k(z') \frac{\exp\left[-(s/c_0)\sqrt{a^2 + (z - z')^2}\right]}{4\pi\sqrt{a^2 + (z - z')^2}} dz' \\
&+ \sum_{\substack{m=1 \\ m \neq k}}^{M} \int_{-L_m/2}^{L_m/2} I_m(z') \frac{\exp\left[-(s/c_0)\sqrt{(x_k - x_m)^2 + (z - z')^2}\right]}{4\pi\sqrt{(x_k - x_m)^2 + (z - z')^2}} dz',
\end{aligned}
\tag{4.17}
$$

where we have approximated the coupling between the current on wire k and the other wires by placing the current on the other wires on the wire axes. We will show that this approximation is valid when the distance between wire k and the other wires is large enough with respect to the radius of the wires and the wavelength.

For the distance between observation point on the axis of wire k and the location of the currents on the mantle of wire m we have

$$
|\boldsymbol{r} - \boldsymbol{r}'| = \sqrt{(x_k - x_m)^2 - 2a(x_k - x_m)\cos(\phi') + a^2 + (z - z')^2}, \tag{4.18}
$$

for $\phi \in (-\pi, \pi]$. Further, we define

$$
R = \sqrt{(x_k - x_m)^2 + (z - z')^2}. \tag{4.19}
$$

To approximate $1/|\boldsymbol{r} - \boldsymbol{r}'|$ by $1/R$ and $\exp(-s|\boldsymbol{r} - \boldsymbol{r}'|/c_0)$ by $\exp(sR/c_0)$, for $s = j\omega$, we have the conditions

$$
\left| 1 - \frac{|\boldsymbol{r} - \boldsymbol{r}'|}{R} \right| \ll 1, \tag{4.20a}
$$

$$
\frac{\omega}{c_0} \left| |\boldsymbol{r} - \boldsymbol{r}'| - R \right| \ll 2\pi. \tag{4.20b}
$$

A Taylor series of $|\boldsymbol{r} - \boldsymbol{r}'|/R$ shows that these inequalities hold under the conditions

$$
a \ll R, \tag{4.21a}
$$

$$
a^2 \ll \lambda R, \tag{4.21b}
$$

$$
a \ll \lambda/2. \tag{4.21c}
$$

We make the following approximations:

$$I_m(z') \exp\left[-\frac{s}{c_0}\sqrt{(x_k - x_m)^2 + (z - z')^2}\right] \doteq \sum_{n=1}^{N-1} \Lambda_{\Delta_m}(z' + (\frac{L_m}{2} - n\Delta_m))$$

$$\times I_m(-\frac{L_m}{2} + n\Delta_m) \cdot \exp\left[-\frac{s}{c_0}\sqrt{(x_k - x_m)^2 + (-\frac{L_m}{2} + n\Delta_m - z)^2}\right], \quad (4.22\text{a})$$

$$I_m(z') \exp\left[-\frac{s}{c_0}\sqrt{a^2 + (z - z')^2}\right] \doteq \sum_{n=1}^{N-1} \Lambda_{\Delta_m}(z' + (\frac{L_m}{2} - n\Delta_m)) \cdot I_m(-\frac{L_m}{2} + n\Delta_m)$$

$$\times \exp\left[-\frac{s}{c_0}\sqrt{a^2 + (-\frac{L_m}{2} + n\Delta_m - z)^2}\right], \quad (4.22\text{b})$$

where

$$\Delta_m = \frac{L_m}{N}, \quad (4.23)$$

for $m = 1, \ldots, M$. Notice that we have discretized all wires with the same number of expansion functions, irrespective of their length. Also, the integrals describing the inter- action between two different wires are computed with the same accuracy as the integrals for a single wire. Although this is not necessary, it leads to a straightforward scheme. We choose piecewise-sinusoidal testing functions $T_k(z + L_k/2 - \ell\Delta_k)$, for $k = 1, \ldots, M$, $\ell = 1, \ldots, N - 1$, since they partially invert the one-dimensional Helmholtz equation, i.e.,

$$T_k(z) = \begin{cases} \sinh\left[(s/c_0)\left(\Delta_k - |z|\right)\right] / \sinh\left((s/c_0)\Delta_k\right) & \text{for} \quad |z| \leq \Delta_k, \ x = x_k, \\ 0 & \text{elsewhere.} \end{cases} \quad (4.24)$$

Introducing the notations

$$I[m, n] = I_m\left(-\frac{L_m}{2} + n\Delta_m\right), \quad (4.25\text{a})$$

$$A[k, \ell] = A_z(x_k, -L_k/2 + \ell\Delta_k), \quad (4.25\text{b})$$

$$G[k, \ell, m, n] = \frac{\exp\left[-(s/c_0)\sqrt{(x_k - x_m)^2 + (n\Delta_m - L_m/2 - z_{k,\ell})^2}\right]}{4\pi}$$

$$\times \int_{-L_m/2}^{L_m/2} \frac{\Lambda(z' + (L_m/2 - n\Delta_m))dz'}{\sqrt{(x_k - x_m)^2 + (z_{k,\ell} - z')^2}} \quad \text{for } m \neq k, \quad (4.25\text{c})$$

$$G[k, \ell, m, n] = \frac{\exp\left[-(s/c_0)\sqrt{a^2 + (n\Delta_m - L_m/2 - z_{k,\ell})^2}\right]}{4\pi}$$

$$\times \int_{-L_m/2}^{L_m/2} \frac{\Lambda(z' + (L_m/2 - n\Delta_m))dz'}{\sqrt{a^2 + (z_{k,\ell} - z')^2}} \quad \text{for } m = k, \quad (4.25\text{d})$$

where

$$z_{k,\ell} = -\frac{L_k}{2} + \ell \Delta_k, \tag{4.26}$$

we end up with

$$\sum_{m=1}^{M} \sum_{n=1}^{N-1} \left\{ G[k, \ell-1, m, n] - 2 \cosh\left(s\Delta_k/c_0\right) G[k, \ell, m, n] + G[k, \ell+1, m, n] \right\}$$

$$\times I[m, n] / \sinh(s\Delta_k/c_0) = -Y_0 \int\limits_{-L_k/2}^{L_k/2} T_k(z + L_k/2 - \ell\Delta_k) E_z^i(x_k, z) dz, \tag{4.27}$$

for $k = 1, \ldots, M$, $\ell = 1, \ldots, N-1$. A closed-form expression for $G[k, \ell, m, n]$ is available. In general, the above system of equations has no convolution symmetry, except for the self-coupling terms. The loss of convolution symmetry is caused by the fact that the wires are not of equal length, and therefore the testing and expansion functions are no longer identical on each wire.

4.2   Perfectly conducting flat plate

Inspired by the formulation of the Hallén equation for the straight thin-wire segment, we will proceed in a similar way for the perfectly conducting flat plate. We will call the result the Hallén-type equation for the flat plate. For this formulation, we consider a rectangular flat plate in the plane $z = 0$, described by $0 < x < a$ and $0 < y < b$. The problem of a flat rectangular plate has been studied numerically by many authors, see e.g., [28, 52, 84, 85], and recently an infinite series of eigenfunctions adapted to this problem has been constructed [34]. We recall the electric-field integral equation of Section 2.5.2

$$-s\varepsilon_0 E_x^i(\boldsymbol{r}) = \left[\partial_x^2 - \frac{s^2}{c_0^2}\right] A_x(\boldsymbol{r}) + \partial_x \partial_y A_y(\boldsymbol{r}), \qquad \boldsymbol{r} \in \mathcal{P}, \tag{4.28a}$$

$$-s\varepsilon_0 E_y^i(\boldsymbol{r}) = \left[\partial_y^2 - \frac{s^2}{c_0^2}\right] A_y(\boldsymbol{r}) + \partial_y \partial_x A_x(\boldsymbol{r}), \qquad \boldsymbol{r} \in \mathcal{P}, \tag{4.28b}$$

where $\mathcal{P} = \{\boldsymbol{r} \mid 0 < x < a, \, 0 < y < b, \, z = 0\}$.

4.2.1 Derivation of the Hallén-type equation

In the formulation of the Hallén-type equation, we will concentrate on the x-component of the electric-field integral equation for a fixed y-coordinate, i.e., we will regard Eq. (4.28a) as a one-dimensional equation in x. In this equation, we notice the same one-dimensional Laplace-transformed wave operator as in the thin-wire equation in front of A_x. To remove the spatial derivatives, we proceed in the same way as in the case of the thin-wire equation. Using Eq. (4.28a) and Eq. (4.2), we write

$$
\begin{aligned}
&\int_0^a \left[G_1(x, x_0)\partial_x^2 A_x(x, y) - A_x(x, y)\partial_x^2 G_1(x, x_0) \right] dx \\
&= -\int_0^a G_1(x, x_0) \left\{ \partial_x \partial_y A_y(x, y) + s\varepsilon_0 E_x^i(x, y) \right\} dx + \int_0^a \delta(x - x_0) A_x(x, y) dx.
\end{aligned}
\tag{4.29}
$$

To obtain a second expression for the left hand side of Eq. (4.29), we apply the one-dimensional version of Green's theorem in Eq. (4.4), setting

$$
f(x) = A_x(x, y) = A_x(\boldsymbol{r}) \quad \text{for} \quad \boldsymbol{r} \in \mathcal{P},
\tag{4.30a}
$$

$$
g(x) = G_1(x, x_0) = \frac{c_0}{2s} \exp\left(-\frac{s}{c_0} |x - x_0| \right),
\tag{4.30b}
$$

to arrive at

$$
\begin{aligned}
&\int_0^a \left[G_1(x, x_0)\partial_x^2 A_x(x, y) - A_x(x, y)\partial_x^2 G_1(x, x_0) \right] dx \\
&= \left[\frac{c_0}{2s} \exp\left(-\frac{s}{c_0} |x - x_0| \right) \partial_x A_x(x, y) \right. \\
&\quad \left. + \frac{1}{2}\mathrm{sgn}(x - x_0) \exp\left(-\frac{s}{c_0} |x - x_0| \right) A_x(x, y) \right]_{x=0}^a .
\end{aligned}
\tag{4.31}
$$

As in the case of the Hallén equation for the thin wire, the right-hand side of this equation can be written in the form

$$
F_0(y) \exp\left(-\frac{s}{c_0} x_0 \right) + F_a(y) \exp\left(\frac{s}{c_0}(x_0 - a) \right),
\tag{4.32}
$$

with $F_0(y)$ and $F_a(y)$ as yet unknown functions of y. This means that we can write the alternative equation

$$
\begin{aligned}
A_x(x_0, y) = \int_0^a G_1(x, x_0) \left[\partial_x \partial_y A_y(x, y) + s\varepsilon_0 E_x^i(x, y) \right] dx + \\
F_0(y) \exp\left(-\frac{s}{c_0} x_0 \right) + F_a(y) \exp\left[\frac{s}{c_0}(x_0 - a) \right] .
\end{aligned}
\tag{4.33}
$$

The first integral on the right-hand side of Eq. (4.33) is further simplified by integration by parts:

$$
\begin{aligned}
\int_0^a G_1(x, x_0) \partial_x \partial_y A_y(x, y) dx = \left[G_1(x, x_0) \partial_y A_y(x, y) \right]_{x=0}^a \\
- \int_0^a \partial_x G_1(x, x_0) \partial_y A_y(x, y) dx.
\end{aligned}
\tag{4.34}
$$

The boundary terms can be included in the boundary terms that are already present in Eq. (4.33), since $F_0(y)$ and $F_a(y)$ until now are arbitrary functions of y, so there is no problem in adding one more function. Eq. (4.33) can now be written as

$$
\begin{aligned}
A_x(x_0, y) =& \frac{1}{2} \int_0^a \mathrm{sgn}(x - x_0) \exp\left(-\frac{s}{c_0}|x - x_0| \right) \partial_y A_y(x, y) dx \\
& + \frac{Y_0}{2} \int_0^a \exp\left(-\frac{s}{c_0}|x - x_0| \right) E_x^i(x, y) dx \\
& + F_0(y) \exp\left(-\frac{s}{c_0} x_0 \right) + F_a(y) \exp\left[\frac{s}{c_0}(x_0 - a) \right],
\end{aligned}
\tag{4.35}
$$

where $Y_0 = \sqrt{\varepsilon_0/\mu_0}$. After a similar analysis for the y-component of the electric-field integral equation, we obtain

$$
\begin{aligned}
A_y(x, y_0) =& \frac{1}{2} \int_0^b \mathrm{sgn}(y - y_0) \exp\left(-\frac{s}{c_0}|y - y_0| \right) \partial_x A_x(x, y) dy \\
& + \frac{Y_0}{2} \int_0^b \exp\left(-\frac{s}{c_0}|y - y_0| \right) E_y^i(x, y) dy \\
& + H_0(x) \exp\left(-\frac{s}{c_0} y_0 \right) + H_b(x) \exp\left[\frac{s}{c_0}(y_0 - b) \right].
\end{aligned}
\tag{4.36}
$$

4.2.2   Discretization of the Hallén-type equation

To find an approximate numerical solution, we enforce Eqs (4.35) and (4.36) at discrete points. First, we divide the rectangular plate into equal rectangles of size $\Delta x \times \Delta y$ in the x- and y-direction, respectively, where $\Delta x = a/M$ and $\Delta y = b/N$. We enforce the x-component of the Hallén-type equation at the points

$$(x_0, y) = (k\Delta x, (\ell + \frac{1}{2})\Delta y), \quad k \in \{0, \ldots, M\}, \quad \ell \in \{0, \ldots, N-1\}. \tag{4.37}$$

Therefore, $A_x(x_0, y)$ should be computed at these points. For the y-component of the Hallén-type equation, we enforce the equality sign at the points

$$(x, y_0) = ((k + \frac{1}{2})\Delta x, \ell\Delta y), \quad k \in \{0, \ldots, M-1\}, \quad \ell \in \{0, \ldots, N\}, \tag{4.38}$$

and therefore $A_y(x, y_0)$ should be computed at these points. In the remaining part we will only consider the x-component of the Hallén-type equation, i.e., Eq. (4.35). We turn our attention to the approximation of the vector potential components. Approximation of the vector potential requires approximating the surface current density $\boldsymbol{J}_S$. We will make use of standard rooftop functions [28] to approximate the surface current density. However, the exponential of the Green's function defined in Eq. (2.44) hampers an analytic expression. Therefore, inspired by the discretization of the thin-wire equation, we approximate the product of the exponential and the surface current density at the same time.

$$J_x(x', y') \exp\left[-\frac{s}{c_0}\sqrt{(x - x')^2 + (y - y')^2}\right] \doteq$$

$$\sum_{m=1}^{M-1}\sum_{n=0}^{N-1} J_x\left[m\Delta x, (n + \frac{1}{2})\Delta y\right] \Lambda_{\Delta x}(x' - m\Delta x)\Pi_{\Delta y}(y' - (n + \frac{1}{2})\Delta y) \tag{4.39}$$

$$\times \exp\left[-\frac{s}{c_0}\sqrt{(x - m\Delta x)^2 + (y - (n + \frac{1}{2})\Delta y)^2}\right],$$

where $J_x(x', y') = \boldsymbol{J}_S(x, y) \cdot \boldsymbol{u}_x$, the pair (x, y) is given by Eq. (4.37), and $\Lambda_{\Delta x}(x)$ is defined by Eq. (4.8) and

$$\Pi_{\Delta y}(y) = \begin{cases} 1 & \text{for} \quad |y| \leq \frac{\Delta y}{2}, \\ 0 & \text{elsewhere.} \end{cases} \tag{4.40}$$

The remaining surface integrals in the expression of A_x are available in closed form [81]. For the y-component of the vector potential, we use an analogous expression for the exponential and J_y, i.e., $J_y = \boldsymbol{J}_S \cdot \boldsymbol{u}_y$.

The line integral containing the y-component of the vector potential in the integrand is approximated by a repeated midpoint rule and the spatial derivative is approximated by a central difference:

$$\frac{1}{2} \int\limits_0^a \mathrm{sgn}(x - k\Delta x) \exp\left(-\frac{s}{c_0}|x - k\Delta x|\right) \partial_y A_y(k\Delta x, y)\big|_{y=(\ell+\frac{1}{2})\Delta y} \, dx$$

$$\doteq \frac{\Delta x}{2\Delta y} \sum_{m=0}^{M-1} \exp\left(-\frac{s}{c_0}|(m + \frac{1}{2} - k)\Delta x|\right) \mathrm{sgn}(m + \frac{1}{2} - k) \tag{4.41}$$

$$\times \left[A_y((m + \frac{1}{2})\Delta x, (\ell + 1)\Delta y) - A_y((m + \frac{1}{2})\Delta x, \ell\Delta y) \right].$$

The central differences can also be obtained by integrating the equation in the y-direction from $\ell\Delta$ to $(\ell + 1)\Delta$, and approximating the terms without a partial derivative in the y-direction by a midpoint rule.

We observe that the summation in Eq. (4.41) can be written as a discrete convolution. Hence, we can use the Fast Fourier Transformation (FFT) to compute the expression efficiently. Also, the expressions for the components of the vector potential at equidistant points have the form of a two-dimensional discrete convolution and can therefore be evaluated by a two-dimensional FFT.

4.2.3   Removing the boundary terms

In Section 4.4.2, we will show that the Hallén-type equation for the rectangular plate suffers from poor convergence and we conjecture that this is caused by the boundary terms in the Hallén-type equation. Therefore, we will show how the boundary terms can be removed from the equation. Consider Eq. (4.35) for fixed y and for three different values of x_0. We now have a set of three equations from which we would like to eliminate the boundary terms with F_0 and F_a. Therefore, we multiply each equation by a suitable constant and add them to form a single equation in which both boundary terms are eliminated. To make this clear we look at the resulting terms for F_0 and F_a, where we have denoted the three different points for x_0 by x_1, x_2 and x_3 and the coefficients, by which we multiply, α, β

and γ:

$$F_0 : \qquad \alpha \exp\left\{-\frac{s}{c_0}x_1\right\} + \beta \exp\left\{-\frac{s}{c_0}x_2\right\} + \gamma \exp\left\{-\frac{s}{c_0}x_3\right\} = 0, \qquad (4.42a)$$

$$F_a : \qquad \alpha \exp\left\{\frac{s}{c_0}(x_1 - a)\right\} + \beta \exp\left\{\frac{s}{c_0}(x_2 - a)\right\} + \gamma \exp\left\{\frac{s}{c_0}(x_3 - a)\right\} = 0. \quad (4.42b)$$

Upon expressing α and γ in terms of β, we obtain

$$\alpha = -\beta \frac{\sinh[(s/c_0)(x_3 - x_2)]}{\sinh[(s/c_0)(x_3 - x_1)]}, \qquad (4.43a)$$

$$\gamma = -\beta \frac{\sinh[(s/c_0)(x_2 - x_1)]}{\sinh[(s/c_0)(x_3 - x_1)]}. \qquad (4.43b)$$

This shows that we can expect problems when $\sinh[(s/c_0)(x_3 - x_1)] = 0$. If s has a non-zero real part, this will not occur. However if s is purely imaginary, i.e., $s = j\omega$, problems arise if $|x_3 - x_1|$ is a multiple of half a wavelength. Therefore, we choose $x_1 = x_2 - \Delta x$ and $x_3 = x_2 + \Delta x$. Since Nyquist's sampling criterion forces the mesh size to be finer than half a wavelength, the problem does not arise.

Instead of removing the boundary term after the equations have been discretized, we can obtain the same result by using the appropriate one-dimensional Green's function. This Green's function can be reconstructed by taking the original Green's function, shifting it over a distance Δx and multiplying it by α or γ. Then we combine the three Green's functions to obtain a new Green's function which does not give rise to the boundary terms.

Following this procedure, we obtain the new one-dimensional Green's function, viz.

$$G_{1m}(x, x_0) = \begin{cases} A\sinh\left[(s/c_0)\left(\Delta x - |x - x_0|\right)\right] & x \in [x_0 - \Delta x, x_0 + \Delta x], \\ 0 & \text{elsewhere}, \end{cases} \qquad (4.44)$$

where A is an appropriate constant to match the amplitude, e.g.,

$$A = \frac{1}{\sinh(s\Delta x/c_0)}. \qquad (4.45)$$

Apparently, the Hallén-type equation is equivalent to the standard EFIE formulation, where the x-component is tested with piecewise-sinusoidal testing functions in the x-direction, when the real part of the Laplace parameter s is zero. A similar interpretation holds for the testing functions that operate on the y-component of the EFIE. In view of the remarks made for the Hallén-type equation, we can summarize our set of testing functions working on the x-component of EFIE as

$$T(x - p\Delta x, y - (q + 1/2)\Delta y) = G_{1m}(x, p\Delta x)\Pi_{\Delta y}[y - (q + 1/2)\Delta y], \qquad (4.46)$$

for $p \in \{1, \ldots, M-1\}$, $q \in \{0, \ldots, N-1\}$. The remaining integrals in the y-direction that are not directly available are approximated by a midpoint rule. For the y-component of EFIE we employ analogous functions.

By using the piecewise-sinusoidal testing functions, we have eliminated the boundary terms, at the expense of a finite-difference formula for A_x and A_y in the left-hand side of Eq. (4.35) and Eq. (4.36), respectively. This difference formula is generated by the testing functions, in the same way as for the wire equation. At the same time, our testing functions have only local support, which allows us to consider more generally shaped flat plates, as long as these shapes can be represented by a uniform rectangular mesh. Finally, we note that the discretized Hallén-type equation and the EFIE that is discretized by means of the piecewise-sinusoidal testing functions are of comparable complexity.

4.3   The conjugate-gradient method

The discretized equations for the thin wire and the flat plate can, at least in principle, be solved by direct matrix methods, such as LU decomposition. However, the number of unknowns in the linear system resulting from the discretization process can become quite large. Solving large systems by such a brute-force method requires considerable storage capacity and computation time. Iterative techniques are an alternative and they require a matrix-vector product only. For the thin wire and the flat plate we have substantiated that the matrix-vector product can be efficiently computed by means of the Fast Fourier Transformation. This reduces the problem to a lower storage requirement and a shorter computation time. Although the family of iterative techniques has become large, the conjugate-gradient method is still one of the most elegant algorithms. A clear exposition of its properties can be found in [6, 7, 84], the most important property being the minimization of the residual. Basically, the conjugate-gradient method is a full projection method with minimal costs, owing to certain orthogonality properties of the Krylov subspace. For the linear system

$$Lu = f, \tag{4.47}$$

where L is an $M \times M$ matrix, u is the unknown vector and f is the excitation vector, the conjugate-gradient method is given by

$$u_0 \text{ arbitrary,} \tag{4.48a}$$

$$r_0 = f - Lu_0, \tag{4.48b}$$

$$u_n = u_{n-1} + \alpha_n v_n, \tag{4.48c}$$

$$v_n = Tr_{n-1} + \beta_{n-1} v_{n-1}, \tag{4.48d}$$

$$r_n = f - Lu_n = r_{n-1} - \alpha_n Lv_n, \tag{4.48e}$$

$$\alpha_n = \frac{(r_{n-1}, Lv_n)}{\|Lv_n\|^2}, \tag{4.48f}$$

$$\beta_n = -\frac{(LTr_n, Lv_n)}{\|Lv_n\|^2}, \tag{4.48g}$$

for $n \geq 1$, $\beta_0 = 0$ and $v_0 = \mathbf{0}$. Further, T should be chosen in such a way that LT is self-adjoint with respect to the inner product between two M-dimensional vectors, defined as

$$(v, w) = \sum_{m=1}^{M} v_m w_m^*, \tag{4.49}$$

where * denotes complex conjugation and v_m denotes the m-th component of v. The norm $\| \cdot \|$ of the vector is generated by the inner product in the natural way. If L is not self-adjoint, the standard choice for T is $T = L^a$, where the superscript ^{a} denotes the adjoint. Typically, we start the algorithm with zero initial estimate, i.e., $u_0 = \mathbf{0}$, and we terminate the algorithm when the residual error $\|r_n\|/\|r_0\|$ has dropped below a preset value. The conjugate-gradient algorithm in combination with a matrix-vector product based on FFTs is usually referred to as CGFFT.

For the conjugate-gradient algorithm, the speed of convergence can be characterized in terms of the condition number of the system LT. The minimization property for the residual, together with the analysis in [59, Section 6.11], gives the result

$$\|r_n\| \leq 2 \left[\frac{\sqrt{\kappa_2} - 1}{\sqrt{\kappa_2} + 1} \right]^n \|r_0\|, \tag{4.50}$$

where κ_2 is the ℓ_2-condition number of the system LT. We note that the conjugate-gradient algorithm given here does not coincide with the one given in [59]. The above bound on the residual indicates that problems in the convergence can be expected for high values of κ_2. Also, if L is not self-adjoint and we choose $T = L^a$, the condition number of LT is the square of the condition number of L. Therefore, if L is already poorly conditioned,

convergence is even further hampered by choosing $T = L^a$. This problem is removed in other Krylov subspace methods, such as the Bi-conjugate-gradient method or the BiCGstab method [59]. However, the property of a monotonically decreasing residual error, which is a feature of full projection methods such as the conjugate gradient algorithm, is lost for the methods mentioned above. Since the minimization of the residual error is also a part of marching on in anything, as discussed in Chapter 6, we will employ the conjugate-gradient method only.

4.4   Numerical results

We have discussed the formulation of the problem, the discretization process and the choice of a scheme to solve the set of linear equations that originates from the discretization. We are now in a position to present some numerical results for the current on a straight thin wire and the surface current density on a perfectly conducting flat plate. For both problems we will examine the Hallén formulation and the piecewise-sinusoidal formulation. We recall from Chapter 3 that the thin-wire integral equation with reduced kernel is ill-posed and we will demonstrate the consequences for the numerical approximation. The EFIE for the plate is well-posed. However, we will show that for the Hallén-type equation the condition number becomes unacceptably high, due to an improper choice for the testing functions.

4.4.1   Results for the thin wire

For a straight thin-wire segment of length $L = 0.5\lambda$ and circular cross-section with radius $a = 5 \cdot 10^{-3}\lambda$, where λ denotes the wavelength, we have computed the current along the segment using 31 basis functions for the current. The incident field is a plane wave, polarized in the z-direction. For the Hallén formulation, the modulus of the current along the segment and the relative error versus the number of iterations of the conjugate-gradient algorithm are given in Figure 4.1. For the formulation with piecewise-sinusoidal testing functions, the results are presented in Figure 4.2. In both cases, the conjugate-gradient method was terminated when the relative error dropped below 10^{-3}. For the current along the wire, both formulations give visually the same results. However, the behavior of the relative error versus the number of iterations is quite distinct, as is the number of iterations

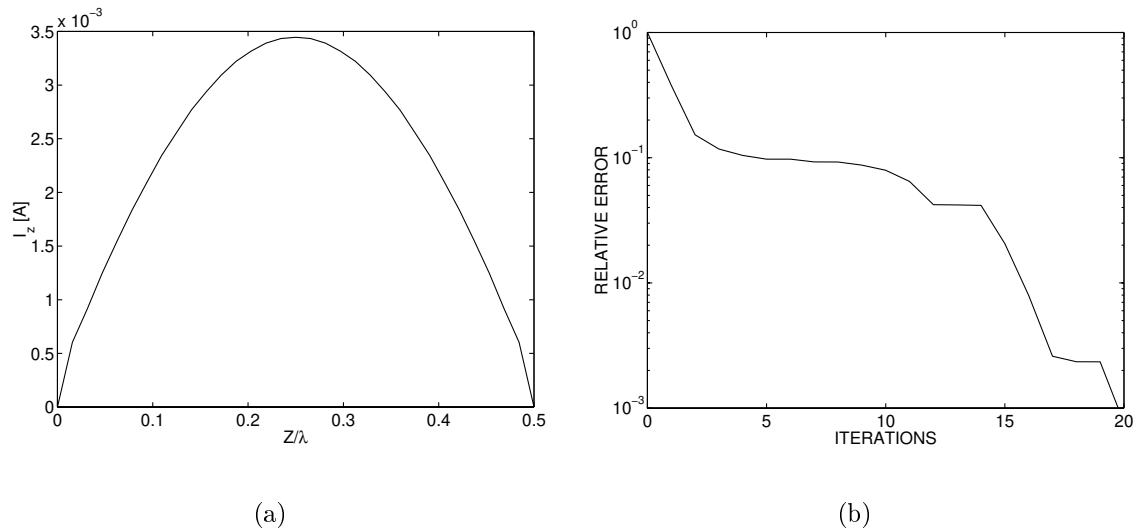(a)   (b)

Figure 4.1: results for a straight thin-wire segment with $L = 0.5\lambda$, $a = 5 \cdot 10^{-3}\lambda$, using the Hallén formulation and 31 basis functions. The incident field is a plane wave, polarized in the z-direction. (a) Modulus of the current distribution versus the position on the wire. (b) Relative error versus the number of iterations for the conjugate-gradient algorithm.
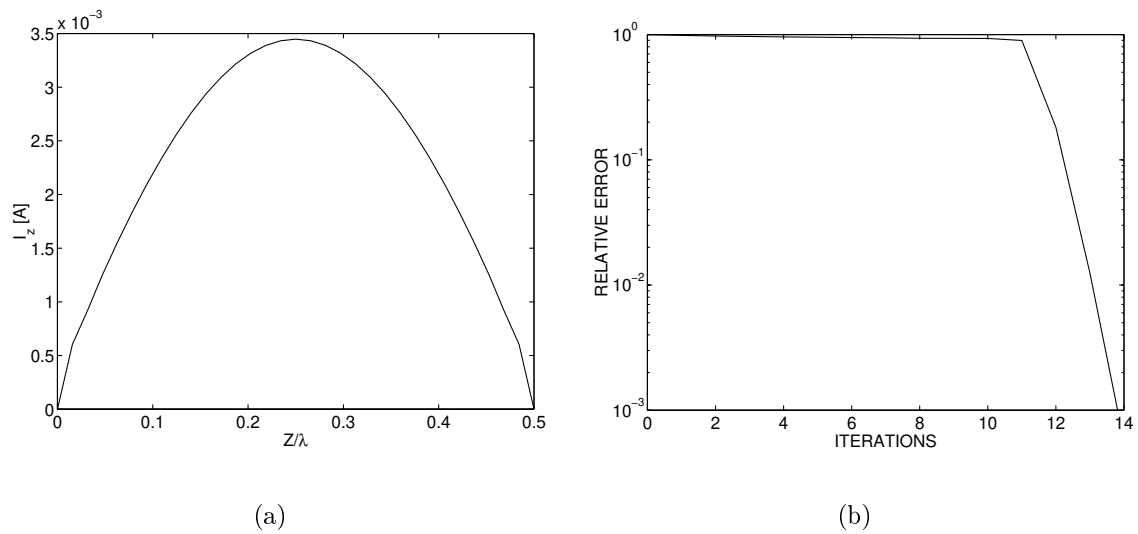

(a)   (b)

Figure 4.2: results for a straight thin-wire segment with $L = 0.5\lambda$, $a = 5 \cdot 10^{-3}\lambda$, using the piecewise-sinusoidal formulation and 31 basis functions. The incident field is a plane wave, polarized in the z-direction. (a) Modulus of the current distribution versus the position on the wire. (b) Relative error versus the number of iterations for the conjugate-gradient algorithm.

required for convergence.

To illustrate the consequences of the ill-posed nature of the thin-wire equation with reduced kernel, we have refined the discretization by a factor of five, i.e., 155 basis functions, for the same excitation and physical dimensions of the wire. The results for the Hallén and the piecewise-sinusoidal formulation are shown in Figure 4.3 and Figure 4.4, respectively. We observe that the Hallén formulation produces erratic results, whereas the piecewise-sinusoidal formulation still gives smooth results except close to the end faces. These results are in agreement with the statements made in Section 3.3.3 about the effect of the end faces. We have computed the condition number of the numerical system for both formulations. For the Hallén equation, the condition number was approximately 285 for 31 basis functions and $2.4 \cdot 10^4$ for 155 basis functions. For the piecewise-sinusoidal formulation the condition number was approximately 169 for 31 basis functions and 422 for 155 basis functions. In view of the fact that the piecewise-sinusoidal formulation can be obtained from the Hallén formulation, the difference between the condition numbers for 155 basis functions is remarkable. A further refinement of the discretization gives unreliable results for both formulations.

To produce reliable results for even finer discretizations, we apply a regularization method, as discussed in Section 3.3.4. We will only discuss the piecewise-sinusoidal formulation. For the penalty term $\|Bu\|_Y^2$ in the minimization problem (3.55), we choose

$$\|Bu\|_Y^2 = \sum_{n=1}^{N-1} |u_{n-1} - 2u_n + u_{n+1}|^2 , \tag{4.51}$$

where u is the vector that contains the current coefficients, i.e., for the n-th component of the vector u we have $u_n = I_z(n\Delta)$. Further, $u_0 = I_z(0) = 0$ and $u_N = I_z(N\Delta) = 0$. This regularizer was also used in [70, p. 361] to suppress unwanted oscillations in an inverse-profiling algorithm. The operator B can be expressed in terms of a tri-diagonal matrix

$$B = \begin{bmatrix} -2 & 1 & 0 & \dots & \dots & \dots & 0 \\ 1 & -2 & 1 & \ddots & & & \vdots \\ 0 & 1 & -2 & \ddots & \ddots & & \vdots \\ \vdots & \ddots & \ddots & \ddots & \ddots & \ddots & \vdots \\ \vdots & & \ddots & \ddots & -2 & 1 & 0 \\ \vdots & & & \ddots & 1 & -2 & 1 \\ 0 & \dots & \dots & \dots & 0 & 1 & -2 \end{bmatrix} . \tag{4.52}$$
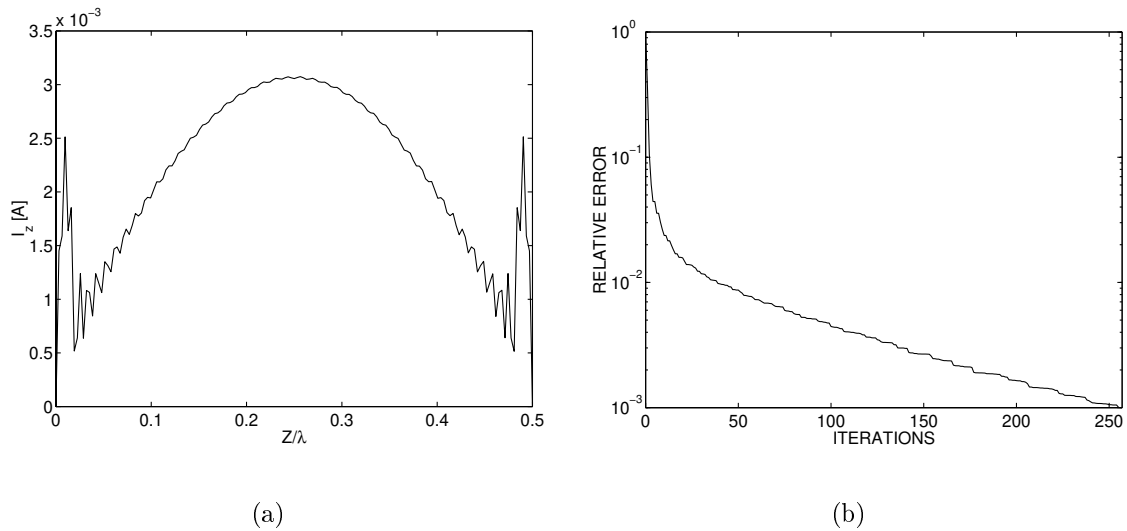
(a)   (b)

Figure 4.3: results for a straight thin-wire segment with $L = 0.5\lambda$, $a = 5 \cdot 10^{-3}\lambda$, using the Hallén formulation and 155 basis functions. The incident field is a plane wave, polarized in the z-direction. (a) Modulus of the current distribution versus the position on the wire. (b) Relative error versus the number of iterations for the conjugate-gradient algorithm.

(a)   (b)

Figure 4.4: results for a straight thin-wire segment with $L = 0.5\lambda$, $a = 5 \cdot 10^{-3}\lambda$, using the piecewise-sinusoidal formulation and 155 basis functions. The incident field is a plane wave, polarized in the z-direction. (a) Modulus of the current distribution versus the position on the wire. (b) Relative error versus the number of iterations for the conjugate-gradient algorithm.
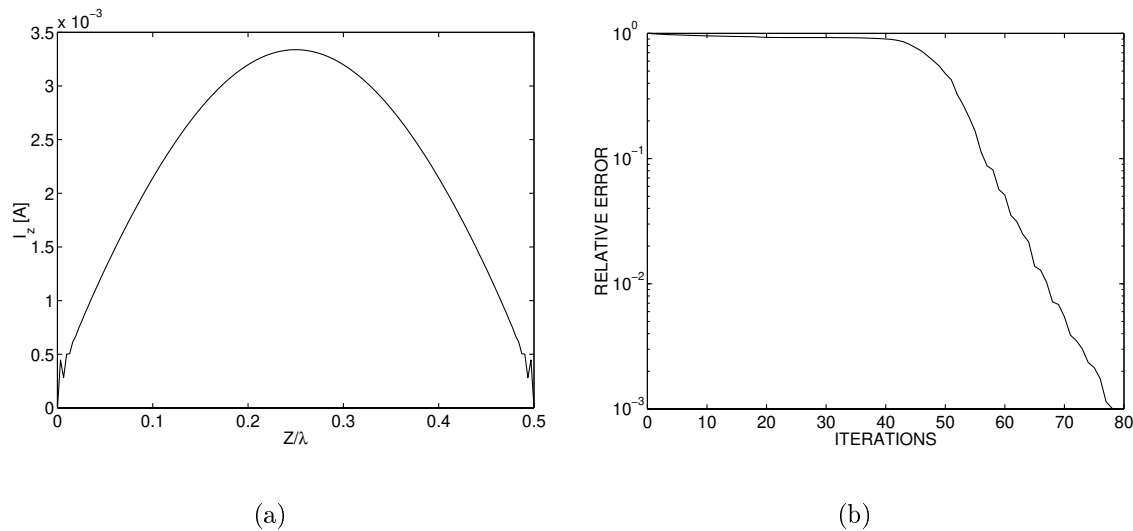
For $u \in \mathbb{C}^{N-1}$, it can be shown, by induction with respect to N, that

$$(u, Bu) = - \left(|u_1|^2 + |u_{N-1}|^2 + \sum_{n=1}^{N-2} |u_n - u_{n+1}|^2 \right), \qquad (4.53)$$

where $(\cdot, \cdot)$ is the inner product in $\mathbb{C}^{N-1}$ and u_n is the n-th component of the vector u. This means that the matrix B is negative definite and therefore it is invertible. Further, B is sparse. Hence, the matrix-vector product $B^a B u$ can be computed efficiently, and the system of Eq. (3.62) can be solved by means of the conjugate-gradient algorithm of Section 4.3 with $T = I$, since the operator $\alpha B^a B + L^a L$ is self-adjoint.

The matrix B is identical to the finite-difference approximation of the one-dimensional Laplace operator $\nabla^2 = \partial_z^2$ on a uniform grid. Since the Laplace operator induces monotonicity, as expressed by the maximum principle, we expect that the matrix B will suppress the highly oscillating behavior of the current $I_z(z)$. Further, we note that the expression

$$\int_0^L \left| \partial_z^2 I_z(z) \right|^2 dz, \qquad (4.54)$$

is a norm if $I_z(z)$ belongs to the Sobolev space $H_0^2(0, L)$. Therefore, the inverse of the Laplace operator is bounded from $L^2(0, L)$ to $H_0^2(0, L)$. However, for a general incident field, the current on the wire close to the end face $z = 0$ will behave as $O(\sqrt{z})$ for $z \downarrow 0$. Hence, the current on the wire will not belong to $H_0^2(0, L)$ in most cases.

To demonstrate the effect of the proposed regularization, we consider the same configuration as above, i.e., a straight thin-wire segment of length $L = 0.5\lambda$ and circular cross-section with radius $a = 5 \cdot 10^{-3}\lambda$, and the incident field is a plane wave, polarized in the z-direction. We have computed the current on the wire using 1000 basis functions. Although the number of basis functions is extremely high for this example, it allows us to clearly demonstrate the effect of regularization. First, we have tried to solve the linear system by the conjugate-gradient method without any regularization, i.e., $Lu = f$. After 65000 iterations, the residual error was $1.8 \cdot 10^{-3}$ and did not yet meet our termination criterion of 10^{-3}. The result for the current on the wire after 65000 iterations is shown in Figure 4.5(a). Subsequently, we have computed the current from the regularized system with the above choice for B and $\alpha = 10^{-11}$. The residual error in the conjugate-gradient method reached the termination criterion of 10^{-3} after 391 iterations. The current on the wire for the regularized system is presented in Figure 4.6(a).

(a)   (b)

Figure 4.5: current along a straight thin-wire segment with $L = 0.5\lambda$, $a = 5 \cdot 10^{-3}\lambda$, using the piecewise-sinusoidal formulation and 1000 basis functions. The incident field is a plane wave, polarized in the z-direction. (a) Modulus of the current distribution versus the position on the wire, without regularization and before filtering. (b) Modulus of the current distribution versus the position on the wire, without regularization and after filtering.

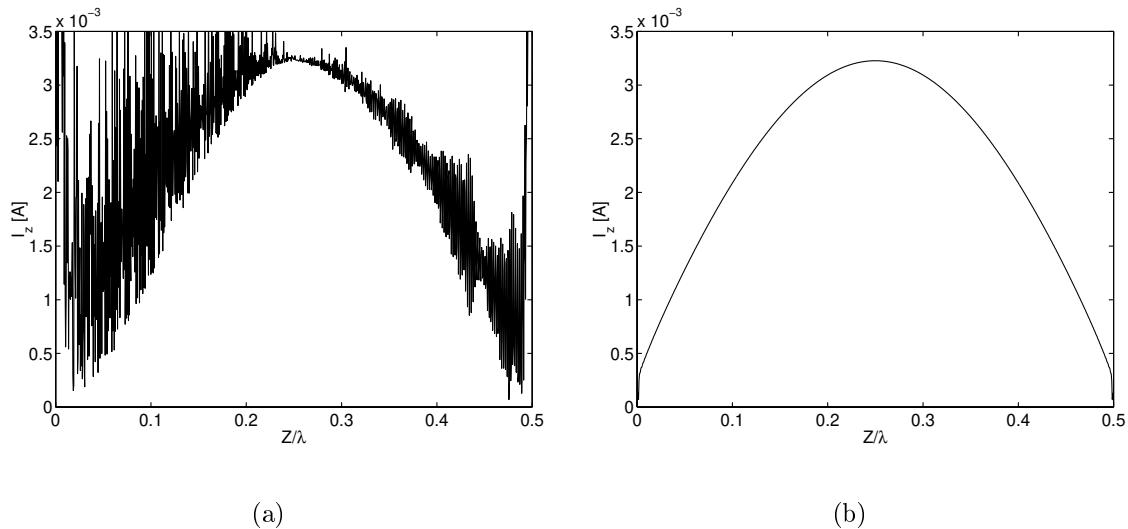(a)   (b)
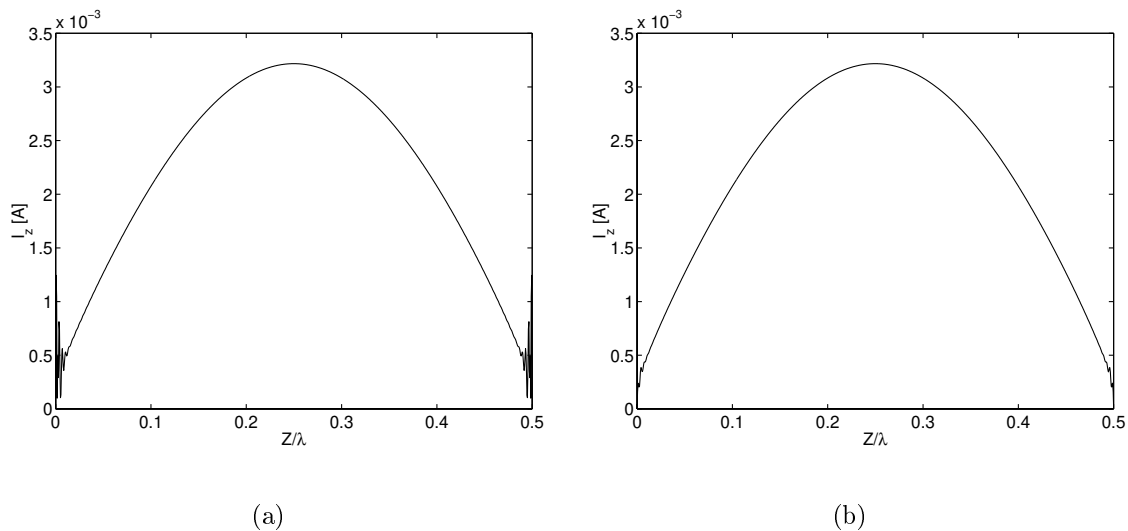
Figure 4.6: current along a straight thin-wire segment with $L = 0.5\lambda$, $a = 5 \cdot 10^{-3}\lambda$, using the piecewise-sinusoidal formulation and 1000 basis functions. The incident field is a plane wave, polarized in the z-direction. (a) Modulus of the current distribution versus the position on the wire, after regularization with $\alpha = 10^{-11}$ and before filtering. (b) Modulus of the current distribution versus the position on the wire, after regularization with $\alpha = 10^{-11}$ and filtering.

We observe that the regularization drastically improves the convergence of the conjugate-gradient method and that the oscillations are suppressed, except at the end faces. To improve the results for the current, we have applied post-processing in the form of a filter. This filter can be expressed in the form of a matrix-vector product, where the current coefficients are stored in the vector u and the matrix is given by

$$C = \frac{1}{4} \begin{bmatrix} 2 & 1 & 0 & \dots & \dots & \dots & 0 \\ 1 & 2 & 1 & \ddots & & & \vdots \\ 0 & 1 & 2 & \ddots & \ddots & & \vdots \\ \vdots & \ddots & \ddots & \ddots & \ddots & \ddots & \vdots \\ \vdots & & \ddots & \ddots & 2 & 1 & 0 \\ \vdots & & & \ddots & 1 & 2 & 1 \\ 0 & \dots & \dots & \dots & 0 & 1 & 2 \end{bmatrix}. \tag{4.55}$$

The matrix C represents a local averaging procedure, which can be applied repeatedly to smooth the current distribution. In particular, we have applied the matrix-vector product nine times to the current coefficients obtained with and without regularization, i.e., we have computed $C^9 u$. The results of the filtering procedure are presented in Figure 4.5(b) and 4.6(b) for the current distribution without and with regularization, respectively. The results in both figures are almost identical. Hence, the most important effect of the regularization procedure is the improved convergence of the conjugate-gradient method.

4.4.2   Results for the flat plate with the Hallén-type equation

For the Hallén-type equation, we have analyzed the surface current density on a square plate with dimensions $\lambda \times \lambda$, where λ denotes the wavelength. We have applied a mesh of 31×31 squares. The incident field was a plane wave at normal incidence with amplitude 1 V/m, polarized in the x-direction. Numerical tests have shown that a converged solution is obtained for relative residual errors smaller than 10^{-5} in the conjugate-gradient scheme. By convergence we mean that the results have become smooth and further iterations show no visual changes. Figure 4.7 shows the progress of the iterative procedure for this case and Figures 4.8(a) and 4.8(b) show the modulus of the surface current densities in the x- and y-direction, respectively. The surface current densities closely resemble the results in [52, 84, 85]. From the progress of the conjugate-gradient method in Figure 4.7, we observe that it requires a large number of iterations to obtain a converged solution. Table 4.1
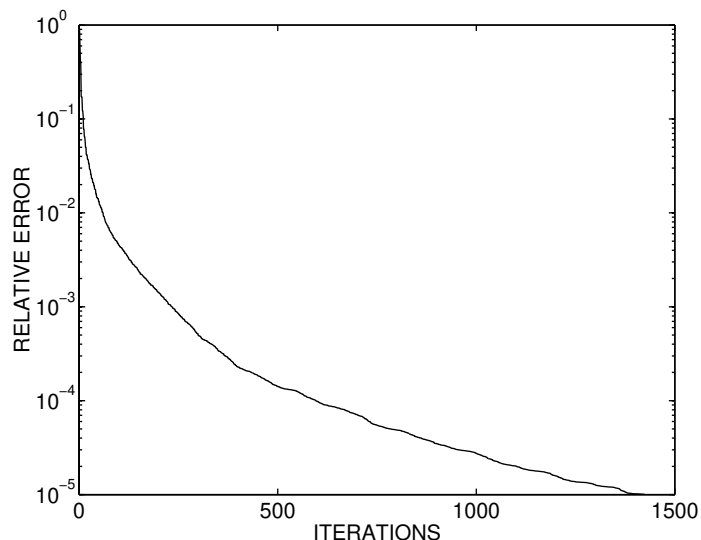
Figure 4.7: progress in the convergence of CGFFT for the Hallén equation.

presents the number of iterations needed for a converged solution for three different cases, all of which are plane-wave excitations at normal incidence with an x-polarized wave.

Dimension	Mesh	# iterations	rel. error
$\lambda \times \lambda$	15×15	459	10^{-5}
$\lambda \times \lambda$	31×31	1418	10^{-5}
$1.5\lambda \times 1.5\lambda$	31×31	2484	10^{-5}

Table 4.1: number of iterations for several meshes.

The large number of iterations needed to obtain a converged solution is an indication that the system matrix has a large condition number, as was explained in Section 4.3. To determine the origin of this large condition number, we have performed an eigenvalue analysis. We have chosen to compute the eigenvalues and eigenvectors instead of the singular values and vectors, since the computation of the eigenvalues and eigenvectors produces one set of vectors instead of two. Moreover, the eigenvectors and eigenvalues have a physical interpretation that can be related to the natural modes of the system.

First of all, we have visually inspected the eigenvectors corresponding to the eigenvalues with the smallest modulus. These eigenvectors are the most interesting, since they will have
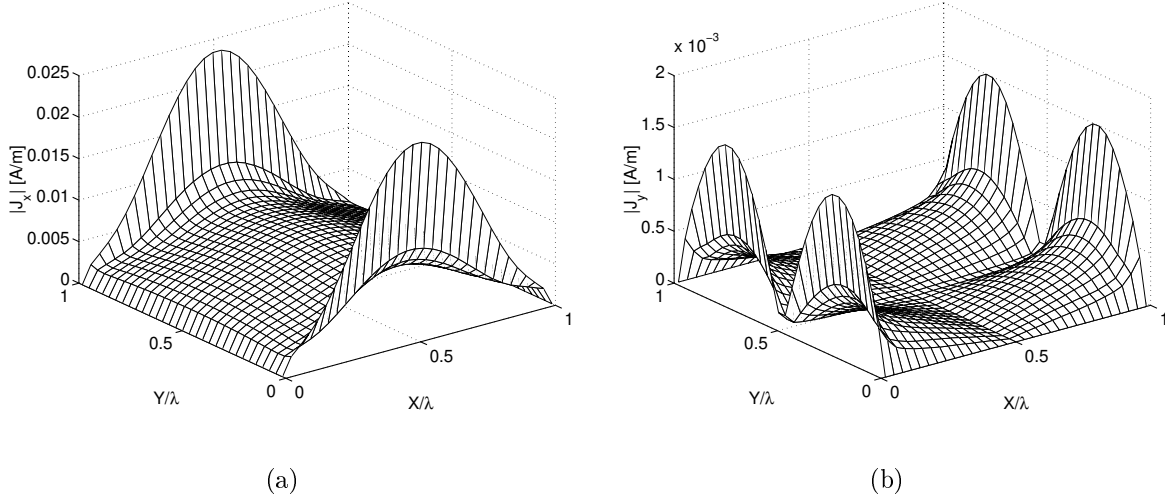
(a)   (b)

Figure 4.8: surface current density for an x-polarized plane wave of 1 V/m at normal incidence on a $\lambda \times \lambda$ plate with the Hallén-type equation (relative residual error $\leq 10^{-5}$). (a) Modulus of the surface current density in the x-direction. (b) Modulus of the surface current density in the y-direction.

eigenvalues with the largest modulus in the inverse discrete system and they will dominate the solution if the eigenvectors are present in the excitation vector. The variables corresponding to the surface current density did not indicate suspicious irregularies. Therefore, the most obvious candidates for causing the ill-conditioning of the system matrix are the variables corresponding to the boundary terms in Eqs (4.35) and (4.36). This observation is in agreement with Lemma 2 of Section 3.4, since the one-dimensional Green's function G_1 is not zero at the edges of the plate.

The eigenvalue analysis also provides a lower bound on the condition number. If we denote the discretized system for the Hallén-type equation as $Lu = f$, then we know

$$\sup_{\|u\|=1} \|Lu\| \geq |\lambda_{max}|, \tag{4.56a}$$

$$\inf_{\|u\|=1} \|Lu\| \leq |\lambda_{min}|, \tag{4.56b}$$

where λ_{max} is the eigenvalue with largest modulus and λ_{min} the eigenvalue with the smallest modulus. A lower bound on the condition number is given by

$$\kappa_2 \geq \kappa = \frac{|\lambda_{max}|}{|\lambda_{min}|}, \tag{4.57}$$

where κ_2 is the spectral condition number. Table 4.2 shows the order of magnitude of the lower bound on the condition number for three discretizations. Further, we note that, in the conjugate-gradient method, we use the product of the system matrix and its adjoint, i.e., LL^a. Therefore, we have to work with the square of the estimated condition number, which is in the order of $10^8 - 10^{10}$ for all cases presented in Table 4.2. This means that, in practice, we need at least double precision to obtain sufficiently accurate results. These estimates for the condition number indicate that discretization errors in the forcing function f of the system $Lu = f$ can affect the results for the unknown u. Apparently, we have been fortunate in this case, since the results for the surface current density in Figure 4.8 are still smooth and resemble the results in [52, 84, 85], which indicates that the forcing function contains only physically relevant components.

Dimension	Mesh	κ
$\lambda \times \lambda$	15×15	10^4
$\lambda \times \lambda$	31×31	10^5
$1.5\lambda \times 1.5\lambda$	31×31	10^5

Table 4.2: estimated condition number for several discretizations.

4.4.3   Results for the flat plate without boundary terms

For the piecewise-sinusoidal formulation, we present the numerical results for the same square plate as in Section 4.4.2. The computed surface current densities are visually indistinguishable from those of the original Hallén-type equation and are therefore not given here. Instead, we focus on the convergence of the conjugate-gradient algorithm, as illustrated in Figure 4.9.

We observe that the convergence has improved drastically. This confirms the conjecture that the ill-conditioning of the matrix equation is caused by the boundary terms. What we cannot observe from the graph is that the results for the surface current densities have already converged for a much larger residual error in comparison with the Hallén-type equation. The formulation with boundary terms has converged for a residual error smaller than 10^{-5}, whereas the formulation without boundary terms requires a residual error smaller than $5 \cdot 10^{-4}$, which is reached after 153 iterations. The fact that we can
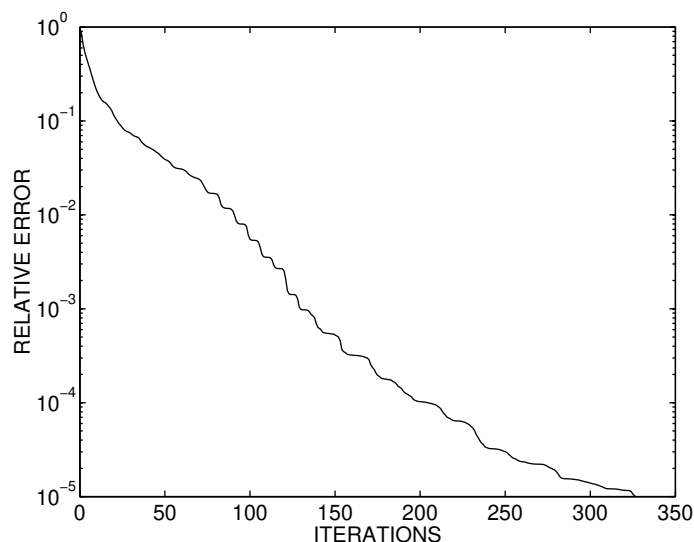
Figure 4.9: progress in the convergence of CGFFT for the piecewise-sinusoidal formulation.

use a different termination criterion is caused by the fact that the discrete system, and therefore also the definition of the residual, has changed. This improves the convergence by more than a factor of two in this case. Table 4.3 presents the number of iterations to obtain convergence for the same configurations as in Table 4.1 for the Hallén-type equation. We observe improvements in the order of a factor of ten to twenty.

Dimension	Mesh	# iterations	rel. error
$\lambda \times \lambda$	15×15	53	$5 \cdot 10^{-4}$
$\lambda \times \lambda$	31×31	153	$5 \cdot 10^{-4}$
$1.5\lambda \times 1.5\lambda$	31×31	126	$5 \cdot 10^{-4}$

Table 4.3: number of iterations for several meshes.

To demonstrate the ability of the piecewise-sinusoidal formulation to cope with more generally shaped flat surfaces as compared to the Hallén-type equation, we give the results for a cross consisting of five attached equal squares, as presented in Figure 4.10. Each square has length $\lambda/3$ and a mesh of 10×10 squares. The incident electric field is an x-polarized plane wave at normal incidence and amplitude of 1 V/m. This type of geometry is often applied as elements in frequency-selective surfaces. Also, it is suggested as a model for

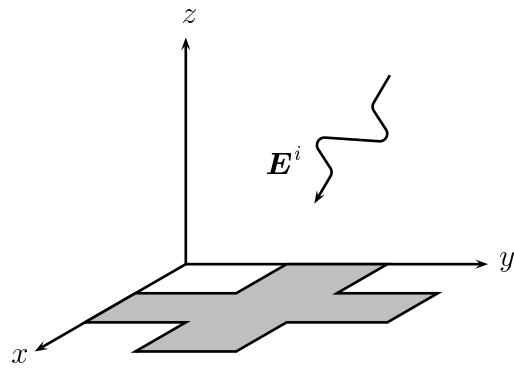Figure 4.10: perfectly conducting flat cross with incident field.

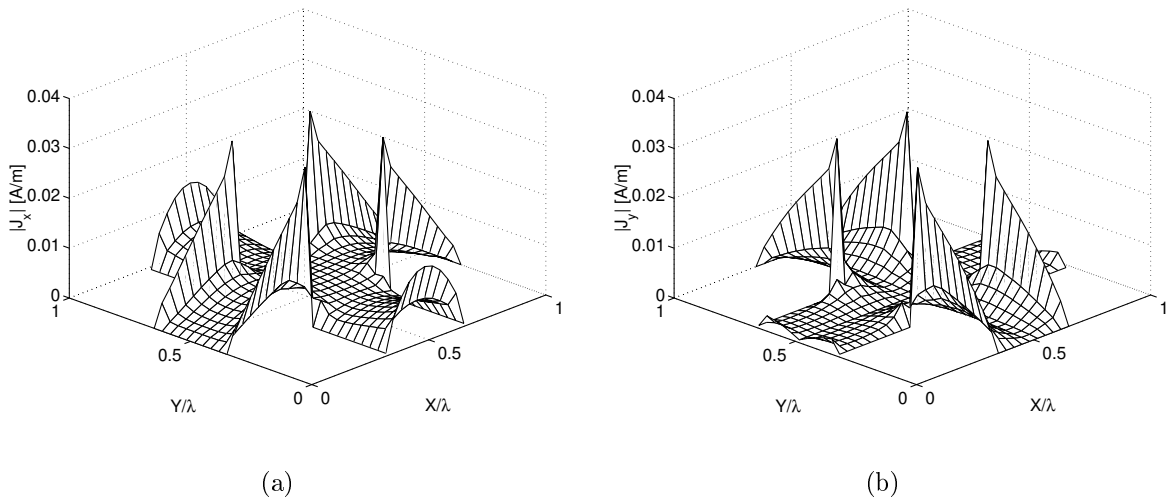<center>(a)</center>   <center>(b)</center>

Figure 4.11: surface current density for a cross with x-polarized normally-incident plane wave. (a) Modulus of the surface current density in the x-direction. (b) Modulus of the surface current density in the y-direction.

strip-line interconnects on printed circuit boards or in integrated circuits. The behavior of the surface current density at corners and edges that are present in this configuration has been studied by many authors. Nevertheless, numerical methods that are both accurate and flexible are not yet available [30]. The surface current densities obtained with the piecewise-sinusoidal formulation are presented in Figure 4.11. The number of iterations to reach a relative error of $5 \cdot 10^{-4}$ was 257. Careful examination of these results points out that the numerical scheme seems to perform poorly at corners, especially at corners pointing into the structure. This is illustrated by the peaks in the current densities in these corners. Hence, the formulation with piecewise-sinusoidal testing functions does not completely solve the above problem either.

Chapter 5

Derivative with respect to length

A way to examine the effect of small parameter variations is to compute the gradient (Fréchet derivative) with respect to these parameters, the so-called sensitivity. We can use sensitivity information in an optimization tool to construct an optimal design. The most challenging sensitivity information, from an analytic point of view, is the shape sensitivity for an infinitely thin plate. The reason for this is that the surface current density may become singular at the edges of the plate, which makes the interpretation of the sensitivity more difficult. For the shape sensitivity, we wonder what the effect is of a slight change in the geometry of the object under study. The general formulation for obtaining shape sensitivity can be found in [33, 62]. The shape sensitivity for a perfectly conducting open screen for the static and the time-harmonic case was studied in [75, 76]. However, this formulation relies on the application of the flux-transport theorem, where, supposedly, flux is represented by continuous functions. This leaves us with an interpretation problem, because of the afore mentioned singular (non-continuous) behavior of the surface current density at the edges of the screen [36, Chapter 9]. Therefore, we will give a derivation, avoiding the flux-transport theorem, in the case of a perfectly conducting flat plate, based on the principles of [33, 62]. Further, we will examine the possibility to obtain an estimate for the sensitivity by means of finite-difference approximations. This is useful for verification purposes. Also, the finite-difference approximations are readily obtained, whereas the analytic formulation and its numerical implementation are relatively time-consuming. Hence, a finite-difference approximation could provide a (temporary) short-cut in a development and design process, provided that it yields a reliable estimate.

5.1   Optimization of energy norms in scattering problems

Many design and detection problems in electromagnetics can be formulated in terms of the maximization or minimization of energy-related quadratic forms. Here, we will consider two cases. The first case is the maximization of the radiated energy in a predetermined direction. This case applies to the design of an antenna that should radiate as much energy as possible in a certain direction. The time-averaged radiated energy per solid angle in the direction $\theta = \theta_0$, $\phi = \phi_0$, denoted by $S(\theta_0, \phi_0)$, can be expressed in terms of the scattered electric field in the far-field region in the same direction, i.e., $\boldsymbol{E}^s(\theta_0, \phi_0)$. If we combine the design parameters $p_1, \ldots, p_n$ of the antenna in a vector $\boldsymbol{p}$, we have the optimization problem

$$\max_{\boldsymbol{p}} S(\boldsymbol{p}; \theta_0, \phi_0) = \max_{\boldsymbol{p}} \frac{|\boldsymbol{E}^s(\boldsymbol{p}; \theta_0, \phi_0)|^2}{2Z_0}, \tag{5.1}$$

where $Z_0 = \sqrt{\mu_0/\varepsilon_0}$, and the semicolon (;) indicates a separation between free and fixed parameters.

The second case is the minimization of a quadratic error ERR between a prescribed electromagnetic field and the actual electromagnetic field of a configuration. We will assume that the error is defined on the surface $\mathcal{S}$. This case is relevant for detection problems, in which we would like to reconstruct material properties from measured data. In that case, $\mathcal{S}$ is the surface on which the receivers are placed. Another example is the optimization of antenna parameters, such that the radiation pattern matches a prescribed radiation pattern, as closely as possible. For this case, the surface $\mathcal{S}$ is a part of the sphere at infinity. If we denote the prescribed electric field by $\boldsymbol{E}^s_d$, the actual electric field by $\boldsymbol{E}^s$, and the optimization parameters by $\boldsymbol{p}$, i.e, the material parameters or geometrical parameters, then we can formulate the problem as

$$\min_{\boldsymbol{p}} ERR(\boldsymbol{p}) = \min_{\boldsymbol{p}} \iint_{\mathcal{S}} |\boldsymbol{E}^s_d - \boldsymbol{E}^s(\boldsymbol{p})|^2 \, w dA, \tag{5.2}$$

where w is a positive weighting function to emphasize or reduce the importance of the behavior of the fields at certain parts of the surface $\mathcal{S}$. In most cases, the ranges of the parameters are restricted by certain constraints. However, for the moment we will ignore this and concentrate on the so-called objective functions S and ERR, which are quadratic forms. If the ranges of the parameters are continuous intervals, many algorithms to solve

the above optimization problems use the gradient of the objective function with respect to the parameters in the vector $\boldsymbol{p}$ to guide the search process. The i-th component of the gradient for the above objective functions, i.e., the derivative of the objective function with respect to p_i, is given by

$$\partial_{p_i} S(\boldsymbol{p}; (\theta_0, \phi_0)) = \frac{\text{Re}\{[\partial_{p_i} \boldsymbol{E}^s(\boldsymbol{p}; \theta_0, \phi_0)] \cdot [\boldsymbol{E}^s(\boldsymbol{p}; \theta_0, \phi_0)]^*\}}{Z_0}, \tag{5.3a}$$

$$\partial_{p_i} ERR(\boldsymbol{p}) = 2\,\text{Re}\left\{\iint\limits_{\mathcal{S}} [\partial_{p_i} \boldsymbol{E}^s(\boldsymbol{p})] \cdot [\boldsymbol{E}_d^s - \boldsymbol{E}^s(\boldsymbol{p})]^*\, w dA\right\}. \tag{5.3b}$$

Hence, to compute the objective function and its gradient, we have to compute $\boldsymbol{E}^s(\boldsymbol{p})$ and $\nabla_{\boldsymbol{p}} \boldsymbol{E}^s(\boldsymbol{p})$, i.e., the gradient with respect to $\boldsymbol{p}$ for each relevant component of $\boldsymbol{E}^s$. In turn, the scattered electric field can be expressed in terms of current densities $\boldsymbol{J}$. For a fixed observation point, the components of the scattered electric field depend linearly on the current densities. For an antenna with perfectly conducting boundary $\partial\mathcal{D}$, we obtain from Eqs (2.42) and (2.46a)

$$\boldsymbol{E}^s = \frac{1}{s\varepsilon_0} \left(\nabla\nabla \cdot - \frac{s^2}{c_0^2}\right) \iint\limits_{\partial\mathcal{D}} G(\boldsymbol{r} - \boldsymbol{r}') \boldsymbol{J}_S(\boldsymbol{r}') dA', \tag{5.4}$$

where $G(\boldsymbol{r})$ is the Green's function of free space. For an observation point outside the boundary $\partial\mathcal{D}$, we can bring the spatial differentiations inside the integral. The resulting expression is

$$\boldsymbol{E}^s = \frac{1}{s\varepsilon_0} \iint\limits_{\partial\mathcal{D}} \nabla_{\boldsymbol{r}} \{[\nabla_{\boldsymbol{r}} G(\boldsymbol{r} - \boldsymbol{r}')] \cdot \boldsymbol{J}_S(\boldsymbol{r}')\} - \frac{s^2}{c_0^2} G(\boldsymbol{r} - \boldsymbol{r}') \boldsymbol{J}_S(\boldsymbol{r}') dA. \tag{5.5}$$

For the component of the electric field in the direction $\boldsymbol{u}_\ell$, this can be denoted as

$$\boldsymbol{u}_\ell \cdot \boldsymbol{E}^s = (\boldsymbol{J}_S, \boldsymbol{g}_\ell), \tag{5.6}$$

where $\boldsymbol{g}_\ell$ is a given vector field, consisting of the Green's function G and spatial differentiations acting on G. In general, $\boldsymbol{g}_\ell = \boldsymbol{g}_\ell(\boldsymbol{p})$, i.e., $\boldsymbol{g}_\ell$ will depend on the design parameters. Further $(\cdot, \cdot)$ is the $L^2(\partial\mathcal{D})^2$ inner product, which acts on the primed coordinates. Hence, the components of the electric field at a fixed observation point can be expressed in terms of functionals acting on the current density. For the derivative with respect to p_i of these functionals we obtain

$$\partial_{p_i}(\boldsymbol{u}_\ell \cdot \boldsymbol{E}^s) = (\partial_{p_i} \boldsymbol{J}_S, \boldsymbol{g}_\ell) + (\boldsymbol{J}_S, \partial_{p_i} \boldsymbol{g}_\ell). \tag{5.7}$$

Finally, $\boldsymbol{J}_S$ depends on $\boldsymbol{p}$ through Maxwell's equations and the boundary conditions, or, alternatively, through an equivalent integro-differential equation.

5.1.1   An adjoint problem to compute a gradient efficiently

From the preceding section, we can conclude that we should consider the following problem. Let $F(\boldsymbol{p})$ be a linear functional in a Hilbert space H, and $\boldsymbol{p}$ a vector of parameters. By the Riesz representation theorem (Theorem 10, Section 3.1), there is an element $g(\boldsymbol{p}) \in H$ such that

$$F(\boldsymbol{p})u = (u, g(\boldsymbol{p})), \tag{5.8}$$

where $(\cdot, \cdot)$ denotes the inner product of H, and $g(\boldsymbol{p}) \in H$ is given. Further, u is the solution of the linear system

$$L(\boldsymbol{p})u = f(\boldsymbol{p}), \tag{5.9}$$

e.g., u represents the current density on an antenna and $Lu = f$ denotes a discretized integro-differential equation for the current density. We denote the solution of this problem by $u(\boldsymbol{p}) = L(\boldsymbol{p})^{-1}f(\boldsymbol{p})$. We define

$$\Psi(\boldsymbol{p}) = F(\boldsymbol{p})u(\boldsymbol{p}), \tag{5.10}$$

and we wish to compute the gradient of $\Psi(\boldsymbol{p})$ with respect to $\boldsymbol{p}$, i.e., $\nabla\Psi(\boldsymbol{p})$. We obtain

$$\partial_{p_i}\Psi(\boldsymbol{p}) = (\partial_{p_i}u(\boldsymbol{p}), g(\boldsymbol{p})) + (u(\boldsymbol{p}), \partial_{p_i}g(\boldsymbol{p})), \tag{5.11}$$

where $\partial_{p_i}u(\boldsymbol{p})$ can be computed from the system

$$L(\boldsymbol{p})\partial_{p_i}u(\boldsymbol{p}) = \partial_{p_i}f(\boldsymbol{p}) - [\partial_{p_i}L(\boldsymbol{p})]\,u(\boldsymbol{p}), \tag{5.12}$$

and where $\partial_{p_i}g(\boldsymbol{p})$ is directly available from the definition of the problem. If the number of parameters in $\boldsymbol{p}$ is large, it seems that we have to solve a large number of linear systems to obtain $\partial_{p_i}u(\boldsymbol{p})$, to compute $\partial_{p_i}\Psi(\boldsymbol{p})$ for all i. If $L(\boldsymbol{p})$ represents a large system of equations, this would make the process of computing the gradient rather expensive. However, there is a way to solve this problem more efficiently [44]. Let us introduce the adjoint problem to Eq. (5.9)

$$L^a(\boldsymbol{p})v(\boldsymbol{p}) = g(\boldsymbol{p}), \tag{5.13}$$

where $L^a(\boldsymbol{p})$ is the adjoint operator of $L(\boldsymbol{p})$ with respect to the inner product $(\cdot, \cdot)$, i.e.,

$$(L(\boldsymbol{p})x, y) = (x, L^a(\boldsymbol{p})y), \tag{5.14}$$

for all $x, y \in H$. Substituting Eq. (5.13) in Eq. (5.11) and using the above definition of the adjoint operator, we obtain

$$\partial_{p_i}\Psi(\boldsymbol{p}) = (L(\boldsymbol{p})\partial_{p_i}u(\boldsymbol{p}), v(\boldsymbol{p})) + (u(\boldsymbol{p}), \partial_{p_i}g(\boldsymbol{p})). \tag{5.15}$$

Finally, the application of Eq. (5.12) yields

$$\partial_{p_i} \Psi(\boldsymbol{p}) = (\partial_{p_i} f(\boldsymbol{p}) - [\partial_{p_i} L(\boldsymbol{p})] u(\boldsymbol{p}), v(\boldsymbol{p})) + (u(\boldsymbol{p}), \partial_{p_i} g(\boldsymbol{p})). \tag{5.16}$$

Hence, we only have to solve two linear systems to compute the gradient of the functional, i.e., one direct problem in the form of Eq. (5.9) and one adjoint problem in the form of Eq. (5.13). Therefore, if the number of parameters is larger than one and only one excitation function f is involved, this way of computing the gradient of $\Psi(\boldsymbol{p})$ is more efficient.

5.2   Sensitivity analysis for the flat plate

In the remaining part of this chapter, we consider the construction of Eq. (5.12), where p_1 is the length of a perfectly conducting flat rectangular plate (a) and the wavelength is fixed. In [76], more general shape deformations have been studied. To obtain a formulation for the sensitivity with respect to the length a, we introduce a parameter τ that controls the length, viz. $a(\tau) = a(1 + \tau/a)$, and we can directly write the electric-field integral equation (EFIE) for the new surface:

$$- s\varepsilon_0 E_x^i(x,y) = \left[\partial_x^2 - \frac{s^2}{c_0^2} \right] A_x(x,y,\tau) + \partial_x \partial_y A_y(x,y,\tau), \tag{5.17a}$$

$$- s\varepsilon_0 E_y^i(x,y) = \left[\partial_y^2 - \frac{s^2}{c_0^2} \right] A_y(x,y,\tau) + \partial_y \partial_x A_x(x,y,\tau), \tag{5.17b}$$

for $0 < x < a(\tau)$, $0 < y < b$, where

$$A_i(x,y,\tau) = \int_0^{a(\tau)} \int_0^b J_i(x',y',\tau) \frac{\exp\left[-(s/c_0)R(x-x',y-y')\right]}{4\pi R(x-x',y-y')} dy' dx', \tag{5.18a}$$

$$R(x,y) = \sqrt{x^2 + y^2}, \tag{5.18b}$$

$i = x, y$. To arrive at a meaningful concept for the sensitivity, we introduce a mapping to stretch our coordinate system in one direction uniformly. For the source and observation coordinates in the x-direction, i.e., x and x', we write

$$x = \left(1 + \frac{\tau}{a}\right) x_0, \tag{5.19a}$$

$$x' = \left(1 + \frac{\tau}{a}\right) x_0', \tag{5.19b}$$

where x_0 and x_0' are variables independent of τ. Using the chain rule, we can replace the derivatives with respect to x by derivatives with respect to x_0:

$$\partial_x = \frac{1}{1 + \tau/a}\partial_{x_0} = \left(1 - \frac{\tau}{a}\right)\partial_{x_0} + O(\tau^2), \tag{5.20a}$$

$$\partial_x^2 = \frac{1}{(1 + \tau/a)^2}\partial_{x_0}^2 = \left(1 - \frac{2\tau}{a}\right)\partial_{x_0}^2 + O(\tau^2). \tag{5.20b}$$

Since no rotations take place in the mapping, the x- and y-components of the vector potential are mapped onto themselves. This yields

$$-s\varepsilon_0 E_x^i((1 + \tau/a)x_0, y) = \left[\left(1 - \frac{2\tau}{a} + O(\tau^2)\right)\partial_{x_0}^2 - \frac{s^2}{c_0^2}\right]A_{x_0}((1 + \tau/a)x_0, y, \tau) +$$
$$\left(1 - \frac{\tau}{a} + O(\tau^2)\right)\partial_{x_0}\partial_y A_y((1 + \tau/a)x_0, y, \tau), \tag{5.21a}$$

$$-s\varepsilon_0 E_y^i((1 + \tau/a)x_0, y) = \left[\partial_y^2 - \frac{s^2}{c_0^2}\right]A_y((1 + \tau/a)x_0, y, \tau) +$$
$$\left(1 - \frac{\tau}{a} + O(\tau^2)\right)\partial_y\partial_{x_0} A_{x_0}((1 + \tau/a)x_0, y, \tau), \tag{5.21b}$$

where

$$A_i\left[\left(1 + \frac{\tau}{a}\right)x_0, y, \tau\right] = \int\limits_0^a \int\limits_0^b \frac{\exp\left\{-(s/c_0)R\left[(1 + \tau/a)(x_0 - x_0'), y - y'\right]\right\}}{4\pi R\left[(1 + \tau/a)(x_0 - x_0'), y - y'\right]} \times$$
$$J_i\left[\left(1 + \frac{\tau}{a}\right)x_0', y', \tau\right]\left(1 + \frac{\tau}{a}\right)dy' dx_0', \tag{5.22}$$

$i = x_0, y$. Now we take the total derivative (d_τ) with respect to τ and set τ to zero in the resulting expression. For $\tau = 0$, we have $x = x_0$ and $x' = x_0'$. Therefore, we will drop the subscript $_0$ in the source and observation coordinates. We arrive at

$$-\frac{1}{a}\left\{s\varepsilon_0 x\partial_x E_x^i(x, y) + \left[\partial_x^2 - \frac{s^2}{c_0^2}\right]A_x^{gr}(J_x)(x, y)\right.$$
$$\left. + \partial_x\partial_y A_y^{gr}(J_y)(x, y) - \left[\partial_x^2 + \frac{s^2}{c_0^2}\right]A_x(J_x)(x, y)\right\} =$$
$$\left[\partial_x^2 - \frac{s^2}{c_0^2}\right]A_x(d_\tau J_x|_{\tau=0})(x, y) + \partial_x\partial_y A_y(d_\tau J_y|_{\tau=0})(x, y), \tag{5.23a}$$

$$-\frac{1}{a}\left\{s\varepsilon_0 x\partial_x E_y^i(x, y) + \left[\partial_y^2 - \frac{s^2}{c_0^2}\right]A_y^{gr}(J_y)(x, y)\right.$$
$$\left. + \partial_y\partial_x A_x^{gr}(J_x)(x, y) + \left[\partial_y^2 - \frac{s^2}{c_0^2}\right]A_y(J_y)(x, y)\right\} =$$
$$\left[\partial_y^2 - \frac{s^2}{c_0^2}\right]A_y(d_\tau J_y|_{\tau=0})(x, y) + \partial_y\partial_x A_x(d_\tau J_x|_{\tau=0})(x, y), \tag{5.23b}$$

where

$$A_i(F_i)(x,y) = \int\limits_0^a \int\limits_0^b \frac{\exp\left[-(s/c_0)R(x-x',y-y')\right]}{4\pi R(x-x',y-y')} F_i(x',y')dy'dx', \tag{5.24a}$$

$$A_i^{gr}(J_i)(x,y) = \int\limits_0^a \int\limits_0^b (x-x')\left[\partial_\xi \frac{\exp\left[-(s/c_0)R(\xi,y-y')\right]}{4\pi R(\xi,y-y')}\bigg|_{\xi=x-x'}\right] \times$$
$$J_i(x',y')dy'dx', \tag{5.24b}$$

for $F_i \in \{J_i, d_\tau J_i|_{\tau=0}\}$, $i \in \{x,y\}$ and

$$d_\tau J_i|_{\tau=0} = d_\tau J_i\left[\left(1+\frac{\tau}{a}\right)x_0', y', \tau\right]\bigg|_{\tau=0}. \tag{5.25}$$

Further, A^{gr} is similar to the vector potential, except for a modified Green's function, which is the product of the derivative of the Green's function and $(x-x')$. We observe that the integro-differential equations for $d_\tau J_x|_{\tau=0}$ and $d_\tau J_y|_{\tau=0}$ assume the same form as Eq. (2.59). Only the forcing functions have changed.

In view of the discussion of the mapping properties of the electric-field integral equation for open screens in Section 3.4, one may wonder whether the forcing function, i.e., the left-hand side, in Eq. (5.23) for $d_\tau \boldsymbol{J}_S|_{\tau=0}$ belongs to $TH^{-1/2}(\mathrm{curl}, \mathcal{P})$. If this were the case, then the well-posedness of the above equations would be established immediately and $d_\tau \boldsymbol{J}_S|_{\tau=0}$ would belong to $\widetilde{TH}^{-1/2}(\mathrm{div}, \mathcal{P})$. At the same time, this would indicate that the numerical scheme of Section 4.2.3 can be applied to the above equations. Unfortunately, we cannot guarantee that the forcing function belongs to $TH^{-1/2}(\mathrm{curl}, \mathcal{P})$. This can readily be seen from the terms $x\partial_x E_x^i(x,y)$ and $x\partial_x E_y^i(x,y)$. Further, the terms that contain spatial differentiations on the vector potential, i.e., $-\partial_x^2 A_x$ and $\partial_y^2 A_y$, no longer represent Cartesian components of $\nabla\nabla\cdot\boldsymbol{A}$. Finally, the terms containing $\boldsymbol{A}^{gr}$ do belong to $TH^{-1/2}(\mathrm{curl}, \mathcal{P})$, since the modified kernel in $\boldsymbol{A}^{gr}$ has the same type of singularity as the Green's function $G(\boldsymbol{r})$, i.e., $1/|\boldsymbol{r}|$, and the terms with spatial differentiations on $\boldsymbol{A}^{gr}$ are Cartesian components of $\nabla\nabla\cdot\boldsymbol{A}^{gr}$. Hence, we need additional information on the incident field and the surface current density to guarantee that the forcing function belongs to the proper function space. At present, we do not have this extra information. Nevertheless, we will discretize the integro-differential equation for the sensitivity with respect to length by means of the numerical scheme presented in Section 4.2.3.

5.3   Discretization

Since we have obtained the same integro-differential equation for the shape derivative with respect to length variation as in case of the surface current density of the flat plate with modified forcing function, we will use the same discretization for $d_\tau J_x|_{\tau=0}$ and $d_\tau J_y|_{\tau=0}$ as we employed for J_x and J_y. Hence, we will use rooftop functions to approximate $d_\tau J_x|_{\tau=0}$ and $d_\tau J_y|_{\tau=0}$ together with the exponential factor of the Green's function and we will use piecewise-sinusoidal testing functions. Therefore, we can use the same computational kernel for the derivative of the current density as we used for the surface current density itself. It remains to approximate the forcing function. To make the scheme consistent, we approximate the product of the surface current density and the exponential factor in the kernel of A_i or A_i^{gr}, for $i \in \{x, y\}$, by rooftop functions. All differentials acting on A_i or A_i^{gr} are brought over to the testing functions by integration by parts. The integrals that cannot be simplified in this manner are approximated by a midpoint rule (in the direction of the pulse function Π) or a trapezoidal rule (in the direction of the sinusoidal function). The remaining integral expressions for A_i or A_i^{gr} are available in closed form, see Appendix C and [81]. The approximated forcing function has the form of a discrete convolution, owing to the uniform coordinate stretch in the formulation of the shape derivative and the translational invariance of the set of expansion and testing functions. Hence, the forcing function of the discrete system can be computed efficiently by two-dimensional FFTs.

5.4   Numerical results

Figure 5.1 presents the results of the computation of the derivative of the surface current density with respect to length for a $\lambda \times \lambda$ flat plate with an x-polarized plane wave incident from the direction $\theta = 45°$, $\phi = 90°$, with the analytic formulation. We have used a mesh of 31×31 rectangles to discretize the surface current density on the plate. To verify the results, a finite-difference approximation with a uniform stretch in the x-direction of the mesh is presented in Figure 5.2. Hence, the mesh points have been shifted according to the coordinate stretch and the number of rectangles in the mesh remained constant. The finite-difference approximation was obtained by computing the surface current density for a plate with length $a = (1 - \Delta)\lambda$ and the surface current density for a plate with length

$a = (1 + \Delta)\lambda$, and approximating the derivative as

$$d_\tau \boldsymbol{J}\big|_{\tau=0} \doteq \frac{\boldsymbol{J}\big|_{\tau=\Delta\lambda} - \boldsymbol{J}\big|_{\tau=-\Delta\lambda}}{2\Delta\lambda}. \tag{5.26}$$

In this case, we used $\Delta = 1/61$. To express the accuracy of this finite-difference approximation, we introduce a norm for $d_\tau J_x|_{\tau=0}$ and $d_\tau J_y|_{\tau=0}$ as

$$\|d_\tau J_x|_{\tau=0}\| = \left\{ \frac{1}{ab} \int\limits_0^a \int\limits_0^b \left| [d_\tau J_x(x,y)|_{\tau=0}] \sqrt{\frac{y}{b}\left(1 - \frac{y}{b}\right)} \right|^2 dy dx \right\}^{1/2}, \tag{5.27a}$$

$$\|d_\tau J_y|_{\tau=0}\| = \left\{ \frac{1}{ab} \int\limits_0^a \int\limits_0^b \left| [d_\tau J_y(x,y)|_{\tau=0}] \sqrt{\frac{x}{a}\left(1 - \frac{x}{a}\right)} \right|^2 dy dx \right\}^{1/2}, \tag{5.27b}$$

where we have assumed that $d_\tau J_x|_{\tau=0}$ and $d_\tau J_y|_{\tau=0}$ have the same type of singularity near the edges of the plate as J_x and J_y, respectively. We compute an approximation of the above norms by means of repeated trapezoidal and repeated midpoint rules, which coincide with the definitions of the rooftop functions for $d_\tau J_x|_{\tau=0}$ and $d_\tau J_y|_{\tau=0}$, i.e.,

$$\|d_\tau J_x|_{\tau=0}\| \doteq \left[\sum_{m=1}^{M-1} \sum_{n=0}^{N-1} |dJ_x[m,n]|^2 \frac{(n+1/2)(N-n-1/2)}{MN^3} \right]^{1/2}, \tag{5.28a}$$

$$\|d_\tau J_y|_{\tau=0}\| \doteq \left[\sum_{m=0}^{M-1} \sum_{n=1}^{N-1} |dJ_y[m,n]|^2 \frac{(m+1/2)(M-m-1/2)}{M^3 N} \right]^{1/2}, \tag{5.28b}$$

where

$$dJ_x[m,n] = d_\tau J_x(m\Delta x, (n+1/2)\Delta y)|_{\tau=0}, \tag{5.29a}$$

$$dJ_y[m,n] = d_\tau J_y((m+1/2)\Delta x, n\Delta y)|_{\tau=0}, \tag{5.29b}$$

and $\Delta x = a/M$ and $\Delta y = b/N$. We denote the finite-difference approximation by a superscript ^{fd} and the approximation of the analytic formulation by a superscript ^{ana}. We define the relative error as

$$\text{relative error} = \sqrt{\frac{\|d_\tau J_x^{ana}|_{\tau=0} - d_\tau J_x^{fd}|_{\tau=0}\|^2 + \|d_\tau J_y^{ana}|_{\tau=0} - d_\tau J_y^{fd}|_{\tau=0}\|^2}{\|d_\tau J_x^{ana}|_{\tau=0}\|^2 + \|d_\tau J_y^{ana}|_{\tau=0}\|^2}}. \tag{5.30}$$

For the finite-difference approximation with coordinate stretch, the relative error is approximately $8.1 \cdot 10^{-3}$. One could also decide to approximate the derivative by computing the surface current density on a fixed mesh for a length $a = (1 - \Delta)\lambda$ and increasing
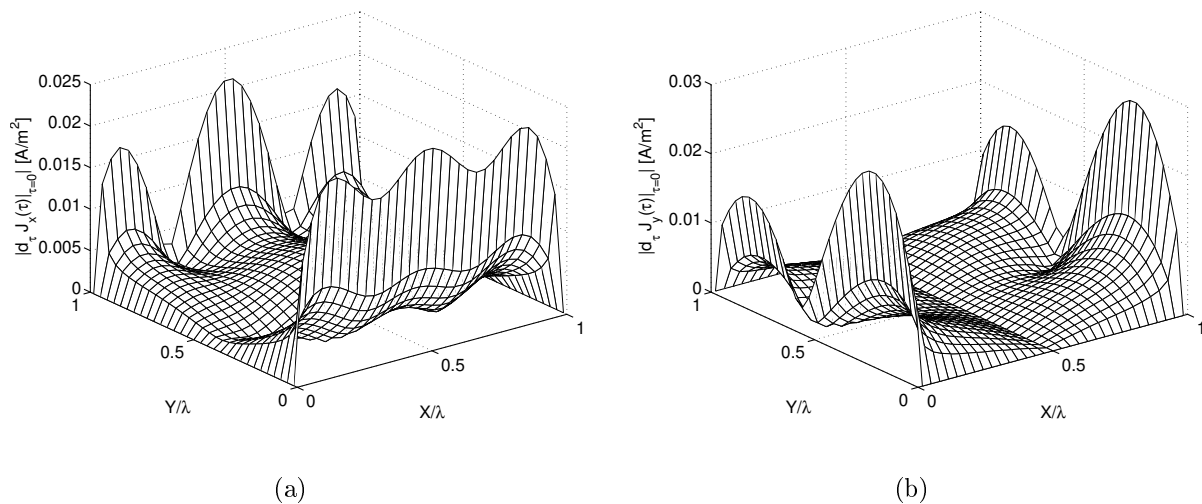
(a)   (b)

Figure 5.1: derivative with respect to length variation of the surface current density for a $\lambda \times \lambda$ flat plate with an x-polarized plane wave incident from the direction $\theta = 45°$, $\phi = 90°$, with the analytic formulation. (a) $d_\tau J_x|_{\tau=0}$, in modulus. (b) $d_\tau J_y|_{\tau=0}$, in modulus.

(a)   (b)

Figure 5.2: finite-difference approximation of the derivative of the surface current density for a $\lambda \times \lambda$ flat plate with an x-polarized plane wave incident from the direction $\theta = 45°$, $\phi = 90°$, with a uniform coordinate stretch. (a) Approximation of $d_\tau J_x|_{\tau=0}$, in modulus. (b) Approximation of $d_\tau J_y|_{\tau=0}$, in modulus.
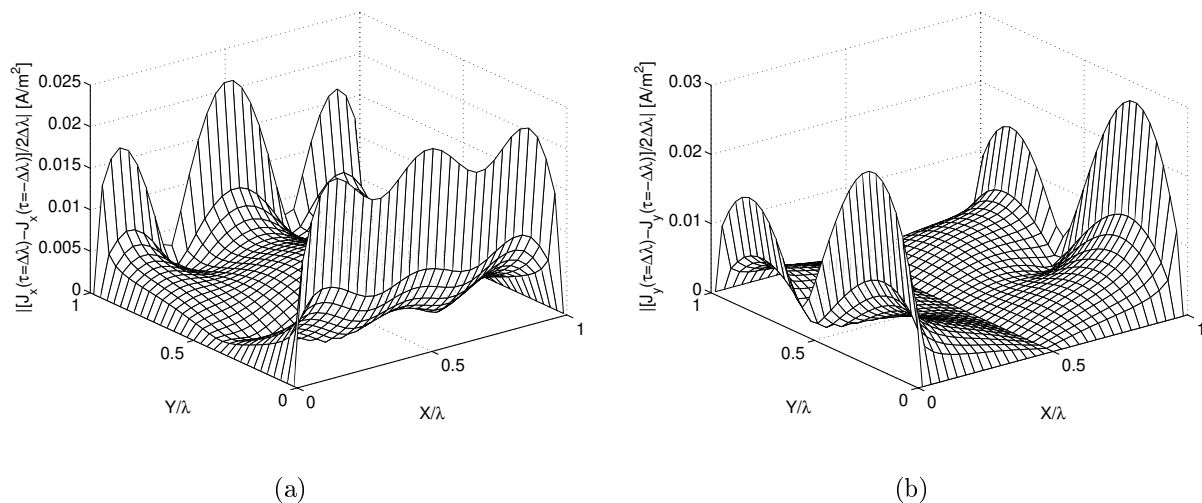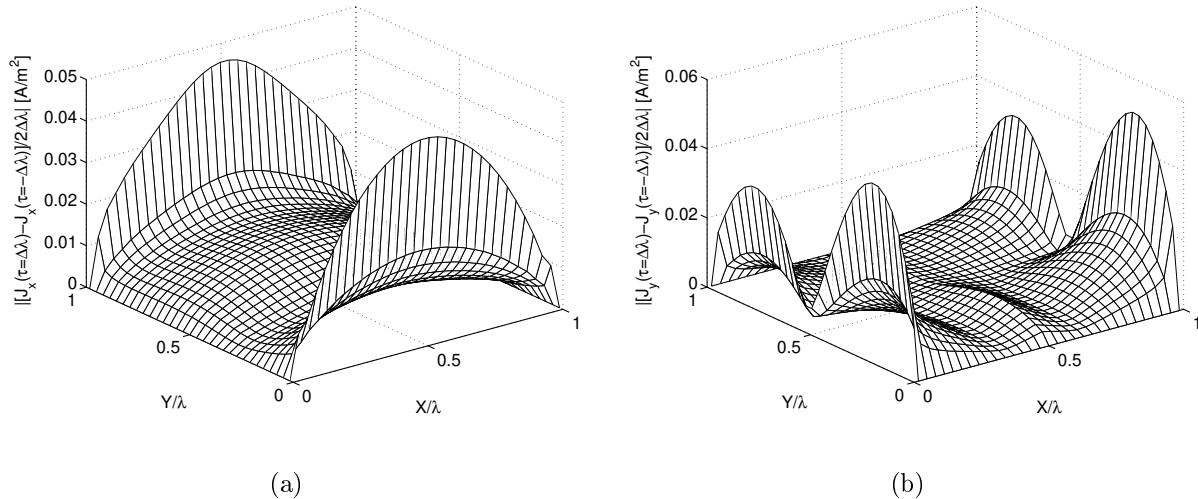
(a)   (b)

Figure 5.3: finite-difference approximation of the derivative of the surface current density for a $\lambda \times \lambda$ flat plate with an x-polarized plane wave incident from the direction $\theta = 45°$, $\phi = 90°$, by a change in the mesh. (a) Approximation of $d_\tau J_x|_{\tau=0}$, in modulus. (b) Approximation of $d_\tau J_y|_{\tau=0}$, in modulus.

the length of the plate by adding a row of squares to the mesh to increase the length of the plate and computing the surface current density for a plate of length $a = (1 + \Delta)\lambda$. The derivative can then be approximated by using an interpolation scheme to match the mesh points of both meshes and by applying a difference formula. In this case we have $2\Delta\lambda = \Delta x$, i.e., the dimension of the rectangles in the meshing in the x-direction. If we use 30 uniform intervals in the x-direction to compute the first surface current density and 31 uniform intervals in the x-direction to compute the second surface current density, we have $\Delta = 1/61$. This corresponds to the above choice of Δ. We have employed linear interpolation in the x-direction and nearest-neighbor interpolation in the y-direction for $d_\tau J_x|_{\tau=0}$ and nearest-neighbor interpolation in the x-direction and linear interpolation in the y-direction for $d_\tau J_y|_{\tau=0}$. The results for this approach are given in Figure 5.3. The interpolation scheme is consistent with the choice of rooftop functions for the surface current density. However, the computed results for the x-component of the derivative do not resemble the results for the analytic formulation and both the x- and the y-component are approximately a factor of two higher. We have also computed the relative error with respect to the results of the analytic formulation, according to Eq. (5.30). The relative error was approximately 1.7, which indicates that this finite-difference approximation yields an

unreliable estimate for the sensitivity.

To explain the difference between the two finite-difference approximations, we return to the discretized system of Eq. (3.18)

$$P_n L(Q_n u) = P_n f, \tag{5.31}$$

where P_n is determined by the set of testing functions, L is the integro-differential operator, $Q_n u$ is the numerical approximation of the surface current density, and f is the forcing function, i.e., the incident electric field. For the finite-difference approximation with uniform coordinate stretch, all operators depend on the stretch variable τ and we obtain

$$P_n(\tau)L(\tau)[Q_n(\tau)u] = P_n(\tau)f(\tau), \tag{5.32}$$

where n is fixed. Differentiation with respect to τ yields

$$
\begin{aligned}
P_n(0)L(0)d_\tau[Q_n(\tau)u]|_{\tau=0} = & - d_\tau P_n(\tau)|_{\tau=0} \left\{ L(0)[Q_n(0)u] - f(0) \right\} \\
& - P_n(0) \left\{ d_\tau L(\tau)|_{\tau=0}[Q_n(0)u] - d_\tau f(\tau)|_{\tau=0} \right\},
\end{aligned}
\tag{5.33}
$$

where $Q_n(0)u$ is the solution of the system

$$P_n(0)L(0)[Q_n(0)u] = P_n(0)f(0), \tag{5.34}$$

and $-d_\tau L(\tau)|_{\tau=0}[Q_n(0)u] + d_\tau f(\tau)|_{\tau=0}$ corresponds to the excitation function on the left-hand side of Eq. (5.23). Owing to the uniform coordinate stretch in the observation coordinates and Eq. (5.34), the term $d_\tau P_n(\tau)|_{\tau=0} \left\{ L(0)[Q_n(0)u] - f(0) \right\}$ is identically zero. Therefore, we obtain from Eq. (5.33)

$$P_n(0)L(0)d_\tau[Q_n(\tau)u]|_{\tau=0} = -P_n(0) \left\{ d_\tau L(\tau)|_{\tau=0}[Q_n(0)u] - d_\tau f(\tau)|_{\tau=0} \right\}. \tag{5.35}$$

Hence, differentiation of the discretized system gives the same result as discretization of the analytic sensitivity for a uniform coordinate stretch, provided that we do not introduce additional approximations in the operators L, P_n and Q_n. In case of the numerical system of Section 4.2.3, we have introduced approximations for the integrals. Also, in Section 5.3, we have introduced approximations in the forcing function of Eq.(5.35). Therefore, the two approaches do not necessarily coincide. However, the small relative error of the finite-difference approximation with respect to the results from the analytic formulation indicates that these approximations do not dominate the solution.

For the finite-difference approximation with a change in the number of variables, the projection operators P_n and Q_n are not differentiable, since the sets of basis and testing functions
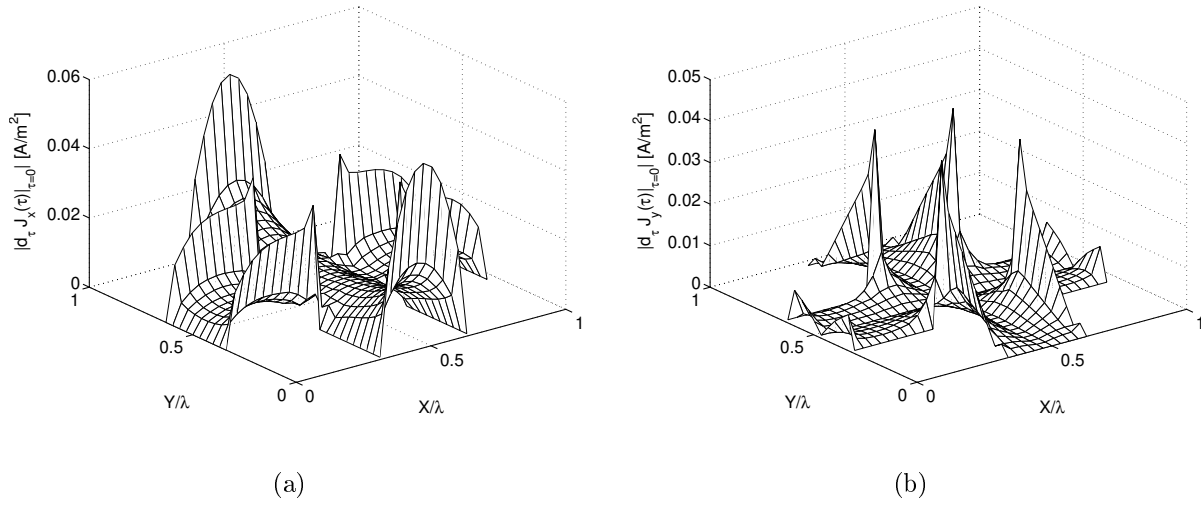
(a)   (b)

Figure 5.4: derivative with respect to length variation of the surface current density for a flat cross, excited by an x-polarized plane wave under normal incidence, for the analytic formulation. (a) $d_\tau J_x|_{\tau=0}$, in modulus. (b) $d_\tau J_y|_{\tau=0}$, in modulus.
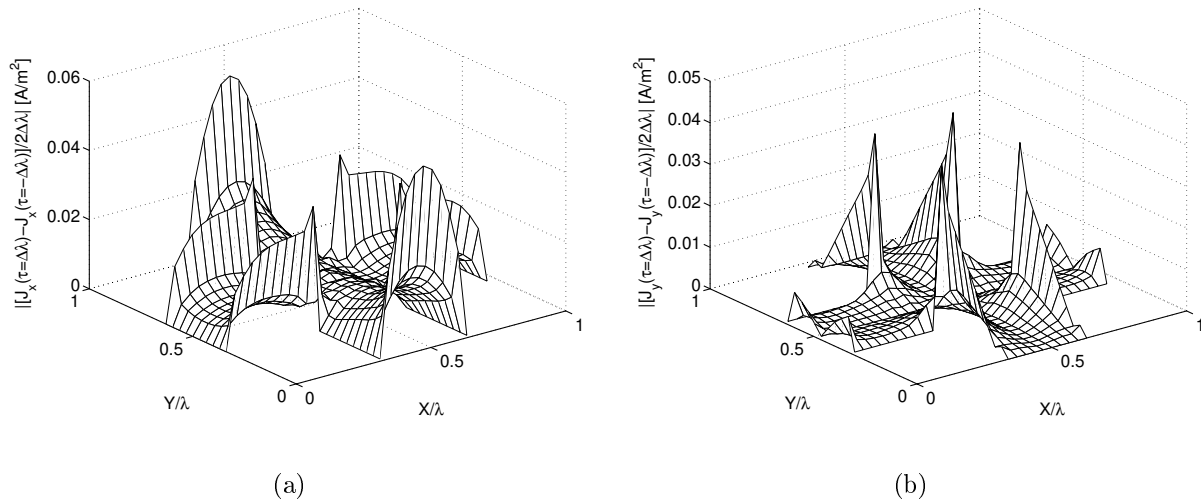

(a)   (b)

Figure 5.5: finite difference approximation of the derivative of the surface current density for a flat cross, excited by an x-polarized plane wave under normal incidence, for a uniform coordinate stretch. (a) Approximation of $d_\tau J_x|_{\tau=0}$, in modulus. (b) Approximation of $d_\tau J_y|_{\tau=0}$, in modulus.

change. The subsequent application of an interpolation operator is an attempt to restore the differentiability with respect to the parameter "length" (a). Therefore, the results will depend highly on the interpolation operator and the changes in the operators P_n and Q_n.

The analytic derivation of the derivative with respect to length variation is not restricted to a rectangular plate. If we change the repeated integrations over the length and the width of the rectangular plate into surface integrations over a more general shape, which can be captured in a uniform rectangular mesh, we obtain an expression for the derivative with respect to a uniform stretch over the full length in the x-direction of the shape. The same discretization scheme as mentioned above can then be used to compute an approximation of this derivative. As an example, we have computed this derivative for a cross consisting of five equal squares of length $\lambda/3$ under normal incidence of a plane wave polarized in the x-direction. The results with the analytic formulation are presented in Figure 5.4 and the finite-difference approximation corresponding to the same coordinate stretch with a fixed number of rectangles is given in Figure 5.5, for $\Delta = 5 \cdot 10^{-3}$. Again, we note that the finite-difference approximation resembles the results for the analytic formulation.

Chapter 6

Marching on in anything

In engineering, we often encounter the problem of computing a numerical approximation to the solution of a given set of differential or integral equations for a range of values of a certain parameter. For instance, in a design process a number of variables are changed several times to obtain an optimal result (in some sense). Another example is the construction of a time-domain result from a large number of frequency-domain computations, to prevent error accumulation or even instabilities in the marching-on-in-time procedure, see e.g. [70]. Additionally, we have the problem that the number of unknowns in a numerical simulation is so large that the time to solve a problem for one single parameter value is already very long. In these circumstances it would be a major improvement if we could speed up the computations by using information of already computed solutions to compute the numerical approximation for a new parameter value, since in general we expect that the approximation will not change drastically if we make a small change in the parameter value. This chapter contains results that have been published previously in [74].

6.1   Main idea

Consider the following linear problem, depending on the parameter p:

$$L(p)u = f(p), \tag{6.1}$$

where, for each p, $L(p)$ is a bounded linear operator on a normed space with bounded inverse $L(p)^{-1}$ and $u = u(p) = L(p)^{-1}f(p)$. We assume that $f(p)$ and $L(p)$ are continuously differentiable with respect to p, for $p \in [p_{-1}, p_0]$. Then we can employ

$$f(p) = f(p_{-1}) + \int_{p_{-1}}^{p} f'(\xi)d\xi, \tag{6.2}$$

to write

$$f(p_0) = f(p_{-1}) + \int_{p_{-1}}^{p_0} f'(\xi)d\xi = L(p_{-1})u(p_{-1}) + \int_{p_{-1}}^{p_0} f'(\xi)d\xi$$

$$\Rightarrow L(p_0)u(p_0) = L(p_{-1})u(p_{-1}) + \int_{p_{-1}}^{p_0} f'(\xi)d\xi \tag{6.3}$$

$$\Rightarrow u(p_0) = L(p_0)^{-1}L(p_{-1})u(p_{-1}) + \int_{p_{-1}}^{p_0} L(p_0)^{-1}f'(\xi)d\xi.$$

We observe that $u(p_0)$ can be approximated by $L(p_0)^{-1}L(p_{-1})u(p_{-1})$. In general, we have no idea of the structure of $L(p_0)^{-1}L(p_{-1})$. However, a similar identity as in Eq. (6.2) shows that

$$L(p_0)^{-1}L(p_{-1}) = I + \int_{p_0}^{p_{-1}} L(p_0)^{-1}L'(\xi)d\xi, \tag{6.4}$$

where I represents the identity operator. Under certain conditions, the expression on the right-hand side of the inequality

$$\left\| \int_{p_0}^{p_{-1}} L(p_0)^{-1}L'(\xi)d\xi - \gamma I \right\| \leq \int_{p_0}^{p_{-1}} \left\| L(p_0)^{-1}L'(\xi) - \gamma I/(p_0 - p_{-1}) \right\| d\xi, \tag{6.5}$$

will be small for some γ, e.g., for small $|p_{-1} - p_0|$ or when $L(p_0)^{-1}L'(\xi)$ closely resembles a multiple of the identity. In these cases we can approximate the expression $L(p_0)^{-1}L(p_{-1})$ by a multiple $\gamma_{-1} = \gamma + 1$ of the identity I. With these simplifications we can approximate $u(p_0)$ as

$$u(p_0) = \left[I + \int_{p_0}^{p_{-1}} L(p_0)^{-1}L'(\xi)d\xi \right] u(p_{-1}) + \int_{p_{-1}}^{p_0} L(p_0)^{-1}f'(\xi)d\xi$$

$$\doteq \gamma_{-1}u(p_{-1}) + \int_{p_{-1}}^{p_0} L(p_0)^{-1}f'(\xi)d\xi. \tag{6.6}$$

Alternatively, the above approximation can be written as

$$0 \doteq L(p_0)^{-1} \left[f(p_{-1}) - \gamma_{-1} L(p_0) u(p_{-1}) \right]. \tag{6.7}$$

However, we emphasize here that the validity of the assumptions strongly depends on the operators $L(p)$, $L'(p)$ and $L(p)^{-1}$, the vectors $f(p)$ and $f'(p)$, and the increment $p_0 - p_{-1}$. Further, the estimate γ_{-1} will depend on p_0 and p_{-1}.

A similar analysis for two extrapolation points can be performed, under the assumption that the second derivative of $f(p)$ also remains integrable. Starting from the expansion

$$f(p) = f(p_0) + (p - p_0)f'(p_0) + \int_{p_0}^{p} (\xi - p_0)f''(\xi)d\xi, \tag{6.8}$$

we arrive at

$$f(p_{-1}) = f(p_0) + (p_{-1} - p_0)f'(p_0) + \int_{p_0}^{p_{-1}} (\xi - p_0)f''(\xi)d\xi, \tag{6.9a}$$

$$f(p_{-2}) = f(p_0) + (p_{-2} - p_0)f'(p_0) + \int_{p_0}^{p_{-2}} (\xi - p_0)f''(\xi)d\xi. \tag{6.9b}$$

Elimination of the terms that contain $f'(p_0)$ gives

$$\begin{aligned} f(p_0) =& \frac{p_0 - p_{-2}}{p_{-1} - p_{-2}} f(p_{-1}) + \frac{p_{-1} - p_0}{p_{-1} - p_{-2}} f(p_{-2}) + \\ & \frac{(p_{-2} - p_0)}{(p_{-1} - p_{-2})} \int_{p_0}^{p_{-1}} (\xi - p_0)f''(\xi)d\xi + \frac{(p_0 - p_{-1})}{(p_{-1} - p_{-2})} \int_{p_0}^{p_{-2}} (\xi - p_0)f''(\xi)d\xi \\ =& \frac{p_0 - p_{-2}}{p_{-1} - p_{-2}} L(p_{-1})u(p_{-1}) + \frac{p_{-1} - p_0}{p_{-1} - p_{-2}} L(p_{-2})u(p_{-2}) + \\ & \frac{(p_{-2} - p_0)}{(p_{-1} - p_{-2})} \int_{p_0}^{p_{-1}} (\xi - p_0)f''(\xi)d\xi + \frac{(p_0 - p_{-1})}{(p_{-1} - p_{-2})} \int_{p_0}^{p_{-2}} (\xi - p_0)f''(\xi)d\xi. \end{aligned} \tag{6.10}$$

If we leave out the Riemannian remainder terms, i.e., the terms containing the integral over $(\xi - p_0)f''(\xi)$, we obtain

$$u(p_0) \doteq \frac{p_0 - p_{-2}}{p_{-1} - p_{-2}} L(p_0)^{-1}L(p_{-1})u(p_{-1}) + \frac{p_{-1} - p_0}{p_{-1} - p_{-2}} L(p_0)^{-1}L(p_{-2})u(p_{-2}). \tag{6.11}$$

An expansion of $L(p)$ shows that

$$L(p_0)^{-1}L(p_{-1}) = I + \int_{p_0}^{p_{-1}} L(p_0)^{-1}L'(\xi)d\xi, \tag{6.12a}$$

$$L(p_0)^{-1}L(p_{-2}) = I + \int_{p_0}^{p_{-2}} L(p_0)^{-1}L'(\xi)d\xi. \tag{6.12b}$$

Again, we assume that the above expressions are close to $\gamma_{-k}I$, for $k = 1, 2$. We arrive at the conclusion that $u(p_0)$ can be approximated by a linear combination of $u(p_{-1})$ and $u(p_{-2})$, i.e.,

$$u(p_0) \doteq \gamma_{-1}u(p_{-1}) + \gamma_{-2}u(p_{-2}), \tag{6.13}$$

where γ_{-1} depends on p_0 and p_{-1}, and γ_{-2} depends on p_0 and p_{-2}. At present, we have no proof that these simplifications are appropriate. Instead, we will apply this strategy to the integro-differential equations of Chapter 2, to explore the merits and limitations of this idea.

6.2   Least-squares approximation

One of the problems that remains unsolved in the theory above is how to estimate the values γ_{-k} such that

$$\left\| L(p_0)^{-1}L(p_{-k}) - \gamma_{-k}I \right\|, \tag{6.14}$$

is small. With the aid of the general definition of the norm of an operator, we can conclude that

$$\sup_{\|u\| \neq 0} \frac{\|L(p_0)^{-1}L(p_{-k})u - \gamma_{-k}u\|}{\|u\|}, \tag{6.15}$$

should be small. In fact, it is not necessary that this estimate on the operator holds for any vector u, since the only relevant vector u is $u(p_{-k})$. However, the most important conclusion of the preceding section is that, under certain conditions, we can approximate $u(p_0)$ by its linear prediction

$$u(p_0) \doteq \sum_{k=1}^{K} \gamma_{-k}u(p_{-k}), \tag{6.16}$$

for some fixed number K. Hence, the coefficients γ_{-k} should be determined from

$$\min_{\gamma_{-k}} \left\| u(p_0) - \sum_{k=1}^{K} \gamma_{-k}u(p_{-k}) \right\|. \tag{6.17}$$

The only remaining issue in the above formulation is the choice of the norm. For reasons of consistency, this choice should coincide with the norm that is used for the solution method for the system $L(p)u = f(p)$. Since we will apply the conjugate-gradient method, which minimizes the norm [6, 7, 84]

$$\|u - L(p)^{-1}f(p)\|_L = \|L(p)u - f(p)\|_2, \tag{6.18}$$

where $\| \cdot \|_2$ denotes the 2-norm in $\mathbb{C}^N$ and N is the dimension of the linear system, it is logical to employ the same norm for the minimization problem of γ_{-k}. The resulting problem can be written in terms of a least-squares problem, which gives the unique best approximation in $\mathbb{C}^N$, which is regarded as a Hilbert space. Hence, γ_{-k} can be determined from the system of normal equations

$$\sum_{k=1}^{K} \gamma_{-k} \left(L(p_0)u(p_{-k}), L(p_0)u(p_{-\ell}) \right) = (f, L(p_0)u(p_{-\ell})) \qquad \ell = 1, \ldots, K, \tag{6.19}$$

and $u(p_{-k})$ is the result of the k-th preceding simulation.

In the general form of the CG algorithm in Section 4.3, the initial estimate u_0 in the notation of Eq. (4.48a) is unspecified. Therefore, we insert our estimate of Eq. (6.16) at this point. The advantage is that the conjugate-gradient algorithm is left untouched and the convergence properties remain unaltered. Also, there is no error accumulation from preceding simulations, since the CG algorithm will improve the solution for $u(p_0)$, until the termination threshold for the residual error has been reached. Extensive numerical tests have shown that the construction of the coefficients γ_{-k} by means of the least-squares approximation yields the most efficient estimate as compared to other constructions that are for instance based on polynomial extrapolation [71].

Combination of a CGFFT scheme together with the above least-squares estimate was first used by Tijhuis et al. [50, 71, 72]. The idea was conceived originally to circumvent insta-bilities in the marching-on-in-time procedure for time-domain integral equations by a large number of frequency-domain computations [71]. Therefore the scheme was called "march-ing on in frequency". The late professor R.E. Kleinman came up with the denomination "marching on in anything", since by then it had been demonstrated that the proposed algorithm performed well for a large number of (physical) parameters.

6.3   Thin wire

To illustrate the behavior of the CG-extrapolation procedure in more detail, we return to the configuration for which the effectiveness of the method was demonstrated first, i.e., a straight thin-wire segment in a homogeneous medium. We solve the system of equations (4.9) repeatedly for $s_m = \delta + j2\pi m \Delta f$ with $\delta \geq 0$ and $m = 0, 1, \ldots, M$, i.e., the parameter p is equal to the frequency f. Subsequently, we determine the spectral integral in the inverse Laplace transformation (2.8) with the aid of a repeated trapezoidal rule and a Fast Fourier Transformation to obtain a time-domain result. This is explained in detail in Appendix D. Throughout the computations, we keep the discretization fixed for all frequencies. This does not affect the accuracy of the computed time-domain signal, since the excitation is bandlimited [71].

To demonstrate the effect of a change in the step size and the error criterion, i.e., the threshold for the relative residual error to terminate the CG iterations, on the performance of the proposed algorithm, we consider a wire of length $L = 1$ m and radius $a = 2$ mm in the frequency range from zero to 3.0 GHz with plane-wave excitation at normal incidence. First, we take a frequency step $\Delta f = 20$ MHz, i.e., $M = 150$, we take $\delta = 10^{-12} c_0 / L$ and a relative error for the conjugate-gradient algorithm of 10^{-8}. Figure 6.1(a) shows the number of iterations needed when we take a zero initial estimate (dashed line) and three preceding results (solid line), i.e., $K = 3$. The number of iterations per frequency can be reduced by allowing for a larger relative error in the CGFFT method. The reduced number of iterations for the same configuration with a relative error of 10^{-3} is given in Figure 6.1(b). Furthermore, the extrapolation procedure becomes more effective. This may seem an unsatisfactory way to reduce the computational load. Our argument is that we are solving a *discretized* system with a discretization error in the order of a few percent. Therefore, reaching high accuracy in the CG process does not contribute significantly to the accuracy of the obtained computational results.

A second way to improve the efficiency of the extrapolation scheme per step is to reduce the frequency step. This is illustrated in Figure 6.2(a) for a frequency step of 5 MHz, i.e., $M = 600$, $\delta = 10^{-12} c_0 / L$ and a relative error of 10^{-3}. From this figure, we observe that the highest peaks are lowered and that the average number of iterations per step is reduced. However, due to the decrease in step size, the number of frequencies for which we have to compute the current increases by a factor of four. A further reduction of

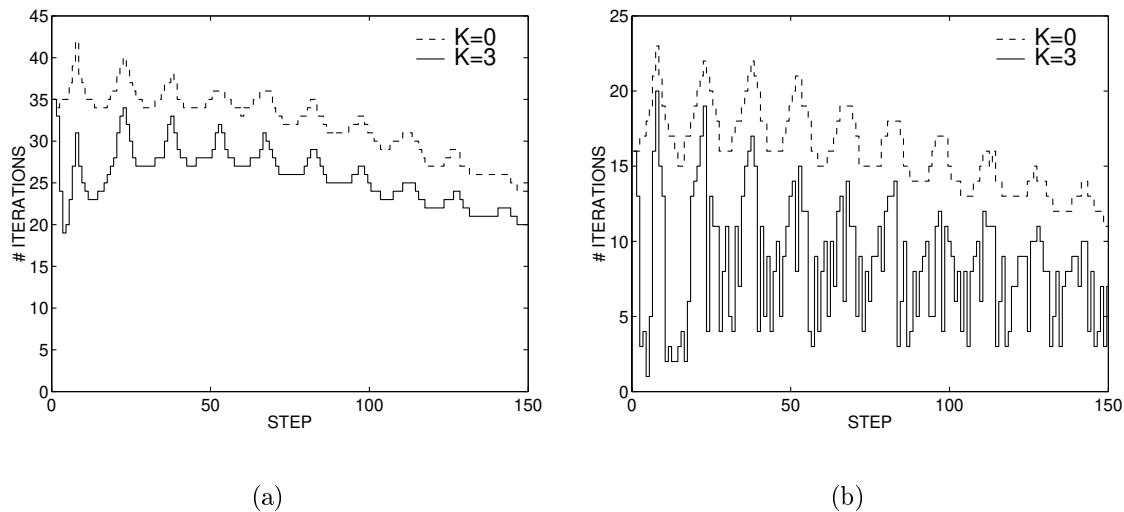(a)   (b)

Figure 6.1: number of iterations versus step for the marching-on-in-frequency version of the CGFFT method for a thin wire with plane-wave excitation at normal incidence with parameters $L = 1$ m, $a = 2$ mm, $\delta L/c_0 = 10^{-12}$ and $\Delta f = 20$ MHz. (a) Number of iterations required to reach a relative error of 10^{-8}. (b) Number of iterations required to reach a relative error of 10^{-3}.

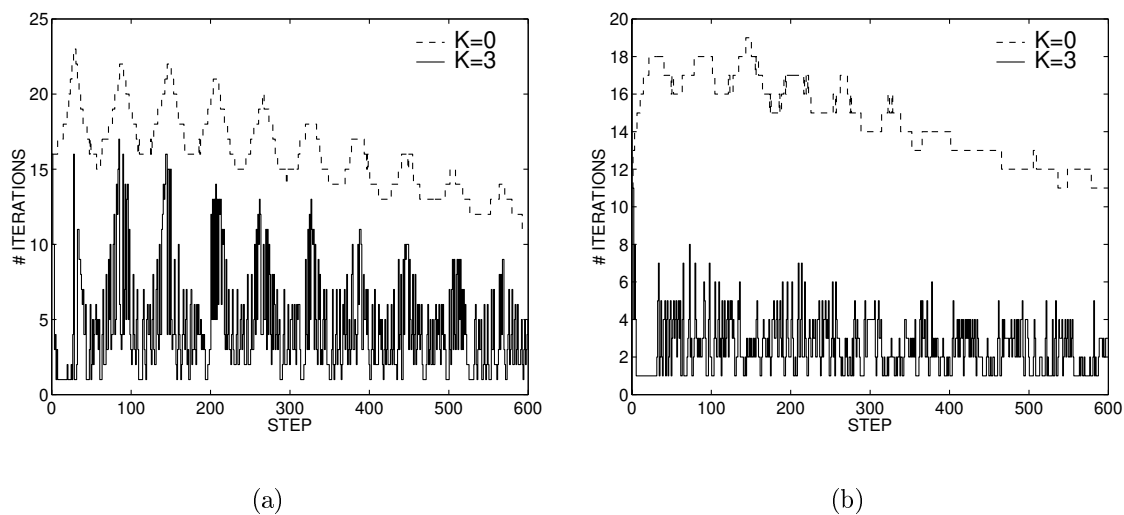(a)   (b)

Figure 6.2: number of iterations required to reach a relative error of 10^{-3} versus step for the marching-on-in-frequency version of the CGFFT method for a thin wire with plane-wave excitation at normal incidence with parameters $L = 1$ m, $a = 2$ mm. (a) $\Delta f = 5$ MHz and $\delta L/c_0 = 10^{-12}$. (b) $\Delta f = 5$ MHz and $\delta L/c_0 = 1$.

the number of iterations per frequency is possible by taking even smaller frequency steps. However, the computation of the extrapolation coefficients also requires the computation of a matrix-vector product for every vector in the extrapolation procedure. Therefore, there is an optimum in the step size for which the total computation time is minimal. This was already reported in [72].

A third parameter that can be used to improve the efficiency of the extrapolation strategy is the parameter δ. In constructing our initial estimate, we assumed that the solution to the system of equations depends in a well-behaved manner on the parameter of interest. However, in the vicinity of a pole in the complex s-plane, this is no longer true. For a stable linear system the poles lie in the left-hand side of the complex s-plane. By choosing $\delta L/c_0$ very small, we may be close to a pole near the imaginary axis, which corresponds to a resonance in the time domain. For the straight thin wire, the positions of the poles correspond to frequencies for which the length of the wire is a multiple of half a wavelength. Therefore, we expect an improvement in the convergence of our algorithm when the ratio $\delta L/c_0$ is increased. This is shown in Figure 6.2(b) for $\delta L/c_0 = 1$. We see that the number of iterations per frequency step indeed decreases for increasing δ. On the other hand, if we take too large a value for $\delta L/c_0$, e.g., 10, the computed time-domain result is no longer reliable. This is caused by the (numerical) effect that, especially for large values of t, the factor $\exp(\delta t)$ in Eq. (2.8) amplifies the errors in the sampled time signal that results from the Discrete Fourier Transformation. This is illustrated in Appendix D.

6.4   Perfectly conducting plate

The second example is a flat, rectangular plate in free space located at $0 < x < a$, $0 < y < b$ and $z = 0$. For this problem, we solve the electric-field integral equation (2.59) numerically. Since we would like to show that our extrapolation scheme performs well for a standard discretization, we use the discretization of [84, 85]. In this discretization, the unknown surface current density $\boldsymbol{J}_S$ is approximated by rooftop functions, the weak form of the Green's function is introduced together with an interpolation scheme for the vector potential. The electric-field integral equation is then weighted by the same rooftop functions. In the resulting discretized form, the convolution symmetry is preserved, so that the matrix-vector products in the conjugate-gradient procedure can be evaluated with the aid of two-dimensional FFT operations. Therefore, the complexity of this scheme

Figure 6.3: number of iterations required to reach a relative error of 10^{-3} versus angle of incidence for the marching-on-in-angle version of the CGFFT method in [84, 85] for a flat $\lambda \times \lambda$ plate using zero (dashed line) and two preceding results (solid line) as an initial estimate.
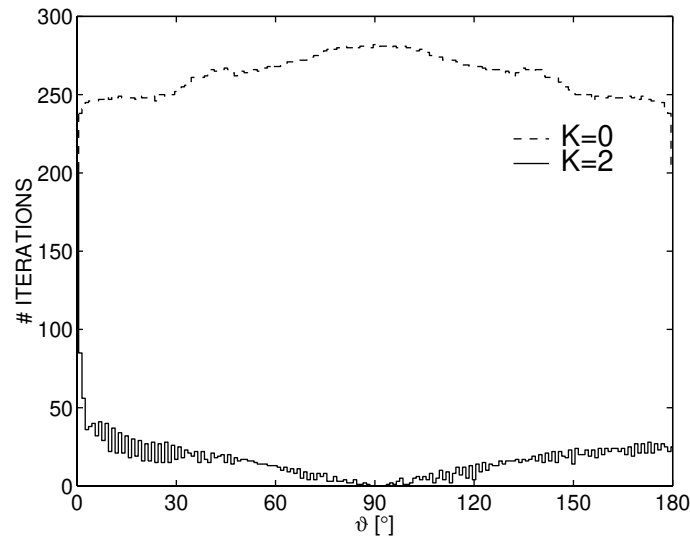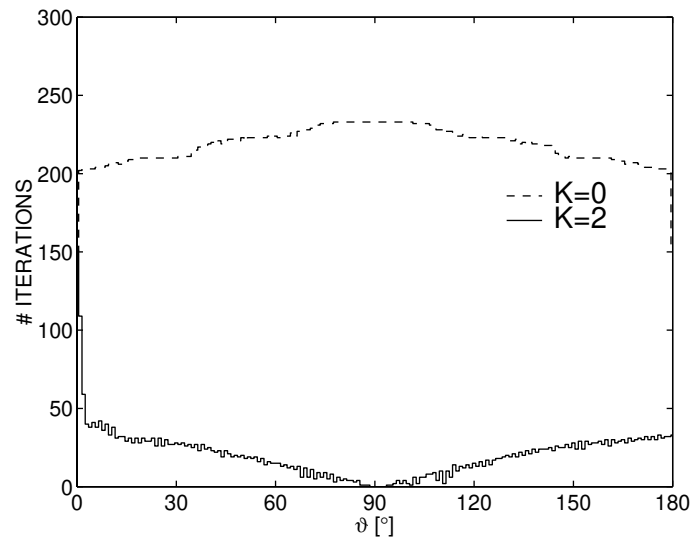

Figure 6.4: number of iterations required to reach a relative error of $5 \cdot 10^{-4}$ versus angle of incidence for the marching-on-in-angle version of the CGFFT method of Section 4.2.3 for a flat $\lambda \times \lambda$ plate using zero (dashed line) and two preceding results (solid line) as an initial estimate.

is comparable to the complexity of the scheme in Section 4.2.3.

In particular, for $s = j\omega$, we have computed the monostatic radar cross-section of a $\lambda \times \lambda$ plate. A plane wave is incident on the plate at an angle θ with respect to the z-axis and an angle $\phi = 90°$ with respect to the x-axis. Hence, the parameter p is equal to θ in this case. The incident plane wave is x-polarized. We have computed the surface current density for $\theta = m\Delta\theta$ with $\Delta\theta = 1°$ and $m = 0, \ldots, 180$. The discretized plate has a mesh of 31×31 squares. Figure 6.3 shows the number of iterations for increasing θ. The dashed line represents starting from a zero initial estimate, and the solid line is for two preceding results in the initial estimate, i.e., $K = 2$. The discretization of Section 4.2.3 exhibits a similar behavior, as shown in Figure 6.4. For both discretizations, we observe that the initial estimate at $\theta = 90°$ does not require improvement by the conjugate-gradient algorithm. This is due to the symmetry in the problem and it confirms the theory in Section 6.1. The monostatic radar cross-section of the $\lambda \times \lambda$ plate in the plane $\phi = 90°$ is presented in Figure 6.5.

Having dealt with marching on in angle, another result for the plate concerns marching on in length. The idea was inspired by the shape sensitivity analysis in [75, 76] and in Chapter 5. Here, we start from a $\lambda \times \lambda$ plate and we increase the length of the plate in 100 steps to a $2\lambda \times \lambda$ plate. We used a fixed spatial discretization of 62×31 rectangles. We employ a fixed mesh, since the results in Chapter 5 indicate that changes in the mesh can give rise to non-smooth results, which would be difficult to extrapolate. The number of iterations required to reach a relative error of 10^{-3} versus the length of the plate, for the numerical scheme in [84, 85], is shown in Figure 6.6. In the computations leading to Figures 6.3 and 6.6, it turned out that extrapolation with $K = 2$ was in fact more efficient than extrapolation with $K = 3$. Moreover, extensive numerical experiments for the parameters frequency, length, and angle of incidence, all with several choices of the step size for these parameters, have shown that $K = 2$ yields the most rapid convergence of the conjugate-gradient method, as compared with $K = 1$, $K = 3$, and $K = 4$. This is caused by the fact that, for values of K larger that two, the linear system for the least-squares estimate in Eq. (6.19) is almost singular, which makes the initial estimate unreliable. From the point of view of memory requirement, this is a convenient result, since we only have to store the results of the last two simulations. The fact that we need only two vectors for the extrapolation indicates that the linear system is stable for modest parameter variations.
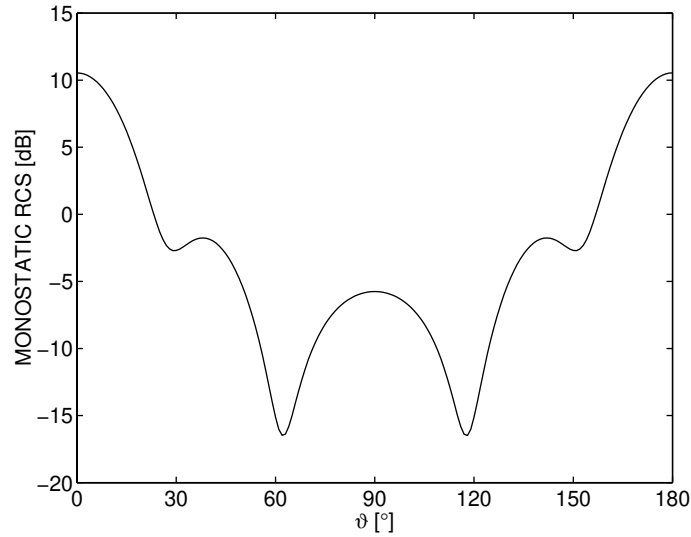
Figure 6.5: monostatic radar cross-section versus angle of incidence for a $\lambda \times \lambda$ plate.
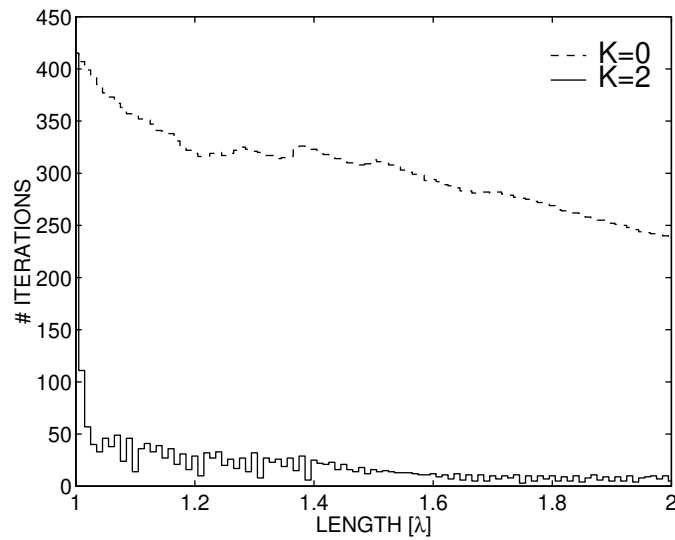

Figure 6.6: number of iterations required to reach a relative error of 10^{-3} versus length of the plate for the marching-on-in-length version of the CGFFT method in [84, 85] for a flat plate using zero (dashed line) and two preceding results (solid line) as an initial estimate.

6.5 Three-dimensional dielectric body

The third example is an inhomogeneous dielectric cube, again in free space. We formulate the scattering problem as a domain integro-differential equation over the object domain $\mathcal{D}$ as in Eq. (2.64) or Eq. (2.66) together with the definition for the contrast-current density of Eq. (2.61) or Eq. (2.67), respectively. We use the discretization of [86, 87], taking the permittivity function constant in each rectangular subdomain in the space discretization. Similar as for the surface current density in the plate problem, the electric-flux density $\boldsymbol{D}(\boldsymbol{r})$, or $\boldsymbol{J}/s + \boldsymbol{D}$, is approximated by an expansion that is piecewise linear in the longitudinal direction and constant in the transverse directions. The Green's function is replaced by its weak form, and the result is weighted by testing functions that are identical to the expansion functions. Again, the space discretization shows a discrete convolution symmetry and can be efficiently computed by three three-dimensional Fast Fourier Transformations.

We have performed a large number of numerical tests for variations in the parameters frequency, contrast, and dimension, all for several choices of the step size for these parameter. We have systematically examined the convergence for $K = 1$ to $K = 4$. In all cases, the most rapid convergence, over a large interval, was found for $K = 2$.

As an illustration, we have modeled a cube of muscle tissue centered inside a cube of fat tissue. The incident field is x-polarized with propagation vector parallel to the z-axis and a strength of 1 V/m. The dispersive tissues are modeled with the aid of a Debye model [43] and the dimensions of the inner and outer cubes are 0.14 m and 0.30 m, respectively. The discretized object has $30 \times 30 \times 30$ mesh points. The field is computed in the middle of the muscle cube for frequencies f from 100 to 600 MHz and then converted to a time-domain signal. Hence, the parameter p is equal to f. We have taken $f = f_0 + m\Delta f$, for $f_0 = 100$ MHz, $m = 0, \ldots, 100$, and $\Delta f = 5$ MHz. The number of iterations needed to reach a relative residual error of 10^{-3} is shown in Figure 6.7, where the dashed line is for a zero initial estimate, and the solid line for minimization using two preceding results, i.e., $K = 2$. The time signal, shown in Figure 6.8, is computed by an FFT for the waveform $\exp\left[-(t - \tau)^2/2T^2\right]\sin(\omega_0 t)$, where $\tau = 14$ ns, $T = 2.75$ ns and $\omega_0/2\pi = 450$ MHz.

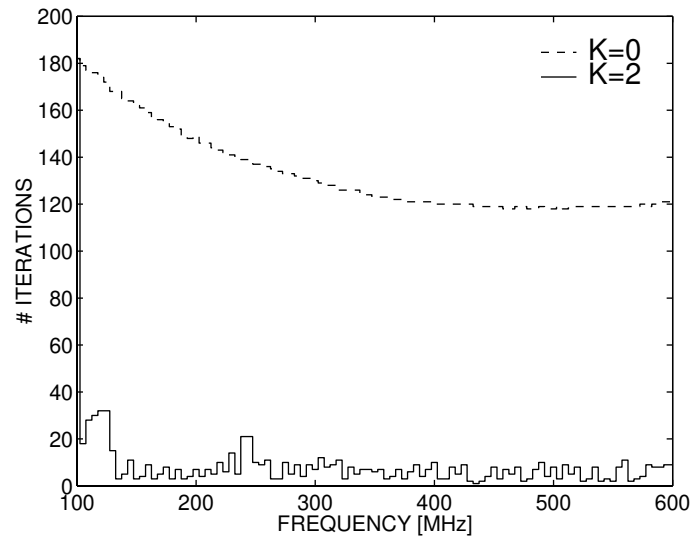Figure 6.7: number of iterations required to reach a relative error of 10^{-3} versus frequency for the marching-on-in-frequency version of the CGFFT method for an inhomogeneous dielectric cube using zero (dashed line) and two preceding results (solid line) as an initial estimate.
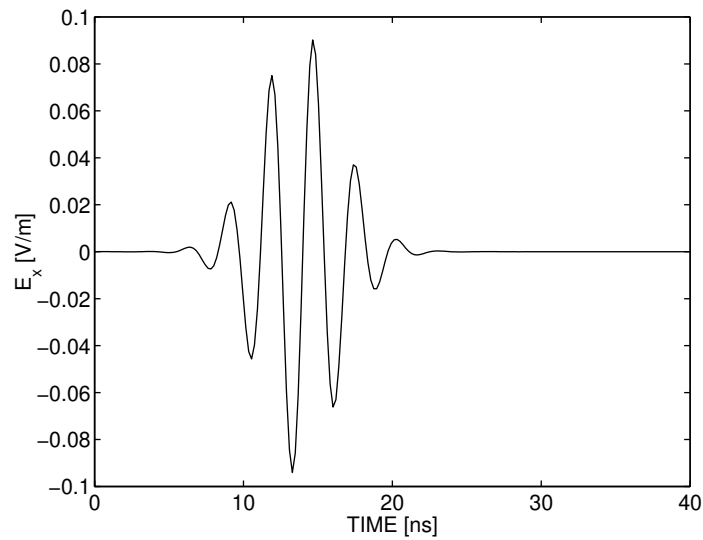

Figure 6.8: time-domain signal at the center of the muscle cube for an incident x-polarized plane wave of 1 V/m.

Chapter 7

Optimization of wire antennas

Many problems in engineering are formulated in terms of design specifications. A classical example within the context of electrical engineering is the design of filter banks. However, as a general rule, these specifications cannot be met in a straightforward manner. Therefore, it is interesting to examine optimal solutions. Optimality means that the design has the least amount of deviation from the original specifications. There are several techniques to study optimal solutions. Here, we will focus on continuous optimization techniques, in which the ranges of the design parameters are continuous intervals. Also, we will assume that an appropriate initial estimate for the parameters is available, which may prevent hitting a local optimum. In most cases, these parameter estimates follow from prior studies, e.g., feasibility studies or results from the literature.

Within the mathematical optimization community software has been developed to optimize large-scale non-linear physical problems, which are discretized by finite-element or finite-difference methods. At the same, time tools have been generated for automatic differentiation [31], to compute gradients and Hessians. Further, two programming languages have been developed suitable for several types of optimization: AMPL [26] and GAMS [10]. Also, several optimization packages together with an AMPL interface have been made accessible via the internet by the Argonne National Laboratory in the U.S.A. through the Network Enabled Optimization System (NEOS). For the optimization of wire antennas, we[1] have used AMPL in combination with NEOS.

---

[1]This research was performed at the University of Dundee from January until June 2000, under the supervision of prof. P.D. Smith and prof. R. Fletcher.

The mathematical optimization community has focused mainly on solving problems based on finite elements or finite differences. However, in electromagnetics an integral-equation method, which gives rise to dense matrices, is expected to be more appropriate to solve optimization problems [2]. In particular, integral equations are generally employed for radiation problems, e.g., in antenna design. It is not obvious that the optimization strategies developed for finite elements and finite differences are also suitable for techniques based on integral equations. The main difference is that integral equations are global formulations whereas differential equations (which give rise to finite elements and finite differences) are essentially local. Therefore, the linear systems that result from integral equations are dense, whereas systems for finite-element and finite-difference methods are sparse.

7.1   Yagi-Uda antenna

To examine whether or not we can use the optimization routines for integral equations, we looked for a simple test case, for which validation of the solutions was possible. A well-known example we found was a Yagi-Uda antenna [66]. This antenna is part of the larger class of wire antennas, which has been studied extensively on both a theoretical and an experimental level. The basic characteristics of a Yagi-Uda antenna are depicted in Figure 7.1. Typically, this antenna consists of a driver to which the feeding network is connected, a reflector to block the energy flow in the negative x-direction, and a series of directors, which guide the energy in the positive x-direction. Several papers have appeared on the optimization of Yagi-Uda antennas, see e.g. [4, 12, 38] and references therein. In these references, gradient optimization together with an analytical model for the antenna or a genetic algorithm together with a numerical model are employed. Our study differs from previous work in the sense that we have used a completely numerical model for the Yagi-Uda antenna and that we have applied a constrained optimization technique based on gradients. In this specific case, it was not our interest to find the best antenna but merely to find out what strategy is the most appropriate to optimize the performance of the antenna.

---

[2]At present, several commercial software packages that are based on integral equations, e.g., Momentum and Sonnet, have integrated their electromagnetic solver with an optimization environment.
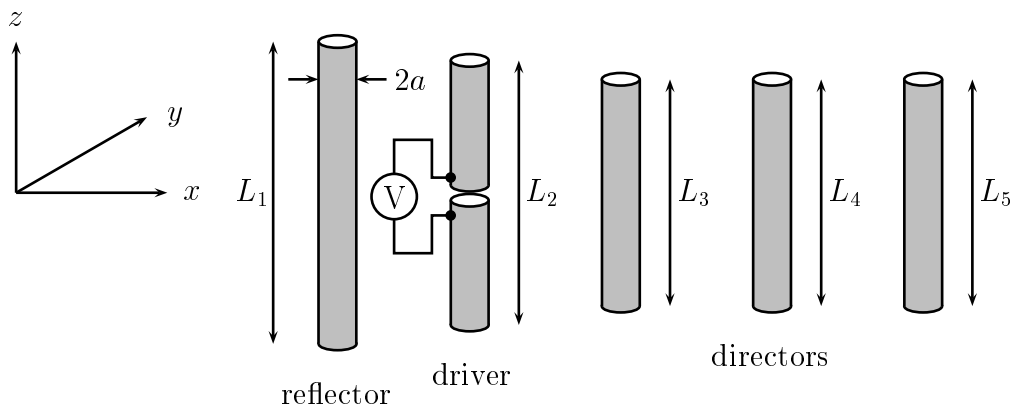
Figure 7.1: example of a Yagi-Uda antenna.

7.1.1   Formulation of the optimization criteria for the Yagi-Uda antenna

We model the antenna by M wires with circular cross-section, all with radius a. The reflector is labeled as wire 1, the driver as wire 2 and the directors as wires 3 to M. We assume that the reflector and driver are always present. Further, the axes of all wires lie in one plane and are parallel to each other. We choose our reference system such that this plane is the xz-plane and the wire axes are parallel to the z-axis. Hence, the axis of wire m has coordinates $(x, y, z){=}(x_m, 0, z)$ for $z \in (-L_m/2, L_m/2)$, and $x_m < x_{m+1}$ for $m = 1, \ldots, M - 1$. This type of symmetry in the z-direction is typical for Yagi-Uda antennas. The feeding network of the antenna is connected to the second wire (the driver) at its center. The symmetry of the antenna configuration can be exploited to reduce the number of unknowns for the currents on the wires. However, for reasons of flexibility, which will become clear later on, we have not used this symmetry. At the same time, the symmetry can be used to check the model and the optimization results.

To model the currents on the wires of the antenna, we have used the linear system of Eq. (4.27), which we denote by

$$Z \cdot I = V, \tag{7.1}$$

where Z is the impedance matrix, I is a vector that contains the current coefficients, and V contains the excitation. We approximate the connection of the feeding network at the

driver by a delta-gap source with voltage V_g, located at the center of the wire, i.e.,

$$E_z^i(x_k, z) = V_g \delta(z) \delta_{x_k, x_2}, \tag{7.2}$$

where

$$\delta_{x_i, x_j} = \begin{cases} 1 & \text{for} \quad x_i = x_j, \\ 0 & \text{elsewhere}, \end{cases} \tag{7.3}$$

which is the Kronecker delta. Although the delta-gap model is problematic for the thin-wire integral equation with reduced kernel, as can be seen from Eq. (3.37a) and the asymptotic behavior of $K_0(z)$ for $z \to \infty$, we will use it as a model for a highly localized source and make sure that the discretization remains coarse enough to prevent numerical problems.

Since we now have a model for the currents on the wires of the Yagi-Uda antenna as a function of the excitation, we can define the resistance of the antenna as

$$R_{in} = \text{Re} \left\{ -\frac{V_g}{I[2, N/2]} \right\}, \tag{7.4}$$

where $I[2, N/2]$ is the current on the driver (wire 2) at $z = 0$, i.e., the position of the delta-gap source. Another definition of the resistance can be obtained by computing the total radiated energy. Although the latter definition is more accurate from a numerical point of view, it is also much more expensive to compute, since we also need to compute the gradient of the resistance with respect to all parameters. Further, we need an expression for the time-averaged radiated energy (S) per solid angle in the direction of the main beam of the Yagi-Uda antenna. In standard spherical coordinates, the main beam is located at $\theta = 90°$ and $\phi = 0°$. The time-averaged radiated energy (S) per solid angle can be expressed in terms of the radiated electric field in the far-field zone as

$$S(\theta, \phi) = \frac{R^2 \boldsymbol{E} \cdot \boldsymbol{E}^*}{2Z_0}, \tag{7.5}$$

where R is the distance between the center of the antenna and the observation point and Z_0 is the wave impedance of free space. The radiated electric field in the far-field region, for $s = j\omega$, has only a component in the direction of $\boldsymbol{u}_\theta$. This component can be written as

$$E_\theta(\theta, \phi) = j\omega\mu_0 \sin(\theta) \frac{\exp(-j\omega R/c_0)}{4\pi R} \sum_{m=1}^{M} \int_{-L_m/2}^{L_m/2} I_m(z') \exp[j\omega(x_m p + z' q)/c_0] dz', \tag{7.6}$$

where

$$p = \cos(\phi)\sin(\theta), \tag{7.7a}$$

$$q = \cos(\theta). \tag{7.7b}$$

After the introduction of a linear-spline approximation for the currents on the wires, the time-averaged radiated energy per solid angle, in the direction $\theta = 90°$, $\phi = 0°$, can be approximated as

$$S(90°, 0°) = \frac{\omega^2 \mu_0^2}{32\pi^2 Z_0} \left| \sum_{m=1}^{M} \sum_{n=1}^{N-1} I[m,n]\Delta_m \exp(j\omega x_m/c_0) \right|^2. \tag{7.8}$$

The goal of the optimization is to maximize the radiated energy in the main direction of the antenna. However, since the antenna will be connected to a coaxial cable of 75 Ω, the input resistance of the antenna has to be commensurate to avoid strong reflections on the feeding network. Hence, we have chosen to apply the constraint $R_{in} \in [50, 100]$ Ω, indicating reflection coefficients not exceeding 20%, if the input reactance is zero. To make the formulation definite, we lock the antenna onto the coordinate system by choosing

$$x_2 = 0. \tag{7.9}$$

Further, we need to impose a few restrictions to ensure the validity of the numerical model for the currents on the wires. The first restriction is

$$x_m \le x_{m+1} - 10a \quad \text{for} \quad m = 1, \ldots, M-1, \tag{7.10}$$

which expresses that there is an ordering between all the wires and that the wires cannot lie closer together than 10 times the radius of the circular cross-section of the wires. We impose this restriction because the approximation of the coupling from one wire to another is only valid if the wavelength and the distance between the wires are sufficiently large, with respect to the radius a. This was already explained in Section 4.1.3. The other restriction is

$$8 \le \frac{2\pi c_0 N}{\omega L_m} \le 100 \quad \text{for} \quad m = 1, \ldots, M. \tag{7.11}$$

This implies that the length of the wire must be such that the number of sampling points per wavelength on that wire is at least 8 and at most 100. The lower bound prevents inaccurate modeling and the upper bound prevents numerical instability, which is caused by the ill-posed nature of the wire equation. However, the formulation of the above restriction is

non-linear, due to the fact that L_m is present in the denominator. Therefore, we will employ the equivalent formulation

$$\frac{2\pi c_0 N}{100\omega} \le L_m \le \frac{2\pi c_0 N}{8\omega} \quad \text{for} \quad m = 1, \ldots, M. \tag{7.12}$$

These inequalities are simple bounds, which are preferred over non-linear inequalities in an optimization solver.

7.1.2   Implicit and explicit physical model

We return to the optimization of the radiated power in the main direction. The optimization problem can be formulated in two different ways. In the first method, which we will call the explicit approach, we regard the matrix equation (7.1) for the currents on the wires as a set of non-linear constraints and only the impedance matrix Z depends on the parameters x_m and L_m. Consequently, the currents are considered as variables that do not depend on the geometrical parameters x_m and L_m. This dependence will enter the problem via the set of constraints, and the currents are explicitly written in the formulation. In this explicit model we write the optimization problem as:

maximize	$S(\{I[m,n]\}, \{x_m\}, \{L_m\}; M, N),$
subject to	$Z \cdot I = V$
	$50\Omega \le R_{in} \le 100 \ \Omega,$
	$x_m \le x_{m+1} - 10a \qquad\qquad\quad$ for $m = 1, \ldots, M-1,$
	$x_2 = 0,$
	$2\pi c_0 N/100\omega \le L_m \le 2\pi c_0 N/8\omega \quad$ for $m = 1, \ldots, M.$

$$\tag{7.13}$$

The notation $S(\{I[m,n]\}, \{x_m\}, \{L_m\}; M, N)$ indicates that the geometrical parameters of the antenna, i.e., x_m and L_m for $m = 1, \ldots, M$, and the current coefficients, i.e., $I[m,n]$ for $m = 1, \ldots, M$ and $n = 1, \ldots, N-1$, are the variables in the optimization process, whereas M and N are fixed. Note that a fixed N corresponds to a restriction of the wire lengths L_m. The above formulation of the optimization problem is a standard approach for finite-element and finite-difference methods.

The second method, called the implicit approach, is to consider the currents on the wires as variables that depend on the geometrical parameters x_m and L_m. In this case, the currents

are only auxiliary variables to compute the functions of interest. Therefore, the currents do not enter the formulation and are only written implicitly. This approach demands that, whenever the geometrical parameters are changed, the currents are recomputed inside the functions for S or R_{in}. The optimization problem is then formulated as:

$$
\begin{array}{|ll|}
\hline
\text{maximize} & S(\{x_m\}, \{L_m\}; \{I[m,n]\}|_{Z \cdot I = V}, M, N), \\
\hline
\text{subject to} & 50 \ \Omega \leq R_{in} \leq 100 \ \Omega, \\
& x_m \leq x_{m+1} - 10a \qquad\qquad \text{for } m = 1, \ldots, M-1, \\
& x_2 = 0, \\
& 2\pi c_0 N/100\omega \leq L_m \leq 2\pi c_0 N/8\omega \qquad \text{for } m = 1, \ldots, M. \\
\hline
\end{array}
\tag{7.14}
$$

The notation $S(\{x_m\}, \{L_m\}; \{I[m,n]\}|_{Z \cdot I = V}, M, N)$ implies that x_m and L_m for $m = 1, \ldots, M$ are the variables in the optimization process. Further, M and N are fixed and the current coefficients $I[m,n]$, for $m = 1, \ldots, M$ and $n = 1, \ldots, N-1$, are determined internally by solving the linear system $Z \cdot I = V$.

The main difference between the two approaches is that, in the explicit case, the solver for the optimization has to be capable of handling large (and possibly sparse) matrices for the Hessian, whereas, in the implicit case, the solver handles only relatively small matrices. Hence, the dimension of the parameter space for the explicit approach is much larger than for the implicit approach, since it also contains the current coefficients. On the other hand, the implicit approach requires solving the numerical model for the currents internally, whereas this step is not present in the explicit approach. Therefore, the implicit approach allows for a straightforward implementation of marching on in anything. Another difference is that, for the implicit approach, we work with a solution of the physical model, i.e., our currents satisfy Eq. (7.1), whereas for the explicit approach the currents do not necessarily satisfy Eq. (7.1) in case constraint violation is allowed.

To see whether it is possible to solve our Yagi-Uda optimization problem, we have considered two test cases: a Yagi-Uda antenna with two wires and a Yagi-Uda antenna with five wires. The remaining parameters of the antenna model are fixed as specified in Table 7.1. The values in this table indicate that we used a frequency of 300 MHz, which corresponds to a wavelength (λ) of 1 meter. As initial estimates for the geometrical parameters of the Yagi-Uda antenna, we used values obtained from [66]. These initial estimates are given in Table 7.2, together with an estimate for the current at the position of the delta-gap source. The estimate for the current was obtained by solving Eq. (7.1) for the initial estimates of

the geometrical parameters of the antenna.

Parameter	Value	Dimension
a	0.001	m
N	32	-
ω/c_0	2π	rad/m
V_g	1	V

Table 7.1: fixed parameters for antenna model.

7.1.3   Optimization algorithms for the explicit approach

The modeling language AMPL [26] has been designed for problems in the form of our explicit approach. The advantage of this language is that it is based on sets and therefore it is very flexible in programming. Another advantage is that it incorporates an automatic differentiation package [31] and therefore the user does not have to supply expressions for the gradient and the Hessian. A third advantage is that at the Network Enabled Optimization System (NEOS) website (www-neos.mcs.anl.gov/neos/) several solvers are available that work with an AMPL interface. These solvers can be used free of charge. A disadvantage of AMPL is that it does not support complex arithmetic and that several numerical facilities, such as Fast Fourier Transformations and matrix decompositions, are not present. Hence, our implicit approach cannot be tested with AMPL.

At the time of our research, six solvers where available on the NEOS website: DONLP2 [63, 64], FILTER [24, 25], LANCELOT [15, 16], LOQO [77], MINOS [48] and SNOPT [27]. Unless stated otherwise, we have used the default versions for all the solvers. Since FILTER was developed by Prof. Fletcher and co-workers, this solver was also available on a local computer at the University of Dundee.

7.1.4   Results for the explicit approach

For the Yagi-Uda problem, three out of the six solvers available provided a converged answer without further tuning of their parameters. The other three gave output messages

Parameter	Value	Dimension
L_1	0.5	m
L_2	0.5	m
L_3	0.4	m
L_4	0.4	m
L_5	0.4	m
x_1	-0.2	m
x_2	0	m
x_3	0.34	m
x_4	0.68	m
x_5	1.02	m
$I[2,16]$	$-0.0057 + j0.0069$	A

Table 7.2: initial estimates for the Yagi-Uda parameters. The parameters with subscripts larger than two apply only to the five-wire Yagi-Uda antenna.

indicating problems with the convergence. We have attempted to tune the parameters for the unsuccessful solvers. However, no improvements have been observed and the final answers were not close to a solution. Therefore, we will only discuss the results of the successful solvers: DONLP2, FILTER and SNOPT. The results of the two-wire problem are given in Table 7.3 and those for the five-wire antenna in Table 7.4. In these tables, we have used the following notations: F is number of Function evaluations, G is the number of Gradient evaluations of the objective function, C is the number of Constraint evaluations, Jac is the number of Jacobian evaluations of the set of constraints, Hes is the number of Hessian evaluations and S_{opt}/S_{ini} is the ratio between the radiated energy found by the solver and the radiated energy of the initial estimate. To compute S_{ini}, we have computed the currents on the wires from Eq. (7.1) with the geometrical parameters from Table 7.2 and we have applied Eq. (7.8).

	F	G	C	Jac	Hes	S_{opt}/S_{ini}
DONLP2	141	50	28667	6232	-	3.88
FILTER	63	89	261	89	143	0.42
SNOPT	21	20	21	20	-	3.88

Table 7.3: algorithmic data from the two-wire Yagi-Uda antenna.

	F	G	C	Jac	Hes	S_{opt}/S_{ini}
DONLP2	357	147	198759	45710	-	6.54
FILTER	147	183	607	183	310	0.29
SNOPT	44	43	44	43	-	6.54

Table 7.4: algorithmic data from the five-wire Yagi-Uda antenna.

	DONLP2	FILTER	SNOPT
L_1	0.480	1.105	0.480
L_2	0.459	1.463	0.459
x_1	-0.214	-0.010	-0.214

Table 7.5: optimized geometrical parameters for the two-wire Yagi-Uda antenna, in meters.

For the results of DONLP2, we have to remark that this solver counts every evaluation of a single constraint, whereas FILTER and SNOPT count only the evaluation of the full set of constraints. This explains why the number of constraint and Jacobian evaluations is relatively high for DONLP2. To compare the results from DONLP2 with the other results, the number of constraint and Jacobian evaluations has to be divided by the number of constraints, i.e., 70 for the two-wire problem and 172 for the five-wire problem, under the assumption that all constraints are evaluated an equal number of times. This is an estimate that holds under most conditions. Further, both DONLP2 and SNOPT use a quasi-Newton estimate of the Hessian matrix, in contrast to FILTER, which uses an exact Hessian. In both tables we see that SNOPT has the best overall performance. We can also see that FILTER found a different and poorer (local) optimum for both problems. Remedies are discussed in the next section. The optimal geometrical dimensions of the two-wire and five-wire antennas are given in Tables 7.5 and 7.6, respectively. Finally, we note that we have not been able to test problems with more than five wires, due to memory constraints on the servers. The most likely cause of this is the use of automatic differentiation in AMPL. To give an idea: the five-wire Yagi-Uda problem required more than 600 MB for FILTER.

	DONLP2	FILTER	SNOPT
L_1	0.479	0.473	0.479
L_2	0.457	1.454	0.457
L_3	0.449	1.126	0.449
L_4	0.446	2.365	0.446
L_5	0.447	0.443	0.447
x_1	-0.335	-0.699	-0.335
x_3	0.372	6.094	0.373
x_4	0.678	6.104	0.680
x_5	1.014	6.723	1.014

Table 7.6: optimized geometrical parameters for the five-wire Yagi-Uda antenna, in meters.

7.1.5   Discussion on local minima in the explicit approach

From Tables 7.3 and 7.4, we see that DONLP2 and SNOPT found the same value for S_{opt}/S_{ini}, whereas FILTER found a value lower than one. This value being lower than one can be explained from the fact that solvers look for a nearby Kuhn-Tucker point [23]. In general, the objective function will have a larger value at this point in comparison with the initial estimate. However, depending on the strategy of handling constraint violation, this property may be destroyed. The question is now whether or not we can force FILTER to find the same or an even better maximum. There are basically three approaches to tackle this problem. First, we can pose extra (linear) constraints on the geometrical parameters of the Yagi-Uda antenna. Second, we can use some of FILTER's parameters to influence the search behavior. Third, we can reformulate the optimization problem or introduce extra non-linear constraints. The third option is not considered here, since the two other solvers already give a better answer than FILTER with the present formulation, and introducing extra non-linear constraints is expensive in computation time.

To examine the first two options, we focus on the five-wire Yagi-Uda antenna. In Figure 7.2 the radiation patterns in the plane $y = 0$ are shown for the Yagi-Uda antenna found by SNOPT and by FILTER, respectively. As regards FILTER, it is clear that the energy is distributed over several lobes in the radiation pattern and therefore the maximum found by FILTER is lower than the one found by SNOPT. The multiple lobes in the radiation pattern

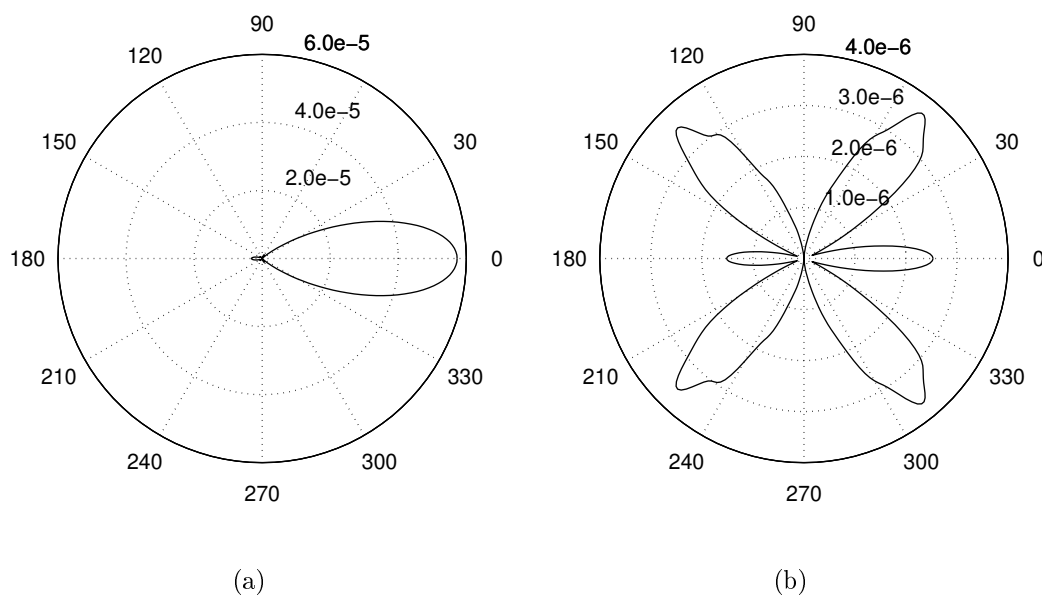(a)   (b)

Figure 7.2: radiation patterns for the Yagi-Uda antenna, on a linear scale. (a) Optimized by SNOPT. (b) Optimized by FILTER.

are due to the lengths of the individual wires in the antenna. Multiple lobes are typically a result of wire lengths longer than $\lambda/2$, which is 0.5 meter in this case. To find out whether a further restriction on the wire lengths gives the same solution for FILTER and SNOPT, we have optimized our Yagi-Uda antenna again with FILTER and SNOPT with the additional constraint that the wires must be shorter than 0.5 meter. SNOPT gave the same solution as before, but again FILTER found a different (and lower) optimum than SNOPT. The resulting radiation pattern for the solution by FILTER is shown in Figure 7.3. For the new solution found by FILTER, the optimum is lower due to radiation in the backward direction. An explanation can be found in the length and position of the reflector: the reflector length is smaller than the driver length and the reflector is positioned at roughly 21 meters from the driver, while in typical Yagi-Uda antennas the reflector is longer than the driver and the distance between reflector and driver is typically in the order of $\lambda/4$, which is 0.25 meter in this case. We could have added two additional constraints to the Yagi-Uda antenna to see if we can find the same optimum with SNOPT and FILTER. However, we have already relied heavily on antenna theory to restrict the problem and in a general antenna optimization problem equivalent antenna knowledge might not be available. Therefore, we continue by examining the second approach, i.e., to use built-in
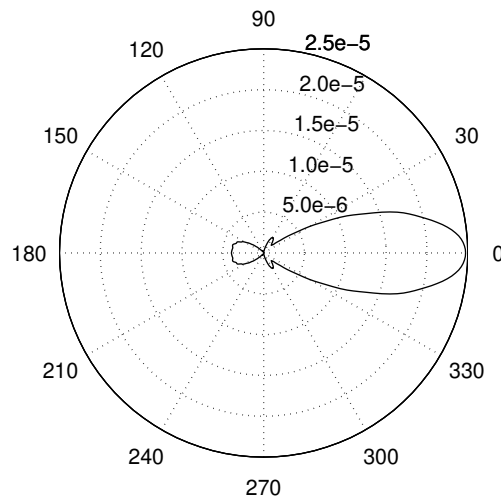
Figure 7.3: radiation pattern for the Yagi-Uda antenna optimized by FILTER solution with restricted wire lengths.

features of FILTER. One of the key features of FILTER is that it allows constraint violation during the search process. In this way it is able to search with a higher efficiency because it can short-cut curved boundaries. However, allowing constraint violation can cause non-local search behavior, i.e., the initial estimate is no longer an indication for the search area. Another way to make this clear is to envisage the entire search domain as consisting of several disconnected areas without constraint violation immersed in areas with constraint violation. Since we regard the initial estimate as a proper starting point for the search process, we would like to control the amount of constraint violation that is acceptable for FILTER.

An indication that we should only allow small constraint violation is that the number of iterations spent on infeasibility (256) is rather high compared to the total number of iterations (353). Infeasibility occurs when the trust region in FILTER becomes too small with respect to the constraint violation [24], i.e., the trust region contains no points without constraint violation in the intermediate quadratic problem. The FILTER user manual [25] hints that the performance of FILTER can possibly be improved by controlling the amount of constraint violation. This can be done by using the parameters `ubd` and `tt`. We have performed several simulations to find the proper value for `ubd` with a fixed value `tt`=10^{-4}. Table 7.7 summarizes the results where the value of S_{opt}/S_{ini} is taken as a criterion to further decrease `ubd` as long as the optimum found by SNOPT is not reached. Table 7.7

ubd	10	1	10^{-1}	10^{-2}
S_{opt}/S_{ini}	0.61	0.65	2.38	6.54
function evaluations	78	109	88	86
gradient evaluations	38	45	29	26
Hessian evaluations	43	50	30	31
constraint evaluations	104	137	90	95
iterations	61	77	58	53
iterations in infeasible NLP	11	11	2	9

Table 7.7: ubd versus objective function value.

shows that FILTER is capable of finding the same optimum as SNOPT by decreasing ubd. Also, the number of evaluations of function, constraints, gradients, and Hessian tends to decrease as well as the number of iterations spent on "infeasible NLP". Since the tuning of parameters requires no additional knowledge of the physical problem, this approach is more satisfactory than posing additional linear constraints on the geometrical parameters.

7.1.6 Algorithms for the implicit approach

The implicit approach is not suitable for the modeling language AMPL, since it has no facilities for matrix decomposition or inversion. Therefore, we have implemented the model in Fortran77. We have programmed the gradient of the objective function and the Jacobian of the set of constraints without automatic differentiation. Also, we have decided not to use an exact Hessian because it is very time consuming to write and error-prone. Therefore, FILTER has been extended with a quasi-Newton estimate of the Hessian and the resulting code is called FILTERQN (FILTER Quasi-Newton).

The constrained-optimization solvers we have used for the implicit approach are: DONLP2 (obtained through netlib), FILTERQN and NPSOL (which is part of the NAG Fortran library as routine E04UCF). We have also used two solvers for unconstrained optimization: L-BFGS-B [83], and BFGS-LS, a BFGS-update routine for the Hessian combined with the line-search algorithm given in [23]. For the unconstrained optimization solvers, the only

non-linear constraint in the problem, i.e., the constraint on the impedance, is handled by adding two penalty functions to the objective function. We use the standard penalty function for inequalities [23]. The new objective function (F_{new}) can now be written as

$$F_{new} = F_{old} + \frac{\Lambda_1}{2} \left(\min\{0, R_{in} - 50\}\right)^2 + \frac{\Lambda_2}{2} \left(\min\{0, 100 - R_{in}\}\right)^2, \qquad (7.15)$$

where F_{old} is the original objective function (S) and $\Lambda_{1,2}$ are the penalty parameters. We start with an initial choice for the penalty parameters (typically 1) and optimize the objective function. After convergence we compute R_{in} and perform two tests:

$$\text{T1}: \quad R_{in} \geq 50 - \epsilon, \qquad (7.16a)$$

$$\text{T2}: \quad R_{in} \leq 100 + \epsilon, \qquad (7.16b)$$

where ϵ is a small positive number (10^{-4}). If test T1 fails, we increase Λ_1 by a factor of ten and start the optimization again with the optimal parameters from the previous step. If test T2 fails, we increase Λ_2 by a factor of ten and return to the optimization process. We continue this process until both T1 and T2 are satisfied.

The linear constraints for the lengths of the wires and their positions can all be rewritten in terms of simple bounds by considering the distances between the wires instead of the position. In this manner we can include the simple bounds in the problem description if we use L-BFGS-B. In case we use BFGS-LS, we cannot include these bounds. This may seem an unfair comparison. However, in the final solutions of the explicit approach, none of these constraints are active.

7.1.7   Results for the implicit approach

The convergence results of the solvers for the two-wire problem are given in Table 7.8 and those for the five-wire problem are given in Table 7.9. In these tables, we have used the same notations as in Section 7.1.4. Again, we note that DONLP2 counts the evaluation of a single constraint or its gradient, whereas FILTERQN and NPSOL count the evaluation of the entire set of constraints or the Jacobian. From the tables, we observe that the implicit approach is more effective in terms of evaluations in comparison with the explicit approach of DONLP2. We also see that the objective values reach the same level as before and that FILTERQN finds the same optimum as the other solvers. For the five-wire problem, FILTERQN performs worse than FILTER in the explicit approach. This is

	F	G	C	Jac	S_{opt}/S_{ini}
DONLP2	19	14	297	9	3.88
FILTERQN	21	14	21	14	3.88
NPSOL	12	12	12	12	3.88
BFGS-LS	85	83	-	-	3.88
L-BFGS-B	118	118	-	-	3.88

Table 7.8: algorithmic data from the two-wire Yagi-Uda antenna with the implicit physical model.

	F	G	C	Jac	S_{opt}/S_{ini}
DONLP2	64	44	1688	42	6.54
FILTERQN	240	152	240	152	6.54
NPSOL	100	100	100	100	6.48
BFGS-LS	432	426	-	-	6.48
L-BFGS-B	395	395	-	-	6.54

Table 7.9: algorithmic data from the five-wire Yagi-Uda antenna with the implicit physical model.

most probably caused by the absence of a second-order correction step [23] and an inexact Hessian in FILTERQN. However, for the two-wire problem, FILTERQN performs better than FILTER. Further, we note that the penalty parameter approach is not very effective compared to the constrained-optimization methods.

For the five-wire problem, we observe that the solvers NPSOL and BFGS-LS find a slightly poorer local optimum than the other solvers. The optimized geometrical parameters for the five-wire problem, obtained from DONLP2 and NPSOL, are summarized in Table 7.10. The parameters from DONLP2 are almost identical to the results for the explicit approach in Table 7.6. However, the results from NPSOL are somewhat different, although the optimized values are still close to the initial estimates. Hence, we have probably found another local optimum, although it does not deviate too much from the other optimum. Finally, we mention that we did not encounter any memory problems: the five-wire problem required approximately 424 kB.

	DONLP2	NPSOL
L_1	0.479	0.482
L_2	0.457	0.475
L_3	0.449	0.457
L_4	0.446	0.447
L_5	0.447	0.449
x_1	-0.335	-0.237
x_3	0.373	0.192
x_4	0.680	0.475
x_5	1.014	0.768

Table 7.10: optimized geometrical parameters for the five-wire Yagi-Uda antenna, in meters, for the solvers DONLP2 and NPSOL.

7.1.8   Conclusions for the Yagi-Uda optimization

The problem formulation with the implicit physical model seems more effective and efficient than the problem formulation with the explicit physical model. For the approach with the explicit physical model we find several local maxima, which differ quite a lot from the best maximum and some of the geometrical parameters have unusual values. For the approach with the implicit physical model we find only one maximum for the two-wire problem and two maxima for the five-wire problem. The two maxima for the five-wire problem do not differ too much and the geometrical parameters for the poorer maximum are still close to the initial values. The best maxima of the implicit approach correspond to the best maxima of the explicit approach. These observations seem to indicate a more local search behavior in case of the formulation with the implicit physical model. Also, there seems to be no advantage of an exact Hessian over a quasi-Newton Hessian in the explicit approach for this particular problem. For FILTER, we have tuned the parameters for constraint violation, and we have shown the effect of this tuning on the solution. For similar optimization problems, it seams worthwhile to tune these parameters before optimizing the full problem, or, alternatively, to optimize the problem for several settings of the parameters that control the constraint violation. Further, the penalty-parameter approach is less effective than the constrained-optimization approach. Finally, we observe that additional linear constraints lead to more local search behavior, but they also require more theoretical knowledge.

7.2   Array of thin wires

From the Yagi-Uda antenna, it is a small step to consider wire-antenna arrays, which form the second class of test problems. We consider an array of M identical parallel dipoles with fixed position and length. Wire m is excited by a delta-gap source with complex voltage V_g^m. We will address the optimization of the phases and amplitudes of the delta-gap sources. In a practical design situation, it frequently occurs that the feeding network and the array of antennas are designed separately. Therefore, our design problem considers the case where the design of the array of antennas has been finished and we are left with the design of an appropriate feeding network.

We will assume that the central axes of all wires lie in the plane $y = 0$ and that the center of the m-th wire is $\boldsymbol{r}_m = x_m \boldsymbol{u}_x + z_m \boldsymbol{u}_z$. The design objective is either an optimal directivity in the main direction or an optimal sidelobe level, possibly subject to constraints. Again, we denote the linear system of Eq. (4.27) by

$$Z \cdot I = V. \tag{7.17}$$

The electric field in the far-field region is given by

$$E_\theta(\theta, \phi) = j\omega\mu_0 \sin(\theta) \frac{\exp(-j\omega R/c_0)}{2\pi R} \sum_{m=1}^{M} \sum_{n=1}^{N-1} I_m[m,n] F(m,n,\theta,\phi), \tag{7.18}$$

where R is the distance between the center of the antenna and observation point and

$$F(m,n,\theta,\phi) = \exp\left\{j\omega[x_m p + z_{m,n} q]/c_0\right\} \frac{1 - \cos(\omega q \Delta_m/c_0)}{(\Delta_m \omega^2 q^2/c_0^2)}, \tag{7.19a}$$

$$z_{m,n} = z_m - L_m/2 + n\Delta_m, \tag{7.19b}$$

$$p = \cos(\phi)\sin(\theta), \tag{7.19c}$$

$$q = \cos(\theta), \tag{7.19d}$$

$$\Delta_m = L_m/N. \tag{7.19e}$$

The time-averaged radiated power per solid angle in the direction (θ, ϕ) can be expressed in terms of the electric field in the far-field region as

$$S(\theta, \phi) = \frac{R^2 |E_\theta(\theta, \phi)|^2}{2Z_0}. \tag{7.20}$$

The time-averaged total power radiated by the array can be approximated as

$$P_t = \frac{1}{2}\mathrm{Re}\left\{\sum_{m=1}^{M} V_g^m I_m^*(z_m)\right\}. \tag{7.21}$$

We can now define the directivity D of the antenna as

$$D(\theta, \phi) = \frac{4\pi S(\theta, \phi)}{P_t}, \tag{7.22}$$

and the sidelobe level (SLL) as

$$SLL = \min_{(\theta, \phi) \notin \text{main lobe}} |D(90°, 90°) - D(\theta, \phi)| . \tag{7.23}$$

For the optimization considered here, we regard the sidelobe level as the minimum of a discrete set of preselected points, instead of the minimum of the continuous set. We denote the K preselected points by (θ_k, ϕ_k), $k = 1, \ldots, K$. Hence, we can write

$$SLL = \min_{k=1,\ldots,K} |D(90°, 90°) - D(\theta_k, \phi_k)| . \tag{7.24}$$

We now turn our attention to the formulation of the optimization problems for the directivity and the sidelobe level. First, we consider the matrix equation (7.17) as a set of equality constraints. Unfortunately, we have to separate the real and imaginary parts of the system and enforce them separately, since all solvers for constrained optimization accept real arithmetic only. Further, we pose additional constraints with respect to the amplitude of the delta-gap sources to prevent ambiguity, and constraints for symmetry on the excitation voltages, if needed. For the optimization of the directivity in the main direction we arrive at

maximize	$D(90°, 90°)$,
subject to	$Z \cdot I = V$,
	$-1 \leq \text{Re}\{V_g^m\} \leq 1 \quad m = 1, \ldots, M,$
	$-1 \leq \text{Im}\{V_g^m\} \leq 1 \quad m = 1, \ldots, M,$
	$V_g^m = V_g^{M+1-m} \qquad m = 1, \ldots, \lfloor M/2 \rfloor \quad \text{(symmetry)},$

$$\tag{7.25}$$

where the symmetry condition is optional. For the optimization of the sidelobe level, we could have used the same formulation. However, this leads to a minimax problem, since we would like to maximize the sidelobe level, which in turn is given by a minimum. We will proceed in a different manner. We introduce a slack variable y [23]:

$$y = \min_{k=1,\ldots,K} |D(90°, 90°) - D(\theta_k, \phi_k)| . \tag{7.26}$$

Then we have

$$D(90°, 90°) - y \geq D(\theta_k, \phi_k) \quad \text{for } k = 1, \ldots, K, \tag{7.27}$$

since the directivity in the main direction, i.e., $D(90°, 90°)$, should always be higher than the directivity outside the main lobe and the difference should be at least as large as the sidelobe level.

Finally, we introduce a minimum level of directivity (D_{min}) in the main direction and optional symmetry conditions. We arrive at the following optimization problem:

maximize	$y,$	
subject to	$Z \cdot I = V,$	
	$D(90°, 90°) - y \geq D(\theta_k, \phi_k)$	$k = 1, \ldots, K,$
	$D(90°, 90°) \geq D_{min},$	
	$-1 \leq \mathrm{Re}\{V_g^m\} \leq 1$	$m = 1, \ldots, M,$
	$-1 \leq \mathrm{Im}\{V_g^m\} \leq 1$	$m = 1, \ldots, M,$
	$V_g^m = V_g^{M+1-m}$	$m = 1, \ldots, \lfloor M/2 \rfloor$ (symmetry).

$$(7.28)$$

7.2.1   Results for the wire array

The optimization problems have been implemented in the programming language AMPL [26] and we have used the optimization tool FILTER [24] to solve the optimization problems for the directivity and the sidelobe level. We have optimized several arrays with various layouts. In all cases we started with an equal excitation of all dipoles. We will illustrate our results by two examples: one to optimize directivity, and one to optimize the sidelobe level. First, we discuss the optimization of the directivity of a planar 5×4 array of dipoles with distance $\lambda/4$ in the x-direction and $\lambda/2$ in the z-direction. The dipoles have a length of 0.45λ. The radius of the circular cross-section of each wire was 0.001λ. The planar array has been depicted in Figure 7.4. The radiation pattern in the plane $z = 0$ before (*coupled uniform*) and after (*coupled optimized*) optimization is shown in Figure 7.5. This figure also includes the radiation pattern for equal amplitude sources when the coupling *between* the wires in not taken into account (*uncoupled uniform*). In all cases we have computed the currents on the wires and the radiated energy with the same numerical method. The results illustrate that the directivity can only be improved by 0.9 dB. Also, the directivity estimate obtained for the case without mutual coupling is too optimistic with respect to the optimized feeding network. This example indicates once more that mutual coupling should be taken into account in array designs.
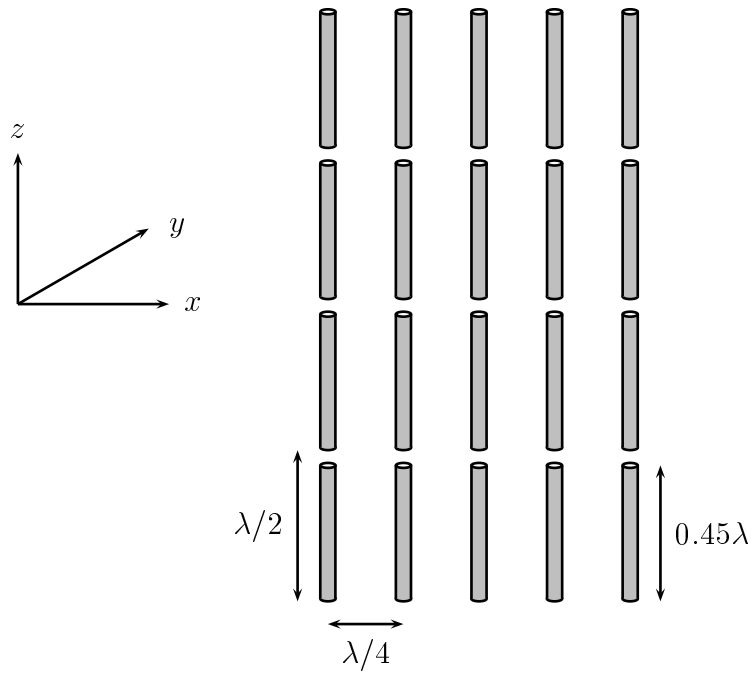
Figure 7.4: 5×4 planar array.
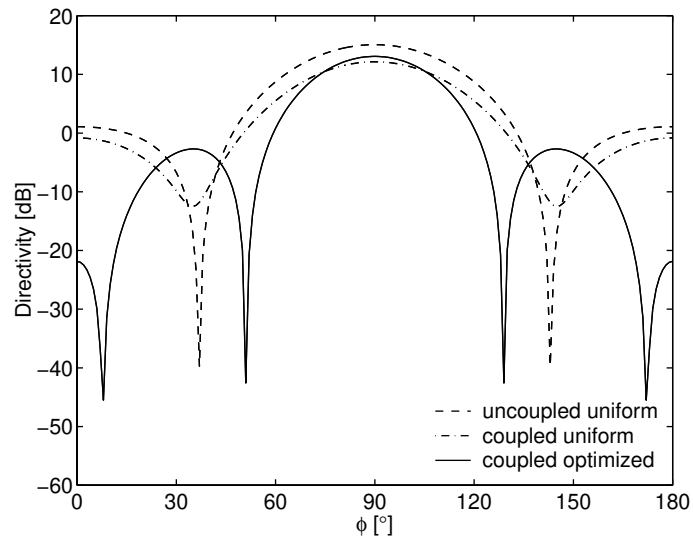
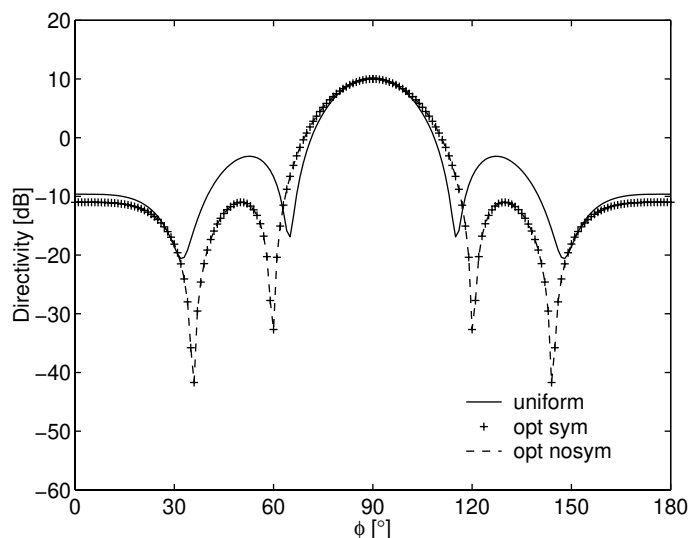Figure 7.5: optimized directivity of a 5×4 planar array.

Figure 7.6: optimized sidelobe level of a five-element linear array. The solid line represents the radiation pattern for uniform excitation, + indicates the pattern after optimization with symmetry constraints and the dashed line is the pattern after optimization without symmetry constraints.

The second example is a linear array of five elements with a spacing of $\lambda/2$. The dipoles have a length of $\lambda/2$ and a circular cross-section with radius $a = 0.001\lambda$. The objective is to reduce the sidelobe level in the plane $z = 0$ and to maintain a minimum gain of 10 dB. We have examined the cases with and without symmetry constraints on the excitation voltages. The radiation patterns in the plane $z = 0$ are presented in Figure 7.6. The performance of the initial excitation of the array is indicated by *uniform*, the optimized array with symmetry constraints on the excitation is indicated by *opt sym* and the array without symmetry constraints on the excitation is indicated by *opt nosym*. For the preselected points outside the main lobe we have chosen $\theta_k = 90°$, for all k. In case we have applied symmetry constraints on the excitation voltages, we have chosen $\phi_k \in \{0, 10, 20, 30, 40, 50, 55, 60\}°$, i.e., $K = 8$. For the case without symmetry constraints, we have used $\phi_k \in \{0, 10, 20, 30, 40, 50, 55, 60, 120, 125, 130, 140, 150, 160, 170, 180\}°$, i.e., $K = 16$. From Figure 7.6, we observe that the cases with and without symmetry constraints give the same result, which indicates that the (non-linear) constraints on the sidelobe level for $\phi > 90°$ can be exchanged for the simple bounds on the excitations. The simple bounds are easier to deal with and much cheaper to evaluate in comparison with the non-linear constraints. We note that, in contrast with the Yagi-Uda optimization, we

did not encounter any trouble in solving these optimization problems. Also, other solvers gave the same results and therefore we expect that we have no problems associated with local maxima and constraint violation. Further, the memory requirements were low, owing to the fact that only the right-hand side of Eq. (7.17) contains design parameters. This confirms the conjecture that the automatic differentiation has caused the excessive memory requirement in case of the Yagi-Uda problem.

Chapter 8

Conclusions and recommendations

At present, the toolbox of designers in electromagnetic engineering contains experiments and numerical simulation tools. With these tools, the designer constructs a blueprint of the design together with a set of parameters, which are, for instance, related to the geometry or the excitation of the design. After the construction of the blueprint, the aim of the design process is to establish proper values for these parameters. The proper values are related to design criteria, which are usually related to directing energy in a certain direction, and criteria for manufacturing. Often, numerical tools are available to compute characteristics of a design for a fixed parameter setting only. However, a large part of the design process consists of finding the proper parameter setting, i.e., fixing values for the parameters, mainly by means of parameter sweeps. Therefore, it would be a major improvement if these sweeps could be dealt with efficiently. In this thesis, we have aimed at the extension of the numerical simulation tools by suggesting "marching on in anything" for efficient parameter sweeps. In particular, we have demonstrated the efficiency of marching on in anything for three types of scattering problems, viz., a straight thin wire, a perfectly conducting flat plate, and a dielectric object, all in free space. Further, we have initiated a study to design antennas by a class of non-linear optimization strategies. With these strategies, the above mentioned parameter values can be found, after the formulation of a proper objective function, which represents the design criteria and criteria for manufacturing. Within the context of electromagnetic engineering, the formulation of a realistic objective function for a practical design remains a challenge. We have started from the simplest case of wire antennas, for which abundant literature is available, to determine the most promising approach for more complicated cases. This approach is based on sequential quadratic

programming in a low-dimensional parameter space, where the physical model is kept outside the optimization problem. Another advantage of this approach is its compatibility with marching on in anything, i.e., the optimization approach and marching on in anything can be combined in a straightforward manner to arrive at an efficient search procedure for appropriate parameter values.

Before we can apply an optimization strategy to a design problem, a number of steps have to be taken. First, we have to find a model, which is sufficiently simple with respect to computer resources, and we have to find a mathematical formulation for the electromagnetic behavior of the blueprint. Then, we have to construct a numerical method, which has a sufficiently flexible discretization with respect to parameter variations, to find an approximation of the solution of this mathematical formulation. Ideally, it would be useful to have some idea about the reliability and the accuracy of this approximation. For certain types of non-linear optimizers, e.g., genetic algorithms, these steps are sufficient to start the optimization process. However, more efficient solvers also employ gradients. These gradients consist of the first derivatives of the above mentioned objective function with respect to all design parameters. The computation of these gradients also requires a mathematical formulation and a numerical method. Although the computation of a gradient requires extra effort and computation time, the total computation time of the optimization process is usually reduced drastically as compared to optimization with genetic algorithms, due to the increased efficiency of the gradient-based solver. Therefore, it is recommended to compute the gradient.

For the straight thin wire, we have formulated two integral equations, which are known as the integral equation with exact kernel and the integral equation with reduced kernel, to describe the interaction between the current on the wire and the incident electric field. For the infinitely long straight thin wire, we have shown that both integral equations are exact with respect to the total current in the axial direction. For the finite straight thin wire, we have shown that there is a conditional equivalence between both formulations, which has enabled us to show uniqueness and conditional existence of the solution for the integral equation with reduced kernel, based on results for the integral equation with exact kernel. Further, we have shown that the integral equation with reduced kernel is severely ill-posed for all standard Lebesgue and Sobolev spaces. Subsequently, we have developed two numerical schemes for the integral equation with reduced kernel. The ill-posed nature of the integral equation with reduced kernel has been illustrated by erratic results for the current on the wire and rapidly increasing condition numbers of the numerical system

for increasingly finer discretizations. We have demonstrated regularization and filtering methods to improve the condition number of the numerical system and the approximation of the current.

For the perfectly conducting flat rectangular plate, we have formulated the standard electric-field integral equation (EFIE), which relates the surface current density on the plate to the incident electric field. From this equation, we have derived a Hallén-type equation, which was inspired by the Hallén equation for straight wires. The merit of this equation is that the spatial derivatives on the vector potential have been removed, at the expense of additional boundary terms. We have constructed a numerical method for the Hallén-type equation. Also, we have derived a numerical method, based on piecewise-sinusoidal testing function, for the EFIE, and we have shown that the resulting scheme can be obtained from the discretized Hallén-type equation as well. We have solved both numerical systems by the CGFFT method, which is a combination of the conjugate-gradient method and the Fast Fourier Transformation. Numerical tests show that the conjugate-gradient method converges much faster for the system with piecewise-sinusoidal testing functions than for the discretized Hallén-type equation, due to the presence of the extra boundary terms in the latter. Further, the method with piecewise-sinusoidal testing functions is much more flexible with respect to the geometries it can handle, since the testing functions have only local support. Hence, it is advantageous to use the numerical scheme with piecewise-sinusoidal testing functions. This conclusion is underlined by results from the literature, which characterize proper testing functions for the EFIE.

For the dielectric object, we have derived three different integro-differential equations, which relate the contrast-current density to the incident electric field. We have analyzed one of these equations in detail and we have established conditions for well-posedness. Also, we have noted that all three integro-differential equations are equivalent and well-posed under the same conditions for the permittivity function of the object. From a theoretical point of view, although not experimentally validated, present numerical schemes can be improved by employing different testing functions.

With respect to the gradient that can be used in an optimization tool, we note that we have not encountered any difficulty in computing the gradient with respect to lengths and distances for an array of parallel wires. However, for the flat plate, the formulation of the derivative with respect to the length of the plate was intricate, due to the presence of singularities in the surface current density. We have carefully formulated and

discretized an integro-differential equation for this derivative. Further, we have examined two finite-difference approximations for this derivative. We have shown that one of these approximations yields a reliable estimate for the derivative. Generally, a gradient also provides information on the sensitivity of the design with respect to small parameter changes, which are due to, e.g., manufacturing tolerances.

As regards marching on in anything, we have proposed a simple theory based on differentiability and boundedness of the linear operators and the excitation vectors involved, to explain the success of this strategy. In particular, marching on in anything is a way to construct an approximate solution for a numerical system, within the context of the conjugate-gradient method, from a linear combination of preceding simulation results with nearby parameter values. We have shown that the efficiency of this strategy is influenced by the residual error of the conjugate-gradient method and the step size of the parameter variation. Also, the number of preceding simulation results that is taken into account in the construction of the initial estimate affects the convergence. It turns out that for a large class of parameter variations, we should take into account two or three preceding results and we recommend that one experiments a little before engaging in large parameter sweeps. For standard numerical schemes for the straight thin wire, the perfectly conducting flat plate, and the dielectric object, we have shown that marching on in anything improves the efficiency of the conjugate-gradient method dramatically for parameters sweeps with respect to frequency, angle of incidence, and length.

For the flat plate and the array of thin wires, we have completed the steps to employ a non-linear optimization solver. For the array of thin wires, we have formulated a number of practical design problems, in terms of energy-related objective functions and a set of constraints. We have optimized a Yagi-Uda antenna, while testing several non-linear optimization strategies. Also, we have examined how to remedy that a solver finds a local optimum. We conclude that it is advantageous to tune the parameters of the solvers a number of times for each problem and to examine the final solutions. In particular, optimization solvers based on sequential quadratic programming have been highly successful. We have also optimized the amplitudes and phases of the sources of an array antenna, with respect to maximum gain or maximum sidelobe level. For the flat plate, we have not performed any optimization, since a flat rectangular plate by itself, or a plate with a fixed shape, does not give rise to an interesting design problem. The simplest step towards a design problem with a flat plate would be to add a dielectric layer and a ground plane with a coaxial feed to the configuration, to model a single patch antenna. Alternatively,

one could consider an infinite periodic arrangement of flat plates together with a number of dielectric layers to form a frequency-selective surface or an array of patch antennas.

With the results summarized above, we have available the key elements to explore the concept of "electromagnetic engineering", i.e., we have efficient numerical methods together with a characterization of their approximation properties, efficient parameter variation, gradient computation, and optimization. However, before we can tackle a realistic design problem, a few extra hurdles have to taken. First of all, a more realistic environment should be taken into account instead of free space. At the same time, we would like to be able to change part of a complicated geometry without repeating expensive field computations for the entire configuration. This can for example be achieved by an embedding approach [74]. In this technique, the complex environment is taken into account via scattering operators, whereas the benefits of an efficient matrix-vector product by means of Fast Fourier Transformations are preserved in the modeling of the object. Further, the mesh of the object under study in CGFFT algorithms is rather rigid. More flexibility in the mesh can be obtained by applying fast multipole methods [13] or the "adaptive integral method" [8], which still give rise to efficient matrix-vector products. Finally, electromagnetic engineering would benefit from a study with respect to the formulation of non-linear optimization problems for realistic design criteria together with a characterization of local optima that arise in these problems. This type of research can for example benefit from methodologies that are applied in circuit theory, where optimization strategies have a longstanding reputation, see e.g. [68]. The results of such a study would enable the application of non-linear optimizers in a much earlier stage of the design process. At present, a number of papers in this direction have appeared or will appear in the near future, see e.g. [20] and references therein.

Appendix A

Surface current and charge densities

A.1 Notion of a surface vector field

Consider an orientable surface $\mathcal{S}$ with continuously differentiable unit normal $\boldsymbol{n}$, parameterized in a Cartesian reference system as

$$\boldsymbol{r}(\xi, \eta) = x(\xi, \eta)\boldsymbol{u}_x + y(\xi, \eta)\boldsymbol{u}_y + z(\xi, \eta)\boldsymbol{u}_z, \tag{A.1}$$

where $(\xi, \eta) \in \mathcal{G}$ and $\mathcal{G}$ is a compact area in $\mathbb{R}^2$. Hence, each point on the surface is related to a unique pair (ξ, η). The parametrization for the normal is given by $\boldsymbol{n}(\xi, \eta)$. We introduce a family of parallel surfaces $\mathcal{S}_h$

$$\mathcal{S}_h = \left\{ \boldsymbol{r} \mid \boldsymbol{r} = \boldsymbol{r}(\xi, \eta) + h\boldsymbol{n}(\xi, \eta), (\xi, \eta) \in \mathcal{G} \right\}, \tag{A.2}$$

for $h \in [-h_0, h_0]$. Hence, we have $\mathcal{S} = \mathcal{S}_0$. The fact that $\mathcal{S}$ has a continuously differentiable normal guarantees the existence of a positive h_0, for which the surfaces $\mathcal{S}_h$ do not intersect. The set of all parallel surfaces $\mathcal{S}_h$ gives rise to a finite volume $\mathcal{V}_{h_0}$ that can be parameterized as $\boldsymbol{r}(\xi, \eta, h)$, for $(\xi, \eta) \in \mathcal{G}$ and $h \in [-h_0, h_0]$. In this volume, the mapping $(\xi, \eta, h) \rightarrow \boldsymbol{r}(\xi, \eta, h)$ is invertible.

Suppose that a continuously differentiable tangential vector field $\boldsymbol{v}_S(\xi, \eta)$ is defined on $\mathcal{S}$, i.e., $\boldsymbol{v}_S \cdot \boldsymbol{n} = 0$. Then we extend the vector field $\boldsymbol{v}_S$ to a vector field $\boldsymbol{v}$ on the volume $\mathcal{V}_{h_0}$ as

$$\boldsymbol{v}(\boldsymbol{r}(\xi, \eta, h)) = \delta_\varepsilon(h)\boldsymbol{v}_S(\xi, \eta), \tag{A.3}$$

where $\delta_\varepsilon(h)$ is a real-valued C_0^∞ function with support $[-\varepsilon, \varepsilon]$, $0 < \varepsilon < h_0$ and

$$\int\limits_{-\varepsilon}^{\varepsilon} \delta_\varepsilon(h)dh = 1. \tag{A.4}$$

The above vector field $\boldsymbol{v}$ is called an extension of $\boldsymbol{v}_S$ from $\mathcal{S}$ to $\mathcal{V}_{h_0}$.

For any continuous function $f(\boldsymbol{r})$, we consider the limiting process

$$\lim_{\varepsilon\downarrow 0} \iiint\limits_{\mathcal{V}_{h_0}} f(\boldsymbol{r})\boldsymbol{v}(\boldsymbol{r})dV$$

$$= \lim_{\varepsilon\downarrow 0} \iint\limits_{(\xi,\eta)\in\mathcal{G}} \left(\int\limits_{-\varepsilon}^{\varepsilon} f(\boldsymbol{r}(\xi,\eta,h))\delta_\varepsilon(h)dh \right) \boldsymbol{v}_S(\xi,\eta) \left|\mathrm{J}(\xi,\eta)\right| d\xi d\eta \tag{A.5}$$

$$= \iint\limits_{(\xi,\eta)\in\mathcal{G}} f(\boldsymbol{r}(\xi,\eta,0))\boldsymbol{v}_S(\xi,\eta) \left|\mathrm{J}(\xi,\eta)\right| d\xi d\eta = \iint\limits_{\mathcal{S}} f(\boldsymbol{r})\boldsymbol{v}_S(\boldsymbol{r})dA,$$

where $\left|\mathrm{J}(\xi,\eta)\right|$ denotes the Jacobian on $\mathcal{S}$. Hence, the limiting process reduces the volume integral over $\mathcal{V}_{h_0}$ to a surface integral over $\mathcal{S}$. This observation has led to the notation

$$\lim_{\varepsilon\downarrow 0} \boldsymbol{v}_S\delta_\varepsilon(h) = \boldsymbol{v}_S(\boldsymbol{r})\delta_\mathcal{S}(\boldsymbol{n}). \tag{A.6}$$

A.2   Surface divergence

The extension of a vector field defined on a surface to a vector field defined on a volume also brings up the question what happens to operations on these vector fields. For our purposes, the divergence operator is the most interesting and we will derive Gauss's theorem on a surface.

Let $\mathcal{C}$ be a Jordan curve on the surface $\mathcal{S}$ and let $\boldsymbol{u}_\tau$ be the tangential unit vector along $\mathcal{C}$, such that $\boldsymbol{u}_\tau$ gives rise to a positive orientation of $\mathcal{C}$ with respect to the normal $\boldsymbol{n}$ on $\mathcal{S}$. We define the vector $\boldsymbol{u}_\nu = \boldsymbol{u}_\tau \times \boldsymbol{n}$, which is the outward-pointing unit normal on $\mathcal{C}$, tangential to $\mathcal{S}$. In the same way as for $\mathcal{S}_h$, we can define a family of parallel curves $\mathcal{C}_h$ with outward-pointing unit normal $\boldsymbol{u}_\nu$, which is independent of h and tangential to $\mathcal{S}_h$. Hence, $\mathcal{C} = \mathcal{C}_0$.

Let $\boldsymbol{v}_S$ be the continuously differentiable vector field on $\mathcal{S}$ with corresponding extension $\boldsymbol{v}$, as defined in the preceding section. Then, we can apply the three-dimensional version of Gauss's theorem to the volume $\mathcal{V}_\mathcal{C}$ in $\mathcal{V}_{h_0}$, bounded by the family of curves $\mathcal{C}_h$ and the surfaces $\mathcal{S}_{-\varepsilon}$ and $\mathcal{S}_\varepsilon$. Owing to the fact that $\boldsymbol{v}_S \cdot \boldsymbol{n} = 0$, the surfaces $\mathcal{S}_{-\varepsilon}$ and $\mathcal{S}_\varepsilon$ do not contribute to the surface integral in Gauss' theorem. Hence, we have

$$\iiint_{\mathcal{V}_\mathcal{C}} \nabla \cdot \boldsymbol{v}(\boldsymbol{r})dV = \int_{-\varepsilon}^{\varepsilon} \delta_\varepsilon(h)dh \int_\mathcal{C} \boldsymbol{v}_S \cdot \boldsymbol{u}_\nu d\ell = \oint_\mathcal{C} \boldsymbol{v}_S \cdot \boldsymbol{u}_\nu d\ell, \tag{A.7}$$

owing to the definition of $\delta_\varepsilon(h)$. The resulting expression is independent of the choice of $\delta_\varepsilon(h)$ and the parametrization of $\mathcal{S}$.

If the parametrization of the surface $\mathcal{S}$ is such that $\{\partial_\xi \boldsymbol{r}, \partial_\eta \boldsymbol{r}, \boldsymbol{n}\}$ forms a (curvilinear) right-handed, orthogonal coordinate system in $\mathcal{V}_{h_0}$, then we can employ the well-known identities for the divergence operator in three dimensions, to work out the left-hand side of Eq. (A.7). We define the quantities

$$h_\xi = \|\partial_\xi \boldsymbol{r}(\xi, \eta)\|, \tag{A.8a}$$

$$h_\eta = \|\partial_\eta \boldsymbol{r}(\xi, \eta)\|, \tag{A.8b}$$

$$\boldsymbol{u}_\xi = \frac{1}{h_\xi}\partial_\xi \boldsymbol{r}(\xi, \eta), \tag{A.8c}$$

$$\boldsymbol{u}_\eta = \frac{1}{h_\eta}\partial_\eta \boldsymbol{r}(\xi, \eta), \tag{A.8d}$$

$$v_{S,\xi} = \boldsymbol{v}_S \cdot \boldsymbol{u}_\xi, \tag{A.8e}$$

$$v_{S,\eta} = \boldsymbol{v}_S \cdot \boldsymbol{u}_\eta, \tag{A.8f}$$

and, after integration in the direction of the normal $\boldsymbol{n} = \boldsymbol{u}_\xi \times \boldsymbol{u}_\eta$, we obtain

$$\iiint_{\mathcal{V}_\mathcal{C}} \nabla \cdot \boldsymbol{v}(\boldsymbol{r})dV =$$
$$\iint_{(\xi,\eta)\in\mathcal{G}} \frac{1}{h_\xi h_\eta} \left\{ \partial_\xi \left[h_\eta v_{S,\xi}(\boldsymbol{r}(\xi, \eta)) \right] + \partial_\eta \left[h_\xi v_{S,\eta}(\boldsymbol{r}(\xi, \eta)) \right] \right\} |J(\xi, \eta)| \, d\xi d\eta. \tag{A.9}$$

Therefore, we define the surface divergence on $\boldsymbol{v}_S$ in the above right-handed orthogonal coordinate system as

$$\nabla_s \cdot \boldsymbol{v}_S = \frac{1}{h_\xi h_\eta} \left\{ \partial_\xi \left[h_\eta v_{S,\xi}(\boldsymbol{r}(\xi, \eta)) \right] + \partial_\eta \left[h_\xi v_{S,\eta}(\boldsymbol{r}(\xi, \eta)) \right] \right\}. \tag{A.10}$$

For the plane with constant z-coordinate, the surface divergence in Cartesian coordinates is given by

$$\nabla_s \cdot \boldsymbol{v}_S = \partial_x v_{S,x} + \partial_y v_{S,y}, \tag{A.11}$$

as expected. On the mantle of a circular cylinder with radius a, the surface divergence is

$$\nabla_s \cdot \boldsymbol{v}_S = \frac{1}{a}\partial_\phi v_{S,\phi} + \partial_z v_{S,z}. \tag{A.12}$$

The definition of the surface divergence in Eq. (A.10) is coordinate dependent. A coordinate-independent definition is obtained in the following way [14, 47]. Let $\mathcal{S}$ be an orientable surface with continuously differentiable normal, and let $\{\mathcal{C}_{,n}\}$ be a sequence of Jordan curves on $\mathcal{S}$. Let the sequence $\{\Sigma_{,n}\}$ of enclosed surfaces on $\mathcal{S}$ by $\mathcal{C}_{,n}$ converge to the point $\boldsymbol{r}$ on $\mathcal{S}$, in the sense that for every $\varepsilon > 0$ there exists an $N(\varepsilon) \in \mathbb{N}$ such that for all $n \geq N(\varepsilon)$ the subset $\Sigma_{,n}$ is contained in the sphere with radius ε and center $\boldsymbol{r}$. Let the surface area of $\Sigma_{,n}$ be denoted by $\sigma(\Sigma_{,n})$. Then we define the surface divergence as

$$\nabla_s \cdot \boldsymbol{v}_S = \lim_{n\to\infty} \frac{1}{\sigma(\Sigma_{,n})} \oint_{\mathcal{C}_{,n}} \boldsymbol{v}_S \cdot \boldsymbol{u}_\nu d\ell. \tag{A.13}$$

A.3 Conservation of surface charge

The introduction of the surface divergence allows us to derive the law of conservation of surface charge. From Eq. (2.13b), we observe that a surface current density $\boldsymbol{J}_S$ corresponds to a jump in the tangential magnetic field. We define a continuously differentiable surface $\mathcal{S}$ at the jump in the magnetic field. As in Section A.1, we can define a family of surfaces parallel to $\mathcal{S}$, which together give rise to the volume $\mathcal{V}_{h_0}$. We divide this volume into two parts:

$$\mathcal{V}_{h_0}^+ = \{\boldsymbol{r} \mid \boldsymbol{r} = \boldsymbol{r}(\xi,\eta) + h\boldsymbol{n}(\xi,\eta), (\xi,\eta) \in \mathcal{G}, 0 < h \leq h_0\}, \tag{A.14a}$$

$$\mathcal{V}_{h_0}^- = \{\boldsymbol{r} \mid \boldsymbol{r} = \boldsymbol{r}(\xi,\eta) + h\boldsymbol{n}(\xi,\eta), (\xi,\eta) \in \mathcal{G}, -h_0 \leq h < 0\}. \tag{A.14b}$$

In both volumes $\mathcal{V}_{h_0}^+$ and $\mathcal{V}_{h_0}^-$, we can apply Stokes's theorem to a Jordan curve $\mathcal{C}_h$ on the surface $\mathcal{S}_h$ with $\boldsymbol{u}_\nu$ the outward-pointing unit normal on $\mathcal{C}_h$, which is tangential to $\mathcal{S}_h$, as defined in Section A.2. Further, the surface enclosed by $\mathcal{C}_h$ on $\mathcal{S}_h$ is denoted by $\mathcal{S}_{\mathcal{C},h}$. For a continuously differentiable vector field $\boldsymbol{v}$ in $\mathcal{V}_{h_0}^+$ or $\mathcal{V}_{h_0}^-$ we obtain

$$\iint_{\mathcal{S}_{\mathcal{C},h}} (\nabla \times \boldsymbol{v}) \cdot \boldsymbol{n}\,dA = \oint_{\mathcal{C}_h} \boldsymbol{v} \cdot \boldsymbol{u}_\tau d\ell = \oint_{\mathcal{C}_h} -(\boldsymbol{n} \times \boldsymbol{v}) \cdot \boldsymbol{u}_\nu d\ell = \iint_{\mathcal{S}_{\mathcal{C},h}} -\nabla_s \cdot (\boldsymbol{n} \times \boldsymbol{v})\,dA. \tag{A.15}$$

Hence, on the surface $\mathcal{S}_{\mathcal{C},h}$, we have the identity

$$\nabla_s \cdot (\boldsymbol{n} \times \boldsymbol{v}) = -\boldsymbol{n} \cdot \nabla \times \boldsymbol{v}, \tag{A.16}$$

where $\boldsymbol{n}$ is the unit normal of the surface on which the surface divergence is defined. If we use the superscript $^+$ for vector fields in $\mathcal{V}_{h_0}^+$ and the superscript $^-$ for vector fields in $\mathcal{V}_{h_0}^-$, the application of the above identity, on opposite sides of the surface $\mathcal{S}$, leads to

$$\begin{aligned}
\nabla_s \cdot \boldsymbol{J}_S &= \lim_{h \downarrow 0} \left[\nabla_s \cdot \left(\boldsymbol{n} \times \boldsymbol{H}^+ \right) - \nabla_s \cdot \left(\boldsymbol{n} \times \boldsymbol{H}^- \right) \right] \\
&= \lim_{h \downarrow 0} \left[-\boldsymbol{n} \cdot \left(\nabla \times \boldsymbol{H}^+ - \nabla \times \boldsymbol{H}^- \right) \right] \\
&= \lim_{h \downarrow 0} \left\{ -\boldsymbol{n} \cdot \left[(\boldsymbol{J}^+ + s\boldsymbol{D}^+) - (\boldsymbol{J}^- + s\boldsymbol{D}^-) \right] \right\} = -\boldsymbol{n}(\boldsymbol{J}^+ - \boldsymbol{J}^-) - s\rho_S,
\end{aligned} \tag{A.17}$$

Hence, we have obtained the law of conservation of surface charge

$$\nabla_s \cdot \boldsymbol{J}_S + \boldsymbol{n} \cdot (\boldsymbol{J}^+ - \boldsymbol{J}^-) + s\rho_S = 0. \tag{A.18}$$

A.4   Vector potential for a surface current density

The extension of a vector field defined on a surface $\mathcal{S}$ to a vector field defined on a volume $\mathcal{V}$, as discussed in Section A.1, suggests that the vector and scalar potentials, as defined in Eqs (2.38) and (2.39), for the electromagnetic field in the presence of a surface current density assume the form

$$\boldsymbol{A}(\boldsymbol{r}) = \iint\limits_{\mathcal{S}} G(\boldsymbol{r} - \boldsymbol{r}') \boldsymbol{J}_S(\boldsymbol{r}') dA', \tag{A.19a}$$

$$\Phi(\boldsymbol{r}) = -\iint\limits_{\mathcal{S}} G(\boldsymbol{r} - \boldsymbol{r}') \nabla_s \cdot \boldsymbol{J}_S(\boldsymbol{r}') dA', \tag{A.19b}$$

where $\mathcal{S}$ is the surface on which the surface current density $\boldsymbol{J}_S$ is defined. For continuously differentiable $\boldsymbol{J}_S$ and $\nabla_s \cdot \boldsymbol{J}_S$, we can define a limiting process, in which the point of observation $\boldsymbol{r}$ approaches the surface $\mathcal{S}$ from one side. A careful examination shows that [14, Sections 2.5 & 2.6]

$$\lim_{h \downarrow 0} (\nabla \times \boldsymbol{A}) (\boldsymbol{r} \pm h\boldsymbol{n}(\boldsymbol{r})) = \mp \frac{\boldsymbol{n}(\boldsymbol{r}) \times \boldsymbol{J}_S(\boldsymbol{r})}{2} + (\nabla \times \boldsymbol{A}) (\boldsymbol{r}), \tag{A.20a}$$

$$\lim_{h \downarrow 0} (\nabla \Phi) (\boldsymbol{r} \pm h\boldsymbol{n}(\boldsymbol{r})) = \pm \frac{\boldsymbol{n}(\boldsymbol{r}) \nabla_s \cdot \boldsymbol{J}_S(\boldsymbol{r})}{2} + (\nabla \Phi) (\boldsymbol{r}), \tag{A.20b}$$

where r is a point on $\mathcal{S}$ and where the integrals in the definition of the potentials exist in the sense of a Cauchy principal value. If we insert the potentials of Eq. (A.19) into Eqs (2.38) and (2.39), the resulting fields satisfy Maxwell's equations in free space outside $\mathcal{S}$ and the radiation conditions (2.32). The boundary conditions (2.13) are satisfied, owing to Eq. (A.20). Finally, owing to the definition of the surface divergence, the potentials satisfy the Lorenz gauge. Therefore, the pertaining definitions of the potentials are in fact the potentials we are looking for and they are consistent with the potentials for volume current and charge densities of Eq. (2.43).

Appendix B

Scattering by a straight thin wire

B.1 Representation of the Green's function in cylindrical coordinates

We will derive an expression for the Green's function for free space, tailored to cylindrical problems. First, we use the integral [21, page 95, Eq. (53)] or [29, Section 6.677, Eq. (5)]

$$
\begin{aligned}
\pi \frac{\exp(-jy\sqrt{a^2+b^2})}{\sqrt{a^2+b^2}} &= 2\int_0^\infty dt\, \cos(bt) K_0(a\sqrt{t^2-y^2}) \\
&= \int_{-\infty}^\infty dt\, \exp(-jbt) K_0(a\sqrt{t^2-y^2}).
\end{aligned}
\tag{B.1}
$$

Further we use Gegenbauer's addition theorem [21, page 44, Eq. (4)]

$$
K_0(w) = I_0(z)K_0(Z) + 2\sum_{n=1}^\infty I_n(z)K_n(Z)\cos(n\varphi) \tag{B.2a}
$$

$$
= \sum_{n=-\infty}^\infty I_n(z)K_n(Z)\exp(-jn\varphi), \tag{B.2b}
$$

where $w = \sqrt{z^2+Z^2-2zZ\cos(\varphi)}$ and $z < Z$.

Choosing

$$a = \sqrt{r_>^2 + r_<^2 - 2r_> r_< \cos(\phi - \phi')}, \tag{B.3a}$$

$$b = (z - z'), \tag{B.3b}$$

$$t = k_z, \tag{B.3c}$$

$$y = -j\frac{s}{c_0}, \tag{B.3d}$$

$$z = \kappa \min\{r, r'\} = \kappa r_<, \tag{B.3e}$$

$$Z = \kappa \max\{r, r'\} = \kappa r_>, \tag{B.3f}$$

$$\varphi = \phi - \phi', \tag{B.3g}$$

$$\kappa = \sqrt{\frac{s^2}{c_0^2} + k_z^2}, \tag{B.3h}$$

we end up with

$$\frac{\exp(-sR/c_0)}{4\pi R} =$$
$$\frac{1}{4\pi^2} \int\limits_{-\infty}^{\infty} dk_z \sum_{n=-\infty}^{\infty} I_n(\kappa r_<) K_n(\kappa r_>) \exp[-jn(\phi - \phi')] \exp[-jk_z(z - z')], \tag{B.4}$$

where $R = \sqrt{r^2 + r'^2 - 2rr' \cos(\phi - \phi') + (z - z')^2}$.

B.2 Far-field approximations for thin wires

For the surface current density on the mantle of a cylinder with circular cross-section and central axis on the z-axis, we can write

$$\boldsymbol{J}_S = J_{S,\phi}\boldsymbol{u}_\phi + J_{S,z}\boldsymbol{u}_z = J_{S,\phi}\left[-\sin(\phi)\boldsymbol{u}_x + \cos(\phi)\boldsymbol{u}_y\right] + J_{S,z}\boldsymbol{u}_z. \tag{B.5}$$

From Eqs (2.38) and (2.46), we obtain the scattered magnetic field outside the mantle of the cylinder as

$$\boldsymbol{H}^s(\boldsymbol{r}) = \iint\limits_{\mathcal{M}} \nabla G(\boldsymbol{r} - \boldsymbol{r}') \times \boldsymbol{J}_S(\boldsymbol{r}')dA', \tag{B.6}$$

where all vectors are expressed in Cartesian coordinates and $\mathcal{M}$ denotes the mantle of the cylinder. Further, we have

$$\nabla G(\boldsymbol{r} - \boldsymbol{r}') = -G(\boldsymbol{r} - \boldsymbol{r}')\frac{\boldsymbol{r} - \boldsymbol{r}'}{|\boldsymbol{r} - \boldsymbol{r}'|} \left(\frac{s}{c_0} + \frac{1}{|\boldsymbol{r} - \boldsymbol{r}'|}\right). \tag{B.7}$$

For $s = j\omega$ and $|\boldsymbol{r}| \to \infty$, we obtain

$$\nabla G(\boldsymbol{r} - \boldsymbol{r}') \doteq -\frac{j\omega G(\boldsymbol{r} - \boldsymbol{r}')}{c_0} \frac{\boldsymbol{r}}{|\boldsymbol{r}|}. \tag{B.8}$$

Hence, for the magnetic field in the far-field region, we obtain the approximation

$$\boldsymbol{H}^s(\boldsymbol{r}) \doteq -\frac{j\omega}{c_0} \left(\frac{\boldsymbol{r}}{|\boldsymbol{r}|} \times \iint_{\mathcal{M}} G(\boldsymbol{r} - \boldsymbol{r}') \boldsymbol{J}_S(\boldsymbol{r}') \right) dA', \tag{B.9}$$

for $|\boldsymbol{r}| \to \infty$. For $s = j\omega$, the scattered electromagnetic field satisfies the radiation conditions of Section 2.4. Hence, we can employ Eq. (2.33a) to express the scattered electric field in the far-field region as

$$\boldsymbol{E}^s(\boldsymbol{r}) \doteq \frac{j\omega Z_0}{c_0} \frac{\boldsymbol{r}}{|\boldsymbol{r}|} \times \left(\frac{\boldsymbol{r}}{|\boldsymbol{r}|} \times \iint_{\mathcal{M}} G(\boldsymbol{r} - \boldsymbol{r}') \boldsymbol{J}_S(\boldsymbol{r}') dA' \right), \tag{B.10}$$

for $|\boldsymbol{r}| \to \infty$. If we introduce standard spherical coordinates for $\boldsymbol{r}$, we can readily show that E_θ^s and H_ϕ^s are generated by $J_{S,z}$ and that E_ϕ^s and H_θ^s are generated by $J_{S,\phi}$. In the remaining part of this section, we will focus on E_θ^s and H_ϕ^s. For these components, we have

$$H_\phi^s(\boldsymbol{r}) \doteq \frac{j\omega \sin(\theta)}{c_0} \iint_{\mathcal{M}} G(\boldsymbol{r} - \boldsymbol{r}') J_{S,z}(\boldsymbol{r}') dA', \tag{B.11a}$$

$$E_\theta^s(\boldsymbol{r}) \doteq j\omega\mu_0 \sin(\theta) \iint_{\mathcal{M}} G(\boldsymbol{r} - \boldsymbol{r}') J_{S,z}(\boldsymbol{r}') dA', \tag{B.11b}$$

for $|\boldsymbol{r}| \to \infty$. To evaluate the integral in the above expressions, we write $J_{S,z}$ in a Fourier series in the ϕ-direction, i.e.,

$$J_{S,z}(\phi, z) = \sum_{m=-\infty}^{\infty} \breve{J}_{S,z}(m, z) \exp(-jm\phi), \tag{B.12}$$

and we use Eq. (B.4), to arrive at

$$\iint_{\mathcal{M}} G(\boldsymbol{r} - \boldsymbol{r}') J_{S,z}(\boldsymbol{r}') dA' =$$

$$\int_0^L dz' \int_{-\pi}^{\pi} a d\phi' \sum_{m=-\infty}^{\infty} \breve{J}_{S,z}(m, z') \exp(-jm\phi') \tag{B.13}$$

$$\times \frac{1}{4\pi^2} \int_{-\infty}^{\infty} dk_z \sum_{n=-\infty}^{\infty} I_n(\kappa a) K_n(\kappa r) \exp[-jn(\phi - \phi')] \exp[-jk_z(z - z')],$$

where L is the length of the cylinder, and a is the radius of the circular cross-section. Further, we have used $r_> = r$ and $r_< = a$, which indicates that the distance between the z-axis and the observation point $\boldsymbol{r}$ is at least a. The integral over ϕ' can now be evaluated and we obtain

$$
\iint\limits_{\mathcal{M}} G(\boldsymbol{r} - \boldsymbol{r}') J_{S,z}(\boldsymbol{r}') dA' =
$$

$$
\frac{a}{2\pi} \int\limits_0^L dz' \int\limits_{-\infty}^\infty dk_z \sum_{n=-\infty}^\infty \breve{J}_{S,z}(n, z') I_n(\kappa a) K_n(\kappa r) \exp(-jn\phi) \exp[-jk_z(z - z')]. \tag{B.14}
$$

Finally, we have the asymptotic expansions

$$
I_n(z) = O(z^n) \quad z \to 0, \tag{B.15a}
$$

$$
K_n(z) = O\left[\frac{\exp(-z)}{\sqrt{z}}\right] \quad z \to \infty, \tag{B.15b}
$$

which show that the component $\breve{J}_{S,z}(0, z')$, i.e., the ϕ-independent part of the surface current density in the z-direction, dominates the far field of E_θ^s and H_ϕ^s, in case $a \ll \lambda = (2\pi c_0)/\omega$.

Appendix C

Integrals in closed form for the gradient

The proposed discretization for the derivative with respect to length in Section 5.3, leads to integrals defined on rectangular domains, which are oriented along the x- and y-axis. The pertaining integrals are

$$\iint \frac{x^2}{x^2+y^2}dxdy = \frac{xy}{2} + \frac{x^2}{2}\arctan\left(\frac{y}{x}\right) + \frac{y^2}{2}\arctan\left(\frac{x}{y}\right), \tag{C.1a}$$

$$\iint \frac{x^3}{x^2+y^2}dxdy = \frac{x^2y}{6} - \frac{y^3}{6}\ln\left(x^2+y^2\right) + \frac{y^3}{9} + \frac{x^3}{3}\arctan\left(\frac{y}{x}\right), \tag{C.1b}$$

$$\iint \frac{x^2y}{x^2+y^2}dxdy = \frac{xy^2}{3} - \frac{y^3}{3}\arctan\left(\frac{x}{y}\right) + \frac{x^3}{6}\ln\left(1+\frac{y^2}{x^2}\right), \tag{C.1c}$$

$$\iint \frac{x^2}{\left(x^2+y^2\right)^{3/2}}dxdy = y\ln\left(x+\sqrt{x^2+y^2}\right), \tag{C.1d}$$

$$\iint \frac{x^3}{\left(x^2+y^2\right)^{3/2}}dxdy = y\sqrt{x^2+y^2}, \tag{C.1e}$$

$$\iint \frac{x^2y}{\left(x^2+y^2\right)^{3/2}}dxdy = -\frac{x}{2}\sqrt{x^2+y^2} + \frac{y^2}{2}\ln\left(x+\sqrt{x^2+y^2}\right). \tag{C.1f}$$

Appendix D

Numerical computation of the inverse Laplace Transformation

Consider the following time-domain signal

$$
\mathcal{P}(t) = \begin{cases} 0 & \text{for } t < 0, \\ A\sin^2(\alpha t) & \text{for } 0 < t < \pi/\alpha, \\ 0 & \text{for } t > \pi/\alpha. \end{cases} \tag{D.1}
$$

The Laplace transform of $\mathcal{P}(t)$ is given by

$$
P(s) = \frac{2\alpha^2 A\left[1 - \exp(-s\pi/\alpha)\right]}{s(s^2 + 4\alpha^2)}. \tag{D.2}
$$

We are interested in computing a numerical approximation of $\mathcal{P}(t)$ from $P(s)$. We recall the definition of the inverse Laplace Transformation of Eq. (2.8) for a causal, real-valued time-domain signal $\mathcal{F}(t)$

$$
\mathcal{F}(t) = \frac{\exp(\delta t)}{\pi}\mathrm{Re}\left\{\int_0^\infty F(\delta + j\omega)\exp(j\omega t)d\omega\right\}. \tag{D.3}
$$

To arrive at an efficient numerical scheme for the inverse Laplace transformation, we truncate the integration interval at $\omega = \omega_{max}$, which is determined by the decay of $F(\delta + j\omega)$ for $\omega \to \infty$. The error in the time-domain signal, due to this approximation, can be estimated from Parseval's identity. We approximate the integral over ω by a repeated trapezoidal

rule, to arrive at

$$\mathcal{F}(t) = \frac{\exp(\delta t)}{\pi} \text{Re} \left\{ \sum_{n=0}^{N-1} F(\delta + jn\Delta\omega) \exp(jn\Delta\omega t) w_n \right\}, \tag{D.4}$$

where

$$\Delta\omega = \frac{\omega_{max}}{N}, \tag{D.5a}$$

$$w_0 = \frac{\Delta\omega}{2}, \tag{D.5b}$$

$$w_n = \Delta\omega \quad \text{for } n = 1, \ldots, N-1. \tag{D.5c}$$

In the repeated trapezoidal rule we have neglected the term $\mathcal{F}(\delta + j\omega_{max})$, since we assume that this is already small, owing to the definition of ω_{max}.

The next step is to sample the time variable t on a uniform grid. We write

$$t = m\Delta t. \tag{D.6}$$

For the inverse Laplace transformation, we obtain

$$\mathcal{F}(m\Delta t) = \frac{\exp(m\delta\Delta t)}{\pi} \text{Re} \left\{ \sum_{n=0}^{N-1} F(\delta + jn\Delta\omega) \exp(jmn\Delta\omega\Delta t) w_n \right\}. \tag{D.7}$$

We introduce the following notations

$$\mathcal{F}[m] = \mathcal{F}(m\Delta t), \tag{D.8a}$$

$$F[n] = \begin{cases} F(\delta + jn\Delta\omega) w_n & \text{for } n = 0, \ldots, N-1, \\ 0 & \text{for } n = N, \ldots, M-1, \end{cases} \tag{D.8b}$$

where M is a power of two, and $M \geq 2N$. The integer M is introduced to obtain a smaller time step and it results in a smoother interpolation of the computed time-domain signal. The sum in Eq. (D.7) assumes the form of an FFT if $m \leq M-1$ and

$$\Delta\omega\Delta t = \frac{2\pi}{M}. \tag{D.9}$$

We end up with

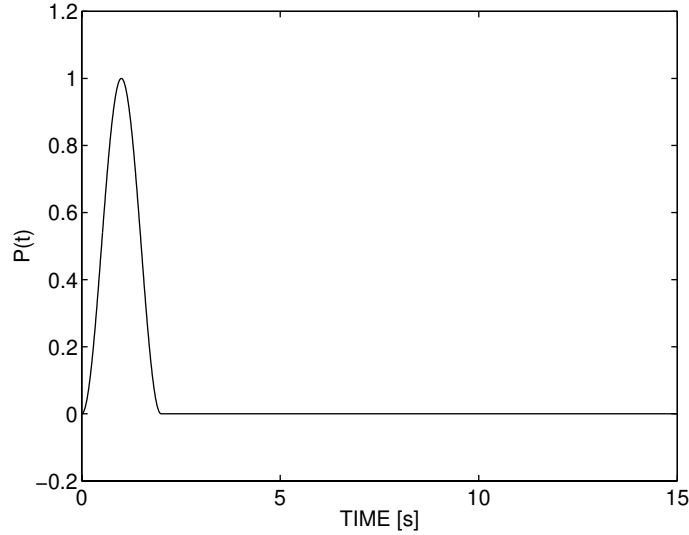$$\mathcal{F}[m] = \frac{\exp(m\delta\Delta t)}{\pi} \text{Re} \left\{ \sum_{n=0}^{M-1} F[n] \exp(j2\pi mn/M) \right\}. \tag{D.10}$$

Figure D.1: numerical inversion of the Laplace transform for $\mathcal{P}(t)$ with $\delta = 0.5$ s^{-1}, $A = 1$, $\alpha = \pi/2$ rad/s, $\omega_{max} = 400$ rad/s and $M = 2N = 2^{11}$.

We illustrate the capabilities of this numerical approximation of the inverse Laplace transformation with the aid of the time-domain signal $\mathcal{P}(t)$. We compute an approximation of $\mathcal{P}(t)$ by means of Eq. (D.10) and Eq. (D.2) with $A = 1$, $\alpha = \pi/2$ rad/s, $\omega_{max} = 400$ rad/s and $M = 2N = 2^{11}$. The results for $\mathcal{P}(t)$ in the first 15 seconds for $\delta = 0.5$ s^{-1} and $\delta = 1.5$ s^{-1} are given in Figure D.1 and Figure D.2, respectively. From these figures, we observe that the time-domain signal becomes unreliable when δt becomes larger than 12. This is caused by the effect that, especially for large values of m, the factor $\exp(m\delta\Delta t)$ in (D.10) amplifies the errors in the sampled time signal that results from the Fast Fourier Transformation. In the case of the time-domain signal $\mathcal{P}(t)$, it is still possible to use $\delta = 0$, since the Laplace transform $P(s)$ does not have a pole on the imaginary s-axis. However, if we consider the time-domain signal $\mathcal{Q}(t)$, defined as

$$\mathcal{Q}(t) = \int\limits_{0}^{t} \mathcal{P}(\tau)d\tau, \tag{D.11}$$

we have a pole at $s = 0$ and the corresponding Laplace transform is given by

$$Q(s) = \frac{P(s)}{s}. \tag{D.12}$$

The results of the numerical reconstruction of $\mathcal{Q}(t)$ for $\delta = 1.5$ is given in Figure D.3. We observe that the numerical reconstruction becomes unreliable for δt larger than 18.
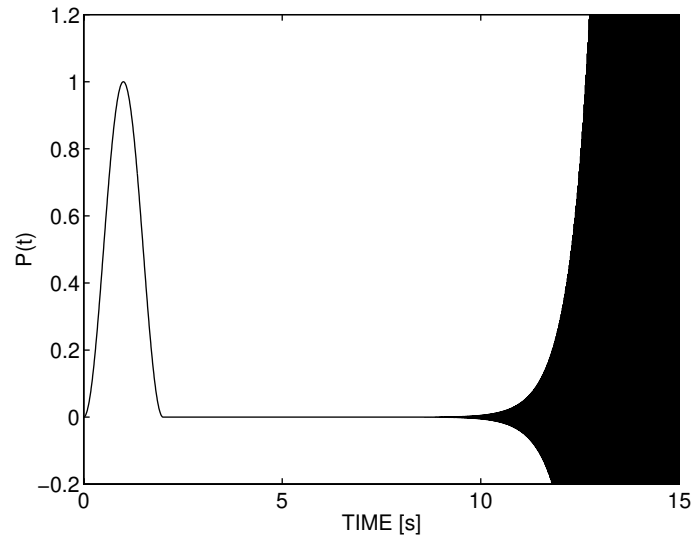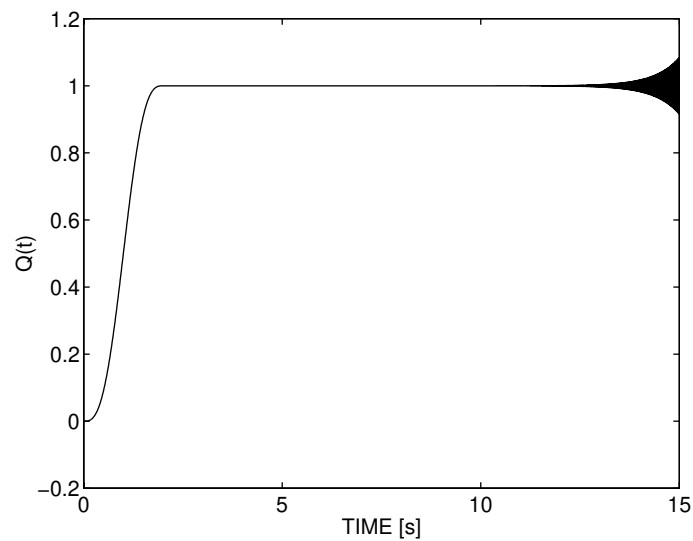
Figure D.2: numerical inversion of the Laplace transform for $\mathcal{P}(t)$ with $\delta = 1.5$ s^{-1}, $A = 1$, $\alpha = \pi/2$ rad/s, $\omega_{max} = 400$ rad/s and $M = 2N = 2^{11}$.

Figure D.3: numerical inversion of the Laplace transform for $\mathcal{Q}(t)$ with $\delta = 1.5$ s^{-1}, $A = 1$, $\alpha = \pi/2$ rad/s, $\omega_{max} = 400$ rad/s and $M = 2N = 2^{11}$.

Bibliography

[1] T. Abboud and F. Starling, "Scattering of an electromagnetic wave by a screen", in Boundary Value Problems and Integral Equations in Non-Smooth Domains, Lecture Notes in Pure and Applied Mathematics, vol. 167, p. 1-17, Marcel Dekker Inc., New York, 1995.

[2] A. Abubakar, "Three-dimensional nonlinear inversion of electrical conductivity", Ph.D. Thesis, Delft Univerity Press, Delft, 2000.

[3] R.A. Adams, "Sobolev spaces", Academic Press, London, 1975.

[4] E.E. Altshuler and D.S. Linden, "Wire-antenna design using genetic algorithms", IEEE Antennas Propagat. Mag., vol. 39, no. 2, p. 33-43, 1997.

[5] J.W. Bandler, R.M. Biernacki, S.H. Chen, P.A. Grobelny, and R.H. Hemmers, "Space mapping technique for electromagnetic optimization", IEEE Trans. Microwave Theory Tech., vol. 42, p. 2536-2544, 1994.

[6] P.M. van den Berg, "Iterative computational techniques in scattering based upon the integrated square error criterion", IEEE Trans. Antennas Propagat., vol. 32, p. 1063-1071, 1984.

[7] P.M. van den Berg, "Iterative schemes based on the minimization of the error in field problems", Electromagnetics, vol. 5, p. 237-262, April 1985.

[8] E. Bleszynski, M. Bleszynski, and T. Jaroszewicz, "AIM: adaptive integral method for solving large-scale electromagnetic scattering and radiation problems", Radio Sci., vol. 31, p. 1225-1251, 1996.

[9] J.J. Bowman, T.B.A. Senior, and P.L.E. Uslenghi (eds), "Electromagnetic and acoustic scattering by simple shapes", Hemisphere Publishing Corporation, New York, 1987.

[10] A. Brooke, D. Kendrick, A. Meeraus, R. Raman, and R.E. Rosenthal, "GAMS, a user's guide", GAMS Development Corporation, Washington DC, 1998.

[11] M. Cessenat, "Mathematical methods in electromagnetism, linear theory and applications", World Scientific, Singapore, 1996.

[12] D.K. Cheng, "Gain optimization for Yagi-Uda arrays", IEEE Antennas Propagat. Mag., vol. 33, no. 3, p. 42-45, 1991.

[13] W.C. Chew, J. Jin, and E. Michielssen (eds), "Fast and efficient algorithms in computational electromagnetics", Artech House, London, 2001.

[14] D. Colton and R. Kress, "Integral equations in scattering theory", Wiley, New York, 1983.

[15] A.R. Conn, N.I.M. Gould, and Ph.L. Toint, "A globally convergent augmented Lagrangian algorithm for optimization with general constraints and simple bounds", SIAM J. Numer. Anal. 28, p. 545-572, 1991.

[16] A.R. Conn, N.I.M. Gould, and Ph.L. Toint, "LANCELOT: A Fortran package for large-scale nonlinear optimization (Release A)", Springer Series in Computational Mathematics 17, Springer-Verlag, Heidelberg, New York, 1992.

[17] R. Courant and D. Hilbert, "Methods of mathematical physics", Volume II, Wiley Classics Edition, Wiley, New York, 1989.

[18] R. Dautray and J.-L. Lions, "Mathematical analysis and numerical methods for science and technology, volume 3: spectral theory and applications", Springer-Verlag, Berlin, 1990.

[19] Ph. De Donker, "A potential integral equation method for electromagnetic scattering by penetrable bodies", IEEE Trans. Antennas Propagat., vol. 49, p. 1037-1042, 2001.

[20] D. De Zutter, J. Sercu, T. Dhaene, J. De Geest, F. Demuynck, S. Hammadi, and C.P. Huang, "Recent trends in the integration of circuit optimization and full-wave electromagnetic analysis", to be published in: IEEE Trans. Microwave Theory Tech., special issue on electromagnetics-based optimization of microwave components and ciruits, January 2004.

[21] A. Erdélyi (ed.), "Higher transcendental functions", vol. 2, McGraw-Hill, New York, 1953.

[22] G. Fikioris, "The approximate integral equation for a cylindrical scatterer has no solution", JEWA, vol. 15, p. 1153-1159, 2001.

[23] R. Fletcher, "Practical methods of optimization", second edition, Wiley, Chichester, 1987.

[24] R. Fletcher and S. Leyffer, "Nonlinear programming without a penalty function", University of Dundee Numerical Analysis Report, NA/171, 22 September 1997, revised 22 December 1998.

[25] R. Fletcher and S. Leyffer, "User manual for filterSQP", University of Dundee Numerical Analysis Report NA/181, April 1998, version 1, June 1998, updated March 1999.

[26] R. Fourer, D.M. Gay, and B.W. Kernighan, "AMPL, A Modelling Language for Mathematical Programming", Boyd and Fraser Publ. Co., Danvers MA, 1993.

[27] Ph. E. Gill, W. Murray, and M.A. Saunders, "SNOPT: an SQP algorithm for large-scale constrained optimization", Report NA 97-2, Dept. of Mathematics, University of California, San Diego (also: Report SOL 97-3, Dept. of EESOR, Stanford University).

[28] A.W. Glisson and D.R. Wilton, "Simple and efficient numerical methods for problems of electromagnetic radiation and scattering from surfaces", IEEE Trans. Antennas Propagat., vol. 28, p. 593-603, 1980.

[29] I.S. Gradshteyn and I.M. Ryzhik, "Table of integrals, series, and products", Academic Press, New York, 1980.

[30] R.D. Graglia and D.R. Wilton, "Vector expansion functions for singular fields: a review", Proc. ICEAA 2001, p.841-843, September 10-14 2001, Torino, Italy.

[31] A. Griewank, "On automatic differentiation", Mathematical Programming: Recent Developments and Applications, M. Iri and K. Tanabe (eds), p. 83-108, Kluwer Academic Publishers, Amsterdam, 1989.

[32] C. Groetsch, "Elements of applicable functional analysis", Marcel Dekker Inc., New York, 1980.

[33] E.J. Haug, K.K. Choi, and V. Komkov ,"Design sensitivity analysis of structural systems", Academic Press, London, 1986.

[34] K. Hongo and H. Serizawa, "Diffraction of electromagnetic plane wave by a rectangular plate and a rectangular hole in the conducting plane", IEEE Trans. Antennas Propagat., vol. 47, p. 1029-1041, 1999.

[35] G.C. Hsiao and R.E. Kleinman, "Mathematical foundations for error estimation in numerical solutions of integral equations in electromagnetics", IEEE Trans. Antennas Propagat., vol. 45, p. 316-328, 1997.

[36] D.S. Jones, "The theory of electromagnetism", Pergamon, Oxford, 1964.

[37] D.S. Jones ,"Note on the integral equation for a straight wire antenna", IEE Proc., vol. 128, Part H, p. 114-116, 1981.

[38] E.A. Jones and W.T. Joines, "Design of Yagi-Uda antennas using genetic algorithms", IEEE Trans. Antennas Propagat, vol. 45, p. 1386-1392.

[39] K. Jörgens, "Linear integral operators", Pitman Advanced Publishing Program, Boston, 1982.

[40] L. Knockaert and D. De Zutter, "Laguerre-SVD reduced-order modeling", IEEE Trans. Microwave Theory Tech., vol. 48, p. 1469-1475, 2000.

[41] M.A. Krasnosel'skii, G.M. Vainikko, P.P. Zabreiko, Ya.B. Rutitskii, and V.Ya. Stetsenko, "Approximate solution of operator equations", Wolters-Noordhoff, Groningen, 1972.

[42] R. Kress, "Linear integral equations", Springer-Verlag, Berlin, 1989.

[43] E.S.A.M. Lepelaars, "Electromagnetic pulse distortion in living tissue", Med. Biol. Eng. Comput., vol. 34, p. 213-220, May 1996.

[44] D. Lesselier, "Optimization techniques and inverse problems: reconstruction of conductivity profiles in the time domain", IEEE Trans. Antennas Propagat., Vol. 30, p. 59-65, 1982.

[45] J.L. Lions and E. Magenes, "Non-homogeneous boundary value problems and applications", Springer-Verlag, Berlin, 1972.

[46] G. Little and J.B. Reade, "Eigenvalues of analytic kernels", SIAM J. Math. Anal., vol 15, p. 133-136, January 1984.

[47] C. Müller, "Foundations of the mathematical theory of electromagnetic waves", Springer-Verlag, Berlin, 1969.

[48] B.A. Murtagh and M.A. Saunders, "MINOS 5.4 User's Guide", Report SOL 83-20R, Systems Optimization Laboratory, Stanford University, December 1983 (revised February 1995).

[49] A.I. Nosich, "The method of analytical regularization in wave-scattering and eigenvalue problems: foundations and review of solutions", IEEE Antennas Propagat. Mag., vol. 41, no. 3, p. 25-49, 1999.

[50] Z.Q. Peng and A.G. Tijhuis, "Transient scattering by a lossy dielectric cylinder: marching-on-in-frequency approach", JEWA, vol. 7, p. 739-763, 1993.

[51] A.J. Poggio and E.K. Miller, "Integral equation solutions of three-dimensional scattering problems", in Computer techniques for electromagnetics, R. Mittra (ed.), p. 159-264, Pergamon, New York, 1973.

[52] S.M. Rao, D.R. Wilton, and A.W. Glisson, "Electromagnetic scattering by surfaces of arbitrary shape", IEEE Trans. Antennas Propagat., vol. 30, p. 409-418, 1982.

[53] F. Rellich, "Über das asymptotische Verhalten der Lösungen von $\Delta u + \lambda u = 0$ in unendlichen Gebeeten", Jahresbericht der Deutschen Mathematiker-Vereinigung, Vol. 53, p. 57-64, 1943.

[54] F. Riesz and B. Sz.-Nagy, "Functional Analysis", Dover publications Inc., New York, 1990.

[55] B.P. Rynne, "The well-posedness of the integral equations for thin wire antennas", IMA J. Appl. Maths., vol. 49, p. 35-44, 1992.

[56] B.P. Rynne, "The well-posedness of the integral equations for thin wire antennas with distributional incident fields", Quart. J. Mech. Appl. Math., vol. 52, p. 489-497, 1999.

[57] B.P. Rynne, "Convergence of Galerkin method solutions of the integral equation for thin wire antennas", Adv. Comp. Math., vol. 12, p. 251-259, 2000.

[58] B.P. Rynne, "On the well-posedness of Pocklington's equation", JEWA, vol. 14, p. 1489-1503, 2000.

[59] Y. Saad, "Iterative methods for sparse linear systems", PWS publishing company, Boston, 1996.

[60] D.H. Schaubert, D.R. Wilton, and A.W. Glisson, "A tetrahedral modeling method for electromagnetic scattering by arbitrarily shaped imhomogeneous dielectric bodies", IEEE Trans. Antennas Propagat., vol. 32, p. 77-85, 1984.

[61] Yu.G. Smirnov, "The solvabiltiy of vector integro-differential equations for the problem of the diffraction of an electromagnetic field by screens of arbitrary shape", Computat. Math. Mathem. Phys., vol. 33, p. 1263-1273, 1993.

[62] J. Sokolowski and J.-P. Zolesio, "Introduction to shape optimization, shape sensitivity analysis", Springer-Verlag, Berlin, 1992.

[63] P. Spellucci, "An SQP method for general nonlinear programs using only equality constrained subproblems", Math. Programming, vol. 82, Ser. A, p. 413-448, 1998.

[64] P. Spellucci, "A new technique for inconsistent QP problems in the SQP method", Math. Methods Oper. Res., vol. 47, p. 355-400, 1998.

[65] J.A. Stratton, "Electromagnetic theory", McGraw-Hill, London, 1941.

[66] W.L. Stutzman and G.A. Thiele, "Antenna theory and design", second edition, Wiley, Chichester, 1998.

[67] D. Sun, J. Manges, X. Yuan, and Z. Cendes, "Spurious modes in finite-element methods", IEEE Antennas Propagat. Mag., vol. 37, no. 5, p. 12-24, 1995.

[68] G.C. Temes and J.W. LaPatra, "Introduction to circuit synthesis and design", McGraw-Hill, New York, 1977.

[69] D. Thompson (ed.), "The concise Oxford dictionary of current English", ninth edition, Oxford University Press Inc., New York, 1998.

[70] A.G. Tijhuis, "Electromagnetic inverse profiling, theory and numerical implementation", VNU Science Press B.V., Utrecht, 1987.

[71] A.G. Tijhuis and Z.Q. Peng, "Marching-on-in-frequency method for solving integral equations in transient electromagnetic scattering", Proc. IEE, Part H, vol. 138, p. 347-355, 1991.

[72] A.G. Tijhuis, Z. Peng, and A. Rubio Bretones, "Transient excitation of a straight thin-wire segment: a new look at an old problem", IEEE Trans. Antennas Propagat., vol. 40, p. 1132-1146, 1992.

[73] A.G. Tijhuis, K. Belkebir, A.C.S. Litman, and B.P. de Hon, "Theoretical and computational aspects of 2-D inverse profiling", IEEE Trans. Geosci. Remote Sensing, vol. 39, p. 1316-1330, 2001.

[74] A.G. Tijhuis, M.C. van Beurden, and A.P.M. Zwamborn, "Iterative solution of field problems with a varying physical parameter", Elektrik (Turk. J. Elec. Engin.), special issue for Prof. Leopold B. Felsen's 75th birthday, vol. 10, p 163-183, 2002.

[75] J. Ureel and D. De Zutter, "Shape sensitivities of capacitances of planar conducting surfaces using the method of moments", IEEE Trans. Microwave Theory Tech., vol. 44, p. 198-207, 1996.

[76] J. Ureel and D. De Zutter, "A new method for obtaining shape sensitivities of planar microstrip structures by a full-wave analysis", IEEE Trans. Microwave Theory Tech., vol. 44, p. 249-260, 1996.

[77] R.J. Vanderbei, "LOQO User's Manual-Version 3.10", Statistics and Operations Research Technical Report No. SOR-97-08, Princeton University, School of Engineering and Applied Science, Department of Civil Engineering and Operations Research, Princeton, NJ, December 10, 1997.

[78] J. Van Bladel, "A discussion of Helmholtz' theorem", Electromagnetics, vol. 13, p. 95-110, 1993.

[79] I.N. Vekua, "New methods for solving elliptic equations", North-Holland Publishing Company, Amsterdam, 1967.

[80] S.S. Vinogradov, P.D. Smith, and E.D. Vinogradova, "Canonical problems in scattering and potential theory", CRC Press, London, 2001.

[81] D.R. Wilton, S.M. Rao, A.W. Glisson, D.H. Schaubert, O.M. Al-Bundak, and C.M. Butler, "Potential integrals for uniform and linear source distributions on polygonal and polyhedral domains", IEEE Trans. Antennas Propagat., vol. 32, p. 276-281, 1984.

[82] M.S. Zhdanov and S. Fang, "Quasi-linear series in three-dimensional electromagnetic modeling", Radio Sci., vol. 32, p. 2167-2188, 1997.

[83] C. Zhu, R. H. Byrd, P. Lu, and J. Nocedal, "Algorithm 778: L-BFGS-B: fortran subroutines for large-scale bound-constrained optimization", ACM TOMS, vol. 23, p. 550-560, 1997.

[84] A.P.M. Zwamborn, "Scattering by objects with electric contrast", Ph.D. Thesis, Delft Univerity Press, Delft, 1991.

[85] A.P.M. Zwamborn and P.M. van den Berg, "The weak form of the conjugate gradient method for plate problems", IEEE Trans. Antennas Propagat., vol. 39, p. 224-228, 1991.

[86] A.P.M. Zwamborn and P.M. van den Berg, "The three-dimensional weak form of the conjugate gradient FFT method for solving scattering problems", IEEE Trans. Microwave Theory Tech., 40, p. 1757-1766, 1992.

[87] A.P.M. Zwamborn and P.M. van den Berg, "Computation of electromagnetic fields inside strongly inhomogeneous objects by the weak conjugate gradient FFT method", JOSA A, vol. 11, p. 1414-1421, 1994.

Summary

When applying non-linear optimization techniques for design and detection in an electromagnetic environment, one is often confronted with the problem that large systems of equations have to be solved for a large number of parameter values. Without additional precautions, this leads to excessively long computation times. Therefore, it is important to construct methods, for which the total computation time in case of varying parameter values is strongly reduced. One way to achieve this would be to combine fast forward algorithms with an extrapolation technique. To examine this idea, we have studied three relevant scattering problems, i.e., the scattering by a perfectly conducting straight thin-wire antenna, by a perfectly conducting infinitely thin flat plate, and by a dielectric object. The latter two always have finite dimensions. In all cases, the scattering problem has been formulated in terms of an integro-differential equation.

Historically, there are two integro-differential equations for the thin wire, which are known as "exact" and "approximated". For the infinitely long straight wire, we show that both equations give the same solution in terms of analytic functions, provided that the excitation is restricted to sources outside the wire and that the proper excitation functions are used. For the finite wire it is known from the literature that the "exact" version is well-posed, which means that the solution to the equation exists, that it is unique, and that it varies continuously as a function of a continuously varying excitation. With the aid of these results, we demonstrate that the solution of the "approximated" version is unique and that the solution exists under certain conditions. Further, we show that the solutions does not necessarily vary continuously as a function of a continuously varying excitation. The behavior of the "approximated" version is illustrated by means of two simple numerical implementations.

For the scattering by a perfectly conducting infinitely thin flat plate, we construct an

efficient numerical scheme, in which the matrix-vector product can be computed by means of Fast Fourier Transformations (FFTs). For this case, we also consider two numerical schemes. The first one is based on an analytically modified version of the classical equation. The second one is a modification of a classical numerical scheme. The numerical solutions are computed by the conjugate-gradient (CG) method. The rate of convergence of the CG method for both schemes is quite distinct. This can be explained by results from functional analysis in the literature, which characterize the solution space of the integro-differential equation for the flat plate. Further, we formulate an analytic equation for the shape derivative for variations of the length or width of the plate. We compute this derivative numerically by solving a discretized version of the analytic formulation and by two finite-difference schemes. The finite-difference scheme that corresponds to a stretch of the coordinate system produces reliable results, in contrast to the finite-difference scheme that alters the mesh of the numerical system. This can be explained from the fact that the matrix elements in the first scheme vary analytically as a function of the length or width of the plate, whereas the matrix elements in the latter do not.

For the integro-differential equation that corresponds to the scattering problem by a dielectric body, we show that the formulation is well-posed. Further, we expose a weak point in the currently available numerical schemes for this equation.

For the three integro-differential equations, we examine the efficiency of parameter variations by using "marching on in anything". "Marching on in anything" is the generic term of the construction of initial estimates from solutions for preceding parameter values in combination with the conjugate-gradient method. Examples of parameters are: frequency, angle of incidence, length and width of an object, and also step size along a search direction in a non-linear optimization process. The initial estimate is used in an iterative technique to improve convergence. We use existing and generally accepted numerical implementations of the integro-differential equations for the three scattering problems, to exclude that considerations in our own implementations influence the efficiency of marching on in anything. We demonstrate the effect of the step size in the parameter variation, the error criterion of the CG method, and the presence of poles in the complex plane of the Laplace parameter by means of the example of the finite straight thin wire. The improvement in efficiency is remarkable for the thin-wire problem. For the flat plate and the dielectric body, we demonstrate a similar improvement in efficiency.

Finally, we consider the possibilities to optimize configurations of straight wires, such as

Yagi-Uda antennas and arrays of dipoles, by means of standard non-linear optimization techniques. We distinguish between introducing the physical model of the wire structure as a set of extra non-linear constraints and solving the physical model internally. The examples show that solving the physical model internally demands less robustness of the optimization strategy and software than the formulation of the physical model in terms of additional non-linear constraints.

Samenvatting

Bij het toepassen van niet-lineaire optimalisatie methoden voor ontwerp en detectie in een elektromagnetische omgeving wordt men geconfronteerd met het feit dat oplossingen van een groot stelsel vergelijkingen moeten worden berekend voor een groot aantal parameterwaarden. Zonder extra maatregelen leidt dit in het algemeen tot een buitensporig hoge rekentijd. Het is dus van belang om methoden te construeren waarvoor niet alleen een probleem voor een vaste parameterinstelling efficiënt kan worden opgelost, maar ook dat het vinden van de oplossing voor variërende parameterwaarden sterk in rekentijd wordt bekort. Eén manier om dit te bereiken is door snelle voorwaartse algoritmen te combineren met een extrapolatie techniek. Om dit idee te testen worden een drietal relevante verstrooiingsproblemen nader bekeken, te weten de verstrooiing aan een rechte dunne ideaal geleidende draad, aan een ideaal geleidende oneindig dunne vlakke plaat en een aan diëlektrisch lichaam. De laatste twee zijn van eindige afmetingen. In alle gevallen kan het verstrooiingsprobleem worden geformuleerd in termen van een integro-differentiaalvergelijking.

Voor de dunne draad zijn er historisch gezien twee integro-differentiaalvergelijkingen, bekend onder de benamingen "exact" en "benaderd". Voor de oneindig lange rechte draad wordt aangetoond dat beide varianten dezelfde oplossing geven in termen van analytische functies, aangenomen dat de excitatie beperkt wordt tot bronnen buiten de draad en dat de excitatiefuncties correct zijn opsteld. Vanuit de literatuur is bekend dat voor een eindige draad de "exacte" variant correct gesteld is, hetgeen betekent dat de oplossing van de vergelijking bestaat, uniek is, en continu variëert als functie van een continu variërende excitatie. In dit proefschrift wordt met behulp van deze resultaten aangetoond, dat de oplossing voor de "benaderde" variant uniek is en dat de oplossing bestaat onder zekere voorwaarden. Tevens wordt aangetoond dat de oplossing niet noodzakelijkerwijs continu variëert als functie van een continu variërende excitatie. Het gedrag van de "benaderde" versie wordt geïllustreerd met behulp van een tweetal eenvoudige numerieke implementa-

ties.

Voor de verstrooiing aan een ideaal geleidende oneindig dunne rechthoekige vlakke plaat wordt een efficiënt numeriek schema geconstrueerd, door het matrix-vector product met behulp van "Fast Fourier Transforms" (FFT's) te berekenen. Ook hier beschouwen we twee schema's. De eerste is gebaseerd op een analytisch gewijzigde versie van de klassieke vergelijking. De tweede is een gemodificeerde variant van een klassiek schema. De numerieke oplossing wordt berekend met behulp van de geconjugeerde gradiënten (CG) methode, waarbij een groot verschil optreedt in het convergentiegedrag van de CG-methode voor de twee numerieke schema's. Dit verschil kan worden verklaard aan de hand van functionaalanalytische resultaten uit de literatuur, die de oplosruimte van de integro-differentiaalvergelijking voor de vlakke plaat karakteriseren. Verder wordt de analytische formulering van de vormafgeleide voor variaties in de lengte of breedte van de plaat bepaald. Deze afgeleide wordt numeriek berekend op basis van deze analytische formulering en op basis van een tweetal differentieschema's. Het differentieschema dat correspondeert met een oprekking van het coördinatenstelsel geeft betrouwbare resultaten, in tegenstelling tot het differentie schema waarbij de vermazing van het numerieke systeem verandert. Dit kan worden verklaard doordat de matrixelementen van het eerste systeem analytisch variëren als functie van lengte en breedte, in tegenstelling tot die van het tweede systeem.

Voor de integro-differentiaalvergelijking die correspondeert met het probleem van de verstrooiing aan een diëlektrisch lichaam, wordt bewezen dat deze formulering correct gesteld is. Tevens wordt een zwak punt van de gangbare numerieke schema's voor deze vergelijking blootgelegd.

Voor de drie integro-differentiaal vergelijkingen wordt de efficiëntie van parametervariaties onderzocht door gebruik te maken van "marching on in anything". "Marching on in anything" is de verzamelnaam voor het construeren van beginschattingen uit oplossingen voor voorafgaande parameterwaarden in combinatie met de geconjugeerde gradiënten methode. Voorbeelden van parameters zijn: frequentie, hoek van inval, lengte en breedte van een object, maar ook stapgrootte langs de zoekrichting in een niet-lineair optimalisatie proces. Deze beginschatting wordt gebruikt in een iteratieve techniek, die gebaseerd is op het minimaliseren van een kwadratische fout, om de convergentie te bevorderen. Er wordt gebruik gemaakt van bestaande en algemeen geaccepteerde numerieke implementaties van de integro-diffentiaalvergelijkingen voor de drie verstrooiingsproblemen. Dit, om uit te sluiten dat afwegingen in onze eigen implementaties van invloed zijn op de efficiëntie van marching

on in anything. Het effect van stapgrootte in de parametervariatie, het afbreekcriterium van de CG-methode en de aanwezigheid van polen in het complexe vlak van de Laplace parameter wordt gedemonstreerd met het voorbeeld van de eindige rechte dunne draad. De met behulp van "marching on in anything" behaalde versnelling voor het draadprobleem is aanmerkelijk. Voor de plaat en het diëlektrisch lichaam wordt tenminste een vergelijkbare winst in efficiëntie aangetoond.

Het proefschrift besluit met een onderzoek naar de mogelijkheden om structuren van rechte draden, zoals Yagi-Uda antennes en arrays van dipolen, te optimaliseren met behulp van standaard niet-lineaire optimalisatie technieken. Hierbij wordt onderscheid gemaakt naar het inbrengen van het fysische model van de draadstructuren als extra niet-lineaire vergelijkingen en het intern oplossen van het fysische model. De voorbeelden laten zien dat het intern oplossen van het fysische model minder zware eisen stelt aan de optimalisatie strategie en software dan het formuleren van het fysische model in termen van extra niet-lineaire vergelijkingen.

Curriculum vitae

Martijn Constant van Beurden was born in Mariaheide, The Netherlands, on January 18, 1974. After he finished secondary school in 1992 at the Zwijsen College in Veghel, he started as a student in Electrical Engineering at the Eindhoven University of Technology. From February until September 1997, he performed his final project on the numerical modeling of array antennas at Hollandse Signaal Apparaten (currently Thales Nederland) to obtain the M.Sc. Degree (cum laude). He won the second prize of the IEEE Region 8 student paper contest and was awarded the C.I.V.I. prize for electrical engineering, both for his M.Sc. thesis. In October 1997, he started Ph.D. research at the Eindhoven University of Technology, under the supervision of prof. A.G. Tijhuis and prof. A.P.M. Zwamborn. From January until June 2000, he conducted research on the optimization of wire antennas at the Mathematics Department of the University of Dundee, under the supervision of prof. P.D. Smith and prof. R. Fletcher. In September 2000, he was appointed Assistant Professor at the Eindhoven University of Technology, while continuing his Ph.D. project.

Acknowledgements

In the first place, I would like express my gratitude towards my supervisors in Eindhoven: prof. Anton Tijhuis, prof. Peter Zwamborn and dr. Stef van Eijndhoven. Anton for his vision, continuing enthusiasm, and original points of view. Peter for being my link to practical relevance and applications, for allowing me to experiment with his software for the flat plate and the dielectric object, and for his positive attitude towards changes and life itself. Stef for his guidance in functional analysis and for all the discussions we had on research and other matters.

Also, I would like to thank the colleagues from the Mathematics Department of the University of Dundee. In particular, prof. Paul Smith and his family, and Stuart Booker and his wife Carolyn for making me and my wife feel at home in Scotland and in particular in Dundee. Prof. Roger Fletcher for his interest in my optimization and design problems, and dr. Sven Leyffer for providing all the information on optimization that I needed.

Further, I would like to thank all my friends and relatives, and my colleagues and students from the electromagnetics group in Eindhoven. In particular dr. Bas de Hon, with whom I had many conversations and discussions on matters related to work and other interesting topics. Also, I thank my parents for their support and interest and last but not least, I thank my wife Mariëlle for her love, patience, understanding, and support.